**Title**

Investigating the Variation of Temperature and Chemical Abundance of H II regions in Nearby Galaxies Observed with Integral Field Spectroscopy

**Author**

Rickards Vaught, Ryan Joseph

**Publication Date**

2024

UNIVERSITY OF CALIFORNIA SAN DIEGO

# Investigating the Variation of Temperature and Chemical Abundance of H II regions in Nearby Galaxies Observed with Integral Field Spectroscopy

A dissertation submitted in partial satisfaction of the
requirements for the degree Doctor of Philosophy

in

Physics

by

Ryan J. Rickards Vaught

Committee in charge:

Professor Karin Sandstrom, Chair
Professor James Day
Professor Alex Frano
Professor Dušan Kereš
Professor Shelley Wright

2024

The Dissertation of Ryan J. Rickards Vaught is approved, and it is acceptable in quality and form for publication on microfilm and electronically.

University of California San Diego

2024

# DEDICATION

I would like to dedicate this work to my partner Alanna, my friends, and to my family.

# EPIGRAPH

It’s a dangerous business, Frodo, going out your door. You step onto the road, and if you don’t keep your feet, there’s no knowing where you might be swept off to.

*-Samwise Gamgee*

# TABLE OF CONTENTS

LIST OF FIGURES

# LIST OF TABLES

# ACKNOWLEDGEMENTS

I would like to acknowledge Professor Karin Sandstrom for her guidance over the several years of my graduate studies. Karin has helped me navigate the transition from student to active participant in the field of galaxy evolution. Alongside her guidance, Karin provided me several opportunities to present my work all over the world. For her support, I will be forever thankful.

I would also like to thank my committee members: Prof. Dusan Keres, Prof. Shelley Wright, Prof. Alex Frano, and Prof. James Day for their time and patience in supervising and reviewing this dissertation. I also want to acknowledge my friend and colleague: Prof. Kate Rubin. Not only did she provide me great advice and opportunities as my Master's advisor, Kate has since become a dear friend to my Alanna and I. We have thoroughly enjoyed our South Park meet-ups.

I would like also to thank Dr. Kathryn Kreckel, Dr. Francesco Belfiore, Dr. Daniel Gonzalez, Evan Anderson, Ian Collicott, Prof. Doug Leonard, Dr. Chris McCarthy, Prof. Ron Marzke, Team Nearby Galaxies: Dr. Yu-Hsuan "Eltha" Teng, Dr. I-Da Chiang, Dr. Petia Yanchulova Merica-Jones, Lindsey Hands, Ilyse Clark and Hanna Koziol for their advice, support, and friendship. Finally, I am grateful for the support of my partner Alanna Rickards Vaught and our dog Jelly. I thank them for their patience, especially when having to skip a walk!

Chapter 2, in full, is a reformatted reprint of the material as it appears in Rickards Vaught, Ryan J.; Sandstrom, Karin M.; Belfiore, Francesco; Kreckel, Kathryn; Méndez-Delgado, José E.; Emsellem, Eric; Groves, Brent; Blanc Guillermo A.; Dale, Daniel A.; Egorov Oleg V; Glover, Simon C. O.; Grasha, Kathryn; Klessen, Ralf S.; Neumann, Justus; Williams Thomas G. "Investigating the Drivers of Electron Temperature Variations in H II Regions with Keck-KCWI and VLT-MUSE," The Astrophysical Journal, 966, 130, 2024. The dissertation author is the primary investigator and author of this material.

Chapter 3, in part is currently being prepared for submission in The Astrophysical Journal. Rickards Vaught, Ryan J.; Sandstrom, Karin. M. The dissertation author is the primary investigator and author of this material.

Chapter 4, in full, is a reformatted reprint of the material as it appears in Rickards Vaught, Ryan J.; Sandstrom, Karin. M.; Hunt, Leslie. K.;“Keck Cosmic Web Imager Observations of He II Emission in I Zw 18,” The Astrophysical Journal Letters, 911, L17, 2021. The dissertation author was the primary investigator and author of this paper.

# VITA

| | |
|---|---|
| 2016 | Bachelor of Science, San Francisco State University |
| 2018 | Master of Science, San Diego State University |
| 2024 | Doctor of Philosophy, University of California San Diego |

# PUBLICATIONS

Rickards Vaught, Ryan J.; Rubin, Kate H. R.; Arrigoni Battaia, Fabrizio; Prochaska, Jason. X.; Hennawi, Joseph F. “A VLT/FORS2 Narrowband Imaging Search for Mg II Emission around z $\sim$ 0.7 Galaxies,” The Astrophysical Journal, 879, 7, 2019.

Rickards Vaught, Ryan J.; Sandstrom, Karin. M.; Hunt, Leslie. K.; “Keck Cosmic Web Imager Observations of He II Emission in I Zw 18,” The Astrophysical Journal Letters, 911, L17, 2021.

Rickards Vaught, Ryan J.; Sandstrom, Karin M.; Belfiore, Francesco; Kreckel, Kathryn; Méndez-Delgado, José E.; Emsellem, Eric; Groves, Brent; Blanc Guillermo A.; Dale, Daniel A.; Egorov Oleg V; Glover, Simon C. O.; Grasha, Kathryn; Klessen, Ralf S.; Neumann, Justus; Williams Thomas G. “Investigating the Drivers of Electron Temperature Variations in H II Regions with Keck-KCWI and VLT-MUSE,” The Astrophysical Journal, 966, 130, 2024.

# ABSTRACT OF THE DISSERTATION

## Investigating the Variation of Temperature and Chemical Abundance of H II regions in Nearby Galaxies Observed with Integral Field Spectroscopy

by

Ryan J. Rickards Vaught

Doctor of Philosophy in Physics

University of California San Diego, 2024

Professor Karin Sandstrom, Chair

The interstellar medium (ISM) consists of the gas and dust in between stars. A critical component that regulates the physics of the ISM is its chemical abundance (i.e. metallicity). Due to the stellar nucleosynthetic origin of metals, a galaxy's metallicity reflects its history of chemical enrichment from stars. A number of astrophysical phenomena (e.g. supernovae, stellar feedback) can mix and redistribute metals throughout the ISM. To distinguish the impact of these competing effects, it is crucial that we observationally constrain the large and small scale variations of metallicity across the ISM. In this dissertation, we investigate the connection between H II region electron temperatures, important for determining metallicities, and the physical properties of the ISM. Additionally, we investigate the source of ionizing photons in an extremely low metallicity galaxy.

In Chapter 2, we compare multi-ion H II region electron temperature measurements to several ISM properties such as electron density, ionization parameter, and molecular gas velocity dispersion. We measure anomalously high doubly-ionized oxygen temperatures from auroral lines in regions with high molecular gas velocity dispersion and low ionization parameter. These anomalous temperature measurements may be explained by the presence of low-velocity shocks.

In Chapter 3, we present H II region metallicities measured using nitrogen and sulfur temperature sensitive lines. We find that temperatures inferred from doubly-ionized sulfur emission lines are impacted by temperature fluctuations. We measure a strong correlation between metallicity and sulfur-to-oxygen and nitrogen-to-oxygen abundance ratios. Furthermore, we report correlations between the scatter in the nitrogen-to-oxygen ratio with the hardness of the ionizing spectrum and with the molecular gas velocity dispersion.

In Chapter 4, we present observations of the very metal-poor galaxy I Zw 18 that reveal two very high ionization regions. The two regions lie along an axis which intercepts the position of I Zw 18's Ultra-luminous X-ray (ULX) source. We explore whether the ULX could power the two regions via jets and/or beamed X-ray emission, and other alternative sources.

# Chapter 1

# Introduction

The abundance of metals (i.e. elements heavier than helium), otherwise known as metallicity, heavily impacts the gas and star-formation physics within the interstellar medium (ISM). For example, the build up of dust mass within the ISM is regulated by metallicity (Asano et al., 2013). Radiative emission processes, which originate from ionized metals, are the primary cooling processes of the ISM (Osterbrock & Ferland, 2006; Draine, 2011). Consequently, the efficiency of these cooling processes determine the reservoir of available cold gas for use in star-formation (Field et al., 1969; Wolfire et al., 1995; Ostriker et al., 2010).

Energetic processes (e.g. supernovae, outflows, etc.) work to redistribute a galaxy's metal content. Because the galaxy-wide variation of metals is tied to the same processes that shape present day galaxies, characterising the variation of galaxy metallicities will provide insight into the processes that drive galaxy evolution. Despite the importance of measuring the magnitude and scale of metallicity variations, our limited understanding of the detailed temperature and chemical structure of the ionized ISM gas leads to uncertainties in the measured metallicities. Towards the goal of obtaining robust metallicities, this dissertation investigates the drivers of temperature variations and chemical abundances within star-forming regions observed in nearby galaxies using integral field spectroscopy.

## 1.1 Metallicity Variations

A galaxy's metallicity reflects its chemical enrichment from stars and the cumulative effect of gas flows (mixing, outflows, inflows of pristine material, etc.). With the exception of hydrogen, helium, deuterium, and lithium, the formation of metals such as oxygen, sulfur, and nitrogen occur within the factory of stellar nucleosynthesis and are released during the terminal stages of stellar evolution (e.g. supernovae, asymptotic giant branch stars). The stellar production of metals effectively connects a galaxy's metallicity to its star-formation history. Moreover, throughout a galaxy's evolution, metal enriched or pristine gas can flow out and into a galaxy's surrounding reservoir of gas, known as the circumgalactic medium (CGM). Consequently, a galaxy's metallicity also traces how the interaction between the ISM and CGM regulates its evolution.

The galaxy-wide distribution of gas-phase (i.e. not locked in dust) metals is commonly traced by the abundance of oxygen, nitrogen, sulfur, and other metals, using their emission from ionized gas inside H II regions (Kennicutt & Garnett, 1996; Bresolin et al., 2012; Hernandez et al., 2013; Ho et al., 2017; Kreckel et al., 2019, 2020; van Loon et al., 2021; Grasha et al., 2022a). From observations of H II regions in nearby galaxies, it is well established that negative radial gradients in oxygen metallicities are ubiquitous in disk galaxies (Searle, 1971; Berg et al., 2015; Bresolin, 2019; Kreckel et al., 2019; Berg et al., 2020), and are possibly reflecting a history of inside-out star-formation. The scatter in metallicity at fixed radius, after removal of the gradient, or with respect to some local median, traces the recent injection of metals and the extent of mixing by turbulent/diffusive ISM processes.

An assortment of numerical chemical evolution studies that investigate the spatial variation of galaxy metallicities have shown that several processes significantly affect the distribution of metals within a galaxy. Stochastic and hydrodynamic modeling of galaxies (Krumholz & Ting, 2018; Emerick et al., 2020) predict that the variation of metallicity depends on the element and its injection sources. For example, the injection of oxygen into the ISM by core collapse supernovae or asymptotic giant branch stars can introduce a variation within the 2D distribution oxygen abundance between 0.01 dex and 0.035 dex depending on the source. Studies have also shown that the efficiency of mixing varies with the mass of the galaxy; for example low-mass galaxies will have shallower gravitation potential wells, such that outflows will be more efficient at removing enriched gas from of the galaxy (Emerick et al., 2020). Conversely, outflows and gas accretion (i.e. inflows) both control the overall mixing in more massive galaxies (Sharda et al., 2024). In addition to feedback, a galaxy's structure can induce metal mixing. Several 2D chemical evolution modeling studies (Spitoni et al., 2019; Mollá et al., 2019; Spitoni et al., 2023) predict a degree of azimuthal variations on order of $\sim 0.1$ dex or higher, due to an increase of feedback from star-formation induced by the passing of spiral arm density waves. The aggregate of chemical evolution models suggest that significant and measurable variations of a galaxy's metallicity are correlated with the properties of it star-formation and structure.

In order to distinguish between these competing effects of feedback and galaxy structure, it is critical that we constrain the level of metallicity variation across the ISM. Despite an already significant amount of observational effort (Berg et al., 2015; Ho et al., 2017; Kreckel et al., 2019, 2020; Grasha et al., 2022b; Williams et al., 2022), systematic uncertainties associated with the measurements of metallicity hinder progress towards this goal. For convenience, we include in Table 1.1 of abbreviations and terms.

## 1.2 Measuring Metallicities

Galaxy metallicities are typically determined using the emission lines observed from the ionized gas inside H II regions. H II regions are volumes of gas that have been ionized by massive stars. As shown in Figure 1.1, emission lines that dominate H II region spectra originate from hydrogen, oxygen, and other metals. These emission lines are the products of both collisional excitation (CEL) and radiative recombination (RL). CELs are produced when electrons in ions, excited to higher energy levels through collisions with electrons in the gas, decay back to lower energy levels via radiative transitions. RLs are produced when a free electron becomes bound to an ion and then radiatively decays downwards through various energy levels. Metallicities can be inferred from the relative strength (i.e integrated intensity ratio) of CEL lines from metals to hydrogen recombination lines. For a given transition, indicated by its wavelength $\lambda$, its intensity, $I(\lambda)$, is described by the following equation,

$$I(\lambda) = \int j_{\lambda} ds = \int n(X^{+i}) n_{\mathrm{e}} \varepsilon(\lambda, T_{\mathrm{e}}) ds, \tag{1.1}$$

where $j_{\lambda}$ is the emission coefficient. The emission coefficient depends on the number density of the relevant ion, $n(X^{+i})$, the electron density, $n_{\mathrm{e}}$, and the emissivity, $\varepsilon(\lambda, T_{\mathrm{e}})$, at the specified wavelength and average kinetic energy of electrons within the plasma (i.e. electron temperature, $T_e$). The emission coefficient for RL and CELs can have different dependencies on the above parameters. Combining the density and the electron temperature with the observed emission line intensity, and the knowledge of the quantum mechanics that govern the transition probabilities, one can calculate the number density of ions contributing to the observed emission. The number density from any one element can be compared to the number density of hydrogen to obtain the specified elemental abundance relative to hydrogen. For example, the gas-phase oxygen abundance is determined from the sum of all the ionization states of oxygen relative to hydrogen. This quantity is expressed as 12+log($O^{+}$/$H^{+}$ + $O^{2+}$/$H^{+}$) or 12+log(O/H).

### 1.2.1 The Direct Method

Metallicities calculated using knowledge of the electron temperature and density are colloquially known as the “direct method”. Of the parameters needed to derive metallicities with the direct method, precise knowledge of the H II region electron temperature is critical. The intensity ratios of select CELs are exceptionally sensitive to to temperature (Peimbert et al., 2017). For insight into this importance, we can consider a two-level atom in statistical equilibrium, that is, where every collisional excitation will be balanced by collisional or radiative decay. This

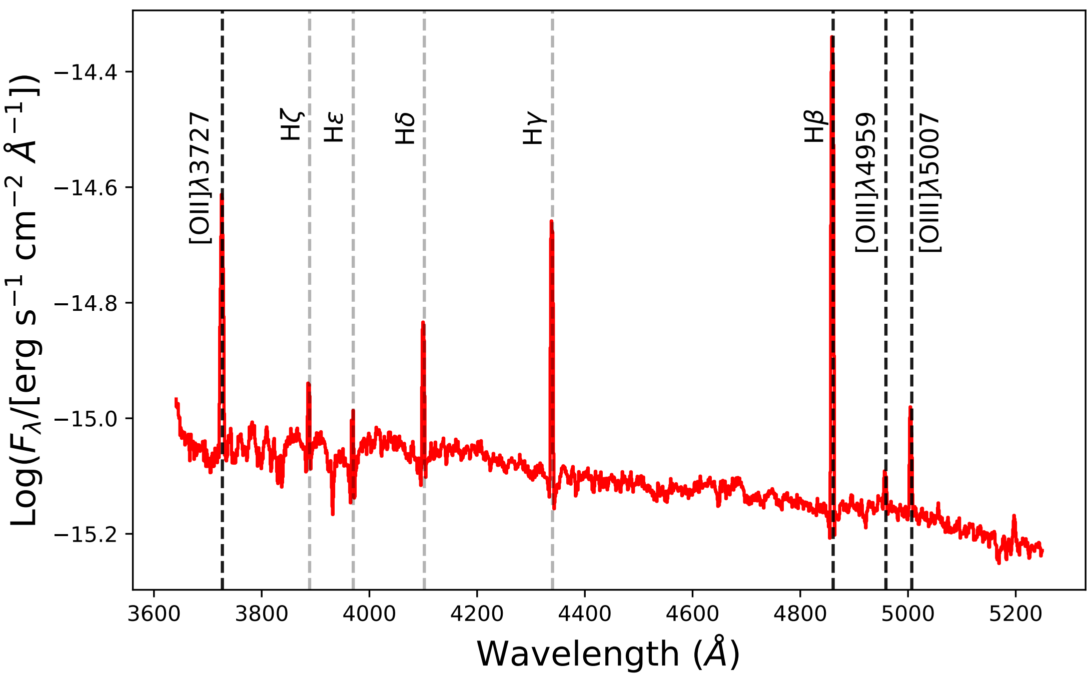

**Figure 1.1.** Sample H II region spectrum obtained from Keck Cosmic Web Imager observations of the galaxy NGC 3627. This portion of the H II region spectrum is dominated by collisionally excited lines of oxygen and recombination lines of hydrogen, all of which are indicated by black or gray dashed vertical lines. The transitions indicated by black dashed lines are used to estimate metallicity.

balance is expressed as,

$$n_l n_\mathrm{e} q_{lk} = n_k n_\mathrm{e} q_{kl} + n_k A_{kl}, \tag{1.2}$$

where $n_k$, $n_l$, are the number of electrons in the upper and lower states, $A_{kl}$, is the probability of spontaneous emission, and the collisional excitation and de-excitation rate coefficients are given by $q_{lk}$ and $q_{kl}$ respectively. The ratio between the number density of ions with electrons in the upper and lower levels is given by

$$\frac{n_k}{n_l} = \frac{q_{lk}}{q_{kl}}(1 + \frac{A_{kl}}{n_\mathrm{e} q_{kl}})^{-1}. \tag{1.3}$$

The density where the rate of radiative and collisional de-excitation are equal is defined as the critical density, $n_\mathrm{crit} = A_{kl}/q_{kl}$. When the density is much less than the critical density, $n_\mathrm{e} << n_\mathrm{crit}$, the ratio of atoms with electrons in the upper and lower levels approaches

$$\frac{n_k}{n_l} = \frac{n_\mathrm{e}}{n_\mathrm{crit}} \frac{q_{lk}}{q_{kl}}. \tag{1.4}$$

Using detailed balance, the $q_{lk}/q_{kl}$ ratio is described by the Boltzmann distribution,

$$\frac{q_{lk}}{q_{kl}} = \frac{g_k}{g_l} e^{-h\nu_{kl}/KT_\mathrm{gas}}, \tag{1.5}$$

where $g_k$ and $g_l$ are the statistical weights of the levels (Osterbrock & Ferland, 2006; Draine, 2011). A more complete formalism of the problem includes the effects of stimulated emission and a radiation field parameterized by the brightness temperature, $T_B(\nu)$ at a given frequency $\nu_{kl}$ (Osterbrock & Ferland, 2006; Draine, 2011; Peimbert et al., 2017). The resulting ratio of atoms with electrons in the upper and lower levels becomes;

$$\frac{n_k}{n_l} = (\frac{1}{1 + \frac{n_\mathrm{crit}}{n_\mathrm{e}}}) \frac{g_k}{g_l} e^{-h\nu_{kl}/KT_\mathrm{gas}} + (\frac{1}{1 + \frac{n_\mathrm{e}}{n_\mathrm{crit}}}) \frac{g_k}{g_l} e^{-h\nu_{kl}/KT_\mathrm{B}}. \tag{1.6}$$

Now the ratio of $n_{\rm e}/n_{\rm crit}$ determines if the ratio of states is tracking the gas or radiation field temperature. In the limit that $n_{\rm e} << n_{\rm crit}$, which may be the case for many CELs, the above can becomes,

$$\frac{n_k}{n_l} = \frac{n_{\rm e}}{n_{\rm crit}} \frac{g_k}{g_l} e^{-h\nu_{kl}/KT_{\rm gas}} + \frac{g_k}{g_l} e^{-h\nu/KT_{\rm B}}. \tag{1.7}$$

Here, $T_{\rm gas}$ will just be the electron temperature, $T_{\rm e}$. Although $n_{\rm e}/n_{\rm crit}$ may be small, $T_{\rm e}$ is typically larger than $T_{\rm B}$, such that the CEL emission is much more sensitive to $T_{\rm e}$.

Temperature sensitive[1] auroral-to-nebular line ratios (e.g. [O III]$\lambda$4363/$\lambda$5007) can be used to measure electron temperature. As shown in Figure 1.2, nebular and auroral lines originate from different excited states of of the same ion. The temperature dependence of auroral-to-nebular ratios is due to relative energy level differences between auroral and nebular lines. Auroral lines originate from higher energy levels that are still accessible for collisional excitation in a $T \sim 10^4$ K gas, typical of photo-ionized gas. Because the excitations to the upper level are only accessible to electrons with higher energy, auroral line emission can be $> 100$ times weaker than their nebular counterpart (Kennicutt et al., 2003; Esteban et al., 2004; Berg et al., 2020). Another method to measure the electron temperature is to observe the ratio between recombination line (RL) emission from various ions relative to H (Peimbert, 1967; Osterbrock & Ferland, 2006; Peimbert et al., 2017). Although RL emission is nearly proportional to $T_{\rm e}^{-1}$, the recombination coefficient of the transition (i.e., probability of recombination) adds an additional, but weak, temperature dependence (Draine, 2011). In practice, measuring the temperature from RLs is difficult. The strong hydrogen RLs have little to no fluctuations with $T_e$ and very deep high signal-to-noise observations are required to detect the weak emission from metal RLs (Peimbert et al., 2017)

Beyond challenges in the faintness of auroral lines, there are additional systemic uncertainties in metallicities derived using the direct method. These uncertainties are rooted in the incomplete understanding of the temperature structure within H II regions (Peimbert et al., 2017).

---

[1] Density sensitive line ratios involve emission from CELs from the same ions with negligible differences in their energies.

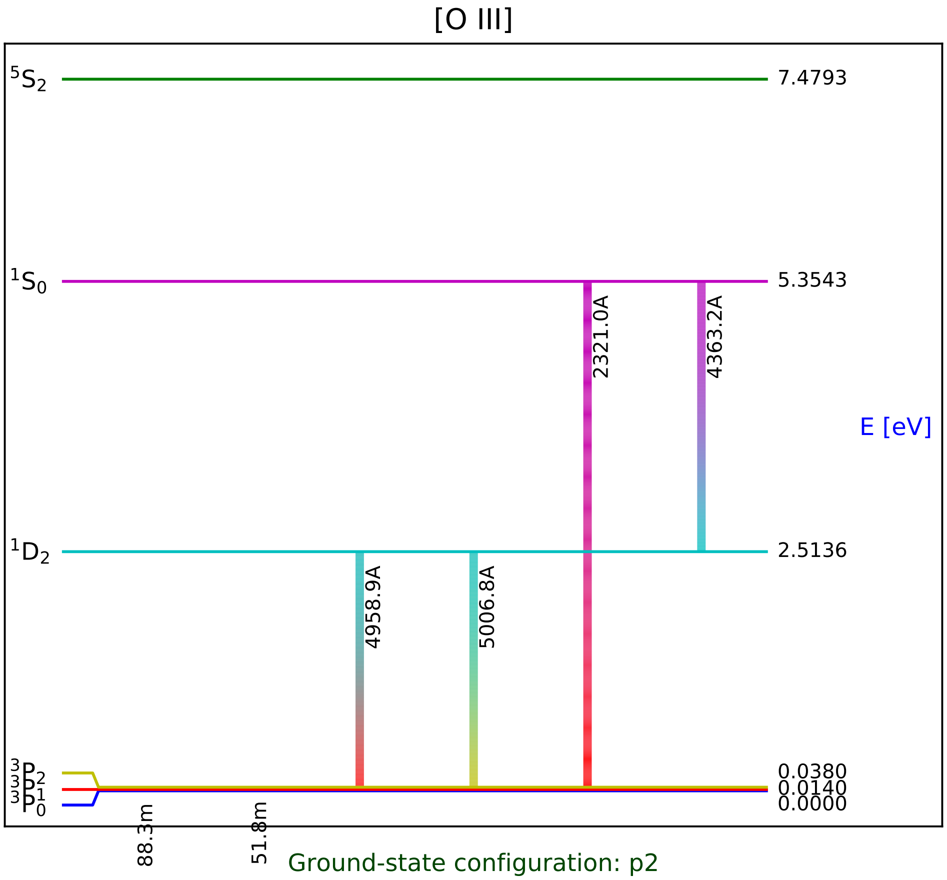

**Figure 1.2.** Diagram summarizing the available energy levels of [O III] generated using PyNeb (Luridiana et al., 2015). The ratio between the nebular lines, [O III]$\lambda\lambda$4959, 5007, and auroral line, [O III]$\lambda$4363, are used to derive the electron temperature. The 88.3 and 51.8 $\mu$m show here are transitions with the triplet 3P ground state and there ratio is a useful density diagnostic.

The first-order approach to calculating direct abundances is to assume that the H II region gas is described by a single electron temperature. However, due to a combination of a hardening stellar radiation field (photons with energies closest to 13.6 eV are absorbed nearest to the star), increasing optical depth, and competing cooling rates between the changing ions that dominate gas cooling, the average $T_e$ can vary within the H II region (Stasińska, 1980; Garnett, 1992).

### 1.2.2 The Three Ionization Zone Model of H II Regions

High spatial resolution observations of the Milky Way's Orion Nebula (Baldwin et al., 2000; O'Dell et al., 2017), and HII regions in the Large Magellanic Cloud (Barman et al., 2022) show that the emission from ions with similar ionization potentials originate from similar volumes within H II regions. This segregation based on the ionization potential is also seen in photoionization models (Garnett, 1992; Ferland et al., 2017). Together, these studies suggest H II regions can be described by different ionization zones.

As shown in Figure 1.3, in a three-zone ionization zone model the zones are described by the properties of $O^{2+}$(35 eV), $S^{2+}$(23 eV), and $O^{+}$, $S^{+}$, or $N^{+}$ (13.6 eV). A four-zone description is needed in the case of very high ionization systems ($He^{2+}$; Berg et al., 2021). The ions listed above each have their own auroral-to-nebular line ratio that can be observed in the optical. This allows for the derivation of an electron temperature for each zone. For example, [O III] is produced in the $O^{2+}$ zone, therefore $T_{e,\text{[O III]}}$ as measured from the [O III]$\lambda4363/\lambda5007$ ratio is designated as a measure of the high ionization zone temperature. However, measuring the temperatures for all three zones is challenging. The wavelength spacing between the requisite optical nebular and auroral lines is large and requires spectral coverage between 3700−10,000 Å.

In order to mitigate challenges associated with the faintness of auroral lines or limited wavelength coverage, $T_e$–$T_e$ relationships have been constructed from both photoionization models (Garnett, 1992; Vale Asari et al., 2016) and observations (e.g. Berg et al., 2015, 2020; Zurita et al., 2021; Méndez-Delgado et al., 2023b; Rogers et al., 2021) to extrapolate temperatures

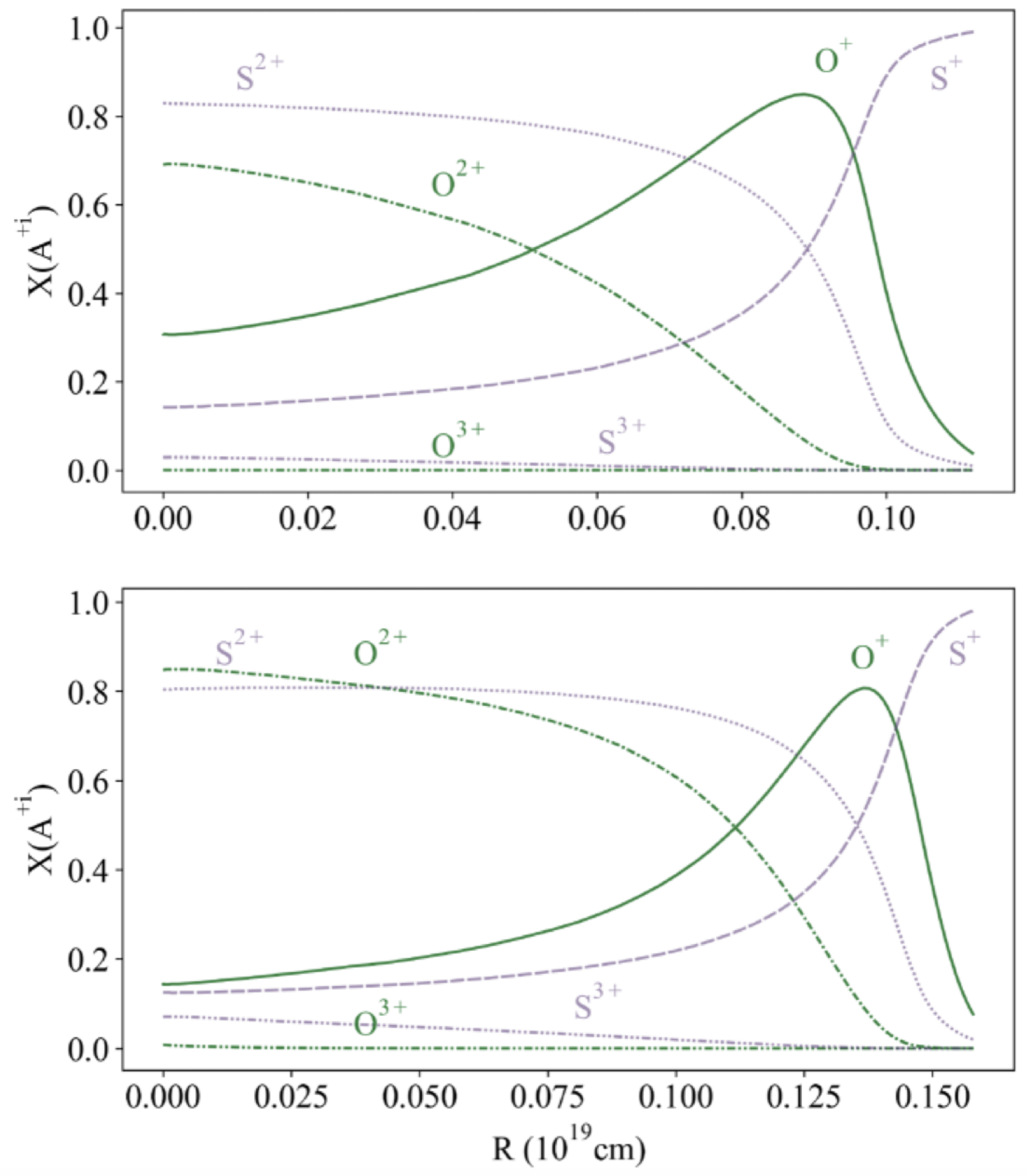

**Figure 1.3.** Ionization structure of H II regions from CLOUDY (version 17.01; Ferland et al., 2013) photoionization models. The top panel shows the structure for an H II region with one-half solar metallicity and the bottom panel shows an H II region with 0.004 solar metallicity. The parameter R is the distance away from the input ionizing star cluster. This figure is adopted from Figure 3 in Díaz & Zamora (2022).

between the different ionization zones. However, these same observations have shown that temperatures between the different ionization zones can exhibit varying behavior that disagrees with theoretical predictions. Studies have shown that offsets and/or scatter away from expected trends in $T_e$'s and $T_e$–$T_e$ relationships are correlated with ionization parameter (Berg et al., 2020; Arellano-Córdova & Rodríguez, 2020; Yates et al., 2020), shocks (Hill & Hollenbach, 1978; Peimbert et al., 1991; Dopita & Sutherland, 1996; Allen et al., 2008; Binette et al., 2012), and density inhomogeneities (Nicholls et al., 2020; Méndez-Delgado et al., 2023b). Moreover, it is unknown how the ionizing source and very low-metallicity environments may impact $T_e$–$T_e$ relationships constructed from high-metallicity systems. Such biases further stress the importance of observing the full set of optical auroral lines and developing $T_e$ priorities that result in accurate metallicities.

### 1.2.3 Temperature Fluctuations

One longstanding problem for metallicities derived with the direct method is the disagreement between abundances derived using CELs or RLs, colloquially known as the abundance discrepancy factor (ADF). Since the work of Wyse (1942), Peimbert & Costero (1969), and Peimbert (1971), it has been repeatedly observed that the ratio, or difference if using logarithmic units, between abundances derived using $T_e$'s estimated from RLs are systematically more metal-rich than those using CELs. The typical value for the ADF for oxygen in H II regions typically varies between 1.5 and 3.0 (Esteban et al., 2014; Corradi et al., 2015; Peimbert et al., 2017; Méndez-Delgado et al., 2023a). Although the source of the ADF is still the subject of debate, one common solution is the presence of temperature fluctuations (Peimbert, 1967; Méndez-Delgado et al., 2023a).

In the presence of temperature fluctuations, the exponential dependence of CEL strengths on temperature make them sensitive to the hottest gas in the resolution element (i.e. in the H II region). As consequence, the auroral-to-nebular temperatures will be biased towards hotter than average temperature (Peimbert, 1967; Peimbert & Costero, 1969). The presence of temperature fluctuations may be related to turbulence, density structure, and shocks associated with either stellar winds or radiation-pressure driven expansion. If these processes are confined towards the inner part of the H II region, than temperature fluctuations are expected to impact the high-ionization zone more so than the low or intermediate ionization zone. However, effects on the intermediate zone have not been fully explored (Méndez-Delgado et al., 2023a). In the framework constructed by Peimbert (1967) and Peimbert & Costero (1969) the average ion weighted temperature, $T_0(X^{i+})$, in a differential volume of gas is given by,

$$T_0(X^{i+}) = \frac{\int T_e n_e n(X^{i+}) \mathrm{dV}}{\int n_e n(X^{i+}) \mathrm{dV}} \tag{1.8}$$

where $n(X^{i+})$ is the relevant ion. If temperature fluctuations are present, the magnitude of the inhomogeneities can be parameterised by the root mean square deviation from the average temperature,

$$t^2(X^{i+}) = \frac{\int [T_e - T_0(X^{i+})]^2 n_e n(X^{i+}) \mathrm{dV}}{T_0(X^{i+})^2 \int n_e n(X^{i+}) \mathrm{dV}}. \tag{1.9}$$

Due to the weak temperature dependence of RL intensities, they respond more linearly with temperature. Consequently, the $T_e(X^{i+})$ estimated from RLs will be less sensitive to volumes with higher than average temperature (i.e temperature fluctuations) and can be interpreted as direct tracers of $T_0(X^{i+})$ (Méndez-Delgado et al., 2023a). There is no general representative value of $t^2$ for H II regions because different ions, with different energy levels, will exhibit different sensitivities to temperature fluctuations.

As an example of the impact of temperature fluctuations, we show in Figure 1.4 a toy-model of the temperature fluctuations affecting CELs from [O III]. Shown in the left panel, we construct a uniform temperature field, $T_0$. We then inject Gaussian distributed temperature perturbations with amplitude $\Delta T_e$. Using this field, we derive emission line maps for both the [O III]$\lambda$4363 auroral and [O III]$\lambda$5007 nebular lines. Next, we generate the integrated auroral-to-nebular line ratio [O III]$\lambda$4363/$\lambda$5007. From this, we calculate the "observed" temperature

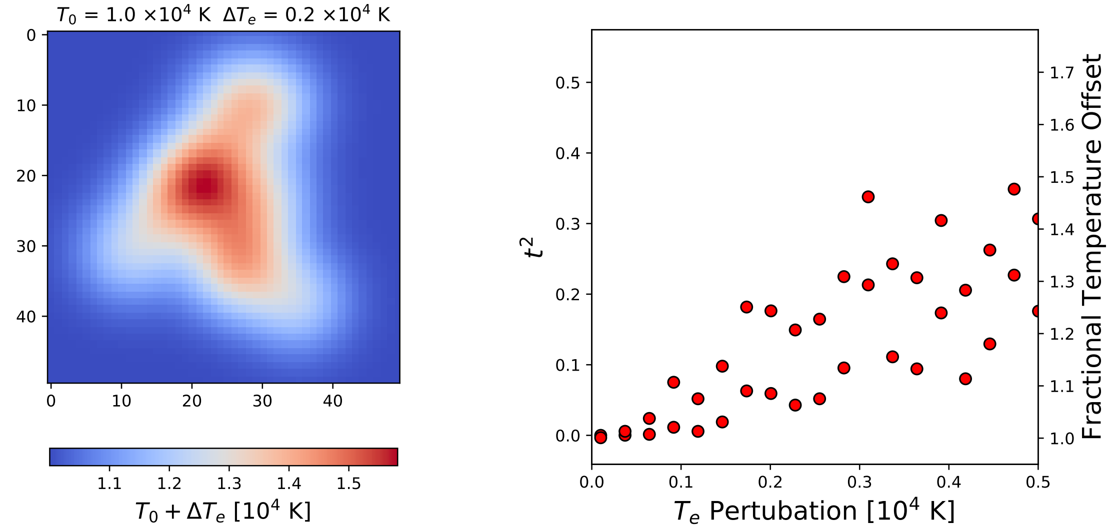

**Figure 1.4.** We show the bias introduced on the temperature measured from [O III]$\lambda 4363/5007$ by the presence of temperature fluctuations. In the left panel we show a uniform temperature field, $T_0 =$10,000 K, that has been injected with Gaussian temperature perturbation with amplitude $\Delta T_\mathrm{e}$. The right panel shows the corresponding level of temperature fluctuations $t^2$ for several realizations of the temperature field, and different magnitudes of temperature perturbations. the magnitude of temperature fluctuations. The electron density is uniform and set to 100 cm$^{-3}$.

which we then compare to the true temperature (i.e. the average of the input temperature field). From these two temperatures, we then calculate the corresponding $t^2$. We repeat this several times for different amplitudes of $\Delta T_\mathrm{e}$. In the right-panel of 1.4, we show that $t^2$ increases with the amplitude of the perturbation. We also show the fractional temperature difference. For observed values of $t^2 \sim 0.02 - 0.25$, the measured auroral line temperature can be biased hotter by 10% to 35% above the true temperature. This level of bias introduces upwards 0.1 dex or higher uncertainties in derived abundances.

### 1.2.4 Strong-line Calibrations for Metallicity

In order to bypass the challenges associated with measuring the emission from faint auroral lines and even fainter recombination lines of ions, there exist a large number of "strong-line calibrations". Strong-line methods are constructed using combinations of nebular lines, whose intensities depend on the metallicity (Peimbert et al., 2017). An example of such lines are highlighted in Figure 1.1. Generally, there are two classes of strong line calibrations. The first class are calibrations which use direct abundances from a combination of single/stacked galaxies and H II regions as the calibrating sample (e.g. Bresolin, 2007; Pilyugin & Grebel, 2016; Curti et al., 2017; Nakajima et al., 2022). Second are strong-line calibrations that are derived from photoionization modeling of H II regions (e.g. Dopita et al., 2000; Kewley & Dopita, 2002).

Although strong-line calibrations make use of optical CEL ratios that exhibit sensitivity to metallicity, the same set of line ratios can also exhibit sensitivity to other properties such as ionization parameter (see, Dopita et al., 2016), or can predict two different values of metallicity for a single value of a line ratio (see, Kobulnicky & Kewley, 2004; Pilyugin & Grebel, 2016). For the class of calibrations constructed from photoionization models, there are uncertainties introduced due to an assortment of commonly employed assumptions. Such assumptions include use of simple nebular geometries (e.g. spherical or plane-parallel), and uniform densities or temperatures (Kewley & Ellison, 2008). These assumptions limit the complexity of H II region models as compared to realistic regions. A larger issue with strong-line calibrations is the large range of derived metallicity values for a single set of observed line ratios. As showing in Figure 1.5, a comparison of the aggregate strong-line calibrations show that the inferred metallicities can disagree by up to 0.7 dex (Kewley & Ellison, 2008). This is nearly an order of magnitude larger than the intrinsic scatter predicted by chemical evolution models (Krumholz & Ting, 2018).

## 1.3 Metallicities for High-$z$ Galaxies and Local Analogs

In the era of the James Webb Space Telescope (JWST), redshifted optical emission arising from ionized gas is a key diagnostic of the physical properties that regulate galaxy evolution. While the 3-zone ionization model may be a good descriptor of metal-rich H II regions, low-metallicity galaxies and nebulae often exhibit very high ionization emission. For example, the nearby low-metallicity galaxy I Zw 18 exhibits recombination emission from He II $\lambda$4686. This emission originates from doubly-ionized helium. The production of He$^{2+}$ requires photons of energies $>$ 54 eV. There have been several studies into the origin of He II emission

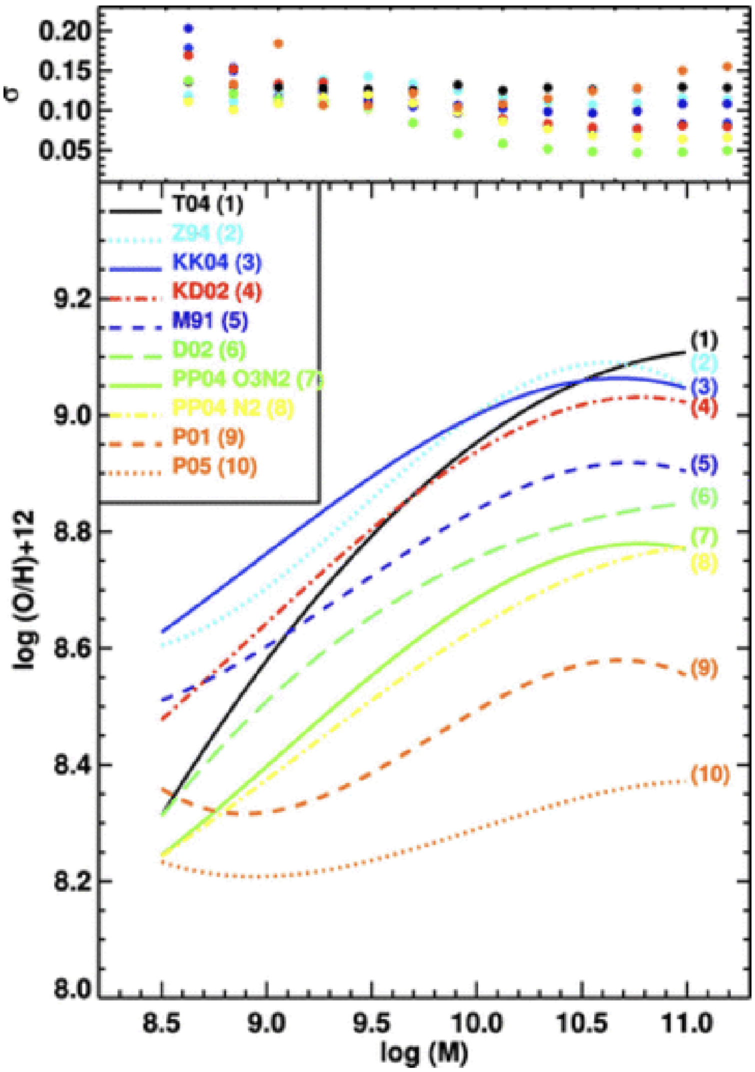

**Figure 1.5.** The mass-metallicity relationship (MZR, Lequeux et al., 1979) of galaxies inferred using a collection of strong-line calibrations. The black solid-dot line shows the MZR determined from metallicities derived using the "direct" method. The remaining lines show the MZR using a mix of empirical and theoretical calibrations. There are significant offsets as well as varying shapes between the metallicity indicators. This figure is originally presented in (Kewley & Ellison, 2008).

(Garnett et al., 1991; Izotov & Thuan, 1998; Kehrig et al., 2011; Shirazi & Brinchmann, 2012; Kehrig et al., 2015; Senchyna et al., 2020; Rickards Vaught et al., 2021), but the source(s) of the required ionizing flux in I Zw 18 remains uncertain. With regards to direct abundances for low-metallicity systems, Berg et al. (2021) designate a set of emission lines for use in deriving the physical properties of the “very-high” ionization zone. However, it is unknown if stellar feedback, especially in extreme ionization conditions/sources, may effect determinations of direct abundances using these diagnostics.

The unknown nature of ionizing sources and the physics of the low-metallicity ISM introduce uncertainties that may challenge our understanding of measuring metallicity in high redshift galaxies, where metal content is expected to be lower than in present day galaxies. Already, JWST observations of direct and strong-line oxygen abundances produce conflicting results (Curti et al., 2023; Laseter et al., 2024; Topping et al., 2024). Shown in Figure 1.6, Cameron et al. (2023) showed that the measurement of the N/O ratio for a $z \sim 11$ galaxy is exceptionally higher than N/O values of $z \sim 0$ H II regions and galaxies. While this observation could suggests many interesting physical explanations, it may also show that our understanding of ISM physics obtained from local metal-rich objects does not transfer so easily to the extreme low-metallicity environment of the early universe.

There are active efforts to re-calibrate strong-line metallicity calibrations for use at high redshift (see, Sanders et al., 2024). Ultimately, one critical step towards this goal is understanding how ionizing sources and the ionization state of metal-poor gas effects our understanding of optical metallicity diagnostics.

## 1.4 Key Advances Made in this Work

There has been considerable effort in characterizing both metallicity variations and temperature structure of H II regions (Zaritsky et al., 1994; Bresolin et al., 2009; Berg et al., 2015; Ho et al., 2017; Kreckel et al., 2019, 2020; Berg et al., 2020; Rogers et al., 2021). However,

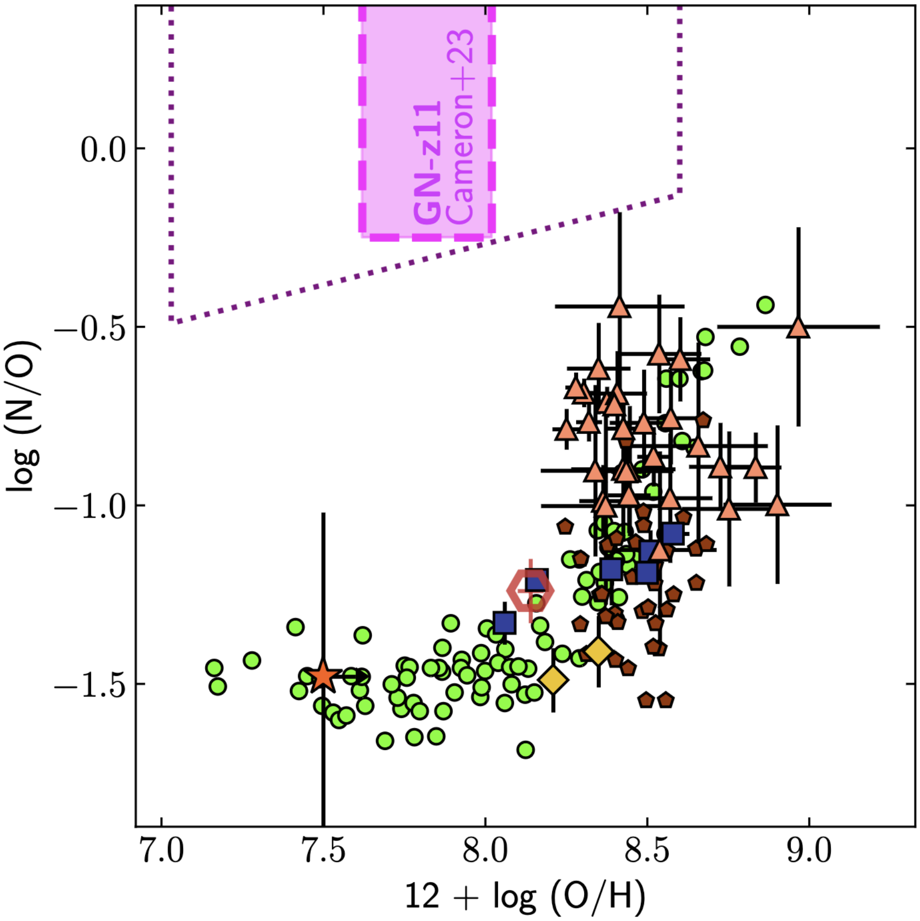

**Figure 1.6.** N/O ratio compared to O abundance. The pink shaded region shows the range of abundance ratios for GN-z11 implied by the measured emission for this high-redshift, $z \sim 11$ galaxy. The individual points show N/O ratios measured from samples of $z \sim 0$ galaxies and H II regions. Figure is adapted from Figure 1 of Cameron et al. (2023).

a sub-sample of these studies have used single-slit spectroscopy to observe nearby Milky Way or extra-galactic H II regions. Due to the relative to size of the H II region and the slit width, these studies are often biased towards the central and highly ionized volumes of H II regions. Moreover, H II regions have to be pre-selected which introduces a selection bias, often towards the largest and brightest H II regions. With the advent of Integral Field Spectroscopy (IFU), these bias can be surpassed, as IFUs can encompass several or many H II regions within a single field of view. But, a majority of optical IFUs, until recently (see Konidaris et al., 2020), have had limited access to the full optical wavelength range and necessary ionized gas diagnostics.

In order to improve our ability to assess both the metallicity and the underlying physics of H II regions, I used IFUs installed on Keck and the Very Large Telescope to observe the full optical spectrum for a sample of H II regions in nearby galaxies. In Chapter 2 of this dissertation, I present a study investigating the drivers of temperature fluctuations using electron temperatures derived from the full-set of optical auroral lines. In Chapter 3, for a sample of new and literature H II regions, I explore trends between direct abundances for oxygen, nitrogen and sulfur, which are derived using temperature prescriptions motivated by the results of Chapter. 2. In Chapter 4, I present an analysis of the nearby low-metallicity galaxy I Zw 18. I investigate the potential ionizing source responsible for the high-ionization He II emission present in two previously unobserved high -ionization regions.

**Table 1.1.** List of Abbreviations and Terms

| | |
|---|---|
| ADF | Abundance discrepancy factor (the ratio between CEL and RL abundances). |
| ALMA | Atacama Large Millimeter/submillimeter Array. |
| CGM | Circumgalactic medium. |
| CEL | Collisionally excited line emission. |
| H II region | Volume of ionized hydrogen around stars. |
| He III region | Volume of doubly-ionized helium around stars. |
| HST | Hubble Space Telescope. |
| IFU | Integral field unit or spectrograph. |
| ISM | Interstellar Medium (i.e. gas and dust in between stars). |
| JWST | James Webb Space Telescope. |
| KCWI | Keck Cosmic Web Imager. |
| Metallicity | Abundance of elements heavier than He. |
| MUSE | Multi-unit Spectroscopic Explorer. |
| $n_{\mathrm{e}}$ | Density of free electrons within a volume of gas. |
| $n_{\mathrm{crit}}$ | Density where rates of decay and collisional de-excitation are equal. |
| PHANGS | Physics at High Angular resolution in Nearby Galaxies Survey |
| Shock | A propagating wave that moves faster than the speed of sound in a medium. |
| SN | Supernova (i.e. the collapse and explosion of a massive star). |
| $T_{\mathrm{e}}$ | Electron temperature, describing the kinetic energy of free electrons. |
| $T_0$ | Ion-weighted gas temperature. |
| $t^2$ | Magnitude of temperature fluctuations. |
| RL | Recombination line emission. |
| VLT | Very Large Telescope. |
| WR | Wolf-Rayet star (i.e. an evolutionary stage of massive stars). |

# Chapter 2

# Investigating the Drivers of Electron Temperature Variations in H II Regions with Keck-KCWI and VLT-MUSE

Abstract of Chapter 2.

H II region electron temperatures are a critical ingredient in metallicity determinations and recent observations reveal systematic variations in the temperatures measured using different ions. We present electron temperatures ($T_e$) measured using the optical auroral lines ([N II]$\lambda$5756, [O II]$\lambda\lambda$7320, 7330, [S II]$\lambda\lambda$4069, 4076, [O III]$\lambda$4363, and [S III]$\lambda$6312) for a sample of H II regions in seven nearby galaxies. We use observations from the Physics at High Angular resolution in Nearby Galaxies survey (PHANGS) obtained with integral field spectrographs on Keck (Keck Cosmic Web Imager; KCWI) and the Very Large Telescope (Multi-Unit Spectroscopic Explorer; MUSE). We compare the different $T_e$ measurements with H II region and interstellar medium environmental properties such as electron density, ionization parameter, molecular gas velocity dispersion, and stellar association/cluster mass and age obtained from PHANGS. We find that the temperatures from [O II] and [S II] are likely over-estimated due to the presence of electron density inhomogeneities in H II regions. We measure high [O III] temperatures in a subset of regions with high molecular gas velocity dispersion and low ionization parameter, which may be explained by the presence of low-velocity shocks. In agreement with previous

studies, the $T_e$–$T_e$ between [N II] and [S III] temperatures have the lowest observed scatter and follow predictions from photoionization modeling, which suggests that these tracers reflect H II region temperatures across the various ionization zones better than [O II], [S II], and [O III].

## 2.1 Introduction

The characterization of abundance variations within galaxies provides insight into the physical processes that drive galaxy and chemical evolution. A galaxy's gas-phase metal abundance (i.e. metallicity) reflects the history of chemical enrichment from stars and the net balance of gas flows (mixing, outflows, inflows of pristine material, etc.). In addition, the metallicity of ISM gas directly controls its cooling and other important ISM physics (Draine, 2011; Peimbert et al., 2017).

The distribution of gas-phase metals in a galaxy is commonly traced by the abundance of oxygen, nitrogen, sulfur, and other metals using the emission from ionized gas located inside H II regions (e.g. Kennicutt & Garnett, 1996; Bresolin et al., 2012; Hernandez et al., 2013; Ho et al., 2017; Kreckel et al., 2019, 2020; van Loon et al., 2021; Grasha et al., 2022a). There are several indirect methods calibrated using strong optical emission lines to derive an estimate of the H II region metallicity (e.g. Kewley & Ellison, 2008; Blanc et al., 2015). A "direct" measure of an H II region metallicity requires knowledge of the electron temperature ($T_e$) of the gas. Due to their exponential dependence on $T_e$, one of the ways to infer electron temperature is through the auroral-to-nebular line ratios of collisionally excited lines (CEL; Peimbert, 1967; Osterbrock & Ferland, 2006; Peimbert et al., 2017). Nebular and auroral lines originate from different excited states of ions. Auroral lines are from higher energy levels, but are still accessible for collisional excitation in a $T \sim 10^4$ K gas. If the density of the gas is below the auroral and nebular line critical densities (i.e. when collisional de-excitation is negligible), then the auroral-to-nebular line ratio is sensitive to the electron temperature (e.g. Osterbrock & Ferland, 2006). Given that the excitations to the auroral level are only accessible to electrons of higher energy, auroral line emission can be $> 100$ times weaker than nebular lines (Kennicutt et al., 2003; Esteban et al., 2004; Berg et al., 2020). One alternative way to measure $T_{\rm e}$ include the ratio between recombination line (RL) emission from H and other species (Peimbert, 1967; Osterbrock & Ferland, 2006; Peimbert et al., 2017). But, because RLs of ions exhibit a much weaker dependence to temperature ($T_{\rm e}^{-\kappa}$ where $-0.2 < \kappa < 0.2$, Peimbert et al., 2017), the optical RLs useful for use as temperature diagnostics are typically reserved for deep high S/N spectra as RL emission is typically much fainter than the emission from auroral lines.

For ions with optical auroral lines studied in this work, we can measure the temperatures for each ion using the following line ratios:

$$T_{\rm e,[O\,III]} \rightarrow {\rm [O\,III]}\lambda4363/\lambda\lambda4959,5007,$$

$$T_{\rm e,[O\,II]} \rightarrow {\rm [O\,II]}\lambda\lambda7320,7330/\lambda\lambda3726,3729^{1},$$

$$T_{\rm e,[S\,III]} \rightarrow {\rm [S\,III]}\lambda6312/\lambda\lambda9069,9532,$$

$$T_{\rm e,[S\,II]} \rightarrow {\rm [S\,II]}\lambda\lambda4069,4076/\lambda\lambda6716,6731,$$

$$T_{\rm e,[N\,II]} \rightarrow {\rm [N\,II]}\lambda5756/\lambda\lambda6548,6584.$$

The $O^{+}$, $N^{+}$, $S^{+}$ ions require energies of 13.6 eV, 14.5 eV, and 10.3 eV to be produced while $S^{++}$ and $O^{++}$ require energies 23 eV and 35 eV, respectively.

Several effects play competing roles in determining the ionization and temperature structure of H II regions. These include a radially decreasing intensity and hardening of the radiation field (photons closest to 13.6 eV are absorbed first) as well as a change in the ions which dominate gas cooling, and therefore the cooling efficiency (Stasińska, 1980; Garnett, 1992). Because of the varying degree of ionization within an H II region, a model of three ionization zones—low-, intermediate- and high—is often used to describe them. Because each ionization zone could theoretically have different temperatures, this further stresses the importance of

---

[1] [O II]$\lambda\lambda7320,7330$ is an unresolved quadruplet with transitions at $\lambda7319$, $\lambda7320$, $\lambda7330$ and $\lambda7331$ Å.

observing multiple auroral lines and developing temperature priorities for use in accurately determining abundances (e.g. Berg et al., 2015, 2020; Rogers et al., 2021).

Observing the full set of optical auroral lines in an H II region can be challenging. In addition to the large wavelength range needed, $\sim$ 3700–10000 Å, some auroral lines are weaker than others depending on the metallicity and temperature of the gas. Because of these challenges, it is very important to establish temperature relationships that allow us to infer the conditions of a certain ionization zone from the others. Photoionization modeling (e.g. Garnett, 1992; Vale Asari et al., 2016) has been used to derive temperature relationships, but standard models consider only simple geometries and homogeneous physical and ionization conditions, that might not be suitable for more complex regions potentially affected by shocks, stellar feedback, or other mechanism that produce density or temperature inhomogeneities (Peimbert, 1967; Peimbert et al., 1991; Binette et al., 2012; Berg et al., 2015, 2020; Arellano-Córdova & Rodríguez, 2020; Nicholls et al., 2020; Méndez-Delgado et al., 2023b,a).

In the presence of temperature fluctuations, the exponential dependence of CEL strengths on temperature will bias auroral-to-nebular temperatures towards higher values than the true average (Peimbert, 1967; Peimbert & Costero, 1969). Such inhomogeneities may be related to the presence of turbulence, density structure, and shocks associated with either stellar winds or radiation–pressure driven expansion. If the sources of temperature inhomogeneities are confined to the central part of the nebula, the effects that these phenomena have on temperature may primarily affect only the high ionization zone. This has been suggested by Méndez-Delgado et al. (2023a) who presented evidence for temperature inhomogeneities affecting only the highly ionized gas traced by [O III]. In a sample of Galactic and extra-galactic H II regions, they observed that differences between [O III] and [N II] temperatures correlated with the degree of deviation from the average temperature measured using faint O II recombination line emission. Furthermore, a strong correlation between the O II recombination and [N II] temperatures observed by Méndez-Delgado et al. (2023a) implies that temperatures inferred from the [N II] auroral line accurately measures the average $T_e$ of the low-ionization zone (Méndez-Delgado et al., 2023a,b).

Due to the importance of obtaining accurate temperatures for precise abundances, significant effort has been devoted to advancing our understanding of the temperatures of different H II region ionization zones. For example, previous works have found that the scatter between temperatures of different ionization zones may be correlated with other properties of the gas such as the ionization parameter and metallicity (Berg et al., 2015; Arellano-Córdova & Rodríguez, 2020; Berg et al., 2020; Yates et al., 2020).

To explore these questions, we use deep 3600–9500 Å IFU mapping to measure the set of optical auroral lines and nebular lines for a sample of H II regions. We use observations obtained from the Keck Cosmic Web Imager (KCWI, Morrissey et al., 2018) and Multi-Unit Spectroscopic Explorer (MUSE, Bacon et al., 2010) to measure the electron temperature from all 3 ionization zones in H II regions in nearby galaxies. In Section 2.2 we present our sample galaxies as well as primary and supplemental observations. In Section 2.3 we discuss the reduction of the KCWI data. We assess the quality of the KCWI mosaics in Section 2.3.5. We construct our H II region sample in Section 2.4. We present the auroral line measurements in Section 2.5. We derive H II region properties from nebular diagnostics and from ALMA and HST data in Section 2.6. The results and discussion are presented in Section 2.7 and 2.8.

## 2.2 Observations

The analysis presented here makes joint use of multi-wavelength observations of seven galaxies obtained with Keck-KCWI, VLT-MUSE, Atacama Large Millimeter/submillimeter Array (ALMA), and the Hubble Space Telescope (HST).

### 2.2.1 Sample Selection

The seven galaxies in this analysis are drawn from the PHANGS-MUSE sample (Emsellem et al., 2022). To date, 90 galaxies make up the full PHANGS sample[2] (Leroy et al.,

---

[2] http://phangs.org/

2021a), and 19 have been observed by MUSE. In order to be observed with KCWI in the northern hemisphere, we selected the seven target galaxies from a subset of PHANGS-MUSE galaxies with declination, $\delta > -30^\circ$. Table 2.1 presents general properties of these galaxies, including distances, masses, sizes, and the angular resolution of the MUSE data.

### 2.2.2 Keck Cosmic Web Imager

We observed each galaxy using KCWI on the Keck II telescope with multiple pointings taken over several nights between the years 2017 and 2021. Clear conditions were present for the majority of observations, except for the nights of October 16 and 17, 2018, which suffered from variable cloud coverage. These poor conditions primarily affect the observations of NGC 628. The instrument was configured with the "Large" slicer and BL grating centered at 4600 Å. The usable spectral range afforded by this configuration is 3650–5550 Å with a spectral resolution $R \sim 900$, corresponding to a full width at half maximum (FWHM) $\sim 5.1$ Å (or $\sim 300$ km s$^{-1}$) at the central wavelength. The Large slicer has an angular slice width of $1.35''$. The field of view (FoV) using the Large slicer and BL grating is $33''$ perpendicular and $20.4''$ parallel to the slicer.

Because the FoV is small compared with the large angular size of each galaxy, we observed each galaxy over multiple fields. Most fields were observed two times using 1200 s (i.e. 20 min) integration times. The only exceptions were: all fields in NGC 3627, which were observed five times each with 120 s (2 min) integration times; field 17 in NGC 628 which was observed 3 times using 1200 s; and field 2 in NGC 5068 and field 5 in NGC 1385, both having only a single observation of 1200 s. A half slice width, or $0.675''$, dither was applied between each exposure. We observed an off-galaxy region, selected to be free of extended emission and/or bright sources, in order to measure a sky spectrum close in time to the observations. These sky frames, observed using an integration time of 600 s (i.e. 10 min), were used for sky subtraction during data reduction. We summarize the number of fields, exposure times, and dates in Table 2.7 of Appendix 2.11. The full data reduction is outlined in Section 2.3.

### 2.2.3 Multi-Unit Spectroscopic Explorer

MUSE observations of these galaxies come from the PHANGS-MUSE survey (Emsellem et al., 2022). MUSE covers wavelengths between 4800–9500 Å. Taken in combination, KCWI and MUSE span the full optical spectrum. The full details of the MUSE data reduction and data products are presented in Emsellem et al. (2022), and we provide a brief overview here. The PHANGS-MUSE program observed 19 galaxies using 168 individual $1' \times 1'$ pointings. The median spatial resolution across all pointings is $\sim 50$ pc (or $\sim 0.80''$) with a typical spectral FWHM of $\sim 2.5$ Å (but varying with wavelength). The data were reduced using the `pymusepipe`[3] and spectral fitting and analysis was performed using the Data Analysis Pipeline [4] packages described in Emsellem et al. (2022). The individual MUSE pointings were homogenized to a uniform Gaussian point-spread-function (PSF) with FWHM set to the largest FWHM measured for each target, resulting in "convolved and optimized" (COPT) mosaics. The PSFs of the COPT mosaics are listed in Table 2.1. We use the COPT mosaics in the following work.

### 2.2.4 ALMA

Our analysis makes use of Atacama Large Millimeter/submillimeter Array (ALMA) data obtained as part of PHANGS–ALMA (Leroy et al., 2021a). PHANGS-ALMA observed the $J = 2 - 1$ rotational transition of $^{12}$CO, hereafter CO, for 90 galaxies. The details of the data reduction are described in Leroy et al. (2021b). We make use of the ALMA datacubes with combined CO measurements from the 12m and 7m arrays plus Total Power (12m+7m+TP). The nominal angular resolution of 12m+7m+TP observations is $\sim 1.3''$, similar to the resolution of both KCWI and MUSE. The velocity resolution is 2.5 km $\mathrm{s}^{-1}$.

---

[3] https://pypi.org/project/pymusepipe/

[4] https://gitlab.com/francbelf/ifu-pipeline

**Table 2.1.** Properties of the PHANGS-MUSE galaxies observed with KCWI.

| Name | Distance$^{(a)}$ [Mpc] | $\log_{10}(M_*)^{(b)}$ [$M_\odot$] | $R_{25}{}^{(c)}$ [Arcmin] | $\mathrm{PSF_{MUSE}}{}^{(d)}$ [Arcsec] | $\mathrm{PSF_{KCWI}}{}^{(e)}$ [Arcsec] |
|---|---|---|---|---|---|
| NGC 628 | 9.8±0.6 | 10.34±0.1 | 4.9 | 0.92 | 2.0 ± 0.4 |
| NGC 1087 | 15.9±2.2 | 9.93±0.1 | 1.5 | 0.92 | 1.2 ± 0.1 |
| NGC 1300 | 19.0±2.3 | 10.62±0.1 | 3.0 | 0.89* | 1.3 ± 0.1 |
| NGC 1385 | 17.2±2.6 | 9.98±0.1 | 1.7 | 0.77* | 1.3 ± 0.1 |
| NGC 2835 | 12.2±0.9 | 10.00±0.1 | 3.2 | 1.15 | 1.4 ± 0.1 |
| NGC 3627 | 11.3±0.5 | 10.83±0.1 | 5.1 | 1.05 | 1.1 ± 0.1 |
| NGC 5068 | 5.2±0.2 | 9.40±0.1 | 3.7 | 1.04 | 1.5 ± 0.4 |

*Notes*: (a) From the compilation of Anand et al. (2021). (b) Derived by Leroy et al. (2021a), using GALEX UV and WISE IR photometry. (c) From LEDA Makarov et al. (2014). (d) The FWHM of the Gaussian PSF for the homogenized COPT mosaic from PHANGS-MUSE (Emsellem et al., 2022). (e) The average FWHM of the KCWI PSF for the set of a galaxy's observed pointings. * Denotes galaxies observed with MUSE using ground based adaptive optics.

### 2.2.5 HST

The PHANGS-HST survey (Lee et al., 2022) observed[5] our target galaxies using 5 HST filters: F275W (NUV), F336W (U), F438W (B), F555W (V), F814W (I). Of the high-level data products produced from this dataset, we make use of compact star cluster catalogs (Thilker et al., 2022, Maschmann & Lee et al. submitted) and multi-scale stellar association catalogs (Larson et al., 2023). The association catalog identifies sources using both the V and NUV filters and has been convolved to several physical resolutions (8, 16, 32 and 64 pc, respectively). Following Scheuermann et al. (2023) we used the NUV selected, 32 pc catalogs.

## 2.3 KCWI Data Reduction

The KCWI observations were reduced using the Version 1.0.1 Python implementation of the KCWI Data Extraction and Reduction Pipeline (KDRP)[6]. It was built using the Keck

---

[5] Lee et al. (2022) use of previous NGC 628 HST imaging obtained as part of the Legacy ExtraGalactic Ultraviolet Survey (Legus; Calzetti et al., 2015).

[6] KCWI DRP-Python

Data Reduction Pipeline Framework package[7] and is a port of the initial IDL reduction pipeline[8] (Morrissey et al., 2018). The pipeline performs basic CCD reduction including bias and over-scan subtraction, gain correction, cosmic ray removal, dark and scattered light subtraction as well as a flat field correction.

Following these basic reductions, the KDRP used the continuum bar and Thorium/Argon arc lamp images to generate geometric and wavelength solutions to convert each 2D science image into a spectral datacube. The accuracy of the wavelength solutions were similar across all the observation nights. The average RMS for the derived wavelength solutions was 0.1 Å.

We derived an inverse sensitivity curve to flux calibrate each datacube from standard star observations. The measured standard deviation between all of the derived inverse sensitivity curves was $\sim 9\%$ at $\lambda = 4600$Å. The maximum standard deviation within the wavelength range containing the lines used in this analysis is $\sim 11\%$. Details of each standard star observation can be found in Table 2.6 of Appendix 2.11. After flux calibration, each datacube was corrected for differential atmospheric refraction.

Because the instrument FoV is much smaller than each galaxy, our images contained no sky pixels. To perform sky subtraction, we observed dedicated sky positions interspersed between science observations. We assigned the sky frame closest in time to each science observation to be used for sky subtraction according to the instructions in the KDRP documentation[9]. The KDRP then performed sky subtraction using our preferred frames. The sky in all pixels was averaged together and scaled by the ratio of science-to-sky exposure time to estimate the sky observed in the “on” position. The final data products output by the pipeline include flux calibrated science and $1\sigma$ uncertainty cubes, as well as a bad-pixel mask cube.

---

[7] KeckDRPFramework

[8] KCWI DRP-IDL

[9] https://kcwi-drp.readthedocs.io/en/latest/sky_subtraction.html

### 2.3.1 Image Re-Projection

Next we constructed mosaics from the individual KCWI pointing datacubes. The steps involved included image registration, matching the flux calibration to MUSE, and image co-addition. We also compared the absolute flux calibration of the final KCWI mosaics to MUSE and SDSS

The datacubes output by the KDRP have rectangular pixels with pixel-scale $1.35'' \times 0.29''$. We reprojected the cubes onto a square pixel grid using the astronomical mosaic software `Montage`[10]. Prior to running `Montage`, we converted the KCWI data to surface brightness units (erg $s^{-1}$ $cm^{-2}$ $Å^{-1}$ $sr^{-1}$) by dividing the flux per pixel by the pixel solid angle in steradians. The reprojected images have a final square pixel grid with a uniform pixel-scale of $0.29''\times 0.29''$. We validated the flux-conservation in our data before and after reprojection.

### 2.3.2 Image Registration

To co-add each galaxy's set of cubes into a spectral mosaic, we placed each cube onto a common world coordinate system (WCS). It is typical to perform image registration by matching the location of foreground stars or background galaxies to known positions found in catalogs. However, in our case most individual fields did not contain a sufficient number of bright point sources. Instead, we performed image registration by maximizing the cross-correlation between individual KCWI fields and overlapping MUSE data in order to match the KCWI pointing astrometry to MUSE. The astrometry of the MUSE galaxy mosaics were validated against wide-field broadband imaging and stellar positions from the Gaia DR1 as described in Emsellem et al. (2022). The MUSE astrometry, when compared to broadband imaging, exhibited better than 100 milli-arcseconds RMS. in both R.A. and Dec.

To cross-correlate KCWI and MUSE, we created synthetic photometry ($P_S$) images from spectral regions where the wavelength coverage of KCWI and MUSE overlap. Because there is some saturation in H$\beta$ and [O III] at the brightest locations in the KCWI data, we masked out

---

[10] See http://montage.ipac.caltech.edu/

those lines in both cubes to avoid any issues with the comparison between the two data cubes.

In order to determine the optimal astrometric shifts to apply to each KCWI science frame, we utilized a two-step grid search operation, first shifting in 1 pixel (or $0.29''$) steps $\pm$ 17 pixels (or $5''$) from the center of the KCWI pointing in order to find the optimal R.A. and Dec. offsets which maximize the correlation of the KCWI and corresponding MUSE $P_S$ images. After locating 1st-pass shifts, we performed a secondary grid search using finer 1/2 pixel increments over a smaller range ($\pm 1''$ from the image center). The 0.5 pixel sampling corresponds to $0.145''$ which is less than the MUSE pixel scale of $0.20''$ but also corresponds to 1/10 the typical KCWI FWHM which is equal to $1.2''$. Across the galaxy sample, the final offsets correspond to correlation coefficients $> 0.9$ between KCWI and MUSE.

### 2.3.3 Matching the MUSE Flux Calibration

In order to correct for any additive and/or multiplicative offsets between the MUSE and KCWI flux calibrations, we compared the surface brightness (SB) calculated in apertures in overlapping position and wavelength. To do this we made use of the $P_S$ images, described in Section 2.3.2, and measured the surface brightness inside a number of $3''$ radius apertures located at randomly drawn positions inside the combined KCWI and MUSE coverage. The aperture size was chosen to be large enough to minimize effects arising from the different PSFs of KCWI and MUSE. We determined the best-fit line to the measured $SB_{\mathrm{KCWI}}$ vs. $SB_{\mathrm{MUSE}}$ relationship, where the slope, $m$, and $y$-intercept, $b$, reflect the multiplicative and additive offset between the KCWI and MUSE flux calibration. We applied the correction by multiplying the KCWI datacubes by $m$ and adding $b$ to the full spectrum in each pixel. The average multiplicative and additive offsets were $m = 1.03 \pm 0.02$ and $b = -7.6 \pm 1.7 \times 10^{-20}$ erg s$^{-1}$ cm$^{-2}$ Å$^{-1}$. This $\sim 3\%$ deviation from a 1–1 slope and low level of additive offset show that the calibrations were already in good agreement.

### 2.3.4 PSF of Individual KCWI Fields

Because the MUSE mosaics have been homogenized to a uniform Gaussian PSF, we have an image with a known (parameterized) PSF. This is advantageous, as we can directly measure the KCWI PSF per pointing using cross-convolution, following the steps outlined in Emsellem et al. (2022). We briefly summarize the procedure here. 1) We produced $P_S$ images of both the MUSE mosaic and the individual KCWI pointings. 2) We re-projected the MUSE cutout onto the KCWI $0.29'' \times 0.29''$ pixel grid. 3) We convolved the KCWI pointing with a 2D Gaussian Kernel with PSF equal to the reference MUSE PSF. 4) In an iterative manner, the reference MUSE image is then convolved with a 2D Gaussian Kernel, $\text{PSF}_k$, where the $\text{PSF}_k$ represents the KCWI pointing PSF which is a free-parameter. We then varied the FWHM of this kernel until we maximized the correlation between the KCWI pointing and the reference MUSE image. For the set of images observed for each galaxy, we present the average and standard deviation of the measured PSFs in Table 2.1. The average PSF across the galaxy sample is $1.4'' \pm 0.2''$ which is consistent with the PSFs measured using the Standard Star observations presented in Appendix 2.11. We chose not to homogenize the PSF of the KCWI data. To do so, would mean convolving the KCWI data to the largest observed PSF. In turn, this would increase the mismatch in resolution between KCWI and MUSE as well as lead to larger H II region boundaries. The larger regions have higher susceptibility of contamination from the diffuse ionized gas.

### 2.3.5 Image Co-Addition

After the KCWI datacubes had been aligned and flux calibrated to match the MUSE mosaics, the KCWI datacubes were co-added to create KCWI galaxy mosaics. The image co-addition was performed with `Montage`. The `mAddCube` call to `Montage` initiates the co-addition. The co-addition is performed by stacking the aligned images, according to the an output WCS determined by `Montage`, and then taking the average value between any overlapping pixels. Pseudo $g$-band images for the final mosaics of each galaxy are shown in Figure 2.1.

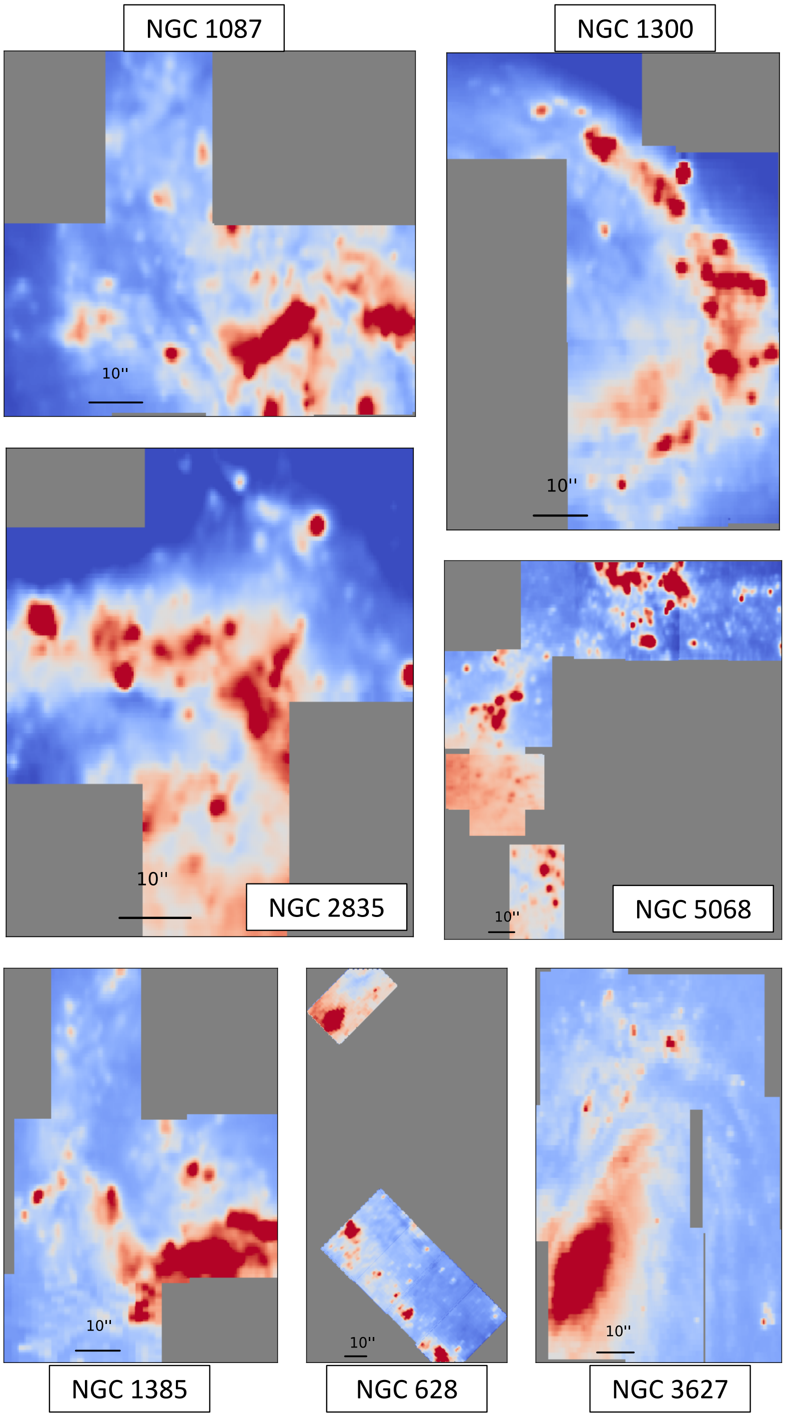

**Figure 2.1.** Pseudo *g*-band images of the KCWI mosaics. A 10″ scale bar is shown in the bottom of each image. Images are oriented to have North pointing upwards.

### 2.3.6 Absolute Calibration of KCWI Compared to MUSE

We assessed the absolute calibration of the co-added KCWI mosaics by comparing the SB's between the KCWI and MUSE mosaics. Comparisons of the MUSE mosaics with SDSS imaging in the $r$-band described in Emsellem et al. (2022) showed that the MUSE absolute flux calibration is consistent with SDSS calibration within the instrument uncertainty of 0.06 mag (Padmanabhan et al., 2008). We calculated the SB inside $r = 3''$ apertures, randomly placed in the KCWI coverage. The SB offsets between the KCWI and MUSE mosaics are shown in Figure 2.2. The resulting offsets, summarized in Table 2.2, reveal acceptable agreement between the MUSE and KCWI absolute calibration. The average percent SB offset with respect to the SDSS imaging, $\Delta\mathrm{SB}/\mathrm{SB}_{\mathrm{SDSS}}$, is between $-1.1\%$ and $0.7\%$ with a median value across all galaxies of $-0.1\% \pm 4\%$.

### 2.3.7 Absolute Calibration of KCWI Compared to SDSS

We have shown agreement between KCWI and MUSE, but this comparison is only an assessment of the flux calibration in the overlapping wavelength range of KCWI and MUSE. To assess the absolute flux calibration across a wider wavelength range, we compared synthetic $g$-band images of the KCWI mosaics to Sloan Digital Sky Survey (SDSS, Abazajian et al., 2003) images of the same galaxies. Only four galaxies with KCWI mosaics have SDSS imaging: NGC 628, NGC 1087, NGC 3627 and NGC 5068. We constructed synthetic $g$-band images of these galaxies by convolving the spectrum in each pixel, $F_\lambda(x,y)$, with the $g$-band transmission curve, $T_g(\lambda)$, according to the following equation:

$$F_g(x,y) = \frac{\int F_\lambda(x,y) T_g(\lambda) d\lambda}{\int T_g(\lambda) d\lambda}. \tag{2.1}$$

The SDSS imaging is presented in units of *nanomaggies* or $f_\nu = 3.631 \times 10^{-6}$ Jy. To compare with the KCWI data, with native units of flux density, $f_\lambda$, we converted to flux density with the

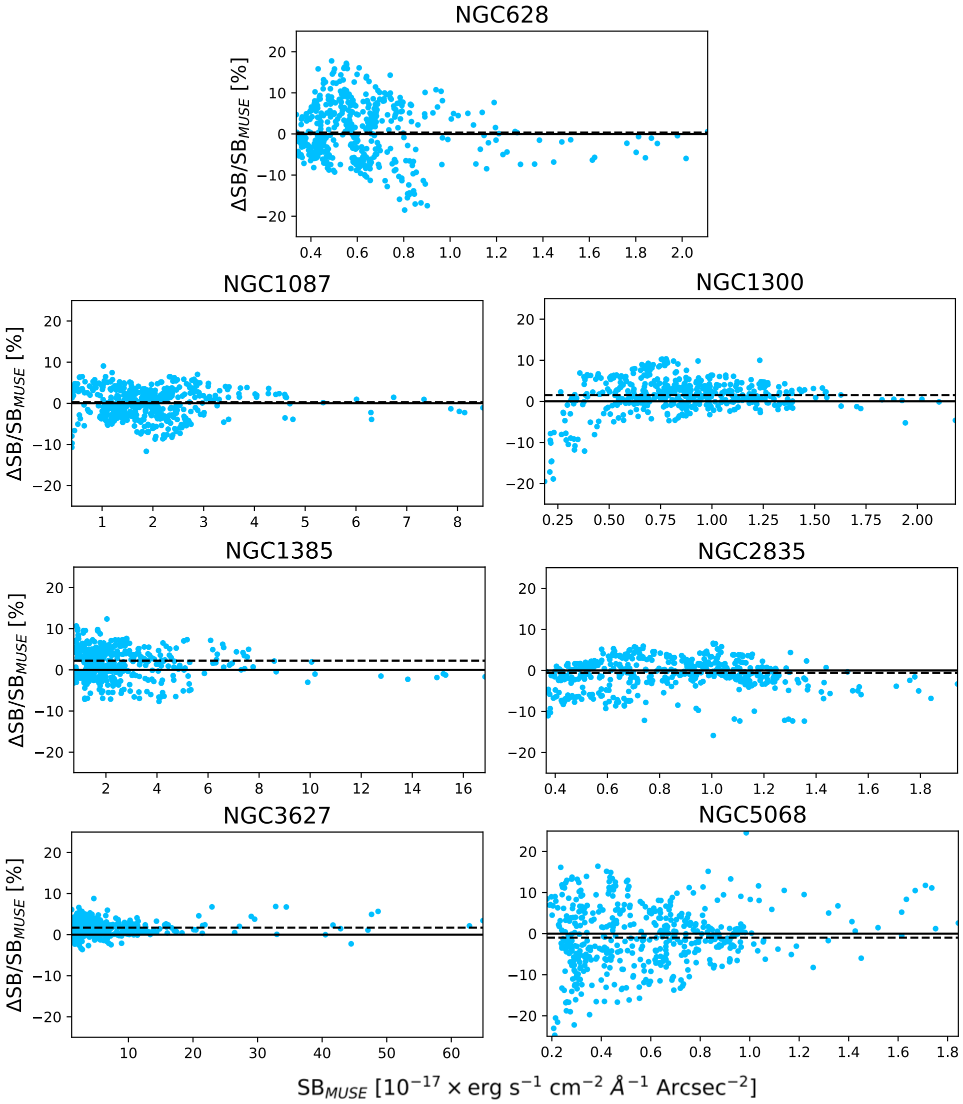

**Figure 2.2.** Comparison of $P_S$ image surface brightness measured in $r = 3''$ apertures from synthetic KCWI and MUSE $P_S$ mosaics of the 7 galaxies. In each panel we show the fractional SB differences between KCWI and MUSE versus the SB of MUSE. The median fractional offset (*black-dashed*) is shown relative to the zero line (*black-solid*). Across all galaxies, the median offset is $\sim -0.1\%$.

following expression (Tokunaga & Vacca, 2005),

$$f_\lambda = \frac{c}{\lambda_p^2} f_\nu, \tag{2.2}$$

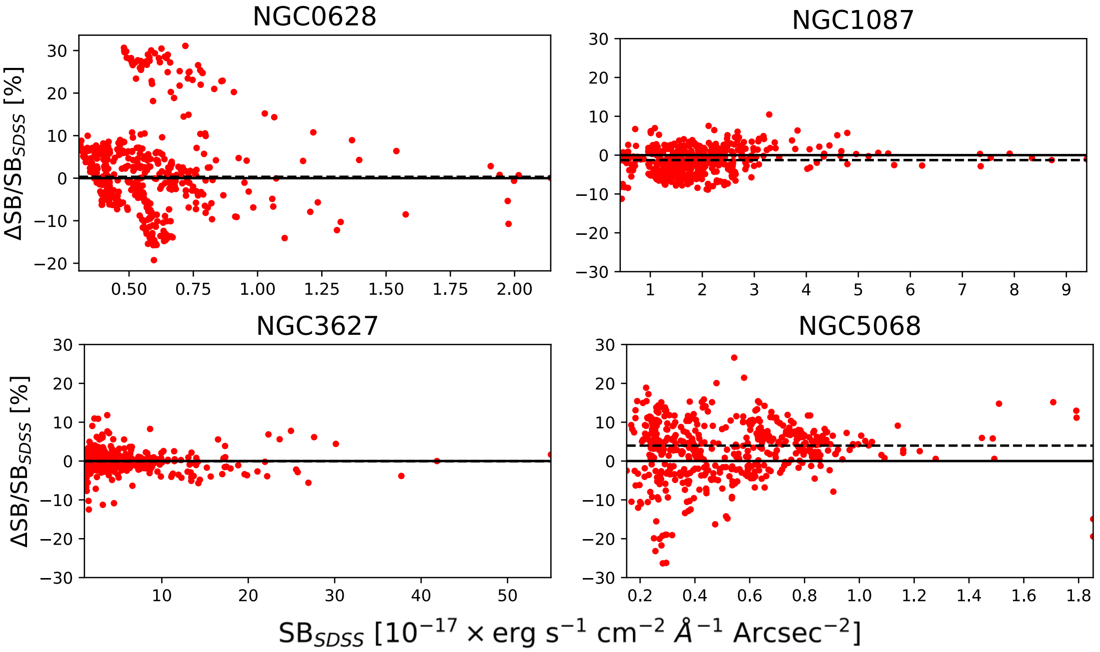

**Figure 2.3.** Comparison of $g$-band surface brightness measured in $r = 3''$ apertures from synthetic KCWI $g$-band mosaics and SDSS imaging for the 4 KCWI galaxies with available SDSS data. The surface brightness offset between KCWI and SDSS is shown versus the SDSS $g$-band surface brightness. The median offset (*black-dashed*) is shown relative to the zero line (*solid-black*). Across the sample, the offset between the KCWI and SDSS surface brightness is $\sim 1\%$.

where $\lambda_p$ is the pivot wavelength of the band-pass. The pivot wavelength for the $g$-band filter is $\lambda_p = 4702$ Å. The surface brightness for both KCWI and SDSS are measured inside $3''$ radius apertures. The mean and $1\sigma$ scatter of the measured surface brightness are shown in Figure 2.3. We found overall agreement of the absolute calibration between KCWI and SDSS for the four galaxies. Summarized in Table 2.2, the median offset across the sample galaxies, $\Delta\mathrm{SB}/\mathrm{SB}_{\mathrm{SDSS}}$ range between $-1.0\%$ and $3.0\%$ and exhibits scatter between $3\%$ and $10\%$. The source of the largest scatter is from the northern most observation of NGC 628. In spite of the quality of this KCWI field, we find that this field contains a single HII region and, as shown in Figure 2.27 of Appendix 2.13, contains detectable auroral and nebular emission from ions only within the MUSE spectrum. Because of this, including this KCWI field will have no negative impact on the overall analysis. The median SB offset across all galaxies is $1 \pm 7\%$ which suggests that the

**Table 2.2.** Flux Calibration Comparisons between KCWI, SDSS and MUSE.

| Name | $\mu(\Delta \mathrm{SB})$ [%] | $\sigma(\Delta \mathrm{SB})$ [%] | $\mu(\Delta \mathrm{SB}_g)$ [%] | $\sigma(\Delta \mathrm{SB}_g)$ [%] |
|---|---|---|---|---|
| NGC 628 | 0.3 | 6.0 | 0.3 | 10.0 |
| NGC 1087 | 0.5 | 3.6 | -1.0 | 3.4 |
| NGC 1300 | 1.5 | 4.0 | - | - |
| NGC 1385 | -0.6 | 4.3 | - | - |
| NGC 2835 | -0.4 | 3.6 | - | - |
| NGC 3627 | 1.7 | 1.6 | -0.05 | 2.6 |
| NGC 5068 | 0.3 | 6.7 | 2.9 | 8.4 |

KCWI calibration is in good agreement with SDSS.

## 2.4 H II Region Catalog

In order to assess the emission line properties of H II regions, we determine the H II region location and boundaries using H$\beta$ maps constructed from the KCWI spectral datacubes and the image segmentation software `HIIphot` (Thilker et al., 2000). Although H II region masks have previously been constructed from the MUSE H$\alpha$ maps for these galaxies (Kreckel et al., 2019; Santoro et al., 2022; Groves et al., 2023; Congiu et al., 2023), the MUSE angular resolution is higher than that of KCWI. Because of this, the H II region boundaries derived from MUSE may not fully encapsulate the spatial extent of the H II regions observed using KCWI. Furthermore, simply convolving or reprojecting the MUSE H II masks to the KCWI resolution or grid would introduce uncertainty on the boundaries for tightly spaced H II regions. We therefore perform H II region identification directly on the KCWI data.

### 2.4.1 Construction of H$\beta$ Maps

H$\beta$ is the brightest H I recombination line observed by KCWI, and maps of this emission for the galaxies will be used to define our H II regions. The continuum near and underlying H$\beta$ emission must be removed in order to accurately map its emission. To remove the continuum we used `LZIFU`, an emission line fitting code designed specifically for use with IFUs (Ho et al., 2016). `LZIFU` implements and streamlines the penalized pixel-fitting software (`PPXF`, Cappellari & Emsellem, 2004; Cappellari, 2017) for using `PPXF` on IFU emission line maps. To fit the continuum of the input spectrum `LZIFU` matches a series of input single-metallicity, $-1.31 <$ [Z/H] $< 0.22$, stellar population models (Vazdekis et al., 2010, MILES) that have been redshifted, and convolved to match the input spectrum PSF. `LZIFU` fits Gaussian models at the location of emission lines. In the output H$\beta$ map, pixels with weak or no H$\beta$ can contain 'NaN' values which can be problematic for `HIIphot`. To avoid these artifacts, we subtract the stellar continuum from each pixel's spectrum and construct the final H$\beta$ maps by integrating the continuum-subtracted spectra between 4856–4876 Å. The final maps are suitable for H II region identification using `HIIphot`.

### 2.4.2 H II Region Identification

`HIIphot` was designed to identify H II regions and complexes (unresolved or blended H II regions) while also minimizing the inclusion of surrounding diffuse ionized gas (or DIG). `HIIphot` works by first defining "seeds" at the location of peak emission in H$\beta$ (or H$\alpha$), then iteratively grows each "seed" and terminates only when the gradient of the H$\beta$ (or H$\alpha$) surface brightness distribution matches a termination value, in mandatory units of emission measure (EM), set by the user. The gradient of the surface brightness distribution is a more robust method of stopping uncontrolled growth at lower S/N compared to using only the average local background level. For each galaxy we apply the the same termination gradient, $\Delta = 5$ EM pc$^{-1}$ or 2.43 × erg s$^{-1}$ arcsec$^{-2}$ pc$^{-1}$, as the recent PHANGS-MUSE work by Santoro et al. (2022).

`HIIphot` uses the PSF to convolve the input H$\beta$ map to different spatial scales to identify seeds. Using a constant PSF for all galaxies can potentially miss valid regions or generate non-physical regions. The PSF of the input H$\beta$ emission map is required by `HIIphot`. For each galaxy mosaic, we used the average PSF from the its KCWI pointings (see Table 2.7 in Appendix 2.11) as the input for `HIIphot`. The resulting 2D mask returned by `HIIphot` contains H II regions with smooth and reasonable boundaries, judged by the distinction between clearly separated HII regions, the minimization of spurious small and pixelated regions or runaway growth. In total, `HIIphot` identifies $\sim$ 688 H II regions or complexes across all of the KCWI mosaics. This number is smaller than the 2169 potential H II regions identified for the Nebular catalog (Kreckel et al., 2019; Santoro et al., 2022; Groves et al., 2023), and 2124 potential H II regions from Congiu et al. (2023), inside the same KCWI footprints. This is largely due to the differences in angular resolution between KCWI and MUSE, and the three-fold decrease in strength of H$\beta$ emission relative to H$\alpha$. In Figure 2.20 of Appendix 2.13 we show histograms of the H$\beta$ luminosity and radii for KCWI and Nebular catalog regions as well a comparisons of the spatial masks in Figures 2.21–2.27 of Appendix 2.13. Additionally, we also present in Table 2.8 of Appendix 2.13 the number of regions detected per galaxy.

### 2.4.3 Generation of Integrated H II Region Spectra

The KCWI H II region masks, produced by `HIIphot`, are used to isolate and sum the spectra in pixels belonging to each H II region, resulting in an integrated H II region spectrum. To produce a matching MUSE H II region mask we transformed the H II regions coordinates/boundaries from the KCWI pixel grid onto the MUSE pixel grid. These are then used to construct MUSE integrated spectra for each H II region. The KCWI and MUSE H II region spectra for a single H II region, with the full set of auroral lines highlighted, is shown in Figure 2.5.

We also produce integrated variance spectra for each H II region. The variance spectra for both KCWI and MUSE H II regions are constructed by propagating the pipeline-produced variance datacubes for pixels contained within each H II region boundary. In the case of MUSE, the datacubes have undergone an additional convolution process in order to generate mosaics with uniform PSF which introduces a correlation between neighboring pixels (Emsellem et al., 2022). Because of the additional convolution, we generated the MUSE variance spectra, assuming fully correlated conditions, by adding the pixel variance spectra linearly (Taylor, 1997).

We verify this choice by comparing the median standard deviation of the propagated

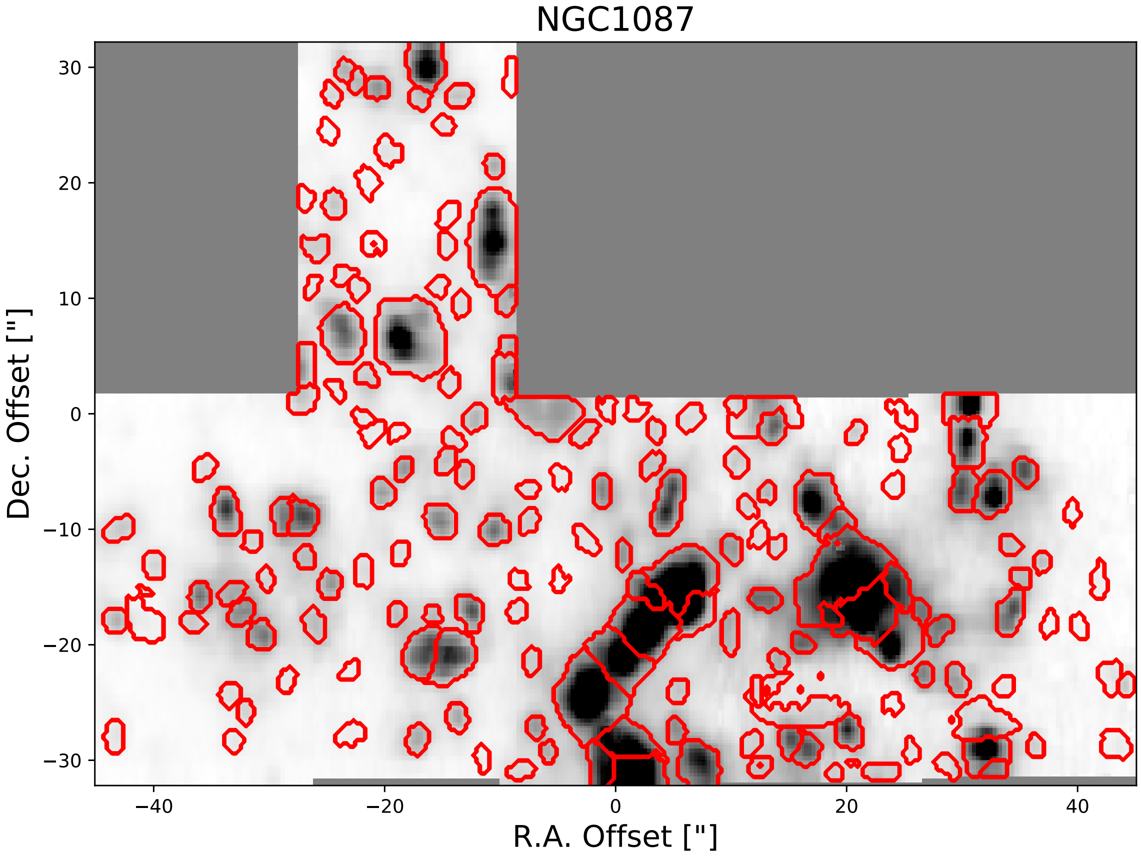

**Figure 2.4.** Region boundaries returned by `HIIPhot`. Pixels within the (*red*) boundaries are identified as corresponding to a potential H II region. The boundaries for the remaining sample galaxies are shown in Appendix 2.13. The R.A. and Dec. offset are centered on the R.A. and Dec. coordinates 02hr 46.0m 25.53s, -00° 29′ 38.8″.

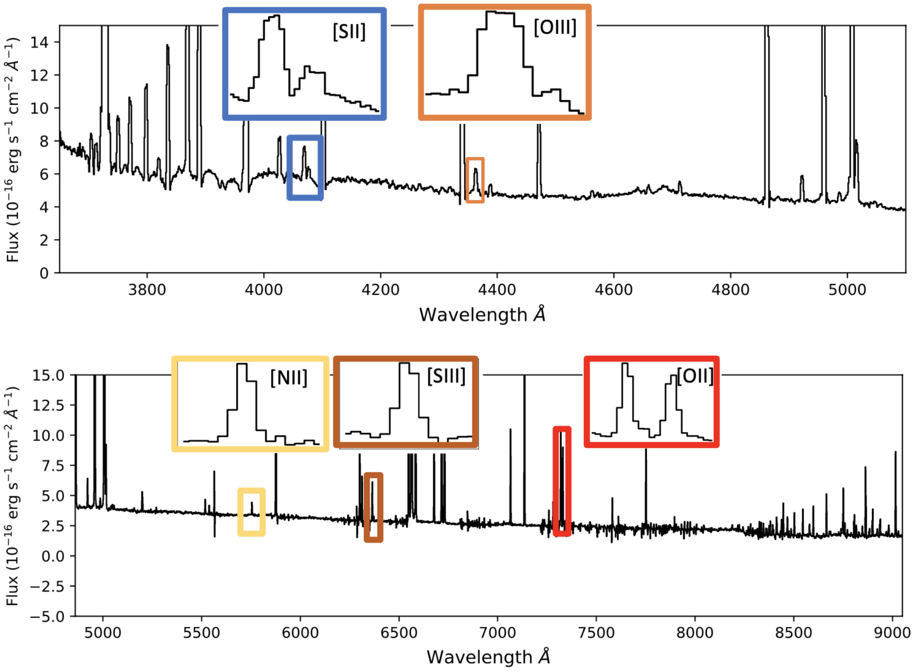

**Figure 2.5.** A KCWI, shown in the top panel, and MUSE, shown in the bottom panel, H II region spectrum. Example spectrum for an H II region in NGC 5068. The full wavelength range afforded by combining both KCWI and MUSE capture the full set of optical auroral lines: [S II]$\lambda\lambda$4068, 4078, [O III]$\lambda$4363, [N II]$\lambda$5756, [S III]$\lambda$6312 and [O II]$\lambda\lambda$7320, 7330, which are identified with zoomed insets.

MUSE variance spectra, $\sigma_{\text{propagated}}$, to the median standard deviation of the H II region spectrum, $\sigma_{\text{measured}}$, in the emission line free wavelength range $5400-5450$ Å. We measured an average ratio between the propagated and measured error of $\sigma_{\text{measured}}/\sigma_{\text{propagated}} = 1.1 \pm 0.2$, implying that we are appropriately propagating the error. We also perform a similar comparison for KCWI, and find agreement, $\sigma_{\text{measured}}/\sigma_{\text{propagated}} = 1.9 \pm 0.5$, between the measured and propagated error using uncorrelated pixel error propagation. To generate the appropriate variance we propagated the error using uncorrelated, for KCWI, and fully correlated error, for MUSE, propagation methods.

### 2.4.4 H II Region Stellar and Emission Line Fitting

We modeled the stellar continuum and emission lines of the integrated H II region spectra using the general `PPXF` toolkit. Although the `LZIFU` implementation of `PPXF` allowed for the streamlined, full datacube, fitting of the KCWI H$\beta$ emission line map, the general `PPXF` toolkit offers more flexibility in the input fitting parameters. For example, we can input a wavelength dependent LSF function as well as fix the kinematics between emission lines of doublets and lines with similar levels of ionization. We followed Emsellem et al. (2022) and fit the emission lines simultaneously with the stellar continuum. This particular fitting recipe was chosen to mirror the philosophy of the Mapping Nearby Galaxies at APO Data Analysis Pipeline (MaNGA DAP, Law et al., 2016; Emsellem et al., 2022) and is suggested to mitigate the biases on emission line fluxes introduced from the masking of stellar absorption features around affected lines (Sarzi et al., 2006; Oh et al., 2011; Belfiore et al., 2019). `PPXF` robustly fits the stellar continuum by matching a set of templates to the observed H II region spectrum. The templates originate from the E-MILES library of simple stellar population (SSP) models (Vazdekis et al., 2016). The SSP ages were between $0.15-13.5$ Gyr. Each age bin contained SSPs with the following metallicities, $[\text{Z/H}] = [-1.49, -0.96, -0.35, 0.06, 0.26, 0.4]$. Typically, `PPXF` convolves the SSP templates with a Gaussian model accounting for the spectral resolution of the input spectrum and the stellar velocity dispersion. However, because the KCWI line profile deviates significantly from a Gaussian (see Appendix 2.12) we convolved the `PPXF` templates with a 4-moment Gauss-Hermite function while fitting KCWI emission lines. We constrained the fits of $h_4$ and $h_3$ in the Gauss-Hermite functions to values listed in Appendix 2.12. We performed the `PPXF` fitting of the KCWI H II region spectra independently from the MUSE H II region spectra. The fractional difference between the H II region H$\beta$ flux for KCWI and MUSE is $-2.3 \pm 7.5\%$.

We obtained errors on the emission line fluxes from the output of `PPXF`. The output errors are considered reliable if the `PPXF` derived reduced $\chi^2 \approx 1$. Together the resulting fits for both the KCWI and MUSE have an average reduced $\chi^2_{\text{reduced}} \approx 2.0$, indicative that the input variance spectra are under-estimated. We obtained a better estimate of the errors by re-scaling the returned errors, for each fit to KCWI and MUSE spectra, by a factor of $\sqrt{\chi^2_{\text{reduced}}}$ (Cappellari & Emsellem, 2004; Cappellari, 2017; Emsellem et al., 2022).

### 2.4.5 Dust Correction

We derive the V-band extinction ($A_V$) for each H II region using the Balmer decrement. To evaluate this decrement while also taking into account the errors on the measured H$\alpha$ and H$\beta$ emission, we construct a distribution of the MUSE H$\alpha$/H$\beta$ ratios by sampling the error for each line. Next, using `PyNeb`, we calculate the extinction by comparing the average of the H$\alpha$/H$\beta$ distribution to the theoretical value assuming the Case B recombination conditions $n_e = 10^3$ cm$^{-3}$ and $T_e = 10^4$ K (Storey & Hummer, 1995). We explore how changing the assumed $T_e$ could affect the derived $A_V$ by sampling a range of temperatures between 5000 K and $1.5 \times 10^4$ K and find that the standard deviation of $A_V$ for a fixed Balmer decrement is $\sim 0.06$ mag. We apply the wavelength dependent extinction correction assuming a O'Donnell (1994) extinction curve. We present a histogram of the derived E($B$-$V$) in Figure 2.6. The average E($B$-$V$) for the regions is 0.30 mag and corresponds to an $A_V \sim 0.9$ mag. We find a negligible difference when using KCWI H$\beta$ in place of the MUSE H$\beta$ flux. We add that a recent investigation shows that correcting, or not correcting, the Balmer lines for DIG contamination can impact the measured E($B$-$V$) (Congiu et al., 2023). For the range of E($B$-$V$) observed, a DIG-corrected

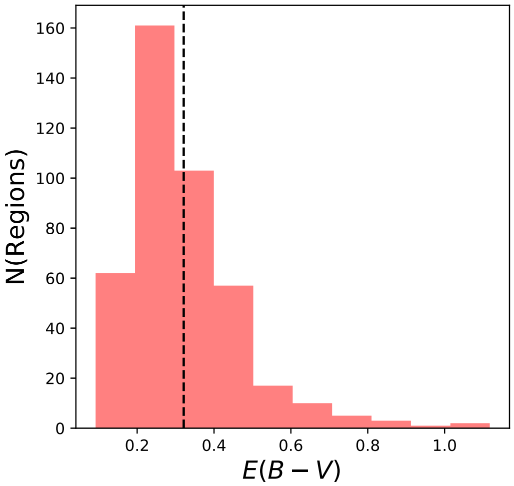

**Figure 2.6.** Histogram of derived extinction, E(B-V). We measured E($B-V$) using the O'Donnell (1994) extinction law for the regions identified by `HIIPhot`. A (*black dashed*) line is located at the mean E($B-V$), 0.30 ±0.14 mag.

E($B$-$V$) may return values of $A_V$ 0.05–0.1 mag lower than presented here. We discuss the effects that under/over-estimated extinction may have on the measured electron temperature in Section 2.7.1. Furthermore, given the good agreement between the integrated KCWI and MUSE H II region fluxes, we replace any saturated integrated H II region KCWI H$\beta$ and [O III] fluxes with those measured from their integrated MUSE spectrum.

### 2.4.6 Diffuse Ionized Gas

Emission from Balmer transitions, [S II]$\lambda\lambda 6716, 6731$, [N II]$\lambda 6584$, and other lines originating from DIG surrounding the H II regions can contaminate the H II region emission line fluxes of the same transitions. Measuring the DIG contribution to H II region line flux is only beginning to being explored by IFU studies (see Belfiore et al., 2022; Congiu et al., 2023). In order to remove regions with a large degree of DIG contamination we calculate the contrast between H II/DIG emission following the scheme outlined in Kreckel et al. (2022). First, we mask each H II region in the MUSE emission line maps for: H$\alpha$, H$\beta$, [S II], [N II] and [O I]. For each emission line, we place a $10'' \times 10''$ aperture around each H II region and measure the median DIG flux in pixels with $\mathrm{S/N} > 3$ and H$\alpha$ surface brightness $\mathrm{Log}_{10}(\mathrm{SB}_{\mathrm{H}\alpha}/[\mathrm{erg\ s^{-1}\ kpc^{-2}}]) < 38$

(see Belfiore et al., 2022). Finally, we calculate the "integrated" DIG emission by multiplying the median DIG flux by the H II region size. For each DIG emission line, we calculate the percent contrast between the measured H II region flux and DIG flux. If the contrast between the H II region flux and DIG flux of any low-ionization emission line is $< 50\%$, we exclude it from the sample.

### 2.4.7 Quality Assessment and Classification of Regions

The regions identified by `HIIphot` are potentially a mix of H II regions, planetary nebulae, supernova remnants or low S/N in critical emission lines. We perform a set of cuts to reject non-H II regions and/or low S/N spectra from the catalog of H II regions.

- We exclude any H II region whose centroid coordinates are within $2''$ from the edge of the mosaic. This step removes 86 H II regions
- We require the strong lines used for temperature determinations: H$\beta$, H$\alpha$, [O III]$\lambda\lambda4959, 5007$ [O II]$\lambda3727$, [N II]$\lambda\lambda6548, 6584$, [S III]$\lambda9069$ and [S II]$\lambda\lambda6716$, 6731 to be detected above a threshold of S/N $> 5$ . This step cuts 72 H II regions from the sample.
- Using the lines of H$\beta$, H$\alpha$, [O III] and [N II] we construct a Baldwin-Phillips-Terlevich (BPT, Baldwin et al., 1981) diagram. We require H II regions to be consistent with photoionization by massive stars. Therefore, we require them to fall below the empirical [O III]/H$\beta$ vs. [N II]/H$\alpha$ (Kauffmann et al., 2003) and [O III]/H$\beta$ vs. [S II]/H$\alpha$ (Kewley et al., 2001) lines. The BPT diagram showing the location of each H II region is shown in Figure 2.7. Out of the sample, 11 H II regions are above the empirical and theoretical line cut-offs and are removed.
- We exclude H II regions that fail our DIG contrast check in Section 2.4.6. This step removes 98 H II regions.

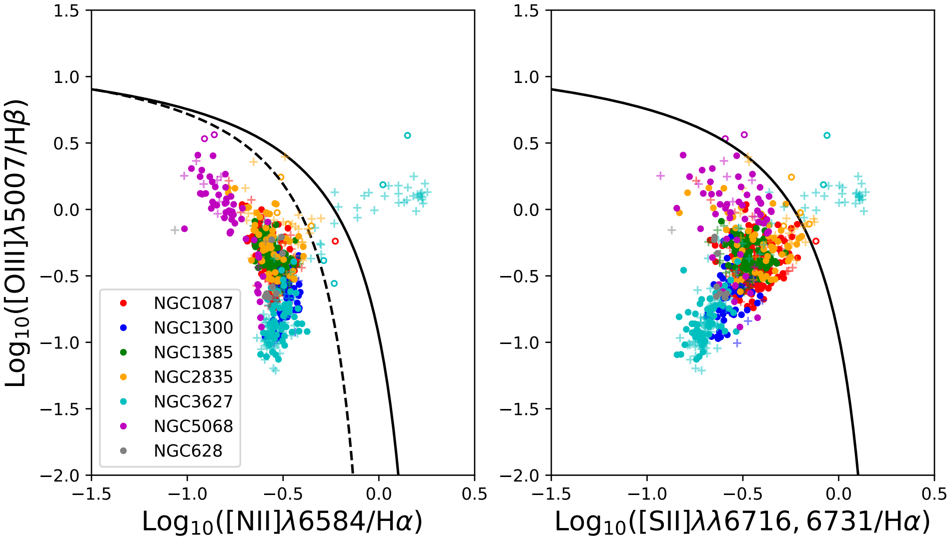

**Figure 2.7.** BPT diagrams showing [O III]/H$\beta$ vs. [N II]/H$\alpha$, in the left panel, and [O III]/H$\beta$ vs. [S II]/H$\alpha$ ratios, in the right panel, for each region identified by `HIIphot`. Regions with emission line ratios consistent with photoionization by stars are expected to populate the parameter space below the theoretical (*solid-black,* Kewley et al., 2001) and empirical (*dashed-black*, Kauffmann et al., 2003) classification lines. The H II regions are marked by filled markers. The regions above either of the classification lines are labeled with non-filled markers and are rejected from the catalog. Regions marked by '+' symbols have been rejected by our other considered constraints.

The constraints together remove 267 out of the 688 detected H II regions leaving 421 H II regions remaining for use in future analysis. For these 421 regions, comparison of line ratios in Figure 2.7 to model classifications in Figure 3 of Congiu et al. (2023) suggest that this sample is consistent with their H II region classification. In order to compare the electron temperatures derived from the lines which are critical for $T_e$–$T_e$ comparisons we also exclude regions with less than 2 significant (i.e. S/N $>$ 3, see Section 2.5) detections in any auroral line. This cut excludes removes 161 regions, leaving a final sample of 260 H II regions. We report in Table 2.8 of Appendix 2.13 the number of regions with at least 2 auroral lines for each galaxy.

## 2.5 Measurement of Auroral Line Emission

In order to robustly measure the flux and uncertainty for the faint, temperature sensitive auroral lines from [N II]$\lambda$5756, [O II]$\lambda\lambda$7320, 7330, [S II]$\lambda\lambda$4069, 4076, [O III]$\lambda$4363, and

[S III]$\lambda$6312 we implement a specific auroral line fitting scheme in place of `PPXF`. This is necessary because any under/over subtraction of the continuum at the location of the faint auroral lines can bias the measured auroral line flux.

The framework of the auroral line fit is as follows. We first subtract the stellar continuum spectrum fitted by `PPXF`. This results in an H II region spectrum that contains only emission lines and residuals from the continuum subtraction. Next, we measure the standard deviation of the residuals, $\sigma_{cont}$, in a region near the auroral line but also free of emission. We then perform a large number of fits to the auroral line with random noise added to each wavelength bin, drawn from a normal distribution with standard deviation $\sigma_{cont}$. In each trial, we fit a single Gaussian (or double depending on the auroral line) plus a linear offset to the spectrum. The linear term is needed to correct for any residual continuum present in the continuum-subtracted spectrum. After completing the $N$ trials, we calculate the average integrated line flux, $F_{avg}$, and the standard deviation of the measured fluxes, $\sigma_{avg}$. If S/N $> 3$ we consider the auroral line detected. In Figure 2.28 of Appendix 2.14 we show the model fits and residuals for a region in NGC 5068.

Although this general process is performed for all the auroral lines, the auroral line from [O III] is subject to additional constraints because emission from the [O III]$\lambda$4363 can be blended with [Fe II]$\lambda$4360. This has been observed in both stacked galaxy and individual H II region spectra (Curti et al., 2017; Berg et al., 2020; Arellano-Córdova & Rodríguez, 2020). The strength of the [Fe II]$\lambda$4360 has been observed to increase with the metallicity of the gas (Curti et al., 2017), although continuum pumping fluorescence contributes strongly to its emissivity (Rodríguez, 1999). [Fe II]$\lambda$4360 and [Fe II]$\lambda$4288 arise from the same atomic upper level and their relative intensities are independent of the physical conditions of the gas and depend solely on the atomic transition probabilities. Since $I(\lambda 4360)/I(\lambda 4288) = 0.73$ (Mendoza et al., 2023), if [Fe II]$\lambda$4360 is detected, [Fe II]$\lambda$4288 should be present too.

To remove blending of the [O III]$\lambda$4363 line by [Fe II]$\lambda$4360, we use the fixed ratio, $I(\lambda 4360)/I(\lambda 4288) = 0.73$, to estimate the degree of contamination by measuring the strength of the brighter [Fe II]$\lambda$4288 emission. For each region we first fit the [Fe II]$\lambda$4288 line using a single Gaussian plus a linear continuum model. The initial guesses for the line center and width are taken from the parameters of H$\gamma$ returned by the `PPXF` fits. In the case that the [Fe II]$\lambda$4288 is not detected above a S/N threshold of 3, we instead use the 3$\sigma$ upper limit. We next fit [O III]$\lambda$4363 using a single Gaussian plus constant offset model. The initial guesses for the kinematics of [O III]$\lambda$4363 are taken from the `PPXF` fit of [O III]$\lambda$4958. After adding random noise, we generate a model for the [Fe II]$\lambda$4360 using the best fit parameters and errors derived from the fit to [Fe II]$\lambda$4288, using the fixed $I(\lambda 4360)/I(\lambda 4288)$ ratio. After generating the [Fe II]$\lambda$4360 model, we subtract it from the trial spectrum and proceed to then fit for the emission line flux originating from [O III]$\lambda$4363. We also note that by performing the above fitting scheme on each region, we may be introducing a bias in the form of a systematic reduction of the [O III]$\lambda$4363 flux. However, this bias would favor systematically lower $T_{\mathrm{e,[O\,III]}}$, but, shown in Section 2.7, we do not observe any behaviour with $T_{\mathrm{e,[O\,III]}}$ that would indicate the presence of such a systematic.

We detect emission from [Fe II]$\lambda$4288 in 30 H II regions, two of these are in regions with measurable [O III]$\lambda$4363. The low number of [Fe II]$\lambda$4288 detections suggest that the combination of high-metallicity, needed for the presence of iron lines, and the exponential dampening of [O III]$\lambda$4363 makes the contamination of [O III]$\lambda$4363 by [Fe II]$\lambda$4360 a rare occurrence in spiral galaxies. From the non-detections, we determined that the 3$\sigma$ upper-limit on the [Fe II]$\lambda$4360 flux is $3.5\ \times 10^{-17}$erg s$^{-1}$ cm$^{-2}$ pc$^{-1}$ which is $\sim$ 20% of the average [O III]$\lambda$4363 flux. We show in Figure 2.29 Appendix 2.14 an example [O III]$\lambda$4363 fit which has had significant [Fe II]$\lambda$4360 contribution removed.

## 2.6 H II Region Nebular, Environmental, and Stellar Properties

We assess the ionized gas physical conditions—$n_{\mathrm{e}}$, $T_e$, and ionization parameter $U$—of each H II region using a subset of the dust-corrected emission line fluxes. We also measure

**Table 2.3.** Transitions Probabilities, Collision Strengths, and Critical Densities for the relevant emission lines used in the PyNeb Temperature Determinations.

| Ion | Transition Probabilities | Collision Strengths | $n_{\mathrm{crit,nebular}}$ [$10^3$ cm$^{-3}$] |
|---|---|---|---|
| [O II] | Zeippen (1982) | Kisielius et al. (2009) | $2^{(a)}$ |
| [O III] | Froese Fischer & Tachiev (2004) | Storey et al. (2014) | 691 |
| [N II] | Froese Fischer & Tachiev (2004) | Tayal (2011) | 88 |
| [S II] | Rynkun et al. (2019) | Tayal & Zatsarinny (2010) | $3^{(b)}$ |
| [S III] | Froese Fischer et al. (2006) | Tayal & Gupta (1999) | $543^{(c)}$ |

*Notes*: (a) Average critical density for [O II]$\lambda\lambda 3726, 3729$ . (b) Average critical density for [S II]$\lambda\lambda 6716, 6731$. (c)Average critical density for [S III]$\lambda\lambda 9069, 9532$.

a number of characteristics of the H II region's environment and local stellar population, as described below.

### 2.6.1 Electron Density

Using `PyNeb` we calculate the electron density $n_e$ for each H II region using the [S II]$\lambda\lambda 6716, 6731$ doublet. Based on our constraints discussed in Section 2.4.7, each H II region is guaranteed to have measured emission from this doublet at S/N $> 5$. The [O II]$\lambda\lambda 3726, 3729$ doublet is also commonly used to estimate $n_e$. The atomic levels responsible for [S II]$\lambda\lambda 6716$, 6731 and [O II]$\lambda\lambda 3726, 3729$ both have critical densities, when collisional and radiative de-excitation are occurring at equal rates, that are of order $10^3$ cm$^{-3}$. The critical densities, as well as other references for the atomic data used, are listed in Table 2.3. Both the [S II]$\lambda\lambda 6716, 6731$ and [O II]$\lambda\lambda 3726, 3729$ doublets are sensitive to densities $10^2$ cm$^{-3}$ $< n_e <$ $10^{3.5}$ cm$^{-3}$. However, in the KCWI measurements, the [O II]$\lambda\lambda 3726, 3729$ doublet is unresolved, and therefore we do not use it to measure $n_e$. With the exception of a handful of regions, the measured electron densities are in the low-density limit, $n_e < 100$ cm$^{-3}$.

**Table 2.4.** Median temperature for each ion.

| $T_{e,Ion}$ | Median$^{(a)}$ [$10^4$ K] | $N_{regions}$$^{(b)}$ |
|---|---|---|
| $T_{e,[O II]}$ | $0.95^{+0.22}_{-0.12}$ | 156 |
| $T_{e,[N II]}$ | $0.81^{+0.12}_{-0.09}$ | 245 |
| $T_{e,[S II]}$ | $0.94^{+0.19}_{-0.14}$ | 305 |
| $T_{e,[S III]}$ | $0.89^{+0.30}_{-0.10}$ | 143 |
| $T_{e,[O III]}$ | $1.20^{+0.35}_{-0.16}$ | 26 |

*Notes*: (a) The 50th ± the 16th – 84th percentile of the measured temperatures. (b) Number of H II regions with temperature measured from the particular ion.

### 2.6.2 H II Region Electron Temperatures

The auroral lines allow the determination of the electron temperatures for the $O^+$, $O^{2+}$, $N^+$, $S^+$ and $S^{2+}$ ions, or $T_{e,[O II]}$, $T_{e,[O III]}$, $T_{e,[N II]}$, $T_{e,[S II]}$, and $T_{e,[S III]}$, respectively. The temperatures are calculated via `PyNeb` using the collision strengths and transition probabilities, listed in Table 2.3, as well the measured upper-limits of the electron density, $n_e$, to convert an auroral-to-nebular ratio to temperature. The critical densities of the requisite lines, see Table 2.3, used to estimate $T_{e,[O III]}$, $T_{e,[N II]}$, and $T_{e,[S III]}$ are high enough such that the auroral-to-nebular lines ratios are insensitive to choice of $n_e < 10^4$ cm$^{-3}$. The density sensitivity in the lines used for $T_{e,[O II]}$ and $T_{e,[S II]}$ begins at smaller densities $n_e \approx 10^3$ cm$^{-3}$ and is further discussed in Section 2.7.3. The uncertainty for each temperature measurement is the standard deviation of the distribution of temperatures constructed by Monte Carlo sampling of the error for each auroral and nebular line included in the temperature determination. We summarize the number of detections and median temperature for each ion in Table 2.4.

### 2.6.3 H II Region Ionization Parameters

The ionization parameter is an indicator of the strength of the ionizing radiation field. The Strömgren sphere descriptions of H II regions define the ionization parameter as $U = Q_0/(4\pi R^2 n_{\rm H} c)$, where $Q_0$ is the emission rate of photons capable of ionizing hydrogen (i.e.

with energy $> 13.6$ eV), $R$ is the radius of the ionized region, $n_{\mathrm{H}}$ and $c$ are the hydrogen density and speed of light. However, calculating the ionization parameter using this definition is difficult (Kreckel et al., 2019, 2022) as resolved studies show that H II regions exhibit a range of non-spherical morphologies and non-uniform densities (Wood & Churchwell, 1989).

Instead, we trace the ionization parameter using both the [S III]/[S II] and [O III]/[O II] emission line ratios. Photoionization modeling has shown that both the [S III]$\lambda\lambda 9069, 9532$/[S II]$\lambda\lambda 6716, 6731$ and [O III]$\lambda\lambda 4959, 5007$/[O II]$\lambda\lambda 3626, 3729$ correlate with the ionization parameter, $U$ (Dors et al., 2011). Although it has a positive correlation with the ionization parameter, the [O III]/[O II] also has a secondary dependence on metallicity, increasing with decreasing metallicity. [S III]/[S II] is not as sensitive to metallicity, making the ratio a more reliable tracer of the ionization parameter (Kewley & Dopita, 2002). Differences between these diagnostics are discussed further in Section 2.7.3. While [S III]$\lambda 9532$ is not observed with MUSE, we measure the [S III]$\lambda 9069$ and assume the fixed theoretical line ratio of [S III]$\lambda 9532/\lambda 9069 = 2.5$ (Froese Fischer et al., 2006) in all calculations. Without observations of [S III]$\lambda 9532$ we can not use this theoretical ratio to assess any impact of atmospheric absorption. Despite this, and discussed in Section 2.7.1, the low scatter between $T_{\mathrm{e,[N\,II]}}$ and $T_{\mathrm{e,[S\,III]}}$ suggest that the decrease in the [S III]$\lambda 9069$ flux due to atmospheric absorption may be negligible.

### 2.6.4 ALMA-CO: Intensity, Peak Temperature, and Velocity Dispersion

Using the ALMA 12m+7m+TP datacubes, we calculate moment 0, and 2 (integrated intensity and velocity dispersion) for molecular gas near each H II region. Because molecular and ionized gas are not entirely co-spatial at our resolution, it is necessary to make a selection to capture gas near the H II region. One possibility is to match H II regions to molecular clouds via a nearest-neighbor algorithm (Grasha et al., 2019; Zhang et al., 2021; Zakardjian et al., 2023). We instead choose to integrate the ALMA spectrum contained in the H II region boundaries in order to measure the properties of the molecular gas closest in projection to the the ionized gas (i.e. in front, behind, or blended due to the resolution of KCWI) and likely affected by the radiative feedback. To measure the CO spectra, we reproject the H II region masks onto the grid of the ALMA datacubes and integrate the ALMA spectra for pixels located inside the footprint of each H II region.

From the ALMA spectrum, we then calculate the integrated intensity, $I_{\rm CO}$, peak temperature, $T_{\rm peak}$ and the velocity dispersion, $\sigma_{v,\rm CO}$. In order to accurately measure these CO moments in the presence of noise, we construct a signal mask following the basic approach from Leroy et al. (2021b). To do this, we locate the velocity channel which contains the peak emission and construct an integration window around this channel by including velocity channels with signal above the $1\sigma$ noise.

As a check on our analysis of molecular gas, we compare the calculated velocity dispersions to those from a sample of nearest-neighbor matched H II regions-GMC's constructed by Zakardjian et al. (2023). We find that our $\sigma_{v,\rm CO}$ span a similar range, up to $\rm Log_{10}(\sigma_{v,CO}/[km\ s^{-1}])=1.5$, with an average and standard deviations of $\rm Log_{10}(\sigma_{v,CO}/[km\ s^{-1}])=0.88 \pm 0.25$; in line with the average from Zakardjian et al. (2023) which suggests that this method of extracting and measuring the CO properties is reasonable.

### 2.6.5 H II Region Compact Clusters and Associations

In order to test for correlations between the young stellar populations that power H II regions and their electron temperatures, we compile the stellar mass and age of compact clusters and multi-scale stellar associations within our KCWI H II regions using results from HST observations.

We match the HST clusters to H II regions, with two or more auroral lines, by simply selecting all the clusters whose on-sky coordinates fall inside any H II region's spatial footprint. For the associations, we match the NUV selected, 32 pc scale, stellar associations to the individual H II regions in the same manner as Scheuermann et al. (2023). The associations catalog comes with spatial masks identifying the footprint of all the detected associations. Because the association masks have a finer pixel scale than the KCWI H II region masks, we reproject the KCWI mask onto the association mask pixel grid. We find for cluster matches that only 65 of 260 or (25%) of our H II regions are matched to a single cluster. 150 of 260 (or 57%) of our H II regions have zero matches. For association matches, only 85 or 260 (or 33%) of our H II regions are matched to a single association 45 of 260 (or 17%) of our H II regions have zero matches.

For the remaining regions with more than one clusters or association match, because we expect that the youngest and most massive clusters or associations contribute most to the overall ionization of the H II region, we assign to each H II region the age (mass) of the youngest (most massive) available cluster/association.

## 2.7 Results

We present electron temperatures derived using the auroral-to-nebular line ratios from [O II], [N II], [S II], [S III], and [O III]. We construct $T_\mathrm{e}$–$T_\mathrm{e}$ diagrams to compare any multi-ionization zone $T_\mathrm{e}$ relationships to recently measured and/or modeled trends. We then compare the temperatures to properties of the ionized gas such as electron density, $n_\mathrm{e}$, and ionization parameter, $U$. We also relate the temperatures to properties of the molecular gas and stellar populations. We present in Table 2.9 a summary of the measured emission lines and derived properties for the H II regions with two or more detected auroral line.

### 2.7.1 Temperature-Temperature Relations

We show $T_\mathrm{e}$–$T_\mathrm{e}$ relations for our sample H II regions in Figures 2.8, 2.9 and 2.10. The left panel displays the individual H II region measurements. To assess the significance of each $T_\mathrm{e}$–$T_\mathrm{e}$ relation, we calculate its p-value. A correlation is judged to be significant if it exhibits $p \lesssim 10^{-3}$. With the exception of $T_{\mathrm{e,[N\,II]}}$–$T_{\mathrm{e,[O\,II]}}$ and the relations involving $T_{\mathrm{e,[O\,III]}}$, the remaining $T_\mathrm{e}$–$T_\mathrm{e}$ relations are deemed significant according to their p-value. For these significant $T_\mathrm{e}$–$T_\mathrm{e}$ relations we derive the best fitting linear relation using the Bayesian linear regression tool LINMIX [11],

---

[11] https://github.com/jmeyers314/linmix

which itself is a Python implementation of linear mixture model algorithm, LINMIX_ERR, constructed by Kelly (2007). The linear regression in LINMIX includes an additional term to represent the intrinsic scatter weighting each data point. In the panels of Figure 2.8 and Figure 2.9 we report $\sigma_{int}$, or the median of the Normal distributed scatter around the linear regression, and the total scatter, $\sigma_{tot}$. Furthermore, to better see $T_{\rm e}$–$T_{\rm e}$ relationships in individual galaxies we show in the right panel the $T_{\rm e}$–$T_{\rm e}$ relations for temperatures binned in steps of 2000 K in the x-axis, with minimum 2 H II regions per bin, for each galaxy. Alongside the binned data we show recent $T_{\rm e}$–$T_{\rm e}$ relations from Berg et al. (2020, hereafter CHAOS-IV), Rogers et al. (2021, hereafter CHAOS-VI), Zurita et al. (2021, hereafter Z21), Garnett (1992, hereafter G92), Vale Asari et al. (2016, hereafter BOND), and Méndez-Delgado et al. (2023b, hereafter MD23).

### Low-Ionization Zone

The low-ionization zone $T_{\rm e}$–$T_{\rm e}$ relations are shown in Figure 2.8. The top figure shows the $T_{\rm e,[N\,II]}$–$T_{\rm e,[O\,II]}$ comparison. We observe that $T_{\rm e,[O\,II]}$ gives higher values than $T_{\rm e,[N\,II]}$ by 1000 K on average. The magnitude of this offset is largest when $T_{\rm e,[O\,II]} > 1.0 \times 10^4$ K. The $T_{\rm e,[O\,II]} > T_{\rm e,[N\,II]}$ inequality is also reflected in the relations from Zurita et al. (2021), Rogers et al. (2021), and Méndez-Delgado et al. (2023b). We also show in grey the best-fit line, and the corresponding $1\sigma$ uncertainty, described by, $T_{\rm e,[N\,II]} = (0.47 \pm 0.13) \times T_{\rm e,[O\,II]} + (0.36 \pm 0.10)$. The Rogers et al. (2021), Méndez-Delgado et al. (2023b), and Zurita et al. (2021) relations are within the uncertainties of the fit, indicating that the $T_{\rm e,[N\,II]}$–$T_{\rm e,[O\,II]}$ relation is in good agreement with these studies. We also measure scatter around the trend line of $\sigma_{int} = 560$ K and $\sigma_{tot} = 844$ K, both of which are in good agreement with the reported values of $\sigma_{int} = 588$ K and $\sigma_{tot} = 810$ K by Rogers et al. (2021).

The comparison between $T_{\rm e,[S\,II]}$–$T_{\rm e,[N\,II]}$ is shown in the middle panel of Figure 2.8. The best-fit line is described by $T_{\rm e,[S\,II]} = (0.85 \pm 0.15) \times T_{\rm e,[N\,II]} + (0.13 \pm 0.12)$. Only the trend from Zurita et al. (2021) is within the uncertainties of our fit. Both Rogers et al. (2021) and Méndez-Delgado et al. (2023b) favor a steep slope (i.e. hotter $T_{\rm e,[S\,II]}$) which are outside the

$1\sigma$ bounds of our fit. We measure a low intrinsic scatter $\sigma_{int} = 735$ K but a larger total scatter $\sigma_{tot} = 4744$ K. For comparison, Rogers et al. (2021) report $\sigma_{int} = 945$ K and $\sigma_{tot} = 1460$ K.

We show the temperature relation between $T_{\mathrm{e,[S\,II]}}$-$T_{\mathrm{e,[O\,II]}}$ in the bottom-left panel. We observe large scatter around the line of equality, $\sigma_{tot} = 2279$ K, towards hot temperatures and measure a p-value, p= 0.09, that suggests the two temperatures are uncorrelated. We discuss a potential, physical explanation of the scatter in Section 2.7.2, but first we explore effects on the correlation due to low S/N detections. Low S/N detections of weak emission can have an intrinsic bias towards higher values (see, Rola & Pelat, 1994), which in the case of weak detections of the auroral lines of [S II] and [O II], would result in high temperatures. To explore how S/N changes the observed trend, we re-calculated the p-value line using only $T_{\mathrm{e}}$ derived from [S II] and [O II] auroral lines with S/N $> 5$. Using the higher S/N threshold, the p-value returned is now, p= 0.04, but not significant according to our criteria. Furthermore, the total scatter, $\sigma_{tot} = 1743$ K, around the 1-to-1 line is trend is high. We observe in the $T_{\mathrm{e}}$–$T_{\mathrm{e}}$ relations that $T_{\mathrm{e,[O\,II]}}$ and $T_{\mathrm{e,[S\,II]}}$ are systematically hotter than $T_{\mathrm{e,[N\,II]}}$. Based on photoionization models (e.g. Campbell et al., 1986; Garnett, 1992), the low-ionization zone temperatures are expected to be equal. There are systematic effects that could increase $T_{\mathrm{e,[O\,II]}}$ and $T_{\mathrm{e,[S\,II]}}$ temperatures such that $T_{\mathrm{e,[O\,II]}} \sim T_{\mathrm{e,[S\,II]}} > T_{\mathrm{e,[N\,II]}}$. The wide wavelength range between [O II]$\lambda\lambda7320,7330$ and [O II]$\lambda\lambda3726,3729$ as well as [S II]$\lambda\lambda4068,4076$ and [S II]$\lambda\lambda6716,6731$, make these ratios sensitive to the applied reddening correction. An overestimate in the extinction would lead to an underestimate of $T_{\mathrm{e,[O\,II]}}$ and underestimate of $T_{\mathrm{e,[S\,II]}}$. At the same time this would leave $T_{\mathrm{e,[N\,II]}}$ relatively unchanged due to the proximity in wavelength of the requisite lines. We see that both $T_{\mathrm{e,[O\,II]}}$ and $T_{\mathrm{e,[S\,II]}}$ are greater than $T_{\mathrm{e,[N\,II]}}$ which is not compatible with the effects of overestimated extinction correction. Despite the above, our temperatures hierarchy could potentially be produced by under-estimated extinction as this would lead to over-estimates of $T_{\mathrm{e,[O\,II]}}$ and $T_{\mathrm{e,[S\,II]}}$ while again leaving $T_{\mathrm{e,[N\,II]}}$ unchanged. We tested two different extinction prescriptions (O'Donnell, 1994; Fitzpatrick, 1999) and found no change in our results. Due to the possible DIG contribution to the measured extinction, it is more likely that we could be overestimating the extinction than underestimating it (Congiu et al., 2023). Telluric contamination to the line emission at [O II]$\lambda\lambda 7320, 7330$ could be an additional systematic error, but is unlikely to be significant in our data because the [O II]$\lambda 7320$/$\lambda 7330$ ratio measured for our sample is $1.27 \pm 0.3$, in agreement with values predicted by the transition probabilities and the collisional strengths (Zeippen, 1982; Kisielius et al., 2009) and observed in nearby H II regions (Seaton & Osterbrock, 1957; Kaler et al., 1976; Yates et al., 2020; Méndez-Delgado et al., 2022). The [S II]$\lambda\lambda 4068, 4076$ doublet may contain $\sim 10\%$ contamination due to O II recombination emission near the location of [S II]$\lambda\lambda 4068, 4076$ (Méndez-Delgado et al., 2023b) that could bias $T_{\rm e,[S\,II]}$ upwards by $\sim 0.2 \times 10^4$ K for $T_{\rm e,[S\,II]} < 2.0 \times 10^4$ K. The KCWI spectral resolution is too low to separate out any contamination in the measurements of [S II]$\lambda\lambda 4068, 4076$. Lastly, $T_{\rm e,[O\,II]}$ and $T_{\rm e,[S\,II]}$ have a higher sensitivity to electron density inhomogeneities than $T_{\rm e,[N\,II]}$ (Rubin, 1989; Osterbrock & Ferland, 2006; Méndez-Delgado et al., 2023b). [O II] and [S II] start to be dependent on density around $n_{\rm e} \approx 10^3$ cm$^{-3}$ while [N II] is independent of density up to $n_{\rm e} \approx 10^4$ cm$^{-3}$.

Despite the all of the above factors, including S/N considerations, and given the agreement of the $T_{\rm e,[S\,II]}$–$T_{\rm e,[N\,II]}$ and $T_{\rm e,[N\,II]}$–$T_{\rm e,[O\,II]}$ trends with those from Zurita et al. (2021) using the S/N $> 3$ [O II] and [S II] auroral lines, we are motivated to explore potential biases due to uncertainties in the measured electron density, see Section 2.7.2.

### Intermediate Ionization Zone

The $T_{\rm e}$–$T_{\rm e}$ relations between the low and intermediate-ionization zone temperatures are shown in Figure 2.9. Given the lower ionization potentials of O$^+$, N$^+$, and S$^+$ with respect to S$^{++}$, it is possible to have differences in the temperature in the different ionization zones (Garnett, 1992). We compare our observed $T_{\rm e}$–$T_{\rm e}$ relations to predictions from photoionization models for giant H II regions produced by the Bayesian Oxygen and Nitrogen abundance project Vale Asari et al. (2016) and found in the Mexican Million Models database (Morisset, 2009). When available, we also compare the observations to relations from Rogers et al. (2021), Méndez-Delgado et al. (2023b), and Zurita et al. (2021).

The top panel of Figure 2.9 shows the temperature comparisons between $T_{\mathrm{e,[S\,III]}}$ and $T_{\mathrm{e,[O\,II]}}$. The best-fit line, $T_{\mathrm{e,[S\,III]}} = (0.67 \pm 0.27) \times T_{\mathrm{e,[O\,II]}} + (0.022 \pm 0.022)$, closely follows the relationship reported by Zurita et al. (2021). We measure an intrinsic, $\sigma_{int} = 1002$ K, and total scatter, $\sigma_{tot} = 1496$ K. The (BOND) models predict that the temperature $T_{\mathrm{e,[S\,III]}}$ should be greater than $T_{\mathrm{e,[O\,II]}}$ by a small constant offset across the full temperature range. However, our data suggest $T_{\mathrm{e,[O\,II]}}$ rises faster than $T_{\mathrm{e,[S\,III]}}$. Our binned data favor the empirical trend line from Zurita et al. (2021). However, there is a grouping of points from NGC 5068 that show contrasting behavior in both the individual and binned data comparisons.

The $T_{\mathrm{e,[S\,III]}}$ and $T_{\mathrm{e,[S\,II]}}$ comparison, comprised of 108 H II regions, is shown in the middle panel of Figure 2.9. The best fit line for this comparisons is described by, $T_{\mathrm{e,[S\,III]}} = (1.11 \pm 0.25) \times T_{\mathrm{e,[S\,II]}} - (0.045 \pm 0.21)$. Within uncertainties, the $T_{\mathrm{e,[S\,III]}} - -T_{\mathrm{e,[S\,II]}}$ agree with trends observed by Zurita et al. (2021) and that derived from Vale Asari et al. (2016). However, both the intrinsic, $\sigma_{int} = 1627$ K, and total scatter, $\sigma_{tot} = 2598$ K, are large. The binned data do not reveal a preference for either of the literature trend.

The series of CHAOS $T_{\mathrm{e}}$–$T_{\mathrm{e}}$ comparisons (see, Berg et al., 2015, 2020; Rogers et al., 2021, 2022) and Zurita et al. (2021) have observed a tight relationship between $T_{\mathrm{e,[S\,III]}}$ and $T_{\mathrm{e,[N\,II]}}$. We show in the bottom panel of Figure 2.9 the $T_{\mathrm{e,[S\,III]}}$ and $T_{\mathrm{e,[N\,II]}}$ comparison. Satisfying the expectations driven by these past studies, we observe that the trend between $T_{\mathrm{e,[S\,III]}}$ and $T_{\mathrm{e,[N\,II]}}$ exhibits the smallest scatter of the $T_{\mathrm{e}}$–$T_{\mathrm{e}}$ relations presented here. The trend between these temperatures is described by, $T_{\mathrm{e,[S\,III]}} = (1.35 \pm 0.15) \times T_{\mathrm{e,[N\,II]}} - (0.24 \pm 0.11)$, and exhibit intrinsic scatter, $\sigma_{int} = 997$ K, and total scatter, $\sigma_{tot} = 1313$ K; both of which are larger than $\sigma_{int} = 173$ K $\sigma_{tot} = 507$ K reported by Rogers et al. (2021).

For the $T_{\mathrm{e,[S\,III]}}$ and $T_{\mathrm{e,[N\,II]}}$ comparison there are available empirical relations from Rogers et al. (2021), Zurita et al. (2021), and Méndez-Delgado et al. (2023b) which we overlay in addition to the Vale Asari et al. (2016) models. The data show a clear disagreement with the trend observed by Méndez-Delgado et al. (2023b). We observe a large fraction of the binned data that lie near the Rogers et al. (2021) model, and Zurita et al. (2021) relations at low $T_{\mathrm{e,[N\,II]}}$. Regions with hotter $T_{\mathrm{e,[N\,II]}}$ and $T_{\mathrm{e,[S\,III]}}$ would be needed to to further differentiate between the models and empirical trends.

### High Ionization Zone

We show $T_{\mathrm{e}}$–$T_{\mathrm{e}}$ relations between [O III] temperatures (which trace the high ionization zone) and those from the low-intermediate ionization zones in Figure 2.10. Additionally, we overlay $T_{\mathrm{e}}$–$T_{\mathrm{e}}$ relations from Berg et al. (2020), Zurita et al. (2021), and Garnett (1992). Although we observe some H II regions with $T_{\mathrm{e}}$–$T_{\mathrm{e}}$ relations that agree with literature relations, we also observe numerous H II regions with much higher $T_{\mathrm{e,[O\,III]}}$ values of than what is predicted by models with the given low and intermediate ionization zone temperatures. The total scatter around the line of equality in $T_{\mathrm{e,[O\,III]}}$ range between 3100 K and 4500 K. Given this large scatter we do not perform a linear regression analysis for these comparisons.

Based on previous findings from Zurita et al. (2021) and Rogers et al. (2021), the scatter towards large excess in $T_{\mathrm{e,[O\,III]}}$ for regions with cooler low and intermediate ionization zone temperatures is unexpected. With IFUs we are perhaps capturing a wider range of H II regions. Furthermore Zurita et al. (2021) and Rogers et al. (2021) extend to lower metallicities, and possibly higher ionization parameters, where $T_{\mathrm{e,[O\,III]}}$ may be better behaved. Nevertheless, these regions represent an extremely limited sub-set of the data and are at the boundary of significant, so are subject to higher uncertainty. For the $\sim$ Solar metallicities for our H II region sample, where the relative flux [O III]$\lambda$4363 is expected to be $< 10^{-2}\times$ H$\beta$ (Berg et al., 2015), the temperature from [O III]$\lambda$4363 would have to be high in order to be detected. The small number of [O III]$\lambda$4363 detections reflects this. Because we do not expect to detect the line in most H II regions, the ones we do detect may be unusual cases or statistical outliers, especially given that the average S/N of the [O III] detections is $\sim$4. We explore S/N effects by increasing the threshold for comparison to S/N $>$ 5 in [O III]$\lambda$4363. This reduces the sample of regions with $T_{\mathrm{e,[O\,III]}}$ measurements to 5 which is too low to confidently fit a trend, but, we measure a large total scatter, $\sigma_{tot} > 2000$ K, around the line of equality. Discussed further in Section 2.7.3 and in Yates et al. (2020), these regions exhibit low [O III]/[O II] ratios, meaning they are systems with low $O^{++}/O^{+}$. This would mean that small fraction of the total nebulae volume would be described by the high $T_{\mathrm{e,[O\,III]}}$. Despite this, there has been evidence (Peimbert et al., 1991; Binette et al., 2012) that shock excitation can preferentially enhance the high ionization zone temperature, with the highest enhancement occurring in high metallicity environments. How this scenario could apply to this small sub-set of H II regions is explored in Section 2.7.3.

### 2.7.2 The Impact of Density Inhomogeneities on [S II] and [O II] Temperatures

Recent studies have suggested that the temperatures obtained from the auroral-to-nebular lines ratios of [O II] and [S II] can be biased upwards due to the presence of density inhomogeneities, even while the average density is underestimated by nebular doublet line [O II]$\lambda\lambda 3726, 3729$ and [S II]$\lambda\lambda 6716, 6731$ diagnostics.

For example, in a sample of 190 high-signal-noise spectra of H II regions and other photoionized nebulae, Méndez-Delgado et al. (2023b) observed systematically hotter $T_{\mathrm{e,[O\,II]}}$ and $T_{\mathrm{e,[S\,II]}}$ relative to $T_{\mathrm{e,[N\,II]}}$, similar to what we observe, which they attribute to the presence of density inhomogeneities. The atomic levels responsible for the nebular lines [S II]$\lambda\lambda 6731, 6716$ and [O II]$\lambda\lambda 3726, 3729$, listed in Table 2.3, have critical densities of order $10^3$ cm$^{-3}$ which are at least two orders of magnitude lower than the critical densities for the nebular levels of [N II]. In addition, the auroral levels of the same ions have very high critical densities. This makes the auroral-to-nebular temperature diagnostics of $T_{\mathrm{e,[O\,II]}}$ and $T_{\mathrm{e,[S\,II]}}$ density sensitive above $10^3$ cm$^{-3}$, and therefore susceptible to biases if there are important contributions to the line flux from gas above that density. The auroral-to-nebular ratio of [N II], however, is not susceptible to such sensitivity until much higher densities.

Both [S II]$\lambda\lambda 6731, 6716$ and [O II]$\lambda\lambda 3726, 3729$ nebular line doublet ratios serve as density diagnostics for densities $10^2$ cm$^{-3}$ $< n_{\mathrm{e}} <$ $10^{3.5}$ cm$^{-3}$. Furthermore, because of the

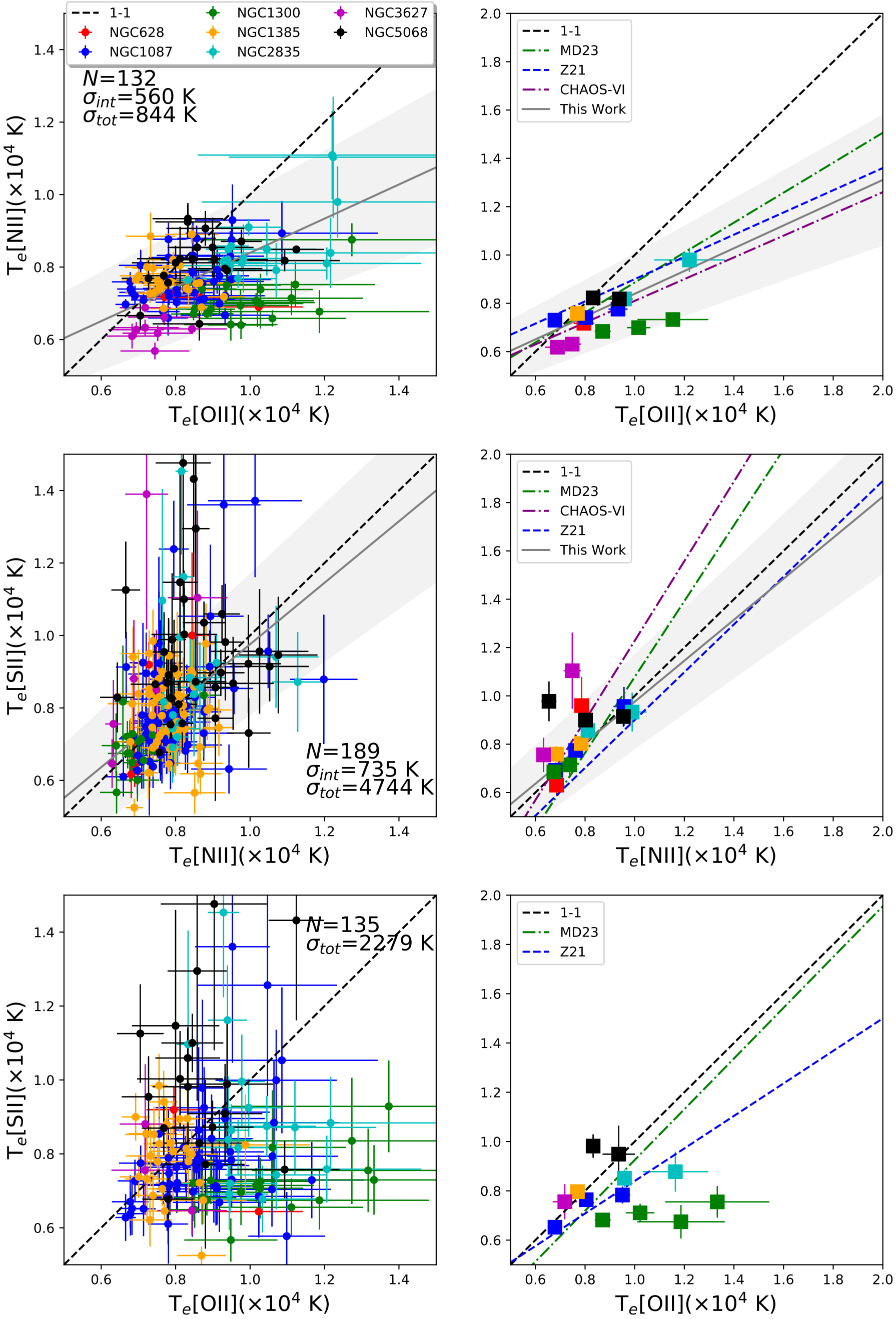

**Figure 2.8.** $T_e$–$T_e$ relationships for the low-ionization zone temperatures measured from H II regions in nearby galaxies. The left panel in each row displays the individual temperatures and errors with each point colored according to the host galaxy. The right panel in each row shows the $T_e$–$T_e$ relations for temperatures binned in steps of 2000 K in the x-axis, with minimum 2 H II regions per bin, for each galaxy, compared to $T_e$-$T_e$ trend lines from Zurita et al. (2021) (*blue dash*), Rogers et al. (2021) (*purple dot-dash*), and Méndez-Delgado et al. (2023b) (*green dot-dash*). To aid the eye, we include in (*black-dash*) the 1–1 line. For comparisons with p-value $< 10^{-3}$, we include the best-fit line (*grey-solid*) and 1$\sigma$ fit uncertainty (*grey-shaded*).

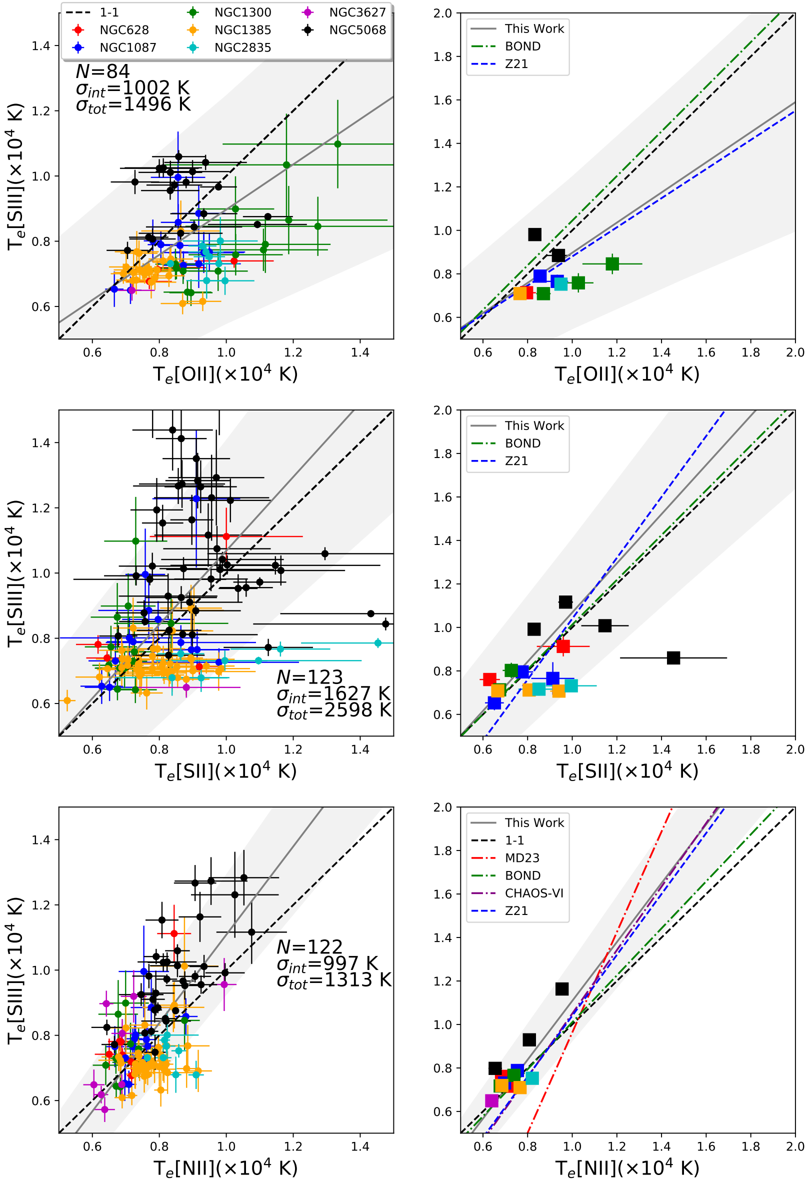

**Figure 2.9.** $T_e$–$T_e$ relationships between the low and intermediate ionization zone temperatures measured from H II regions in nearby galaxies. The temperatures measured from H II regions in this work are color coded by host galaxy. The left panel in each row displays the individual temperatures and errors with each point colored according to the host galaxy. The right panel in each row show the $T_e$–$T_e$ relations for temperatures binned in steps of 2000 K in the x-axis, with minimum 2 H II regions per bin, for each galaxy, compared to $T_e$–$T_e$ trend lines from Zurita et al. (2021) (*blue dash*), Rogers et al. (2021) (*purple dot-dash*), Vale Asari et al. (2016) (*green dot-dash*) and Méndez-Delgado et al. (2023b) (*red dot-dash*). To aid the eye, we include in (*black dash*) the 1–1 line. For comparisons with p-value $< 10^{-3}$, we include the best-fit line (*grey-solid*) and $1\sigma$ fit uncertainty (*grey-shaded*).

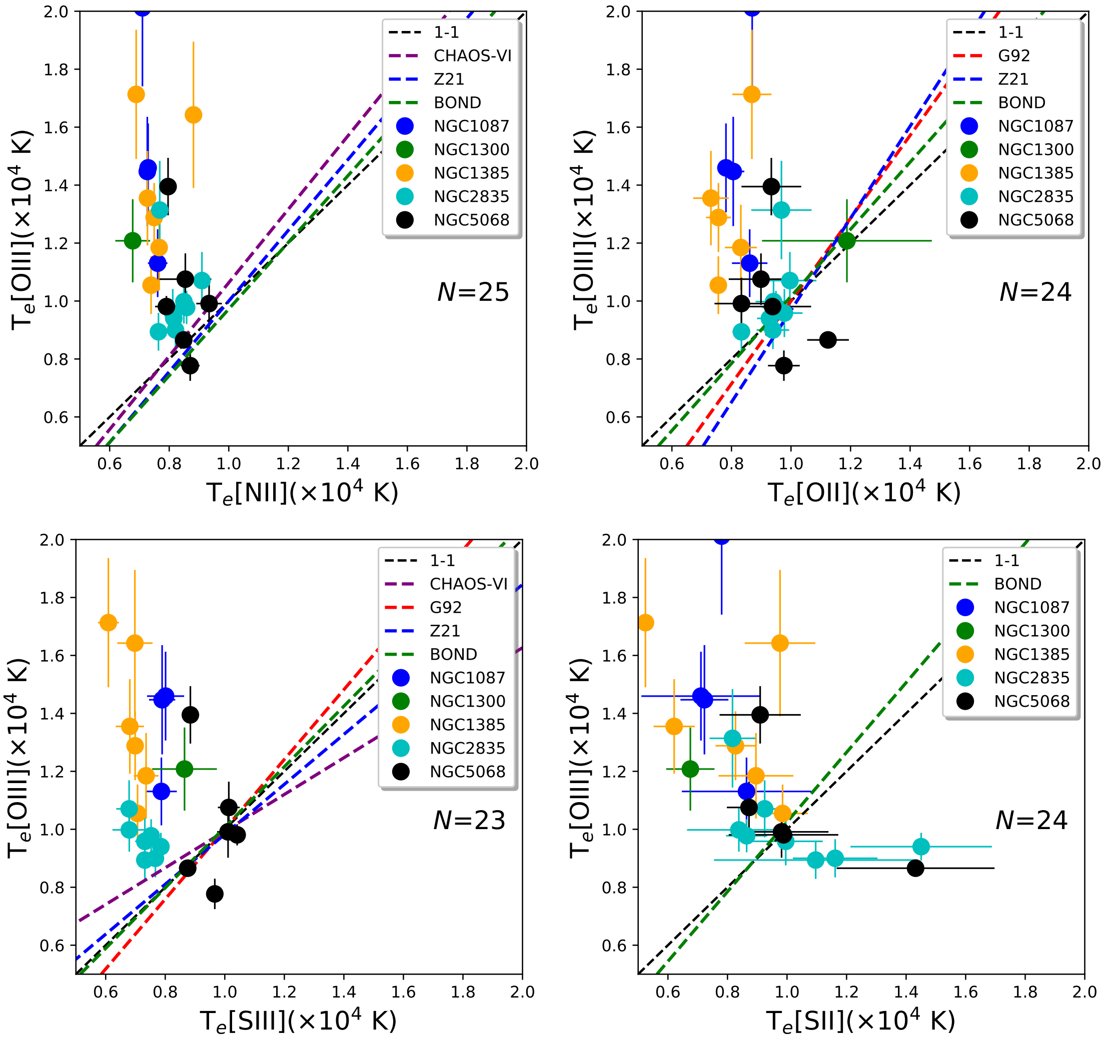

**Figure 2.10.** $T_e$–$T_e$ relationships for the high ionization zone. The temperatures measured from H II regions in this work are color coded by host galaxy. The (*blue-dashed*) line show the $T_e$–$T_e$ relationships from Zurita et al. (2021). The (*red-dashed*) line show trends from Rogers et al. (2021). The (*purple-dashed*) and (*green-dashed*) line trends from the photoionization models of Garnett (1992) and Vale Asari et al. (2016). To aid the eye, we include show in *black* line the 1–1 line in each panel.

bias described above, Méndez-Delgado et al. (2023b) show that at fixed temperature the auroral-to-nebular line ratios for [O II] and [S II] can serve as a density diagnostic over a large range of electron density, $10^2$ cm$^{-3}$ $< n_e <$ $10^6$ cm$^{-3}$. For a uniform density H II region, the $n_e$ returned from both of these diagnostics should be identical, as long as $n_e$ is within the sensitivity range of the diagnostics. However, in the presence of density inhomogeneities, different density diagnostics can return conflicting values. Even if high density gas clumps make up a small fraction of the gas, such regions can continue to contribute to the auroral line emission while no longer contributing significantly to the nebular lines, since the effects of collisional de-excitation on the nebular lines will reduce their emissivities relative to the auroral lines (Rubin, 1989). Because of this, the nebular [S II] and [O II] lines can reflect the dominant contribution of low-density gas, while the auroral [S II] and [O II] lines will be sensitive to volume of high-density gas (Peimbert, 1971; Rubin, 1989; Méndez-Delgado et al., 2023b).

To investigate if the presence of density inhomogeneities could bias our measured $T_{e,[\mathrm{S\,II}]}$ and $T_{e,[\mathrm{O\,II}]}$ we compare the observed auroral-to-nebular line ratios [O II] and [S II] to those predicted using fixed $T_{e,[\mathrm{N\,II}]}$. For this comparison we use the regions with auroral line detections for all three low-ionization zone ions. We show in Figure 2.11 the measured [O II]$\lambda\lambda7320,7330/\lambda\lambda3726,3729$ and [S II]$\lambda\lambda4069,4076/\lambda\lambda6716,6731$ line ratios versus the region's $T_{e,[\mathrm{N\,II}]}$. We overlay the predicted trends of auroral-to-nebular line ratios calculated using $n_e = 10^2$ cm$^{-3}$, $10^{2.5}$ cm$^{-3}$, and $10^3$ cm$^{-3}$. We see in Figure 2.11 that under the assumption that $T_{e,[\mathrm{N\,II}]}$=$T_{e,[\mathrm{S\,II}]}$=$T_{e,[\mathrm{O\,II}]}$, the largest measured auroral-to-nebular line ratios could be consistent with $T_e$ traced by $T_{e,[\mathrm{N\,II}]}$ but with a higher electron density than that returned by [S II]$\lambda\lambda6731,6716$ in the low-density limit. This suggests that under inhomogenous conditions, underestimated contributions from $> 10^3$ cm$^{-3}$ gas to the nebular [O II] and [S II] lines could bias the density diagnostics and then the use of underestimated densities in temperature calculations for ions with low critical densities like [O II] and [S II] could lead to hotter estimated temperatures inferred from auroral-to-nebular ratios.

At the same time, Figure 2.11 also shows that the lowest measured auroral-to-nebular ratios lie below the theoretical curves for ratios with densities equal to the low-density limit. It may be the case that, under our assumption that the H II region low-ionization zone $T_{\rm e}$ is described by $T_{\rm e,[N\,II]}$, these regions physically exhibit volumes of gas with $n_{\rm e} \lesssim 10$ cm$^{-3}$ or lower (Kennicutt, 1984). However, we are unable to verify this using the available diagnostics because densities returned by either the [O II] and [S II] doublet or their auroral-to-nebular line ratios are uncertain in this regime. For these reason we do not pursue further interpretation of these points.

We can further explore potential density inhomogeneities by comparing the measured auroral-to-nebular lines to the regions H$\beta$ surface brightness. The emission from any recombination lines is proportional to $n_{\rm e} n({\rm X}^{+})\alpha_{eff}$, where $n({\rm X}^{+})$ is the number density of the emitting ion and $\alpha_{eff}$ is the effective recombination coefficient (Peimbert et al., 2017). For H$\beta$, $n({\rm X}^{+}) \propto n_{\rm e}$ because 90% of free electrons will come from the photoionization of H which represents ~90% of all the gas. For a uniform density H II region, the H$\beta$ surface brightness, SB$_{\rm H\beta}$, would be proportional to $n_{\rm e}^2$. In the case of H II regions with high density inclusions, the variance of $n_{\rm e}$ would be expected to rise due to the increase in the average of the density squared (i.e. $< n_{\rm e}^2 >$). Under such conditions, it would be reasonable to expect that H$\beta$ surface brightness would increase as ${\rm SB}_{\rm H\beta} \propto < n_{\rm e}^2 >$.

If we interpret the departure of the measured auroral-to-nebular lines ratios from the theoretical ratios calculated by fixing the electron density at the low-density limit, $n_{\rm e} = 100$ cm$^{-3}$ and $T_{\rm e} = T_{\rm e,[N\,II]}$, then we could expect that this deviation would correlate with the H$\beta$ surface brightness. We show in the bottom panels of Figure 2.11 the degree of inhomogeneities, measured by [S II]-[S II]($n_{\rm e} = 100$, $T_{\rm e,[N\,II]}$) and [O II]-[O II]($n_{\rm e} = 100$, $T_{\rm e,[N\,II]}$), against the regions H$\beta$ surface brightness.

We find a significant correlation, p-value $< 10^{-3}$, between [S II]-[S II]($n_{\rm e} = 100$, $T_{\rm e,[N\,II]}$) and SB$_{\rm H\beta}$, which suggests that the regions with large deviations from the predicted low-density limit auroral-to-nebular line ratios are consistent with density inhomogeneities. The best-fit line is described by [S II]-[S II]($n_{\rm e} = 100$, $T_{\rm e,[N\,II]}$) $= 0.0147(\pm0.004) \times {\rm SB}_{\rm H\beta} + 0.20(\pm0.05)$. To account for any uncertainties in the atomic data, we vary the absolute value of the [S II]($n_{\rm e} = 100$,

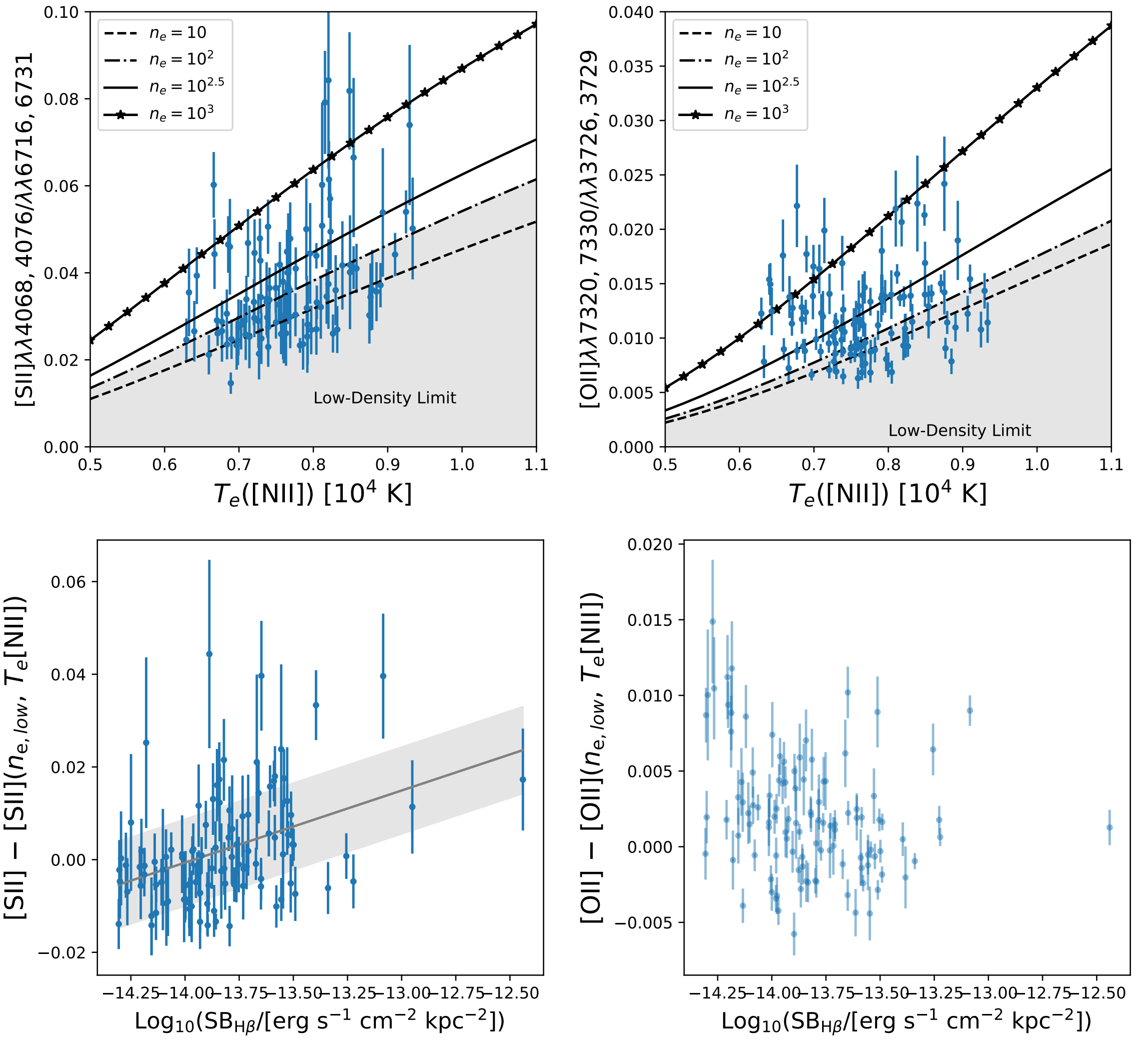

**Figure 2.11.** In the top panels we show auroral-to-nebular line ratios measured from [S II] and [O II] against their measured $T_{\rm e,[N\,II]}$. We assume equality between the low- ionization zone temperatures and overlay lines of predicted [S II] and [O II] auroral-to-nebular line ratios for fixed electron densities $n_e = 10$ cm$^{-3}$,$n_e = 10^2$ cm$^{-3}$, $10^{2.5}$ cm$^{-3}$, and $10^3$ cm$^{-3}$, vs. $T_{\rm e,[N\,II]}$. The (*grey-shaded*) region, in the top panels, show regime where auroral-to-nebular lines ratios for densities below the low-density limits for the [S II] and [O II] density diagnostics. In the bottom panels we show the departure of the measured [S II] and [O II] auroral-to-nebular line ratios from the theoretical auroral-to-nebular line ratio predicted using $n_{\rm e} = 100{\rm cm}^{-3}$ and $T_{\rm e,[N\,II]}$ against the the H$\beta$ surface brightness. For the bottom-left [S II] panel we show the best-fit line (*grey-solid*) and 1$\sigma$ fit uncertainty (*grey-shaded*).

$T_{\mathrm{e,[N\,II]}}$) curve by ± 10% (Mendoza & Bautista, 2014) and find no change in correlation strength. While this correlation is suggestive of density inhomogeneities, we acknowledge that the H II regions are not fully resolved which means we are measuring a PSF-averaged surface brightness. Because of this, it is unclear if this correlation can be fully link to density inhomogeneities.

For the comparison involving [O II]-[O II]($n_{\mathrm{e}} = 100$, $T_{\mathrm{e,[N\,II]}}$), we find no significant correlation with H$\beta$ surface brightness, even when using S/N$>$ 5 auroral lines. While the exact reason for the non-correlation between [O II]-[O II]($n_{\mathrm{e}} = 100$, $T_{\mathrm{e,[N\,II]}}$) and H$\beta$ surface brightness is unknown it is important to note that the ionization potential of [S II] is less than both $H\beta$ and [O II]. This difference in ionization potential means that H II region [S II] and [O II] may not be co-spatial, and may have different sensitivities as tracers of high density inclusions. However, given that these regions have measurements of all three low-ionization zone auroral lines and survive a DIG contrast constraint, we find that the correlation between [S II]-[S II]($n_{\mathrm{e}} = 100$ and $\mathrm{SB}_{\mathrm{H}\beta}$ suggests that density inhomogeneities may be affecting the low-ionization zone temperatures. Future studies with multiple density diagnostics and high spatial resolution will be valuable to exploring the potential impact inhomogeneous conditions have on these diagnostics.

### 2.7.3 Temperature Differences Compared to H II Region Ionized Gas, Stellar Population, and Molecular Gas Properties.

Studies have shown that H II region temperatures for different ionization zones can be differently impacted by properties of the ISM. Temperature comparisons presented in Berg et al. (2020) using H II regions observed in four nearby galaxies revealed that the dispersion around low-intermediate and intermediate-high $T_{\mathrm{e}}$–$T_{\mathrm{e}}$ relation ships increased (or decreased) with the ionization parameter. Another trend with ionization parameter was observed by Yates et al. (2020). They found that systems with low ionization, or larger ratios of $\mathrm{O}^{+}/\mathrm{O}^{2+}$ parameter would exhibit systematically hotter $T_{\mathrm{e,[O\,III]}}$. Though Arellano-Córdova & Rodríguez (2020) argue this could be explained by increased iron contamination to [O III]$\lambda$4363. Discussed in

Section 2.7.2, density fluctuations can also bias the temperatures for the low-ionization zone due to the sensitivity of [O II] and [S II] with density (Méndez-Delgado et al., 2023a,b).

Given that stars are the primary source of ionizing photons, it is reasonable to suspect that the properties of the stellar population ionizing the H II region can potentially play a role in setting the $T_{\mathrm{e}}$ structure of H II regions. Another potential factor on the $T_{\mathrm{e}}$ structure, and traced by its effects on the surrounding molecular gas, is the degree of stellar feedback within H II regions. Although very important to our understanding, the physical processes that impact the $T_{\mathrm{e}}$ structure in H II regions remain uncertain (Garnett et al., 1991; Nicholls et al., 2020).

The KCWI+MUSE H II regions combined with the PHANGS-HST and PHANGS-ALMA observations allow us to investigate how $T_{\mathrm{e}}$ is impacted by different H II ISM, stellar and molecular gas properties. We compare temperature differences, $\Delta(T_{\mathrm{ion},1}, T_{\mathrm{ion},2}) = T_{\mathrm{ion},1} - T_{\mathrm{ion},2}$, between the low, intermediate, and high-ionization zone temperatures. with H II region properties derived from emission line diagnostics; with the properties of the surrounding molecular gas measured from ALMA (Leroy et al., 2021b); and with stellar population masses/ages from SED fitting to HST photometry (Lee et al., 2022; Thilker et al., 2022; Larson et al., 2023).

To gauge the significance and monotonicity of each comparison we calculate the Pearson correlation coefficient (i.e. p-value or $p$), as well as the Spearman Rank Correlation Coefficient, $\rho$. A correlation is judged to be significant if it exhibits $p \lesssim 10^{-3}$. The strength of the correlation is separated into the following regimes: $1 > |\rho| > 0.8$ corresponds to a *strong* correlation, $0.8 > |\rho| > 0.4$ corresponds to a *moderate* correlation and $0.4 > |\rho| > 0$ identifies a *weak* or no correlation.

As expected, we observe strong correlations between temperatures differences with ionization parameter. We do not report any significant correlations between $\Delta T_{\mathrm{e}}$ with any of the following properties: integrated CO intensity, CO peak temperature, molecular gas velocity dispersion, cluster mass, cluster age, association age, association age. Figures showing the $\Delta T_{\mathrm{e}}$ comparisons to these parameters are shown in Appendix 2.15. Despite no significant correlations, we do find interesting behavior between $\Delta(T_{\mathrm{e,[N\,II]}}, T_{\mathrm{e,[S\,III]}})$ with association mass, and excess

**Table 2.5.** Summary of the p-values and Spearman Rank coefficients for comparisons between $\Delta T_{\rm e}$ with the ionization and radiation softness parameter of the H II regions.

| $\Delta T_{\rm e}$ | [S III]/[S II]<br>$(\rho, {\rm p})$ | [O III]/[O II]<br>$(\rho, {\rm p})$ | $\eta$<br>$(\rho, {\rm p})$ |
|---|---|---|---|
| $\Delta(T_{\rm e,[O\,II]}, T_{\rm e,[N\,II]})$ | - | - | - |
| $\Delta(T_{\rm e,[N\,II]}, T_{\rm e,[S\,II]})$ | $(-0.27, < 10^{-3})$ | - | - |
| $\Delta(T_{\rm e,[S\,II]}, T_{\rm e,[O\,II]})$ | $(0.32, < 10^{-3})$ | - | - |
| $\Delta(T_{\rm e,[O\,II]}, T_{\rm e,[S\,III]})$ | - | - | - |
| $\Delta(T_{\rm e,[N\,II]}, T_{\rm e,[S\,III]})$ | - | - | - |
| $\Delta(T_{\rm e,[S\,II]}, T_{\rm e,[S\,III]})$ | $(0.53, < 10^{-3})$ | - | $(0.46, < 10^{-3})$ |
| $\Delta(T_{\rm e,[O\,II]}, T_{\rm e,[O\,III]})$ | - | $(0.85, < 10^{-3})$ | - |
| $\Delta(T_{\rm e,[N\,II]}, T_{\rm e,[O\,III]})$ | $(0.72, < 10^{-3})$ | $(0.82, < 10^{-3})$ | - |
| $\Delta(T_{\rm e,[S\,II]}, T_{\rm e,[O\,III]})$ | $(0.75, < 10^{-3})$ | $(0.75, < 10^{-3})$ | - |
| $\Delta(T_{\rm e,[S\,III]}, T_{\rm e,[O\,III]})$ | - | $(0.82, < 10^{-3})$ | - |

$T_{\rm e,[O\,III]}$ with molecular gas velocity dispersion. We discuss these special cases and the details of the comparisons in the following subsections. The statistics of the correlations with H II region ionization parameter are summarized in Table 2.5.

### Correlations between Temperature Differences, Ionization Parameter, and Radiation Softness Parameter

We show in Figures 2.12 and 2.13 the comparisons between temperature differences and the ionization parameter, $U$, traced with both [S III]/[S II] and [O III]/[O II]. In both comparisons the low-ionization zones show no correlations, but there is a moderate correlation the low and intermediate-ionization zone, traced by $\Delta(T_{\rm e,[S\,II]}, T_{\rm e,[S\,III]})$, with [S III]/[S II]. The comparisons of the low-intermediate and high-ionization zones have high correlation with both [S III]/[S II] and [O III]/[O II].

We observe correlations between $\Delta(T_{\rm e,[S\,II]}, T_{\rm e,[S\,III]})$ with [S III]/[S II]. For all temperature differences with $T_{\rm e,[O\,III]}$ we also observe strong correlations between $\Delta T_{\rm e}$ and [S III]/[S II]. The largest temperature differences are associated with the smallest values of [S III]/[S II]. As [S III]/[S II] increases, $\Delta T_{\rm e}$ converges to $\Delta T_{\rm e} = 0$. Shown in Figure 2.13, we present the same temperature differences but using [O III]/[O II] as a tracer for $U$. All the correlations with

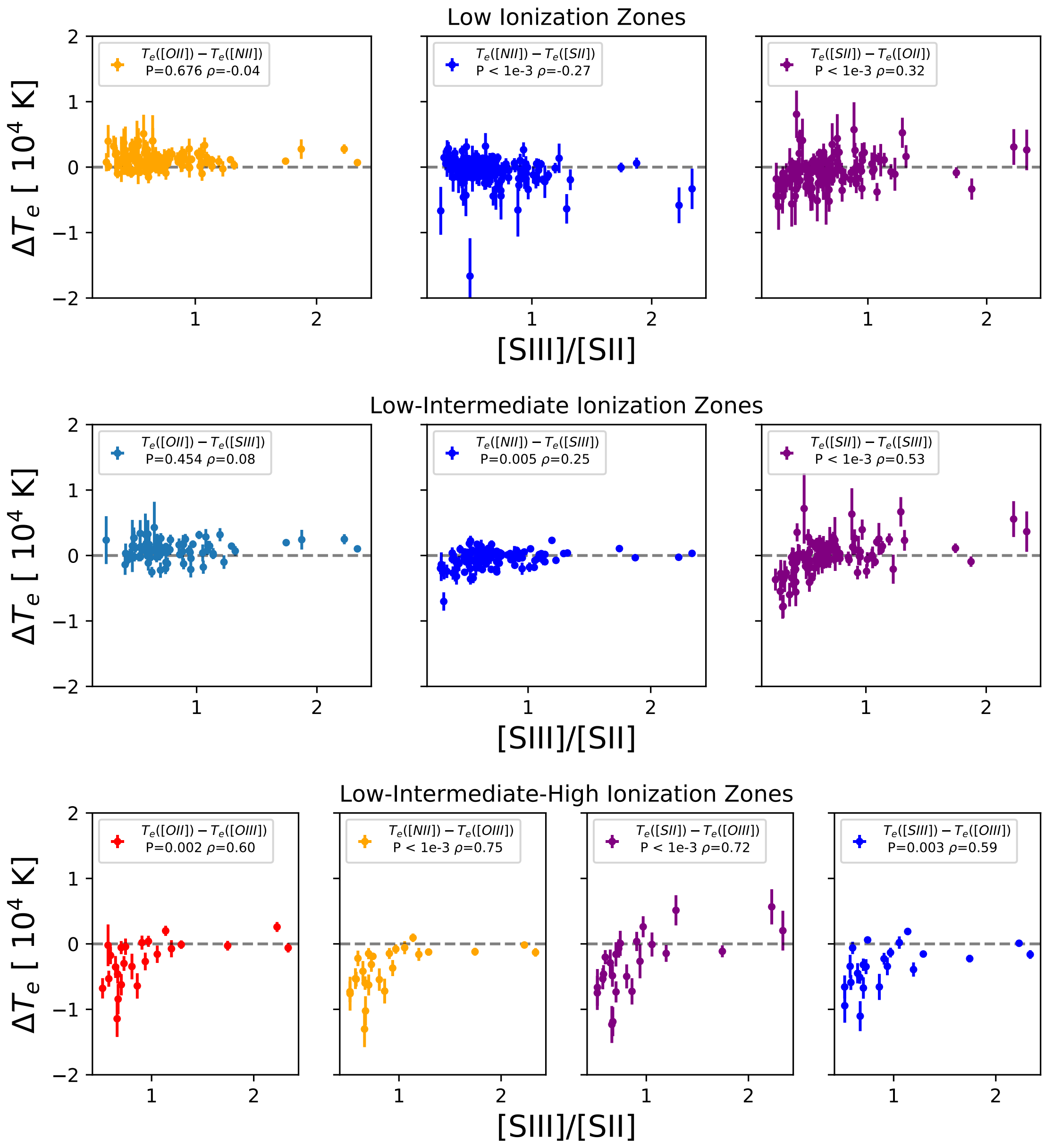

**Figure 2.12.** Electron temperature differences compared to the H II region ionization parameter, $U$, traced by [S III]/ [S II]. Top: The $\Delta T_e$'s between the low ionization zone temperatures. Middle: The $\Delta T_e$'s between the low and intermediate ionization zone temperatures. Bottom: The $\Delta T_e$'s between the low, intermediate and high ionization zone temperatures. We observe significant correlations with $U$, traced by [S III]/ [S II], between the temperatures differences $\Delta(T_{e,[N\,II]}, T_{e,[S\,II]})$ and $\Delta(T_{e,[S\,II]}, T_{e,[O\,II]})$; between $\Delta(T_{e,[S\,II]}, T_{e,[S\,III]})$; and $\Delta(T_{e,[N\,II]}, T_{e,[S\,III]})$ and $\Delta(T_{e,[S\,II]}, T_{e,[O\,III]})$.

ionization parameter that do not involve $T_{e,[O\,III]}$ disappear when using [O III]/[O II] as a tracer. The remaining $\Delta T_e$ that include $T_{e,[O\,III]}$ show similar correlations as before with ionization

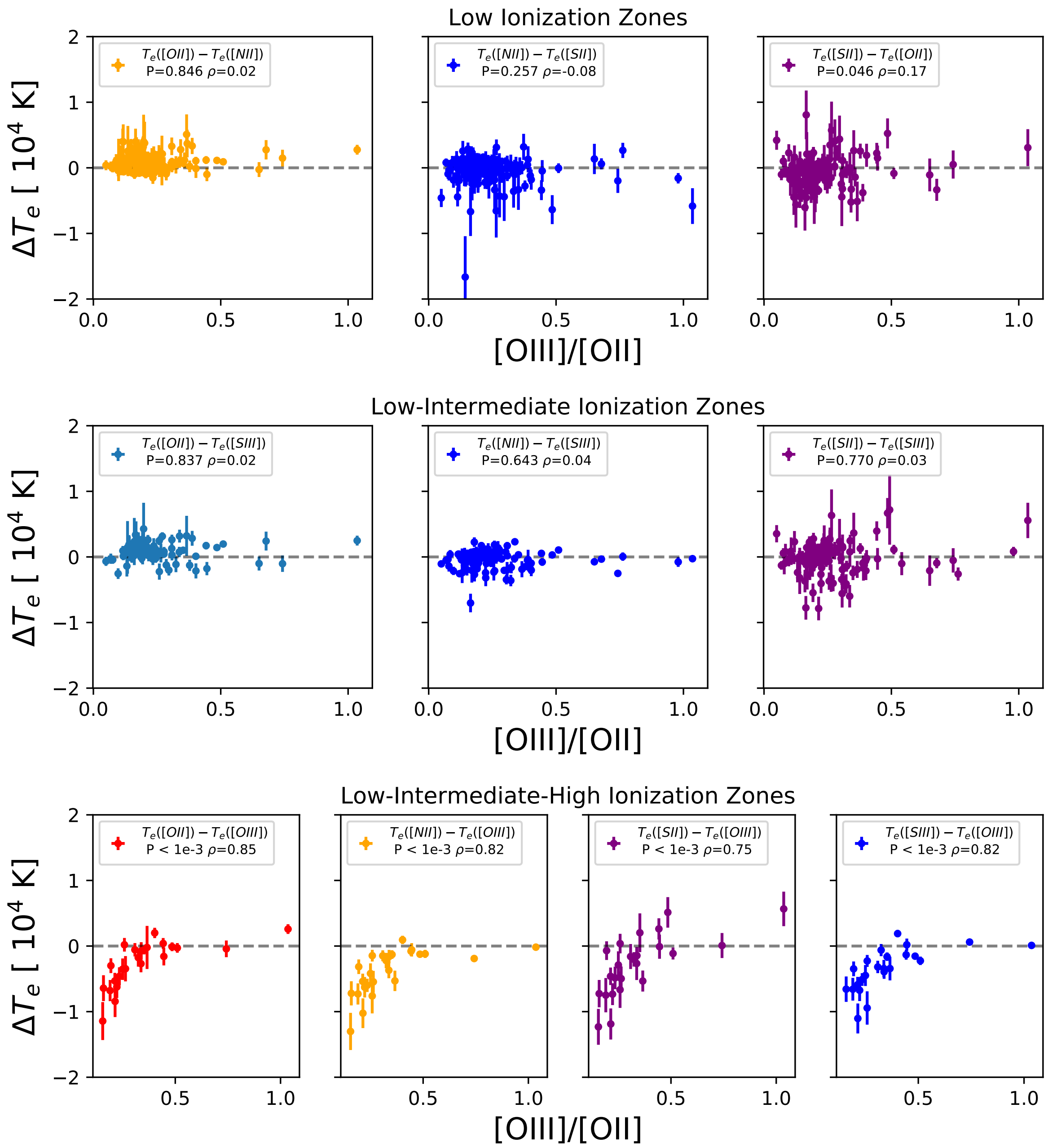

**Figure 2.13.** Electron temperature differences compared to the H II region ionization parameter, $U$, traced by [OIII]/ [OII]. The ionization zones depicted in each row follow those in Figure 2.12. We observe strong correlations between all the $\Delta T_\mathrm{e}$ involving $T_{\mathrm{e,[O\ III]}}$. The correlations between the low and intermediate ionization zones and $U$, traced by with [S III]/ [S II] and shown in Figure 2.12, do not appear when tracing $U$ with [OIII]/[OII].

parameter when using [O III]/[O II]. In both cases, the largest temperature differences occur at the lowest values of ionization parameter, traced by either [S III]/[S II] or [O III]/[O II].

Our correlations with ionization parameter tracers are similar to the results presented in Yates et al. (2020). When comparing the temperatures of the low and high ionization zone for oxygen, Yates et al. (2020) observed an increase in the $T_{\rm e,[O\,III]}/T_{\rm e,[O\,II]}$ ratio that is anti-correlated with the ratio of $\rm O^{2+}/O^{+}$ (which closely follows the ionization parameter traced by [O III]/[O II]). Our H II regions are all likely to be in the relatively high metallicity regime, where $\rm O^{+}$ should be the dominant ionization state of oxygen. Here, the average electron temperature will be best described by the auroral-to-nebular line ratio of [O II] (with caution about density inhomogeneities, as previously noted). Nevertheless, emission from [O III]$\lambda$4363 can still be produced, albeit more weakly, and given the exponential temperature dependence, it will be biased towards hotter gas. Therefore, if there are temperature inhomogenieities, the [O III] temperatures may reflect a small amount of hot, high ionization gas and may not agree with the auroral-to-nebular line ratio of [O II]. Yates et al. (2020) predict that regions with $T_{\rm e,[O\,III]} > T_{\rm e,[O\,II]}$ will be $\rm O^{+}$ dominant, i.e. $\rm O^{+}/H^{+} > O^{2+}/H^{+}$ . Because [O III]/[O II] $\propto$ $\rm O^{2+}/O^{+}$, we would expect to see the largest deviations in $T_{\rm e,[O\,III]}$ at the lowest [O III]/[O II]. To summarize, Yates et al. (2020) postulate that the differences between hotter high ionization zone temperatures, $T_{\rm e,[O\,III]}$ and the low ionization zone temperature, $T_{\rm e,[O\,II]}$ will increase with decreasing ionization parameter. These trends should in theory also be evident for sulfur, although these correlations were not explored by Yates et al. (2020). Similar trends of temperature differences associated with different ionization states of the gas have been discussed by Berg et al. (2020).

In Figure 2.14, we plot the $T_{\rm e}$–$T_{\rm e}$ between $T_{\rm e,[O\,III]}$–$T_{\rm e,[O\,II]}$ and $T_{\rm e,[S\,III]}$–$T_{\rm e,[S\,II]}$ colored by the value of [O III]/[O II] and [S III]/[S II]. We also annotate the plot according to the schematics from Figure 3 of Yates et al. (2020). For both oxygen and sulfur, the largest ratios of $T_{\rm e,[X\,III]}/T_{\rm e,[X\,II]}$, where X is either S or O, occur for the lowest values of ionization parameter, as indicated by the value of the line ratio. This suggests we are observing a similar correlation with ionization parameter as postulated by Yates et al. (2020).

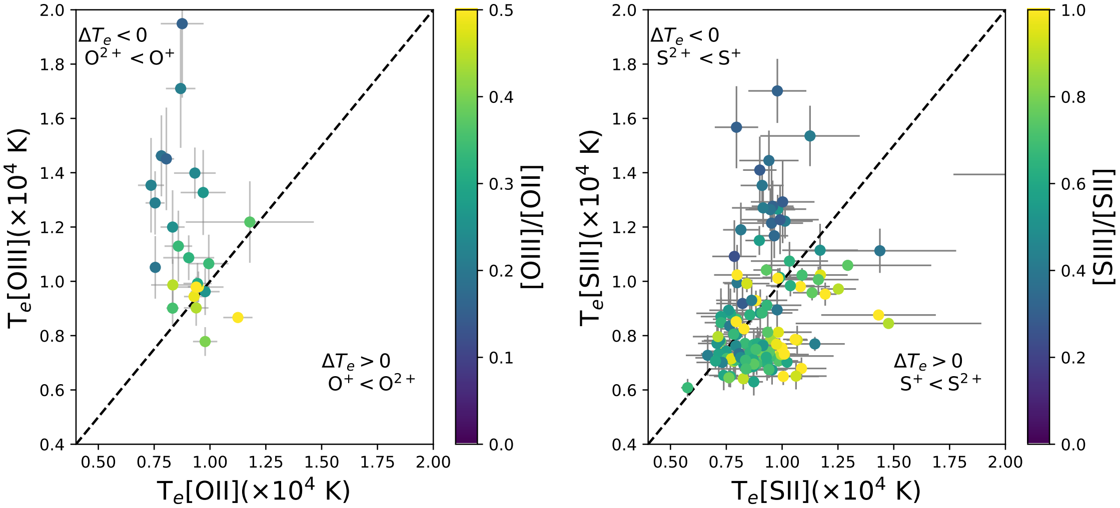

**Figure 2.14.** The $T_{\rm e}$–$T_{\rm e}$ relation between (left) $T_{\rm e,[O\,III]}$–$T_{\rm e,[O\,II]}$ and (right) $T_{\rm e,[S\,III]}$–$T_{\rm e,[S\,II]}$ colored by the value of [O III]/[O II] and [S III]/[S II]. In both panels, the largest ratios of $T_{\rm e,[X\,III]}/T_{\rm e,[X\,II]}$, where X is either S or O, occur for the lowest values of ionization parameter, as indicated by the value of the line ratio, as expected according to the results of Yates et al. (2020).

If we consider the similarity between our results and Yates et al. (2020) as evidence for correlations between $\Delta T_{\rm e}$ and $U$, then why is it that the correlation between $\Delta(T_{\rm e,[S\,II]}, T_{\rm e,[S\,III]})$ and $U$ traced by [S III]/[S II] is not evident when using [O III]/[O II] as a tracer for $U$? It might be the case that [S III]/[S II] and [O III]/[O II] do not change with $U$ in similar ways, as [S III] and [O III] arise from different ionization zones and conditions. It is possible that density inhomogeneities may be playing a role, both [S II] and [O II] have similar low critical densities, unlike either [S III] and [O III]. It remains unclear why some $\Delta T_{\rm e}$ vs. $U$ trends disappear.

We explore the correlations with $\Delta T_{\rm e}$ using a combination of both [S III]/[S II] and [O III]/[O II]. Vilchez & Pagel (1988) define the "radiation softness" parameter, $\eta$ = ([O II]/ [O III]) / ([S II]/[S III]), as a diagnostic of the effective temperature of the ionizing stars. Shown in Appendix 2.15 Figure 2.31, we find a correlation between $\Delta(T_{\rm e,[S\,II]}, T_{\rm e,[S\,III]})$ and $\eta$ with similar $p$ and $\rho$ values as the correlation with $U$. There are no correlations between temperature differences involving $T_{\rm e,[O\,III]}$ with $\eta$. Because $\eta$ is a measure of ionizing properties of the ionizing stars, the correlation between $\eta$ and $\Delta(T_{\rm e,[S\,II]}, T_{\rm e,[S\,III]})$ may suggest that $T_{\rm e}$'s derived from sulfur lines are sensitive to the stellar population while $T_{\rm e}$'s from oxygen are more sensitive to the physical conditions of the ionized gas. However, a future comparison with a larger sample of $T_{\rm e,[O\,III]}$'s would be beneficial in solidifying such an interpretation.

### Temperatures Differences with Stellar Mass and Age

Next we compare temperature differences to stellar mass and ages from compact stellar clusters and associations matched to our H II regions. As presented in Appendix 2.13 Figures 2.32–2.34, we find no correlations between $\Delta T_{\rm e}$ with cluster mass, cluster age, or with association mass and age.

Although the correlation is not statistically significant according to our criteria, we speculate on a possible positive correlation, between the most reliable $\Delta T_{\rm e}$ indicator without density inhomogeneity issues, $\Delta(T_{\rm e,[N\,II]}, T_{\rm e,[S\,III]})$ with the association mass. Figure 2.15 shows the comparisons between $\Delta(T_{\rm e,[S\,II]}, T_{\rm e,[S\,III]})$, $\Delta(T_{\rm e,[O\,II]}, T_{\rm e,[S\,III]})$, and $\Delta(T_{\rm e,[O\,II]}, T_{\rm e,[S\,III]})$. While the scatter for both $\Delta(T_{\rm e,[S\,II]}, T_{\rm e,[S\,III]})$ and $\Delta(T_{\rm e,[O\,II]}, T_{\rm e,[S\,III]})$ are centered around zero, it appears to be the case that $T_{\rm e,[N\,II]}$ is cooler than $T_{\rm e,[S\,III]}$ towards the low-mass end and vice-versa on the high-mass end. As discussed in Section 2.6.5, we assigned the largest mass stellar population to the H II region if the region was matched to more than one association. To see if this choice has any impact on the strength of the correlation, we plot in Figure 2.16 the $\Delta(T_{\rm e,[N\,II]}, T_{\rm e,[S\,III]})$ against the sum of the matched association masses. Using the total masses, we observe no change in the strength of the correlation.

It is possible that the correlation between $\Delta(T_{\rm e,[N\,II]}, T_{\rm e,[S\,III]})$ and association mass may result from biases introduced by an under-sampling of initial mass function. Similar to our study, Scheuermann et al. (2023) matched the stellar association catalog (Larson et al., 2023) to H II regions in the Nebular catalog (Kreckel et al., 2019; Groves et al., 2023). Instead of including all masses measured for the associations, which we do in this work, Scheuermann et al. (2023) implement a cut-off and assume masses $< 10^4 M_\odot$, as masses below the threshold do not sample the IMF (da Silva et al., 2012). We perform no such cutoff in this study. The correlation between $\Delta(T_{\rm e,[N\,II]}, T_{\rm e,[S\,III]})$ and $M_{\rm Association}$ correlation includes many regions with masses $< 10^4 M_\odot$,

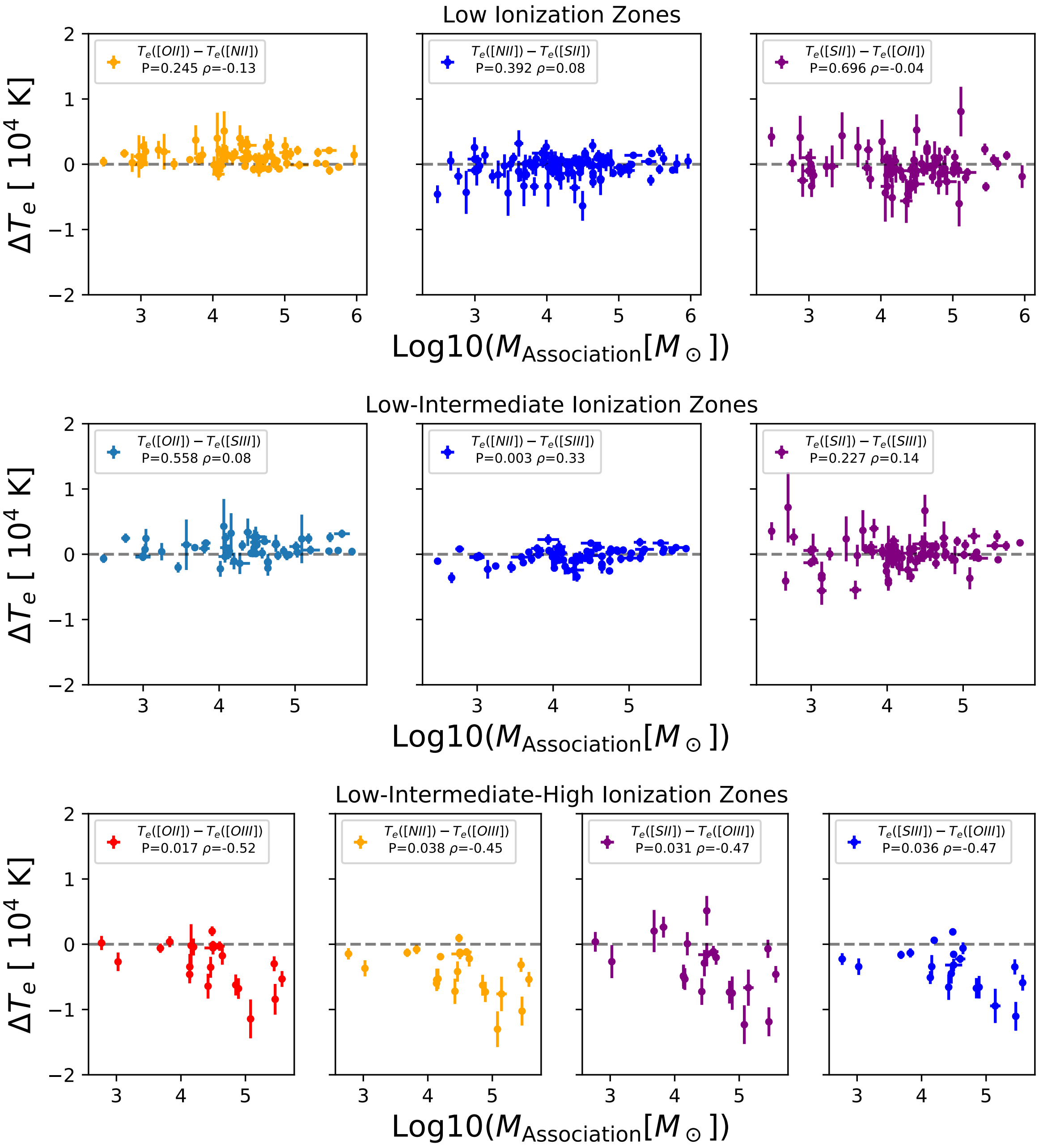

**Figure 2.15.** Electron temperature differences compared to stellar association mass. The ionization zones depicted in each row follow those in Figure 2.12. Although the correlations are insignificant according to their p-value, we observe potential, weak, correlations between $\Delta(T_{\mathrm{e,[N\,II]}}, T_{\mathrm{e,[S\,III]}})$, and all $\Delta T_{\mathrm{e}}$ involving $T_{\mathrm{e,[O\,III]}}$, with stellar association mass.

where the IMF may not be fully sampled. Despite this, we do not fully dismiss this correlation; however, the effects that undersampling the IMF could have on the correlation with $\Delta(T_{\mathrm{e,[N\,II]}}$,

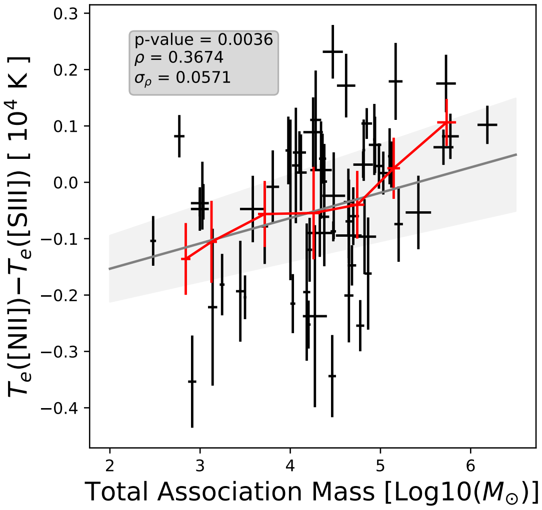

**Figure 2.16.** The $T_{\mathrm{e,[N\,II]}}-T_{\mathrm{e,[S\,III]}}$ temperature difference versus the total stellar association mass. The *black-points* are individual H II region association masses. In *red* we show the average temperature differences and H II region association masses calculated in Log10($M_\odot$)=0.5 bins. We also show a fit and $1\sigma$ fit in *grey*. Compared to using the largest mass measurement, see middle row Figure 2.15, the p-value using total stellar mass p-value is higher, indicating a less statistically significant correlation.

$T_{\mathrm{e,[S\,III]}}$) warrants further investigation with a larger sample size on order to expand the dynamic range of association mass.

### Temperatures Differences and Molecular Gas Properties

We compare temperature differences to the properties of the molecular gas derived from CO emission measured within the projected boundaries of our sample of H II regions. For the comparisons to $I_{\mathrm{CO}}$, shown in Figure 2.35 of Appendix 2.15 , and comparisons to $T_{\mathrm{peak}}$, shown in Figure 2.36 of Appendix 2.15, we observe no correlations with temperature differences between the low, intermediate, and high ionization zones.

We show in Figure 2.17 the temperature differences compared to the CO velocity dispersion ($\sigma_{v,\mathrm{CO}}$). We observe a moderate correlation between $\sigma_{v,\mathrm{CO}}$ and $\Delta(T_{\mathrm{e,[N\,II]}}, T_{\mathrm{e,[S\,III]}})$. The values of $\Delta(T_{\mathrm{e,[N\,II]}}, T_{\mathrm{e,[S\,III]}})$ over the range of $\sigma_{v,\mathrm{CO}}$ is small, only encompassing $\Delta(T_{\mathrm{e,[N\,II]}}, T_{\mathrm{e,[S\,III]}})$ from $-1000$ K to 2000 K. Given the possible correlation with association mass, and this correlation with $\sigma_{v,\mathrm{CO}}$, we find it intriguing that these correlations between the low and intermediate ionization zone are only seen in $\Delta(T_{e,[N\ II]}, T_{e,[S\ III]})$. It is possible that the low scatter in $T_e$–$T_e$ relationship between $T_{e,[S\ III]}$ and $T_{e,[N\ II]}$ in the presence of density inhomogeneities, contrary to the temperatures from [S II] and [O II], allow for better insight into these underlying trends.

We observe that all the correlations of $\Delta T_e$ involving $T_{e,[O\ III]}$ and $\sigma_{v,CO}$ have large, negative, $\rho$ values, but are all insignificant according to their p-values. The high Spearman rank values for the comparisons between $\Delta T_e$ and $\sigma_{v,CO}$ appears to be largely driven by the highest values of $T_{e,[O\ III]}$. Despite the fact that the correlations are not strong, it is clear that the high $T_{e,[O\ III]}$ regions go along with high CO velocity dispersion.

The CO velocity dispersion can be enhanced by low-velocity shocks originating from the interaction of molecular gas with late-time-expansion of supernovae remnants (see Koo et al., 2001; Zhou et al., 2023), as well as from interaction with low-velocity shocks from pressure-radiation driven H II region expansion (Hill & Hollenbach, 1978; Kothes & Kerton, 2002; Watkins et al., 2023). These low-velocity shocks are also predicted to enhance $T_{e,[O\ III]}$. Shock modeling has shown that outward expanding low-velocity shocks can create conditions, such as pockets of high post-shock temperature, where the strength of [O III]$\lambda$4363 emission will be enhanced compared to the little to no increase in emission from [O III]$\lambda$5007 (Peimbert et al., 1991; Binette et al., 2012; Méndez-Delgado et al., 2021). The combination of large temperature differences with $T_{e,[O\ III]}$ and high $\sigma_{v,CO}$ suggests that we may be observing the effects of low-velocity shocks. Motivated by this scenario, we search the H II regions for evidence of low-velocity shocks in the following section.

### Investigating H II Regions for Presence of Low-Velocity Shocks

The correlations of $\Delta T_e$ involving the high ionization zone and H II region properties: [S III]/[S II], [O III]/[O II], and the CO velocity dispersion appears to be driven by the presence of regions with high $T_{e,[O\ III]}$, high $\sigma_{\rm v,CO}$ and low $U$. One potential explanation is the presence of low velocity shocks enhancing $T_{e,[O\ III]}$ (Peimbert et al., 1991; Binette et al., 2012; Méndez-

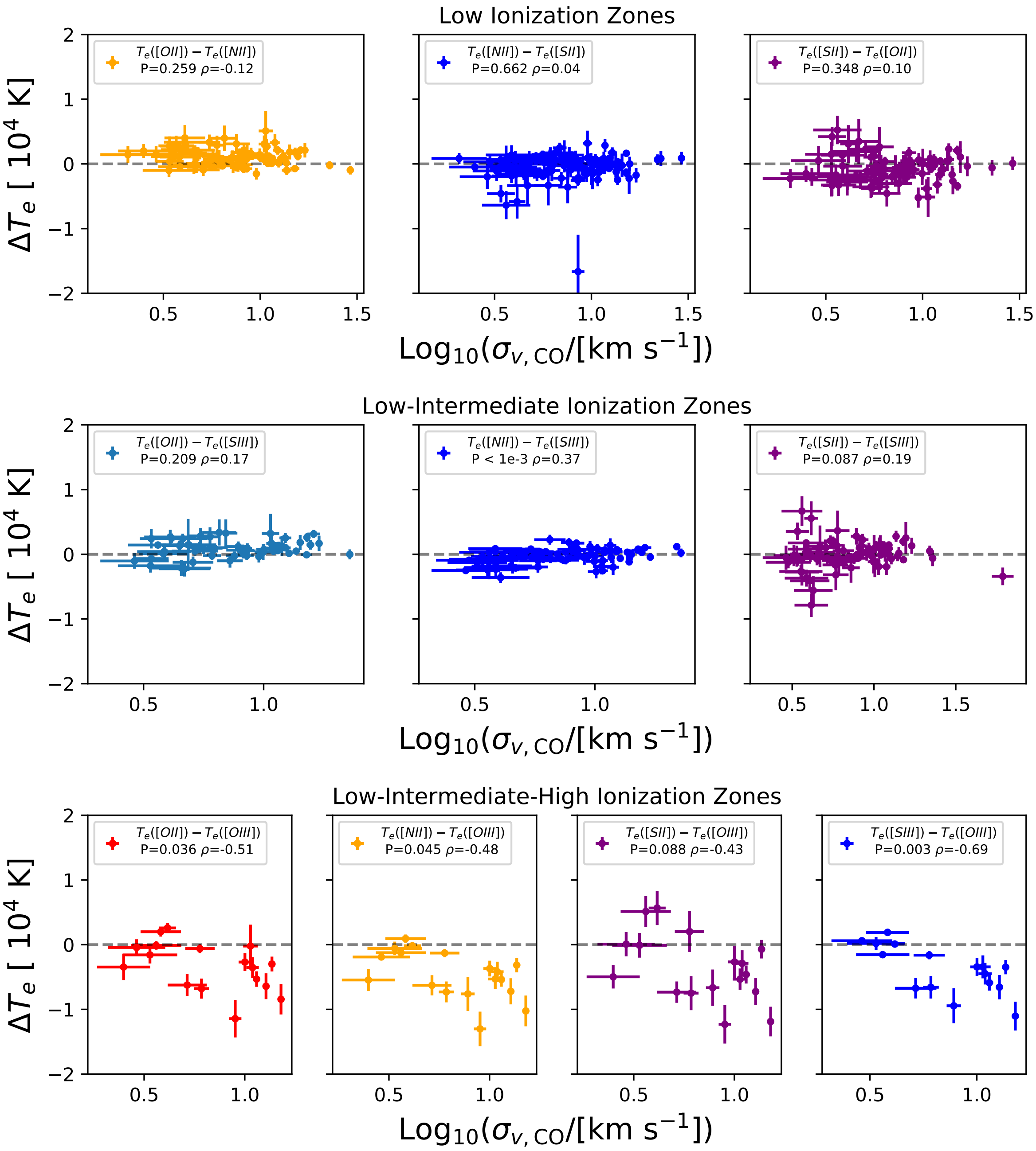

**Figure 2.17.** Electron temperature differences compared to the CO velocity dispersion, $\sigma_{v,\mathrm{CO}}$. The order of the panels follow those in Figure 2.12. We observe a weak correlation between $\Delta(T_{e,[\mathrm{N\,II}]}, T_{e,[\mathrm{S\,III}]})$. Although insignificant according to their p-values, we also observe that highest $T_{e,[\mathrm{O\,III}]}$ values are associated with the highest $\sigma_{v,\mathrm{CO}}$.

Delgado et al., 2021). To test this explanation, we search for evidence of shocks in enhanced optical line ratios and line broadening.

When shocks collide with and compress gas, the ionization parameter of the gas is reduced leading to partially ionized zones of enhanced nebular emission of low-ionization species such as $S^+$ and O relative to H$\beta$ and/or H$\alpha$ (Dopita & Sutherland, 1996; Allen et al., 2008). In Figure 2.18, we show the [S II]/H$\alpha$ vs. [O I]/H$\alpha$ ratios, color-coded by $T_{e,[\mathrm{O\,III}]}$, for regions with measured [O III]$\lambda$4363. We find that H II regions with hotter $T_{e,[\mathrm{O\,III}]}$ tend to populate a region with enhanced [S II]/H$\alpha$ and [O I]/H$\alpha$ ratios which suggests that these regions may host a partially ionized zone due to shocks. Between the two line ratios, $T_{e,[\mathrm{O\,III}]}$ is better correlated with [S II]/H$\alpha$, p-value$=0.0004$, than [O I]/H$\alpha$, p-value$=0.0016$. We note here that it is possible that harder photons and X-rays produced by X-ray binaries also enhance [S II] and [O I] relative to the Balmer emission (Abolmasov et al., 2007; Grisé et al., 2008). Furthermore, X-rays would provide high energy photons able to boost [O III]$\lambda$4363. However, lacking the high spatial resolution X-ray imaging of these H II regions, exploration of X-ray contributions to [O III]$\lambda$4363 emission is beyond the scope of this paper.

Another tracer that may indicate presence of shocks is the He II $\lambda$4686/H$\beta$ ratio (Allen et al., 2008) though it is also sensitive to the shape of the Lyman continuum below 228 Å (Garnett et al., 1991; Guseva et al., 2000; Allen et al., 2008). Wolf-Rayet (WR) stars are capable of releasing photons able to produce He II $\lambda$4686. WR stars host stellar winds and can be a source of high energy photons, E$>$ 54 eV, capable of doubly ionizing Helium. We measured the He II$\lambda$4686/H$\beta$ in H II regions with $T_{e,[\mathrm{O\,III}]}$ detections and found that these regions exhibit an average He II $\lambda$4686/H$\beta$ $= 4.1 \pm 1.6\%$. This value is within the expected range of He II $\lambda$4686/H$\beta$ values for H II regions with WR, 0.04%-7% (Guseva et al., 2000; Thuan & Izotov, 2005; Mayya et al., 2023), and 100 km $s^{-1}$ shocks, 4%-6% (Allen et al., 2008). We visually inspected the spectra of regions with measured $T_{e,[\mathrm{O\,III}]}$ for the characteristic red/blue bump associated with the presence of WR stars. We found the blue bump in only 2 regions with measurable [O III]$\lambda$4363, both of which have $T_{e,[\mathrm{O\,III}]} < 10^4$ K. Nevertheless, the He II

$\lambda$4686/H$\beta$ for the high $T_{\mathrm{e,[O\,III]}}$ regions lends evidence that these regions may host shocks or undetected WR stars.

We also searched for kinematic signatures of shocks, but find no clear kinematic evidence. Shocks can imprint asymmetries and/or broad emission near the base of an emission line. We inspected the fit residuals of [O III]$\lambda$5007 in H II regions with measured $T_{\mathrm{e,[O\,III]}}$ and found no evidence of line broadening due to shocks. Next, we inspected the measured line widths of [O III]$\lambda$5007 in these regions. We compared the line-spread-function corrected [O III]$\lambda$5007, as measured by MUSE, velocity dispersion, $\sigma_{v,\lambda 5007}$ vs. the CO velocity dispersion, $\sigma_{v,\mathrm{CO}}$. The line-widths of the optical and CO emission for regions with high $T_{\mathrm{e,[O\,III]}}$ are comparable to regions with low, or not detected $T_{\mathrm{e,[O\,III]}}$. Despite this, the absence of these features may only exclude the presence of high-velocity shocks.

If the regions do host low-velocity shocks, then their impact on the line width of the optical emission may be too small to be resolved given the MUSE resolution; $\sim 70$ km s$^{-1}$ at $\lambda = 5007$ Å. The high velocity resolution, 2.5 kms$^{-1}$ of the PHANGS-ALMA data, are more sensitive than MUSE to low-velocity shocks, and are the strongest evidence for their presence in the high $T_{\mathrm{e,[O\,III]}}$ H II regions.

## 2.8 Discussion

### 2.8.1 Electron Density Inhomogeneities

Similar to the results of Méndez-Delgado et al. (2023b), described in Section 2.7.2, we have found that the presence of electron density inhomogeneities may cause the temperatures measured from [O II] and [S II] to be biased hotter compared to those measured using the [N II] auroral lines.

The critical densities of the nebular lines of [S II]$\lambda\lambda 6716, 6731$ and more so [O II] $\lambda\lambda 3726, 3729$ are low enough that at densities $n_{\mathrm{e}} > 10^3$ cm$^{-3}$ the lines will undergo increased collisional de-excitation. In the presence of density inhomogoneities above this value, the

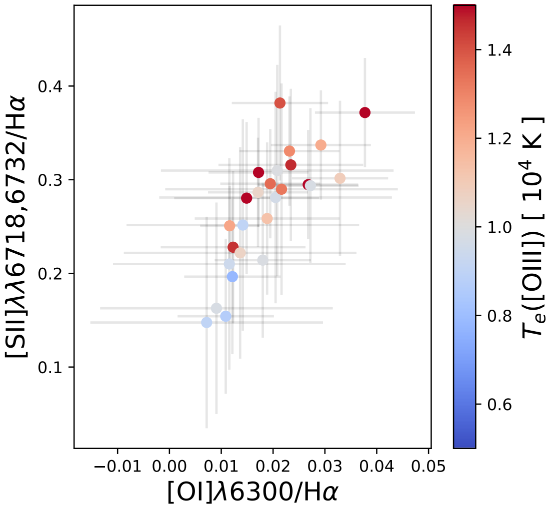

**Figure 2.18.** We compare the relative strength of the low-ionization species [O I] and [S III] to Balmer emission. We color-code each data point by the value of its measured [O III] temperature. The hottest $T_{\mathrm{e,[O\,III]}}$ regions also have the highest line ratios. The higher line ratios are indicative of the existence of a partially-ionized zone that may be due to the presence of shocks or harder photons such as X-rays (Grisé et al., 2008).

low critical densities will reduce the emissivity of the nebular emission lines from [S II] and [O II]. Because of this, the nebular diagnostic lines of [S II] and [O II] will mainly describe gas component with $n_{\mathrm{e}} < 10^3$ cm$^{-3}$. This biases the [S II] and [O II] density diagnostic to return electron densities that are lower than the true average density of the H II region. Since the auroral line critical densities are far higher, this also makes the measured [S II] and [O II] temperatures appear to reflect hotter values.

This effect has been observed in many studies. Densities measured in Milky Way H II regions (the Orion Nebula, NGC 3604 and NGC 3576) using [Cl III], which is sensitive to greater densities than [S II], routinely show that the [S II] diagnostic returns lower values than [Cl III]. (Pogge et al., 1992; García-Rojas & Esteban, 2007; Núñez-Díaz et al., 2013; Weilbacher et al., 2015). Although densities derived from the [S II] doublet are commonly used in the literature due to their strengths and their insensitivity to dust extinction, the [S II]$\lambda 6731/\lambda 6716$ ratio is less sensitive to density than [Cl III], [Ar IV], and [Fe III] diagnostics when $n_{\mathrm{e}} > 10^3$ cm$^{-3}$ (see Figure 2 in Méndez-Delgado et al., 2023b). If the equality $T_{\mathrm{e,[O\,II]}} \approx T_{\mathrm{e,[S\,II]}} \approx T_{\mathrm{e,[N\,II]}}$ predicted by photoionization models is true, then the auroral-to-nebular line ratios would suggest a factor of 10 higher density than the [S II] doublet, but neither may well represent the true average density of the region.

Electron density variations may arise from shocks, turbulence, and pre-existing non-uniform structure in the ISM (Hill & Hollenbach, 1978; Dopita & Sutherland, 1996; Allen et al., 2008). Jin et al. (2022) have extended photoionization modeling of ionized nebulae to more complex geometries. Starting with an initial clumpy ISM, ionizing photons will pass through diffuse regions more readily than denser clumps. The resulting photoionized region will exhibit fluctuations in density and irregular geometry as opposed to a uniform density and spherical morphology. The ionization parameter in the dense clumps will be relatively lower than other regions of the nebulae due to the increased density. At these locations, the emission of low-ionization species, including [S II] and [O II], will be enhanced compared to higher ionization species. Due to the higher critical densities of the auroral lines of these ions, the emissivity of the auroral lines will be greater than those of the nebular lines in the high-density portion the nebula. In this scenario, the nebular density diagnostics can return an average density that traces the low-density portion of the nebula. In doing so, the value of $n_{\rm e}$ returned by the nebular diagnostics may inaccurately describe the ionizing conditions of the high-density clumps where the auroral line emissivities are greater than the nebular lines, and overestimate [S II] temperatures.

Density inhomogeneities have been reported in studies of highly resolved local HII regions like Orion where the inhomogeneities can be spatially resolved (Baldwin et al., 1991; Pogge et al., 1992; Weilbacher et al., 2015; McLeod et al., 2016; O'Dell et al., 2017). Weilbacher et al. (2015) mapped the spatial variation of density in the Orion nebulae and found variations of density between 500 cm$^{-3}$ and in excess of 10,000 cm$^{-3}$. A maximum of 25,000 cm$^{-3}$ is measured using [Cl III] at the location of the ionization front in the "Orion S" area. Density inhomogeneities, associated with turbulence driven velocity fluctuations, have been invoked as one mechanism to generate surface brightness fluctuations within the Orion Nebula (Kainulainen et al., 2017).

The Orion Nebula is not particularly comparable to the H II regions studied here due to the difference in scales (i.e. Orion is more compact) and resolution. A subset of our H II regions, as shown in the comparison between the MUSE H II regions mask in Appendix 2.13, are unresolved clusters of individual regions. Measurements of density inhomogeneities using density diagnostics besides the nebular [O II] and [S II] doublets for extragalactic H II regions that more closely match our sample are rare and require deep, high $S/N$ spectra (Méndez-Delgado et al., 2023b). One consequence of the lack of different diagnostics is that many studies will often assume a fixed density of 100 $\mathrm{cm}^{-3}$ when either [S II], or [O II], return a density in the low-density limit (e.g. Kreckel et al., 2019). Studies using mid-infrared observations have shown this latter assumption could be incorrect, as densities up to 1000 $\mathrm{cm}^{-3}$ have been measured using the [S III]$\lambda 18.7/33.5$ $\mu$m density diagnostic (see Rubin et al., 2016), and indicate that density inhomogeneities are present in extra-galactic H II regions.

The consistency of auroral-to-nebular ratios with $n_{\mathrm{e}} \sim 1000$ $\mathrm{cm}^{-3}$ assuming $T_{\mathrm{e}} = T_{\mathrm{e,[N\,II]}}$ in Figure 2.11, as well as the correlation between degree of inhomogeneities with H$\beta$ surface brightness observed for [S II], supports this picture that inhomogeneities must be considered when deriving temperatures from the [O II] and [S II]. As a result, we consider $T_{\mathrm{e,[N\,II]}}$ a more reliable indicator of the low-ionization zone temperature due to its relative insensitivity to density.

### 2.8.2 $T_{\mathrm{e,[N\,II]}}$ and $T_{\mathrm{e,[S\,III]}}$ as Accurate Tracers of HII Region Temperatures

Within the set of $T_{\mathrm{e}}$–$T_{\mathrm{e}}$ between the low and intermediate ionization zones, we observed that the comparisons between $T_{\mathrm{e,[S\,III]}}$–$T_{\mathrm{e,[O\,II]}}$ and $T_{\mathrm{e,[S\,III]}}$–$T_{\mathrm{e,[S\,II]}}$ largely agree with those from Zurita et al. (2021). However, similar to recent studies Berg et al. (2015, 2020); Zurita et al. (2021); Rogers et al. (2021) and Rogers et al. (2022), we observed that the $T_{\mathrm{e}}$–$T_{\mathrm{e}}$ trend between $T_{\mathrm{e,[N\,II]}}$ and $T_{\mathrm{e,[S\,III]}}$ exhibits the lowest scatter and agrees with many of the literature trends presented in Figure 2.9. These results suggest $T_{\mathrm{e,[N\,II]}}$ and $T_{\mathrm{e,[S\,III]}}$ temperatures are optimal tracers of H II region temperatures, more so than $T_{\mathrm{e,[S\,II]}}$, $T_{\mathrm{e,[O\,II]}}$ and $T_{\mathrm{e,[O\,III]}}$.

Judged from the Oxygen CEL and RL temperatures, the high ionization zone is expected to be most affected by temperature fluctuations due to its proximity to sources of feedback (Méndez-Delgado et al., 2023a). To what degree the intermediate ionization zone temperatures are affected is unclear (Méndez-Delgado et al., 2023b). In Figure 2.9, we showed that our best-fit trend, including those from the literature, between $T_{\mathrm{e,[N\,II]}}$ and $T_{\mathrm{e,[S\,III]}}$ "generally" (within $2\sigma$) follow trends predicted from the Vale Asari et al. (2016) photoionization models with temperature fluctuations set to zero. This suggests that $T_{\mathrm{e,[S\,III]}}$ may be minimally affected by temperature inhomogeneities. Díaz & Zamora (2022) provide additional arguments for the use of $T_{\mathrm{e,[S\,III]}}$ over $T_{\mathrm{e,[O\,III]}}$, including: 1) the emission lines of [S III] have a lower exponential dependence on electron temperature and 2) because [S III] overlaps gas volumes containing both $O^{2+}$ and $O^{+}$ that $T_{\mathrm{e,[S\,III]}}$ can be representative of the entire H II region.

We also showed that $\Delta(T_{\mathrm{e,[N\,II]}}, T_{\mathrm{e,[S\,III]}})$ is stable around the zero line for across the range of molecular gas velocity dispersion and the low values of ionization parameter, traced by both [O III]/[O II] and [S III]/[S II], observed in this work. This result follows the observations of Berg et al. (2020), whom find that agreement between these two temperature tracers become more uncertain in high ionization parameter, traced by [O III]/[O II], H II regions. Due to stable behavior of between $T_{\mathrm{e,[N\,II]}}$ and $T_{\mathrm{e,[S\,III]}}$ across the multiple H II region properties observed in this work, and following the suggestions of Berg et al. (2015, 2020) and Rogers et al. (2021), we will compare "direct" metallicities derived prioritizing [N II] and [S III] temperatures to several calibrated methods (Rickards Vaught et al., in prep).

### 2.8.3 The High-Ionization Zone Temperature Excess

Within the sample of H II regions with measured [O III]$\lambda$4363, there are a small number of H II regions with high $T_{\mathrm{e,[O\,III]}}$, enhanced velocity dispersion in the surrounding molecular gas, and low-ionization parameter. We investigated these H II regions for enhanced low-ionization species emission line ratios [S II]/H$\alpha$, [O I]/H$\alpha$ and the high-ionization ratio He II/H$\beta$. We found that the high $T_{\mathrm{e,[O\,III]}}$ regions exhibited enhanced low-ionization line ratios suggestive of shock ionization (or possibly X-ray ionization). We also found that the He II/H$\beta$ ratios for these regions are within the range of those expected from shock velocities $< 100$ km s$^{-1}$ (Allen et al., 2008) and/or WR stars (Guseva et al., 2000; Thuan & Izotov, 2005; Mayya et al., 2023), though we only find characteristic red/blue bumps associated with the presence of WR stars, in 2 H II regions neither of which had elevated $T_{\mathrm{e,[O\,III]}}$. Absent the WR signatures, we are motivated to explore shocks as enhancers of the [O III] temperature.

We did not find any kinematic signatures of shocks in the optical emission line profiles. We determine that if shocks are present and broadening the CO emission, then the shock velocities are too low to be resolved by the MUSE spectral resolution. Either way, high-velocity shocks are not expected to effectively boost $T_{\mathrm{e,[O\,III]}}$ (Méndez-Delgado et al., 2021). Despite the uncertainty in whether shocks are present in the high [O III] temperature regions, we can discuss the plausibility that low-velocity shocks are the cause for excess $T_{\mathrm{e,[O\,III]}}$.

### Shock-enhanced [O III] Temperature

Low velocity, $< 100$ km s$^{-1}$, shocks can increase [O III]$\lambda$4363 while leaving [O III] $\lambda$5007 unchanged (Peimbert et al., 1991; Binette et al., 2012; Méndez-Delgado et al., 2021). For a sample of giant H II regions, Binette et al. (2012) measured $T_{\mathrm{e,[O\,III]}}$ up to 6000 K higher than $T_{\mathrm{e,[S\,III]}}$ in regions with $T_{\mathrm{e,[S\,III]}} < 10^4$ K. To explore if shocks were boosting their [O III] temperatures relative to [S III], they model outward expanding shocks, mimicking those generated by stellar winds, by combining shock+photoionization models, with increasing shock velocities (analogous to increasing the post-shock temperature from $1.6\times10^4$ K to $7.2\times10^4$ K) between 20 and 60 km s$^{-1}$. Additionally, the models span 5 different metallicities between Z=0.01 Z$_\odot$ to Z=1.6 Z$_\odot$. Comparing the average properties of between the lowest and highest shock velocity models, Binette et al. (2012) found that mean doubly ionized fraction of oxygen, O$^{2+}$/O , decreases while at the same time leaving the doubly ionized fraction of sulfur, S$^{2+}$/S, unchanged. The imbalance of the ionization fraction between oxygen and sulfur means that hotter, post-shock gas contributes proportionally more to the observed [O III] emission than [S III]. Because of the exponential sensitivity to temperature, the [O III] auroral line will be enhanced, tracing the hotter post-shock temperature rather than the local photoionized nebula temperature returned by $T_{\rm e,[S\,III]}$. Furthermore, the highest metallicity models show the largest temperature differences between $T_{\rm e,[S\,III]}$ and $T_{\rm e,[O\,III]}$, up to $\sim 7000$ K. Although this difference is 3000 K lower than our largest measured $\Delta(T_{\rm e,[S\,III]}, T_{\rm e,[O\,III]})$, a complete understanding of the degree of enhancement of [O III]$\lambda$4363 with shocks require more complex 3D hydro-dynamical simulations (Binette et al., 2012). Despite this, one extreme example of shock impact on electron temperatures was observed in the outflow of the H II region Sh 2-129 (Corradi et al., 2014). This outflow, with velocity $\approx 100$ kms$^{-1}$, exhibits $T_{\rm e,[O\,III]} = 55,000$ K and $T_{\rm e,[O\,II]} \sim 20,000$ K. Much larger than $\Delta T_{\rm e}$ observed in this study.

It has also been shown that shocks driven by pressure–radiation H II region expansion, and SNR, impact the surrounding cold molecular and ionized gas. If the velocity of the expansion is greater than the sound speed ionized gas $\sim 10$ km s$^{-1}$, a layer of shocked H gas will form in-between the expanding ionization front and a surrounding molecular gas (Hill & Hollenbach, 1978; Kothes & Kerton, 2002; Tremblin et al., 2014; Watkins et al., 2023). The impact of shock interaction with molecular gas has been studied in 18 galaxies observed as part of PHANGS-ALMA (Leroy et al., 2021a,b), where Watkins et al. (2023) identified hundreds of super bubbles (i.e. pockets of expanding gas arising as byproducts of feedback). The superbubbles were identified using spatial correspondence between CO shells and stellar populations contained in PHANGS-HST catalogs (Lee et al., 2022; Thilker et al., 2022; Larson et al., 2023). Due to the ALMA spatial resolution (50–150 pc), Watkins et al. (2023) measured the expansion velocity only for the largest superbubbles. Assuming the CO expansion velocity is equal to the shock velocity, Watkins et al. (2023) measure the velocity of the approaching/receding CO shells and determine an average, line-of-sight, expansion velocity of $v_{\rm exp} = 9.8 \pm 4.3$ km s$^{-1}$. Although this value is similar to the sound speed of the ionized gas, superbubbles exhibit asymmetries in their morphology, and the velocity can potentially reach up to a few tens of km s$^{-1}$ depending on the conditions of the gas, source or energy injection, and age (Watkins et al., 2023). 1D models indicate that, at minimum, H II regions exhibit expansion speeds of a $\sim$few km s$^{-1}$ (Tremblin et al., 2014). This suggests that H II regions expand with a large range of velocities.

As for ionized gas, Egorov et al. (2023) identify in the PHANGS-MUSE galaxies more than 1400 regions of ionized gas with elevated intrinsic H$\alpha$ velocity dispersions $> 45$ km s$^{-1}$, and, under the assumption that these regions are undergoing expansion, Egorov et al. (2023) infer expansion velocities between $v_{\rm exp} = 10$–$40$ km s$^{-1}$ (see also Egorov et al., 2014, 2017; Cosens et al., 2022). The ubiquity of H II region expansion, as well as their effects on the surrounding molecular gas, make them good candidates for drivers of low-velocity shocks capable of boosting [O III] temperatures.

### Temperature Inhomogeneities

Temperature fluctuations within H II regions are another potential explanation for the high [O III] temperature. As discussed in Section 2.1, RL emissivities have a linear sensitivity to temperature rather than the exponential sensitivity of CELs. In the presence of temperature fluctuations CELs will return higher estimates of temperature. Méndez-Delgado et al. (2023a) have recently shown that differences between [O III] and [N II] temperatures are strongly correlated with the temperature fluctuations parameter, $t^2$, of the highly ionized gas. This suggests that $T_{\rm e,[O\,III]}$ is likely to overestimate the representative H II region temperature. The observed excess in $T_{\rm e,[O\,III]}$ are likely to be produced by phenomena other than those commonly observed in H II regions. Simple models from Binette et al. (2012) and the observations from Méndez-Delgado et al. (2023a) show that the effect from $t^2 > 0$ is more pronounced in lower-metallicity/high ionization parameter regions. Furthermore, the temperature excess $T_{\rm e,[O\,III]}$ relative to the other ionization zones is too large in our observations to be caused solely by inhomogeneities. Using our measured $\Delta(T_{\rm e,[N\,II]}, T_{\rm e,[O\,III]})$, we can infer from Méndez-Delgado et al. (2023a) that $t^2 > 0.2$ for $\Delta(T_{\rm e,[N\,II]}, T_{\rm e,[O\,III]}) > 5000$ K. These values are much higher than what has been observed for nearby H II regions (Peña-Guerrero et al., 2012; Binette et al., 2012;

Méndez-Delgado et al., 2023a). Even in the presence of classical temperature inhomogeneities, a secondary effect would also need to be included to explain our [O III] temperatures.

**Potential Observation Bias**

Another possibility is that the high [O III] temperatures are statistical outliers. The galaxies in our sample exhibit strong line oxygen abundances $\gtrsim 8.3$ (Kreckel et al., 2019). Because electron temperature is anti-correlated to the metallicity of the gas, the [O III]$\lambda$4363 temperatures for these galaxies are expected to be low. For [O III]$\lambda$4363 to be detectable, the temperature would need to be high, otherwise, we would likely not detect the auroral line. [O III] temperatures from a lower-metallicity sample may be compatible with photoionization models and $T_\mathrm{e}$–$T_\mathrm{e}$ relations. Finally, Rola & Pelat (1994) have shown that emission line measurements with S/N $< 5$ can potentially overestimate the true intensity by 80%. The average S/N [O III]$\lambda$4363 measured from our sample is $\sim 4.5$. Nevertheless, why we would measure high [O III]$\lambda$4363, even after removal of [Fe II]$\lambda$4360 contamination, that also exhibit enhanced molecular gas velocity dispersions is difficult to explain purely with statistical outliers.

## 2.9 Conclusions

We presented combined KCWI and MUSE observations of the [N II]$\lambda$5756, [O II]$\lambda\lambda$7320,7330, [S II]$\lambda\lambda$4069,4076, [O III]$\lambda$4363, and [S III]$\lambda$6312 auroral lines in a sample of 421 H II regions in 7 nearby galaxies. We compared the derived electron temperatures and temperature differences between multiple H II region ionization zones to several H II region properties such as electron density, ionization parameter, molecular gas velocity dispersion, stellar mass, and age obtained from PHANGS observations. We found that:

- Similar to the results from Méndez-Delgado et al. (2023b), temperatures obtained from [S II] and [O II] are consistent with being overestimated due to the presence of density inhomogeneities in the H II regions. Because of these potential biases, we recommend the use [N II] temperatures to trace the low ionization zone.

- In addition to previous studies: Berg et al. (2015, 2020); Rogers et al. (2021), and Zurita et al. (2021), we found that the [N II] and [S III] temperatures exhibited the lowest scatter of the $T_e$– $T_e$ relations and follow trends predicted from photoionization models. The well-behaved relationship between [N II] and [S III], even in potentially inhomogeneous conditions, may be better tracing the underlying H II region temperatures. This result, and those from the above studies, further stress the prioritization of [N II] and [S III] temperatures for metallicity determinations.

- We observed a subset of H II regions with high [O III] temperatures that do not agree with the cooler temperatures measured in the low and intermediate ionization zones. We found that the regions with high [O III] temperature tended to have enhanced molecular gas velocity dispersion and lower ionization parameter than those regions with [O III] temperatures that were in better agreement with other ionization zones. These regions also showed enhanced [S II]/H$\alpha$, [O I]/H$\alpha$, and He II/H$\beta$ ratios indicating the presence of secondary ionization sources (e.g. shocks, Wolf-Rayet and X-ray binary stars). Absent direct detection of shocks, we explored whether or not shocks are able to both enhance $T_{e,\text{[O III]}}$ and CO velocity dispersion. We found that low-velocity shocks are a plausible explanation for the observed [O III] temperatures and CO velocity dispersions. However, disentangling the effects of shocks from possible contributions to [O III] temperatures by harder ionization sources such as Wolf-Rayet stars or X-ray binaries require further investigation.

- We also explored temperature inhomogenities and observational uncertainties as causes for high [O III] temperatures measured for a small sub-sample of H II regions. We found that the degree of temperature inhomogeneity that would be required to produce the difference between high [O III] temperatures and those of the low and intermediate ionization zone are larger than what has been observed in most star-forming regions. Furthermore, if the regions with high [O III] temperatures are statistical outliers leading to overestimated temperatures, we lack an explanation as to why these temperatures would correlate with high molecular gas velocity dispersion.

In a follow-up paper, Rickards Vaught et al. (in prep), We will test temperature recommendations for measuring "direct" metallicities using our full set of measured auroral line temperatures. This work, along with the PHANGS-MUSE survey, demonstrate the power of integral field spectrographs on 10m class telescopes for measuring faint auroral emission lines from large samples of H II regions in nearby galaxies. Future efforts with deeper observations or expanded samples will be critical for further elucidating the temperature and ionization behavior of these regions, particularly as [O III]$\lambda$4363 and other faint lines are now being routinely detected in galaxies at high redshift with JWST and used in metallicity determinations.

## 2.10 Acknowledgements

The authors thank the referee for a very thorough report which significantly improved the analysis presented here. The data presented herein were obtained at the W. M. Keck Observatory, which is operated as a scientific partnership among the California Institute of Technology, the University of California and the National Aeronautics and Space Administration. The Observatory was made possible by the generous financial support of the W. M. Keck Foundation. The authors wish to recognize and acknowledge the very significant cultural role and reverence that the summit of Maunakea has always had within the indigenous Hawaiian community. We are most fortunate to have the opportunity to conduct observations from this mountain. We also wish to thank all the Keck Observatory staff, including Gregg Doppman, Luca Rizzi, Sheery Yeh, and Rosalie McGurk for observational support.

This research is also based on observations collected at the European Southern Observatory under ESO programmes 094.C-0623 (PI: Kreckel), 095.C-0473, 098.C-0484 (PI: Blanc), 1100.B-0651 (PHANGS-MUSE; PI: Schinnerer), as well as 094.B-0321 (MAGNUM; PI: Marconi), 099.B-0242, 0100.B-0116, 098.B-0551 (MAD; PI: Carollo) and 097.B-0640 (TIMER; PI:

Gadotti).

RRV and KS acknowledge funding support from National Science Foundation Award No. 1816462. FB acknowledges funding from the INAF Fundamental Astrophysics 2022 program. RRV wishes to thank Jonah Gannon, and Maren Consens for fruitful discussions on reducing the KCWI data. RRV would also like to acknowledge discussions with JEM-D, KK, OVE which greatly improved the manuscript. KK, JEM-D and OVE gratefully acknowledge funding from the Deutsche Forschungsgemeinschaft (DFG, German Research Foundation) in the form of an Emmy Noether Research Group (grant number KR4598/2-1, PI Kreckel). KG is supported by the Australian Research Council through the Discovery Early Career Researcher Award (DECRA) Fellowship (project number DE220100766) funded by the Australian Government. KG is supported by the Australian Research Council Centre of Excellence for All Sky Astrophysics in 3 Dimensions (ASTRO 3D), through project number CE170100013. JN acknowledges funding from the European Research Council (ERC) under the European Union's Horizon 2020 research and innovation programme (grant agreement No. 694343). RSK acknowledges funding from the European Research Council via the ERC Synergy Grant "ECOGAL" (project ID 855130), from the German Excellence Strategy via the Heidelberg Cluster of Excellence (EXC 2181 - 390900948) "STRUCTURES", and from the German Ministry for Economic Affairs and Climate Action in project "MAINN" (funding ID 50OO2206). He also thanks for computing resources provided by *The Länd* and DFG through grant INST 35/1134-1 FUGG and for data storage at SDS@hd through grant INST 35/1314-1 FUGG. G.A.B. acknowledges the support from the ANID Basal project FB210003.

This research made use of Montage. It is funded by the National Science Foundation under Grant Number ACI-1440620, and was previously funded by the National Aeronautics and Space Administration's Earth Science Technology Office, Computation Technologies Project, under Cooperative Agreement Number NCC5-626 between NASA and the California Institute of Technology. This research has made use of NASA's Astrophysics Data System. This research made use of Astropy, a community-developed core Python package for Astronomy (Astropy

Collaboration et al., 2013), as well as substantial use of the nebular diagnostics toolkit Pyneb (Luridiana et al., 2015).

The distances in Table 2.1 were compiled by Anand et al. (2021) and are based on Freedman et al. (2001); Nugent et al. (2006); Jacobs et al. (2009); Kourkchi & Tully (2017); Shaya et al. (2017); Kourkchi et al. (2020); Anand et al. (2021); Scheuermann et al. (2022)

## 2.11 Appendix A: KCWI Seeing FWHM from Standard Star Observations and Table of Observations

We summarize the details of all of the KCWI observations and standard star observations in Table 2.7 and 2.6. Additionally, we describe below the measurement of seeing from the set of standard stars.

To measure seeing, we fit a 2D Gaussian to each standard star observation. We find an average FWHM of $\sim 1.2''$, however, at some points during the nights of 10-17-2018, 03-27-2019, and 03-28-2019 the seeing was poorer with values between $1.6''$-$2''$. Aside from these portions of the nights, the seeing was stable near the average FWHM. The FWHM measurements for each standard star observation are summarized in Table 2.6.

**Table 2.6.** Summary of KCWI Standard Star Observations.

| Star[a] | RA | Dec | Date (UTC) | Exposure (s) | Airmass | FWHM[b] ($''$) |
|---|---|---|---|---|---|---|
| He3 | 06:47:37.99 | +37:30:57.1 | 2018-10-16T15:00:13 | 20.0 | 1.06 | 1.32 |
| Feige15 | 01:49:09.49 | +13:33:11.7 | 2018-10-17T09:04:57 | 10.0 | 1.07 | 1.69 |
| Feige15 | 01:49:09.49 | +13:33:11.7 | 2018-10-17T09:06:11 | 1.0 | 1.07 | 1.12 |
| Feige15 | 01:49:09.49 | +13:33:11.7 | 2018-10-16T10:44:02 | 10.0 | 1.01 | 1.04 |
| Feige34 | 10:39:36.71 | +43:06:10.1 | 2019-03-27T09:21:06 | 5.0 | 1.10 | 1.28 |
| Feige34 | 10:39:36.71 | +43:06:10.1 | 2019-03-27T09:22:26 | 1.0 | 1.10 | 1.21 |
| Feige66 | 12:37:23.52 | +25:03:59.3 | 2019-03-27T13:45:25 | 1.0 | 1.35 | 1.99 |
| Feige66 | 12:37:23.52 | +25:03:59.3 | 2019-03-28T13:19:36 | 1.0 | 1.26 | 1.83 |
| Feige66 | 12:37:23.52 | +25:03:59.3 | 2019-03-28T13:20:57 | 5.0 | 1.26 | 1.83 |
| GD50 | 03:48:50.31 | -00:58:35.8 | 2021-10-06T10:17:51 | 1.0 | 1.47 | 1.13 |
| GD50 | 03:48:50.31 | -00:58:35.8 | 2021-10-06T10:19:37 | 1.0 | 1.46 | 1.13 |
| GD50 | 03:48:50.31 | -00:58:35.8 | 2021-10-06T10:20:53 | 10.0 | 1.45 | 1.18 |
| GD50 | 03:48:50.31 | -00:58:35.8 | 2021-10-06T10:22:37 | 15.0 | 1.44 | 1.22 |
| GD50 | 03:48:50.31 | -00:58:35.8 | 2021-10-06T14:13:09 | 10.0 | 1.11 | 1.01 |
| GD50 | 03:48:50.31 | -00:58:35.8 | 2021-10-06T14:14:54 | 15.0 | 1.11 | 1.04 |

**Table 2.6.** Summary of KCWI Standard Star Observations.(Continued)

| | | | | | | |
|---|---|---|---|---|---|---|
| GD50 | 03:48:50.31 | -00:58:35.8 | 2021-10-06T14:16:28 | 1.0 | 1.11 | 1.06 |
| GD50 | 03:48:50.31 | -00:58:35.8 | 2021-10-07T10:29:40 | 1.0 | 1.38 | 1.07 |
| GD50 | 03:48:50.31 | -00:58:35.8 | 2021-10-07T10:30:56 | 10.0 | 1.38 | 1.11 |
| GD50 | 03:48:50.31 | -00:58:35.8 | 2021-10-07T10:32:17 | 15.0 | 1.37 | 1.10 |
| GD50 | 03:48:50.31 | -00:58:35.8 | 2021-10-07T13:19:16 | 10.0 | 1.07 | 1.11 |
| GD50 | 03:48:50.31 | -00:58:35.8 | 2021-10-07T13:20:43 | 15.0 | 1.07 | 1.18 |

*Notes*: (a) The name of each standard star as displayed in the KDRP list of standards. The angular FWHM was measured from a 2D Gaussian fit to a white-light image of the standard star.

**Table 2.7.** Summary of KCWI Observations. This table reports the the galaxy and the field observed (Field). Note the repeated fields are offset by 1/2 slice width, with the exception of all the fields in NGC3627. The table also reports: the original coordinates of the field center in right ascension and declination (RA, DEC), the applied astrometric correction in right ascension and declination ($RA_{corr}$, $DEC_{corr}$) determined from the image registration, the UTC start-time and total integration the exposure in seconds (Date, Exposure) as well as the airmass (Airmass), position angle (Angle) and the angular FWHM of the pointing.

| Field[(a)] | RA (°) | $RA_{corr}$[(b)] (″) | Dec (°) | $Dec_{corr}$[(b)] (″) | Date (UTC) | Exposure (s) | Airmass | PA (°) | FWHM[(c)] (″) |
|---|---|---|---|---|---|---|---|---|---|
| NGC0628F17 | 24.188826 | 0.16 | 15.771491 | -1.75 | 2018-10-17T07:00:46 | 1200.0 | 1.46 | 45.0 | 2.14 |
| NGC0628F17 | 24.189230 | -1.30 | 15.771380 | -1.35 | 2018-10-17T07:35:05 | 1200.0 | 1.28 | 45.0 | 1.79 |
| NGC0628F17 | 24.189230 | -1.30 | 15.771380 | -1.35 | 2018-10-17T07:56:17 | 1200.0 | 1.20 | 45.0 | 1.97 |
| NGC0628F18 | 24.189057 | -0.68 | 15.771546 | -1.95 | 2018-10-17T08:29:45 | 1200.0 | 1.11 | 45.0 | 2.49 |
| NGC0628F18 | 24.188941 | -0.26 | 15.771657 | -2.35 | 2018-10-17T08:51:03 | 1200.0 | 1.07 | 45.0 | 2.49 |
| NGC0628F22 | 24.189576 | -2.55 | 15.771268 | -0.95 | 2018-10-17T09:29:26 | 1200.0 | 1.02 | 45.0 | 2.20 |
| NGC0628F22 | 24.189461 | -2.13 | 15.771380 | -1.35 | 2018-10-17T09:50:42 | 1200.0 | 1.01 | 45.0 | 2.49 |
| NGC0628F23 | 24.189519 | -2.34 | 15.770380 | 2.25 | 2018-10-17T10:24:20 | 1200.0 | 1.00 | 45.0 | 1.49 |
| NGC0628F23 | 24.189634 | -2.75 | 15.770324 | 2.45 | 2018-10-17T10:45:51 | 1200.0 | 1.01 | 45.0 | 1.60 |
| NGC0628F04 | 24.190558 | -6.08 | 15.770213 | 2.85 | 2018-10-16T10:08:04 | 1200.0 | 1.00 | 45.0 | 2.48 |
| NGC1087F10 | 41.606106 | -1.05 | -0.494058 | -0.15 | 2018-10-17T11:23:24 | 1200.0 | 1.07 | 90.0 | 1.26 |
| NGC1087F10 | 41.606106 | -1.05 | -0.494058 | -0.15 | 2018-10-17T11:44:36 | 1200.0 | 1.07 | 90.0 | 1.29 |
| NGC1087F09 | 41.605773 | 0.15 | -0.494446 | 1.25 | 2018-10-17T12:17:46 | 1200.0 | 1.09 | 90.0 | 1.19 |

**Table 2.7.** Summary of KCWI Observations.(Continued)

| | | | | | | | | | |
|---|---|---|---|---|---|---|---|---|---|
| NGC1087F09 | 41.605773 | 0.15 | -0.494391 | 1.05 | 2018-10-17T12:38:58 | 1200.0 | 1.12 | 90.0 | 1.15 |
| NGC1087F08 | 41.605884 | -0.25 | -0.494391 | 1.05 | 2018-10-17T13:12:00 | 1200.0 | 1.19 | 90.0 | 1.16 |
| NGC1087F08 | 41.605884 | -0.25 | -0.494446 | 1.25 | 2018-10-17T13:33:09 | 1200.0 | 1.25 | 90.0 | 1.27 |
| NGC1087F04 | 41.606050 | -0.85 | -0.494169 | 0.25 | 2018-10-17T14:06:31 | 1200.0 | 1.39 | 90.0 | 1.21 |
| NGC1087F04 | 41.606050 | -0.85 | -0.494113 | 0.05 | 2018-10-17T14:27:51 | 1200.0 | 1.52 | 90.0 | 1.31 |
| NGC1087F11 | 41.605884 | -0.25 | -0.494391 | 1.05 | 2018-10-16T13:30:01 | 1200.0 | 1.23 | 90.0 | 1.24 |
| NGC1087F11 | 41.605773 | 0.15 | -0.494391 | 1.05 | 2018-10-16T13:08:26 | 1200.0 | 1.17 | 90.0 | 1.16 |
| NGC1087F12 | 41.606939 | -4.05 | -0.495113 | 3.65 | 2018-10-16T11:36:44 | 1200.0 | 1.07 | 90.0 | 1.07 |
| NGC1087F12 | 41.606050 | -0.85 | -0.494724 | 2.25 | 2018-10-16T12:11:21 | 1200.0 | 1.08 | 90.0 | 1.19 |
| NGC1087F12 | 41.606050 | -0.85 | -0.494669 | 2.05 | 2018-10-16T12:32:55 | 1200.0 | 1.11 | 90.0 | 1.19 |
| NGC1300F1 | 49.903140 | -2.39 | -19.400675 | 1.25 | 2021-10-07T10:58:14 | 1200.0 | 1.44 | 90.0 | 1.14 |
| NGC1300F1 | 49.903140 | -2.39 | -19.400786 | 1.65 | 2021-10-07T11:19:16 | 1200.0 | 1.38 | 90.0 | 1.50 |
| NGC1300F2 | 49.903022 | -1.96 | -19.401008 | 2.45 | 2021-10-07T11:52:07 | 1200.0 | 1.32 | 90.0 | 1.14 |
| NGC1300F2 | 49.903022 | -1.96 | -19.400953 | 2.25 | 2021-10-07T12:13:05 | 1200.0 | 1.30 | 90.0 | 1.33 |
| NGC1300F3 | 49.902963 | -1.75 | -19.401619 | 4.65 | 2021-10-07T12:45:25 | 1200.0 | 1.29 | 90.0 | 1.34 |
| NGC1300F3 | 49.902963 | -1.75 | -19.401508 | 4.25 | 2021-10-07T13:06:26 | 1200.0 | 1.30 | 90.0 | 1.20 |
| NGC1300F4 | 49.903788 | -4.72 | -19.401341 | 3.65 | 2021-10-07T13:42:40 | 1200.0 | 1.35 | 90.0 | 1.04 |

**Table 2.7.** Summary of KCWI Observations.(Continued)

| | | | | | | | | | |
|---|---|---|---|---|---|---|---|---|---|
| NGC1300F4 | 49.903729 | -4.51 | -19.401341 | 3.65 | 2021-10-07T14:03:37 | 1200.0 | 1.40 | 90.0 | 1.03 |
| NGC1300F5 | 49.903611 | -4.08 | -19.401730 | 5.05 | 2021-10-07T14:36:25 | 1200.0 | 1.51 | 0.0 | 1.33 |
| NGC1300F5 | 49.903552 | -3.87 | -19.401730 | 5.05 | 2021-10-07T14:57:23 | 1200.0 | 1.62 | 0.0 | 1.34 |
| NGC1385F1 | 54.372099 | -2.25 | -24.496321 | 1.65 | 2021-10-06T10:52:05 | 1200.0 | 1.70 | 90.0 | 1.52 |
| NGC1385F1 | 54.372099 | -2.25 | -24.496321 | 1.65 | 2021-10-06T11:13:46 | 1200.0 | 1.59 | 90.0 | 1.43 |
| NGC1385F2 | 54.372038 | -2.03 | -24.496265 | 1.45 | 2021-10-06T11:50:22 | 1200.0 | 1.47 | 90.0 | 1.26 |
| NGC1385F2 | 54.372038 | -2.03 | -24.496321 | 1.65 | 2021-10-06T12:11:22 | 1200.0 | 1.43 | 90.0 | 1.20 |
| NGC1385F3 | 54.371916 | -1.59 | -24.496432 | 2.05 | 2021-10-06T12:44:09 | 1200.0 | 1.40 | 90.0 | 1.06 |
| NGC1385F3 | 54.371916 | -1.59 | -24.496487 | 2.25 | 2021-10-06T13:05:09 | 1200.0 | 1.39 | 90.0 | 1.35 |
| NGC1385F4 | 54.371794 | -1.15 | -24.496265 | 1.45 | 2021-10-06T13:38:12 | 1200.0 | 1.42 | 90.0 | 1.16 |
| NGC1385F4 | 54.371794 | -1.15 | -24.496265 | 1.45 | 2021-10-06T13:59:12 | 1200.0 | 1.45 | 90.0 | 1.06 |
| NGC1385F5 | 54.371611 | -0.49 | -24.495710 | -0.55 | 2021-10-06T14:41:06 | 1200.0 | 1.57 | 0.0 | 1.21 |
| NGC2835F1 | 139.471355 | -3.51 | -22.341874 | 0.05 | 2019-03-27T05:57:41 | 1200.0 | 1.47 | 90.0 | 1.42 |
| NGC2835F1 | 139.471355 | -3.51 | -22.341874 | 0.05 | 2019-03-27T06:18:44 | 1200.0 | 1.42 | 90.0 | 1.52 |
| NGC2835F2 | 139.471475 | -3.95 | -22.342430 | 2.05 | 2019-03-27T06:52:51 | 1200.0 | 1.36 | 90.0 | 1.51 |
| NGC2835F2 | 139.471475 | -3.95 | -22.342430 | 2.05 | 2019-03-27T07:13:56 | 1200.0 | 1.35 | 90.0 | 1.42 |
| NGC2835F3 | 139.471114 | -2.65 | -22.342874 | 3.65 | 2019-03-27T07:47:08 | 1200.0 | 1.36 | 90.0 | 1.39 |

**Table 2.7.** Summary of KCWI Observations.(Continued)

| | | | | | | | | | |
|---|---|---|---|---|---|---|---|---|---|
| NGC2835F3 | 139.471054 | -2.43 | -22.342874 | 3.65 | 2019-03-27T08:08:11 | 1200.0 | 1.38 | 90.0 | 1.52 |
| NGC2835F4 | 139.470694 | -1.14 | -22.343041 | 4.25 | 2019-03-27T08:42:01 | 1200.0 | 1.45 | 90.0 | 1.26 |
| NGC2835F4 | 139.470634 | -0.92 | -22.342985 | 4.05 | 2019-03-27T09:03:11 | 1200.0 | 1.51 | 90.0 | 1.17 |
| NGC3627F1 | 170.056873 | -2.92 | 12.998914 | 1.45 | 2017-12-24T12:43:33 | 120.0 | 1.32 | 90.0 | 1.27 |
| NGC3627F1 | 170.056873 | -2.92 | 12.998858 | 1.65 | 2017-12-24T12:46:31 | 120.0 | 1.30 | 90.0 | 1.27 |
| NGC3627F1 | 170.056873 | -2.92 | 12.998858 | 1.65 | 2017-12-24T12:49:28 | 120.0 | 1.29 | 90.0 | 1.26 |
| NGC3627F1 | 170.056873 | -2.92 | 12.998858 | 1.65 | 2017-12-24T12:52:26 | 120.0 | 1.28 | 90.0 | 1.27 |
| NGC3627F1 | 170.056873 | -2.92 | 12.998858 | 1.65 | 2017-12-24T12:55:24 | 120.0 | 1.26 | 90.0 | 1.27 |
| NGC3627F1 | 170.056132 | -0.26 | 12.999192 | 0.45 | 2017-12-24T15:33:08 | 120.0 | 1.01 | 90.0 | 1.16 |
| NGC3627F1 | 170.056132 | -0.26 | 12.999192 | 0.45 | 2017-12-24T15:36:06 | 120.0 | 1.01 | 90.0 | 1.22 |
| NGC3627F1 | 170.056132 | -0.26 | 12.999192 | 0.45 | 2017-12-24T15:39:04 | 120.0 | 1.01 | 90.0 | 1.21 |
| NGC3627F1 | 170.056132 | -0.26 | 12.999192 | 0.45 | 2017-12-24T15:42:02 | 120.0 | 1.01 | 90.0 | 1.20 |
| NGC3627F2 | 170.057215 | -4.16 | 12.998747 | 2.05 | 2017-12-24T13:02:38 | 120.0 | 1.24 | 90.0 | 1.21 |
| NGC3627F2 | 170.057215 | -4.16 | 12.998747 | 2.05 | 2017-12-24T13:05:35 | 120.0 | 1.23 | 90.0 | 1.23 |
| NGC3627F2 | 170.057215 | -4.16 | 12.998747 | 2.05 | 2017-12-24T13:08:33 | 120.0 | 1.22 | 90.0 | 1.22 |
| NGC3627F2 | 170.057215 | -4.16 | 12.998747 | 2.05 | 2017-12-24T13:11:31 | 120.0 | 1.21 | 90.0 | 1.19 |
| NGC3627F2 | 170.057215 | -4.16 | 12.998747 | 2.05 | 2017-12-24T13:14:29 | 120.0 | 1.20 | 90.0 | 1.23 |

**Table 2.7.** Summary of KCWI Observations.(Continued)

| | | | | | | | | | |
|---|---|---|---|---|---|---|---|---|---|
| NGC3627F3 | 170.057215 | -4.16 | 12.998747 | 2.05 | 2017-12-24T13:20:54 | 120.0 | 1.18 | 90.0 | 1.13 |
| NGC3627F3 | 170.057215 | -4.16 | 12.998747 | 2.05 | 2017-12-24T13:23:52 | 120.0 | 1.17 | 90.0 | 1.12 |
| NGC3627F3 | 170.057215 | -4.16 | 12.998747 | 2.05 | 2017-12-24T13:26:50 | 120.0 | 1.16 | 90.0 | 1.12 |
| NGC3627F3 | 170.057215 | -4.16 | 12.998747 | 2.05 | 2017-12-24T13:29:48 | 120.0 | 1.15 | 90.0 | 1.12 |
| NGC3627F3 | 170.057215 | -4.16 | 12.998747 | 2.05 | 2017-12-24T13:32:45 | 120.0 | 1.14 | 90.0 | 1.14 |
| NGC3627F4 | 170.057215 | -4.16 | 12.998580 | 2.65 | 2017-12-24T13:40:31 | 120.0 | 1.12 | 90.0 | 1.14 |
| NGC3627F4 | 170.057215 | -4.16 | 12.998580 | 2.65 | 2017-12-24T13:43:29 | 120.0 | 1.12 | 90.0 | 1.14 |
| NGC3627F4 | 170.057215 | -4.16 | 12.998580 | 2.65 | 2017-12-24T13:46:27 | 120.0 | 1.11 | 90.0 | 1.14 |
| NGC3627F4 | 170.057215 | -4.16 | 12.998580 | 2.65 | 2017-12-24T13:49:25 | 120.0 | 1.10 | 90.0 | 1.15 |
| NGC3627F4 | 170.057215 | -4.16 | 12.998580 | 2.65 | 2017-12-24T13:52:23 | 120.0 | 1.10 | 90.0 | 1.15 |
| NGC3627F5 | 170.057215 | -4.16 | 12.998525 | 2.85 | 2017-12-24T13:58:52 | 120.0 | 1.09 | 90.0 | 1.06 |
| NGC3627F5 | 170.057158 | -3.95 | 12.998525 | 2.85 | 2017-12-24T14:01:50 | 120.0 | 1.08 | 90.0 | 1.07 |
| NGC3627F5 | 170.057158 | -3.95 | 12.998525 | 2.85 | 2017-12-24T14:04:48 | 120.0 | 1.08 | 90.0 | 1.07 |
| NGC3627F5 | 170.057158 | -3.95 | 12.998525 | 2.85 | 2017-12-24T14:07:46 | 120.0 | 1.07 | 90.0 | 1.07 |
| NGC3627F5 | 170.057158 | -3.95 | 12.998525 | 2.85 | 2017-12-24T14:10:44 | 120.0 | 1.07 | 90.0 | 1.07 |
| NGC3627F6 | 170.056246 | -0.67 | 12.999136 | 0.65 | 2017-12-24T14:24:16 | 120.0 | 1.05 | 90.0 | 1.12 |
| NGC3627F6 | 170.056189 | -0.46 | 12.999136 | 0.65 | 2017-12-24T14:27:14 | 120.0 | 1.04 | 90.0 | 1.15 |

**Table 2.7.** Summary of KCWI Observations.(Continued)

| | | | | | | | | | |
|---|---|---|---|---|---|---|---|---|---|
| NGC3627F6 | 170.056189 | -0.46 | 12.999136 | 0.65 | 2017-12-24T14:30:11 | 120.0 | 1.04 | 90.0 | 1.17 |
| NGC3627F6 | 170.056189 | -0.46 | 12.999136 | 0.65 | 2017-12-24T14:33:10 | 120.0 | 1.04 | 90.0 | 1.17 |
| NGC3627F6 | 170.056189 | -0.46 | 12.999136 | 0.65 | 2017-12-24T14:36:07 | 120.0 | 1.03 | 90.0 | 1.15 |
| NGC3627F7 | 170.056303 | -0.87 | 12.999136 | 0.65 | 2017-12-24T14:42:14 | 120.0 | 1.03 | 90.0 | 1.16 |
| NGC3627F7 | 170.056303 | -0.87 | 12.999136 | 0.65 | 2017-12-24T14:45:11 | 120.0 | 1.03 | 90.0 | 1.16 |
| NGC3627F7 | 170.056303 | -0.87 | 12.999136 | 0.65 | 2017-12-24T14:48:09 | 120.0 | 1.02 | 90.0 | 1.17 |
| NGC3627F7 | 170.056303 | -0.87 | 12.999136 | 0.65 | 2017-12-24T14:51:07 | 120.0 | 1.02 | 90.0 | 1.18 |
| NGC3627F7 | 170.056303 | -0.87 | 12.999136 | 0.65 | 2017-12-24T14:54:05 | 120.0 | 1.02 | 90.0 | 1.20 |
| NGC3627F8 | 170.056303 | -0.87 | 12.998914 | 1.45 | 2017-12-24T15:00:09 | 120.0 | 1.02 | 90.0 | 1.05 |
| NGC3627F8 | 170.056303 | -0.87 | 12.998914 | 1.45 | 2017-12-24T15:03:07 | 120.0 | 1.01 | 90.0 | 1.05 |
| NGC3627F8 | 170.056246 | -0.67 | 12.998914 | 1.45 | 2017-12-24T15:06:05 | 120.0 | 1.01 | 90.0 | 1.05 |
| NGC3627F8 | 170.056246 | -0.67 | 12.998914 | 1.45 | 2017-12-24T15:09:03 | 120.0 | 1.01 | 90.0 | 1.06 |
| NGC3627F8 | 170.056246 | -0.67 | 12.998914 | 1.45 | 2017-12-24T15:12:00 | 120.0 | 1.01 | 90.0 | 1.05 |
| NGC3627F9 | 170.056018 | 0.15 | 12.998803 | 1.85 | 2017-12-24T15:15:05 | 120.0 | 1.01 | 90.0 | 1.12 |
| NGC3627F9 | 170.056018 | 0.15 | 12.998803 | 1.85 | 2017-12-24T15:18:03 | 120.0 | 1.01 | 90.0 | 1.12 |
| NGC3627F9 | 170.056018 | 0.15 | 12.998803 | 1.85 | 2017-12-24T15:21:01 | 120.0 | 1.01 | 90.0 | 1.12 |
| NGC3627F9 | 170.056018 | 0.15 | 12.998803 | 1.85 | 2017-12-24T15:23:59 | 120.0 | 1.01 | 90.0 | 1.11 |

**Table 2.7.** Summary of KCWI Observations.(Continued)

| | | | | | | | | | |
|---|---|---|---|---|---|---|---|---|---|
| NGC3627F9 | 170.056018 | 0.15 | 12.998803 | 1.85 | 2017-12-24T15:26:57 | 120.0 | 1.01 | 90.0 | 1.11 |
| NGC5068F1 | 199.704057 | -2.20 | -21.023638 | 0.85 | 2019-03-27T09:49:19 | 1200.0 | 1.47 | 90.0 | 1.51 |
| NGC5068F1 | 199.704057 | -2.20 | -21.023694 | 1.05 | 2019-03-27T10:10:22 | 1200.0 | 1.41 | 90.0 | 1.33 |
| NGC5068F2 | 199.703819 | -1.34 | -21.023638 | 0.85 | 2019-03-27T10:44:05 | 1200.0 | 1.35 | 90.0 | 1.40 |
| NGC5068F3 | 199.703938 | -1.77 | -21.023971 | 2.05 | 2019-03-27T11:38:24 | 1200.0 | 1.32 | 90.0 | 2.49 |
| NGC5068F3 | 199.703938 | -1.77 | -21.023971 | 2.05 | 2019-03-27T11:59:28 | 1200.0 | 1.34 | 90.0 | 2.49 |
| NGC5068F4 | 199.703700 | -0.91 | -21.024138 | 2.65 | 2019-03-27T12:32:51 | 1200.0 | 1.39 | 90.0 | 1.55 |
| NGC5068F4 | 199.703700 | -0.91 | -21.024194 | 2.85 | 2019-03-27T12:53:55 | 1200.0 | 1.45 | 90.0 | 1.88 |
| NGC5068F5 | 199.703403 | 0.16 | -21.023860 | 1.65 | 2019-03-27T13:28:21 | 1200.0 | 1.58 | 90.0 | 1.97 |
| NGC5068F5 | 199.703998 | -1.98 | -21.023694 | 1.05 | 2019-03-28T10:19:33 | 1200.0 | 1.38 | 90.0 | 1.69 |
| NGC5068F7 | 199.704057 | -2.20 | -21.023694 | 1.05 | 2019-03-28T10:54:58 | 1200.0 | 1.33 | 90.0 | 1.68 |
| NGC5068F7 | 199.703998 | -1.98 | -21.023694 | 1.05 | 2019-03-28T11:16:01 | 1200.0 | 1.32 | 90.0 | 1.67 |
| NGC5068F8 | 199.703879 | -1.55 | -21.024082 | 2.45 | 2019-03-28T11:49:43 | 1200.0 | 1.33 | 90.0 | 1.86 |
| NGC5068F8 | 199.703819 | -1.34 | -21.024027 | 2.25 | 2019-03-28T12:10:49 | 1200.0 | 1.36 | 90.0 | 1.87 |
| NGC5068F9 | 199.703403 | 0.16 | -21.024138 | 2.65 | 2019-03-28T12:44:48 | 1200.0 | 1.43 | 90.0 | 1.67 |
| NGC5068F9 | 199.703343 | 0.37 | -21.024138 | 2.65 | 2019-03-28T13:05:52 | 1200.0 | 1.50 | 90.0 | 1.65 |
| NGC5068F9 | 199.703700 | -0.91 | -21.023138 | -0.95 | 2022-02-24T14:57:54 | 1200.0 | 1.46 | 0.0 | 1.39 |

**Table 2.7.** Summary of KCWI Observations.(Continued)

| | | | | | | | | | |
|---|---|---|---|---|---|---|---|---|---|
| NGC5068F9 | 199.703641 | -0.70 | -21.023138 | -0.95 | 2022-02-24T15:08:56 | 600.0 | 1.50 | 0.0 | 1.46 |
| NGC5068F10 | 199.703700 | -0.91 | -21.023527 | 0.45 | 2022-02-24T15:30:23 | 800.0 | 1.59 | 90.0 | 1.17 |
| NGC5068F10 | 199.703700 | -0.91 | -21.023471 | 0.25 | 2022-02-24T15:38:22 | 420.0 | 1.63 | 90.0 | 1.13 |

*Notes*: (a) The field numbering is from internal lists of potential pointings which were not performed in numerical order, therefore the field number does not reflect the sequence of observations. (b) The astrometric correction is described in Section 2.3.2. (c) The measured angular FWHM for the pointing, see Section 2.3.4.

## 2.12 Appendix B: KCWI Line Spread Function

The KCWI line spread function in the large slicer is non-Gaussian. Deviations from a Gaussian profile have been observed in KCWI data before. For example, using a combination of the medium slicer and grating van Dokkum et al. (2019). Following van der Marel & Franx (1993), in order to parameterize the degree of deviation from a Gaussian profile, we fit the spectra from a pipeline reduced arc lamp exposure a Gauss-Hermite function of the form:

$$\begin{aligned} G(X) = \frac{\gamma}{\sigma\sqrt{2\pi}} \exp\left(-X^2/2\right) \Bigg[ 1 + \ldots \\ h_3 \frac{X(2X^2-3)}{\sqrt{3}} + h_4 \frac{4(X^2-3)X^2+3}{\sqrt{24}} \Bigg], \end{aligned} \tag{2.3}$$

with $X = (\lambda - \lambda_0)/\sigma$, amplitude ($\gamma$) and spectral width ($\sigma$). The anti-symmetric and symmetric deviations from pure Gaussian profiles are captured by the constants, $h_3$ and $h_4$. A Gaussian function is recovered by setting $h_3 = h_4 = 0$. In Figure 2.19 we show histograms of the fitted values from $h_3$ and $h_4$ after fitting Eq. 2.3 to approximately 20 isolated arc lamp emission lines. We find that the emission lines in the arc lamp images are consistently flat topped, with an average value of $h_4 = -0.14 \pm 0.01$ across all spatial pixels. The degree that the line profile is non-Gaussian due to asymmetric deviations is small compared to symmetric deviations with an average value of $h_3 = -0.007 \pm 0.01$.

The authors state that the root cause of the deviation from a Gaussian profile is due to the slit width-limited resolution of the medium slicer (see, Casini & de Wijn, 2014). We posit that a similar limitation for the large slicer is responsible for the deviations measured in this work.

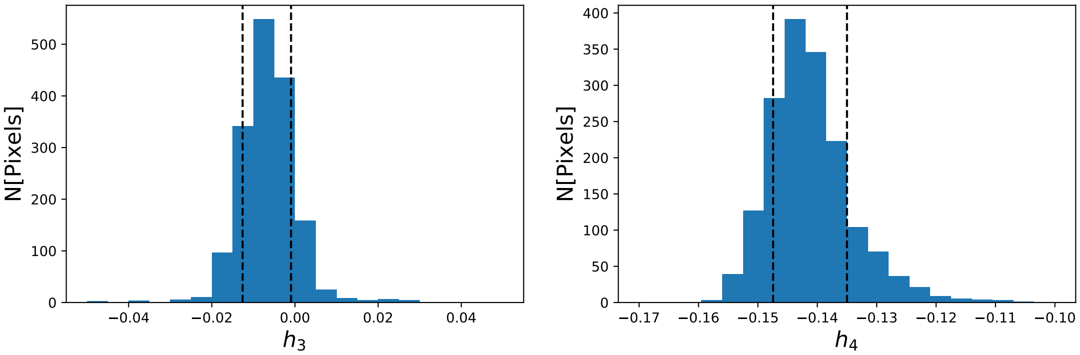

**Figure 2.19.** Histograms of the the Gauss-Hermite parameters $h_3$, shown in the left panel, and $h_4$, shown in the right panel. The above histograms show the distribution of values for the fitted constants $h_3$ (anti-symmetric) and $h_4$ (symmetric) from all pixels in the datacube. A Gaussian profile would exhibit $h_3 = h_4 = 0$, however, the above distributions show that the line profile of the instrument exhibits symmetric deviations. The broken black vertical lines represent the position of $\pm 1\sigma$.

## 2.13 Appendix C: Comparison of H II Region Identification Between KCWI and MUSE

We identify potential H II regions with H$\beta$ emission maps constructed from the KCWI galaxy mosaics using `HIIPhot`. H II regions, for the same galaxies, in the PHANGS Nebular Catalog were identified with `HIIPhot` and MUSE H$\alpha$ maps (Kreckel et al., 2019; Groves et al., 2023). Given the higher resolution of the MUSE imaging, as well as the three-fold brightness increase of H$\alpha$ relative to H$\beta$, we expect our H II region catalog to be less sensitive to the faintest and smallest H II regions.

In Figure 2.20 we show both the distribution of dust-corrected H$\beta$ luminosity, $L_{\mathrm{H}\beta}$, and radii, for regions identified by *HIIPhot* using KCWI H$\beta$ maps, “KCWI–H$\beta$ regions”, and MUSE H$\alpha$ maps or “MUSE–H$\alpha$ regions” within the KCWI mosaic footprint. For KCWI–H$\beta$ regions we measure a median $\mathrm{Log}_{10}(L_{\mathrm{H}\beta}/[\mathrm{erg\ s}^{-1}])$ of $37.7^{+0.9}_{-0.7}$ while for MUSE–H$\alpha$ regions the median is $37.1^{+0.8}_{-1.7}$. This comparison shows that the KCWI H$\beta$ maps is less sensitive to regions with $\mathrm{Log}_{10}(L_{\mathrm{H}\beta}/[\mathrm{erg\ s}^{-1}]) < 37$.

We also observe in Figure 2.20 that regions with radii less than the KCWI angular

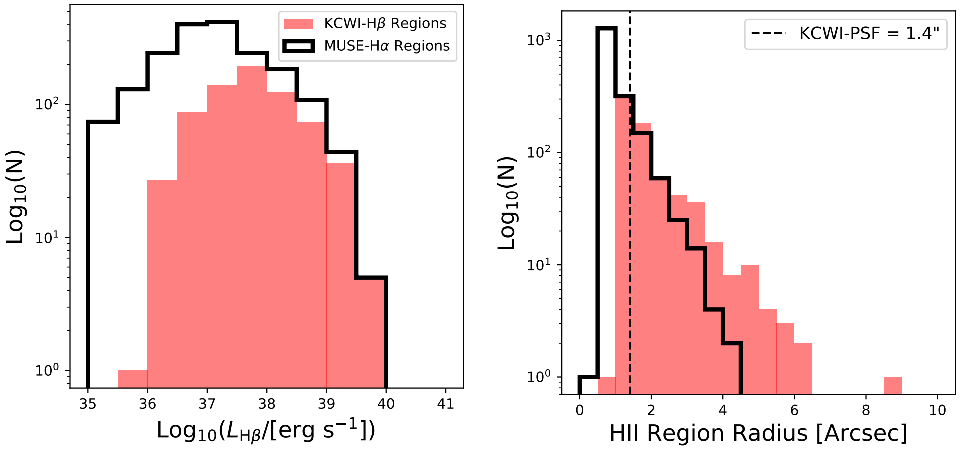

**Figure 2.20.** Histogram of the dust-corrected H$\beta$ luminosity for regions identified by `HIIPhot` using KCWI–H$\beta$ maps (*red*) and regions in the Nebular Catalog identified using MUSE–H$\alpha$ maps (*black*). The number of faint regions detected using the KCWI–H$\beta$ map is set by the limiting sensitivity, $\mathrm{Log}_{10}(L_{\mathrm{H}\beta}/[\mathrm{erg\ s}^{-1}]) < 37$, and angular resolution, FWHM=1.4″.

resolution are missed KCWI–H$\beta$ region sample. This can be seen clearly in Figures 2.21–2.27, where we compare the boundaries of the MUSE–H$\alpha$ and KCWI–H$\beta$ regions. In these figures, we see that many of the missed regions are small, and unresolved in the KCWI H$\beta$ map. Also owing to the larger number of detections is that many of the larger KCWI–H$\beta$ regions are resolved into smaller structures in the MUSE–H$\alpha$ regions.

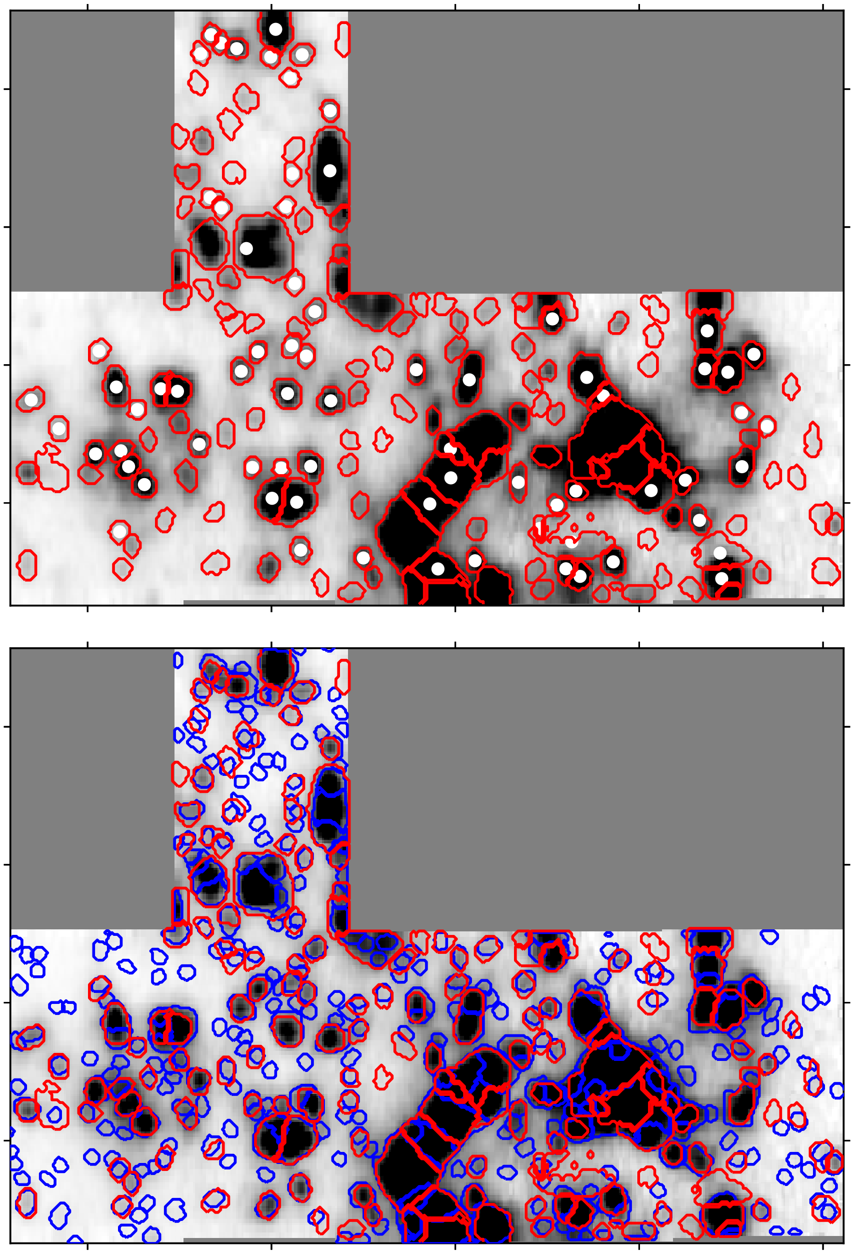

**Figure 2.21.** Comparison of region boundaries identified using `HIIPhot` and either KCWI–H$\beta$ or MUSE–H$\alpha$ emission line maps for the galaxy NGC 1087. The KCWI–H$\beta$ emission line map is shown in both panels. We overlay in *red* the morphology of regions identified by `HIIPhot` using the KCWI–H$\beta$ emission line map. A white marker indicates a region with significant auroral line detections in 2 or more auroral lines. In *blue* we overlay region boundaries from `HIIPhot` using the MUSE H$\alpha$ emission line maps (Kreckel et al., 2019; Groves et al., 2023).

**Table 2.8.** Total number of regions identified by `HIIphot` as potential H II regions per galaxy using both KCWI–H$\beta$ and MUSE–H$\alpha$, as well as number of KCWI–H$\beta$ regions with significant with significant auroral lines detections (in 2 or more auroral lines).

| Name | $N_{\mathrm{KCWI}}$ | $N_{\mathrm{MUSE}}$ | $N_{\mathrm{A}}$ |
|---|---|---|---|
| NGC 628$^{(a)}$ | 10 | 230 | 8 |
| NGC 1087 | 173 | 364 | 73 |
| NGC 1300 | 60 | 191 | 28 |
| NGC 1385 | 133 | 417 | 58 |
| NGC 2835 | 87 | 135 | 26 |
| NGC 3627 | 163 | 451 | 19 |
| NGC 5068 | 62 | 392 | 48 |

*Notes*: (a) NGC 628 was imaged in the least ideal observing conditions.

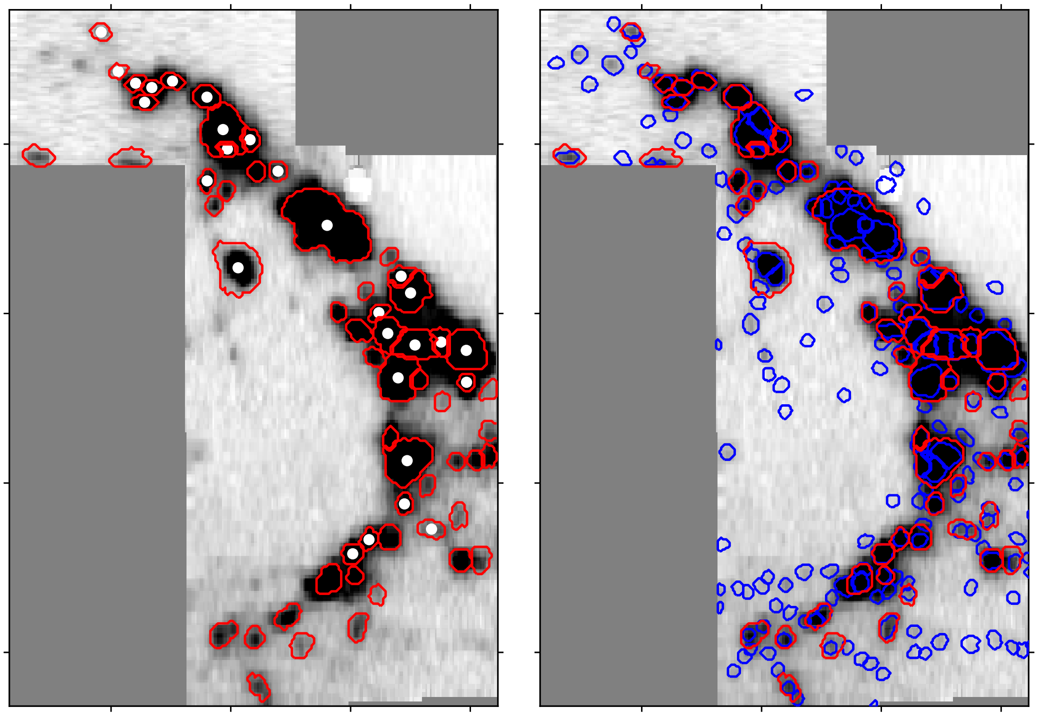

**Figure 2.22.** Comparison of H II region boundaries in NGC 1300, following Figure 2.21.

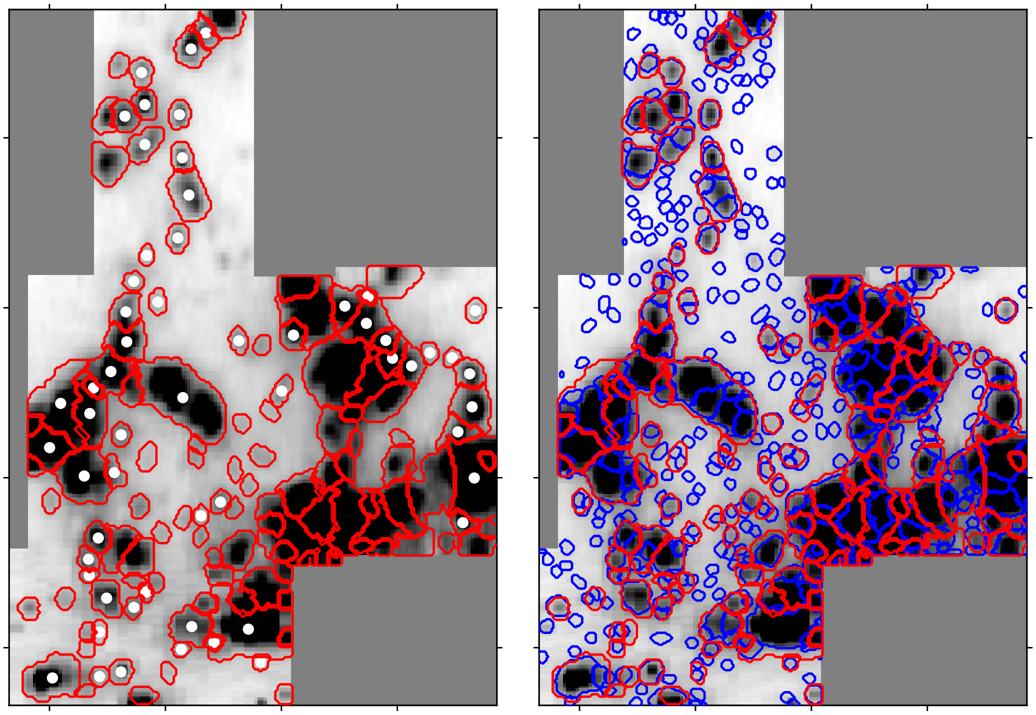

**Figure 2.23.** Comparison of H II region boundaries in NGC 1385, following Figure 2.21.

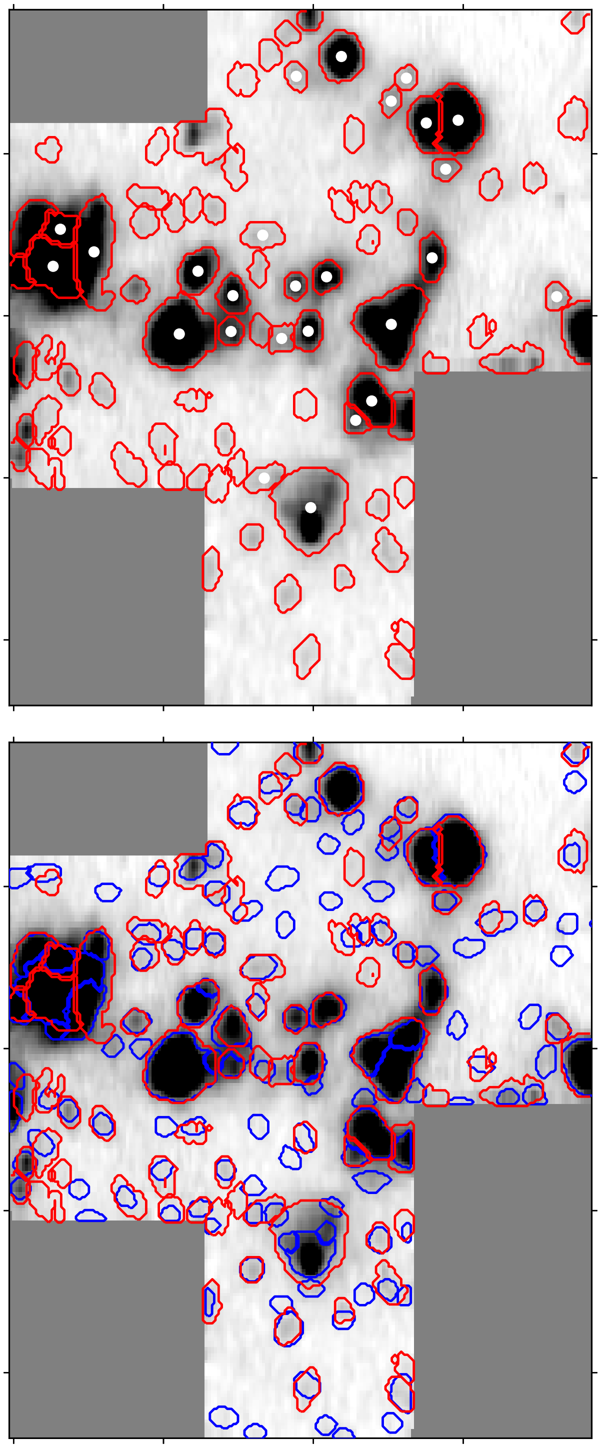

**Figure 2.24.** Comparison of H II region boundaries in NGC 2835, following Figure 2.21.

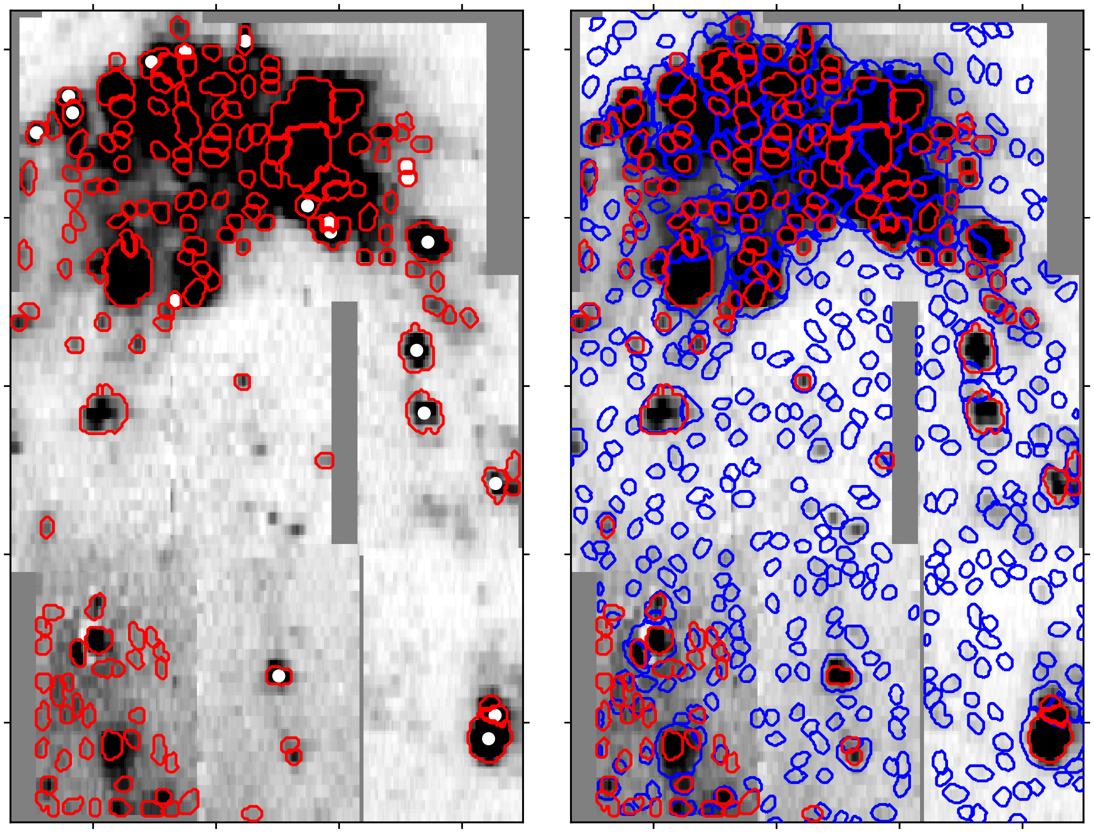

**Figure 2.25.** Comparison of H II region boundaries in NGC 3627, following Figure 2.21.

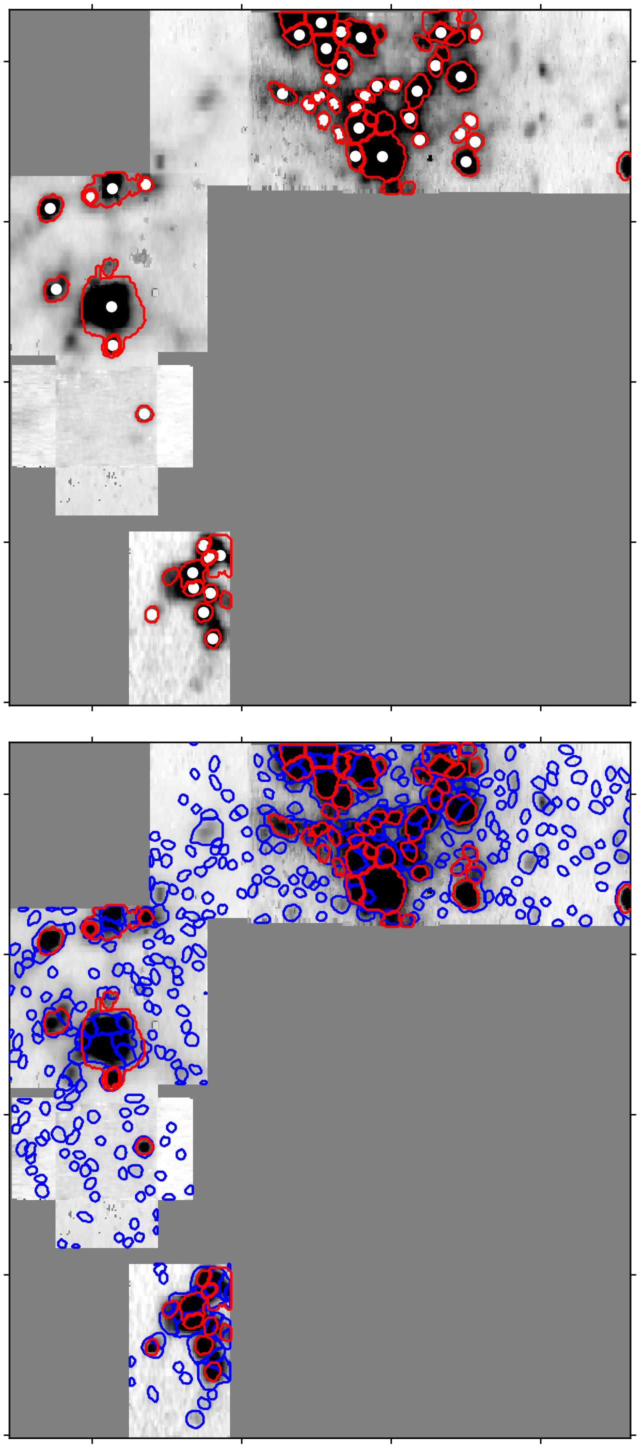

Figure 2.26. Comparison of H II region boundaries in NGC 5068, following Figure 2.21.

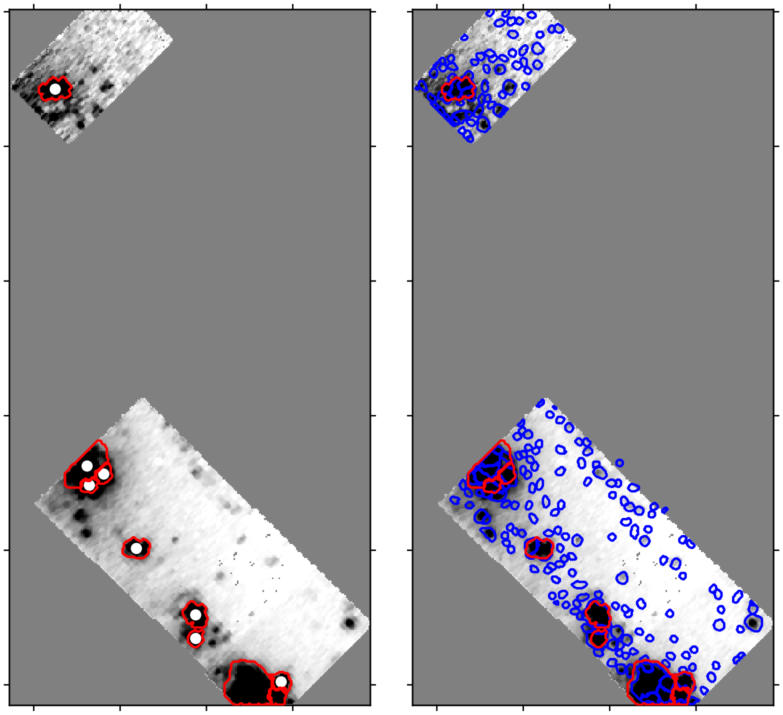

**Figure 2.27.** Comparison of H II region boundaries in NGC 628 following Figure 2.21.

## 2.14 Appendix D: Example Gaussian Fits to Auroral Lines

In this section we show example auroral line fits. In Figure 2.28 we show fits to high S/N auroral lines from an H II region in NGC 5068. We also include in Figure 2.28 annotations describing the the standard deviation of the fit residuals, $\sigma_{res}$, the S/N for a single emission line (or in the instance of simultaneous double line fits the S/N of the *red* and *purple* Gaussian fit: S/N$_r$ and S/N$_p$), the continuum noise, $\sigma_{cont}$ and reduced $\chi^2$. In this particular example, the auroral line in these fits are isolated from contaminating sky lines or nearby emission, especially in the case of [O III]$\lambda$4363 Å where the contribution from [Fe II]$\lambda$4360 Å is negligible. To demonstrate fitting [Fe II]$\lambda$4360 alongside [O III]$\lambda$4363 we show a low S/N detection with non-negligible contamination from [Fe II]$\lambda$4360 Å in Figure 2.29.

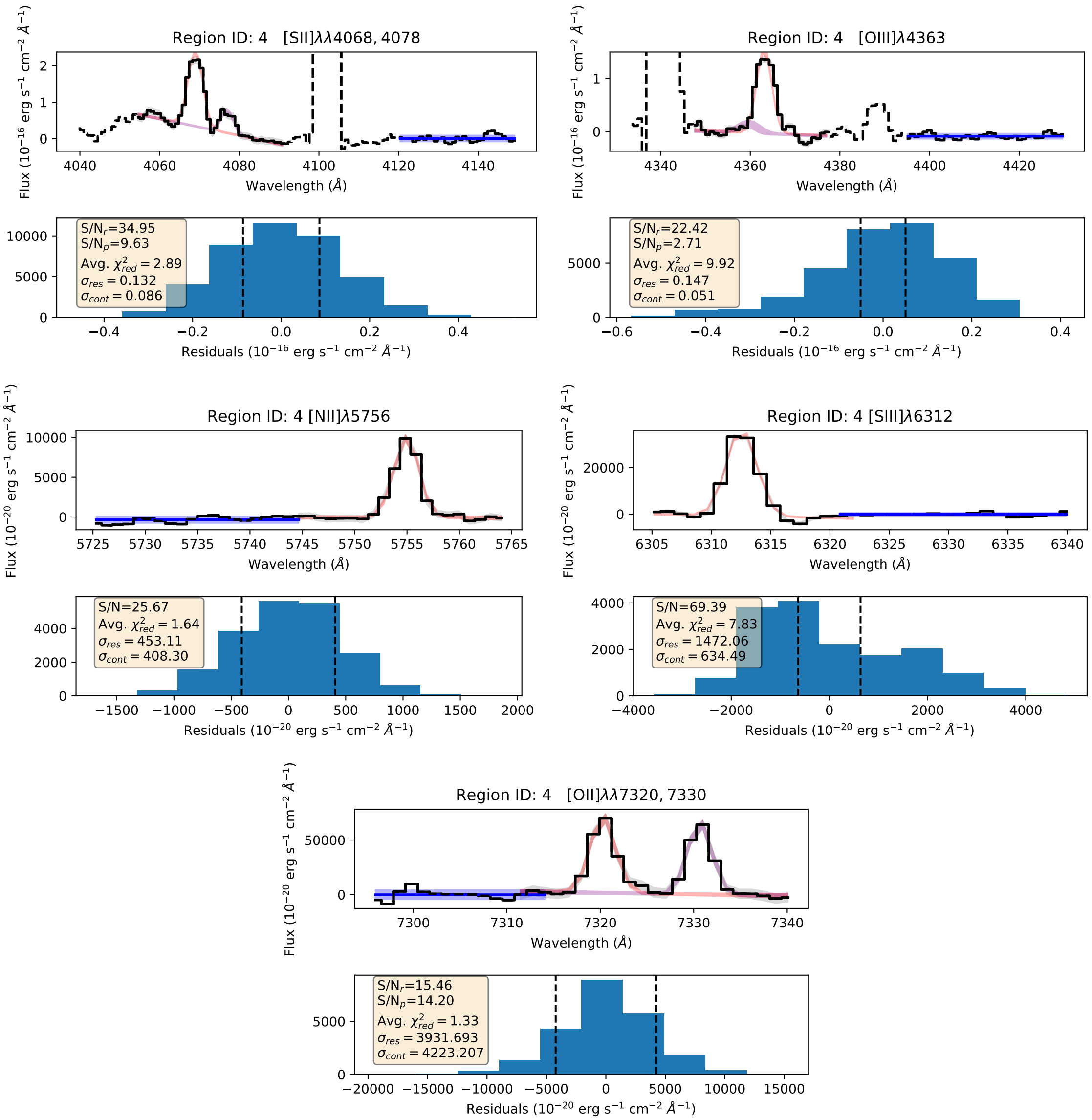

**Figure 2.28.** Auroral Line fits for an H II region in NGC 5068. We show in each panel a summary of auroral line fits for a single H II region in NGC 5068. The top frame in each panel shows the data, (*black-solid*), for the fitting and continuum wavelength ranges. In the wavelength range where $\sigma_{cont}$ is measured, we overlay $\pm\sigma_{cont}$ region (*blue-shaded*) around the line indicating the average value of the continuum (*blue-solid*). The (*red-shaded*) and *purple-shaded* for the double Gaussian fits, show the $1\sigma$ ranges of the fitted models. The bottom frame in each panels shows a histogram of the residuals. We also print text summarizing the S/N and average reduced $\chi^2$ of the fits as well as the $1\sigma$ of the residuals and value of $\sigma_{cont}$

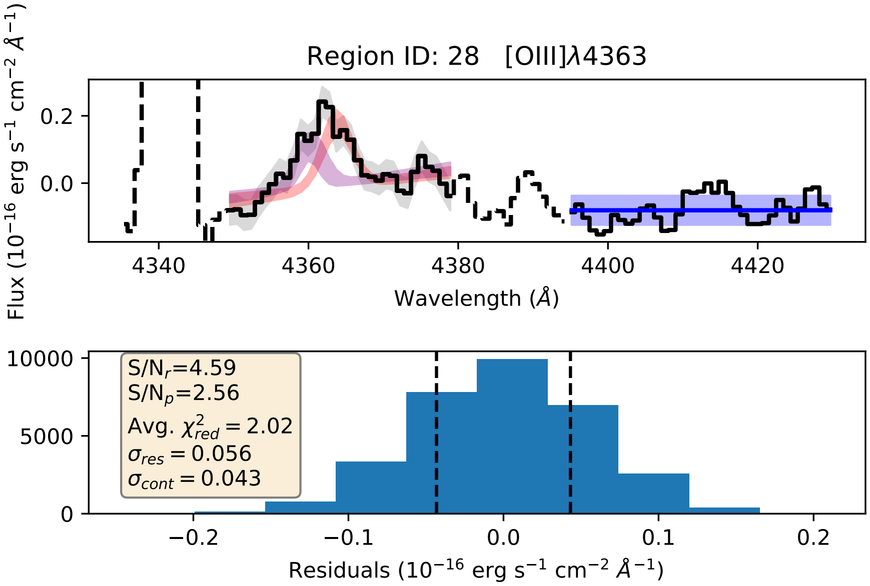

**Figure 2.29.** Example of auroral line fit measuring [O III]$\lambda$4363 Å flux with non-negligible [Fe II]$\lambda$4360 contribution for an H II region in NGC 1087. Annotations follow those in Figure 2.28.

## 2.15 Appendix E: Figures of the $\Delta T_\mathrm{e}$ and H II Region Property Comparisons

In the section we present the comparisons between H II region properties that exhibit no significant correlations with $\Delta T_e$.

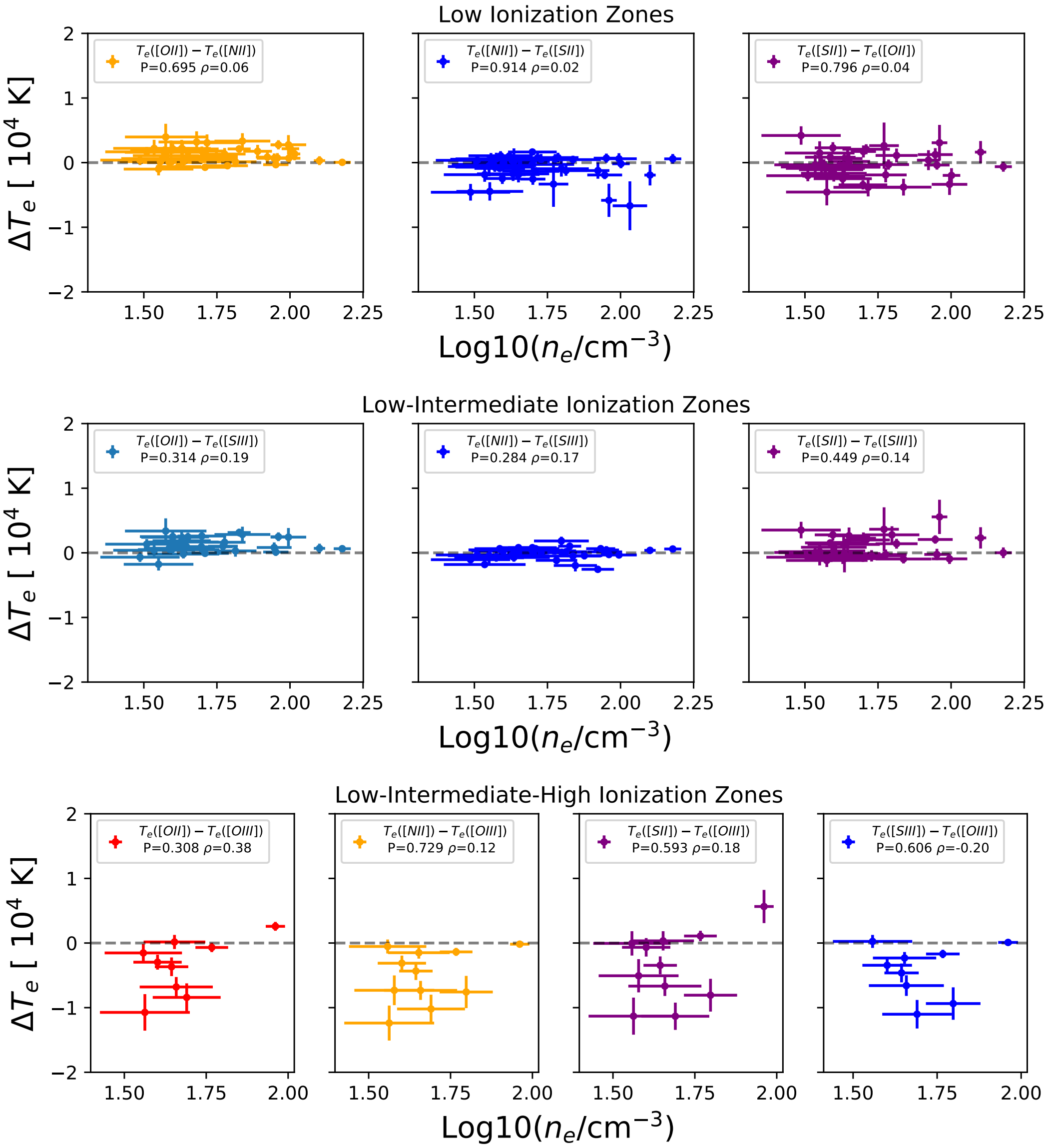

**Figure 2.30.** Electron temperature differences compared to the H II region electron density, $n_\mathrm{e}$. Top: The $\Delta T_e$'s between the low ionization zone temperatures. Middle: The $\Delta T_e$'s between the low and intermediate ionization zone temperatures. Bottom: The $\Delta T_e$'s between the low, intermediate and high ionization zone temperatures.

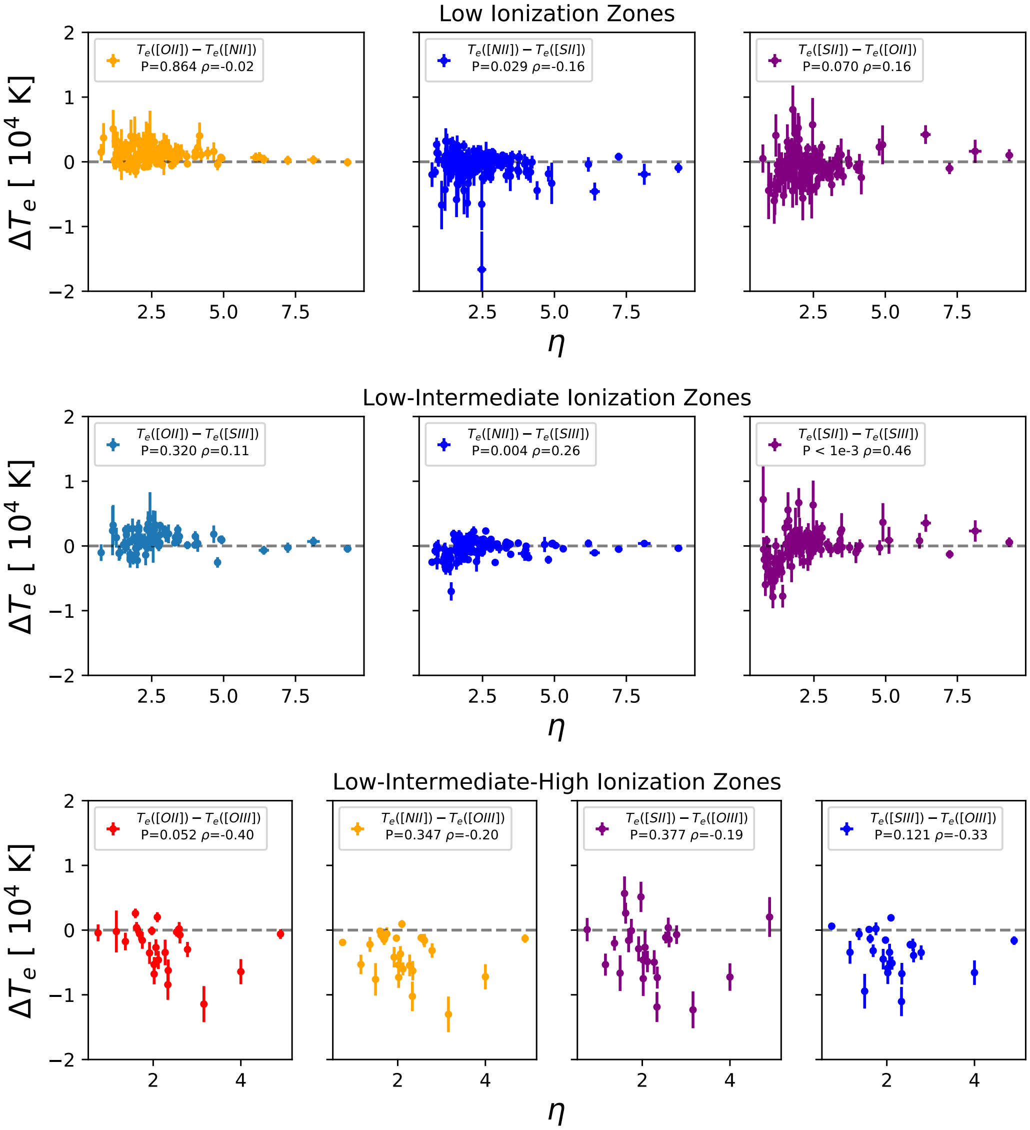

**Figure 2.31.** Electron temperature differences compared to the radiation softness parameter. The order of the panels follow those in Figure 2.30.

## 2.16 Appendix F: H II Region Measurements

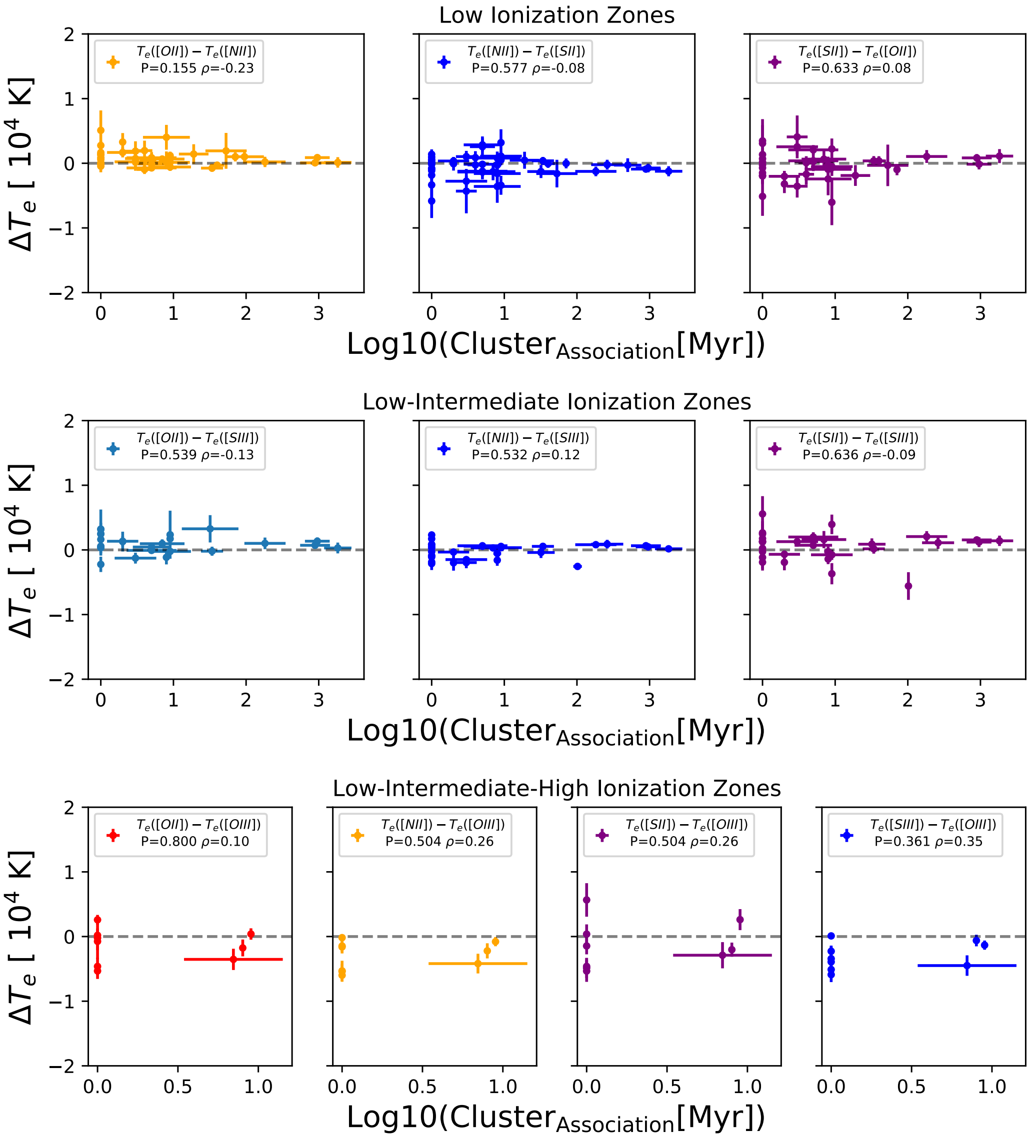

**Figure 2.32.** Electron temperature differences compared to the stellar cluster age. The order of the panels follow those in Figure 2.30.

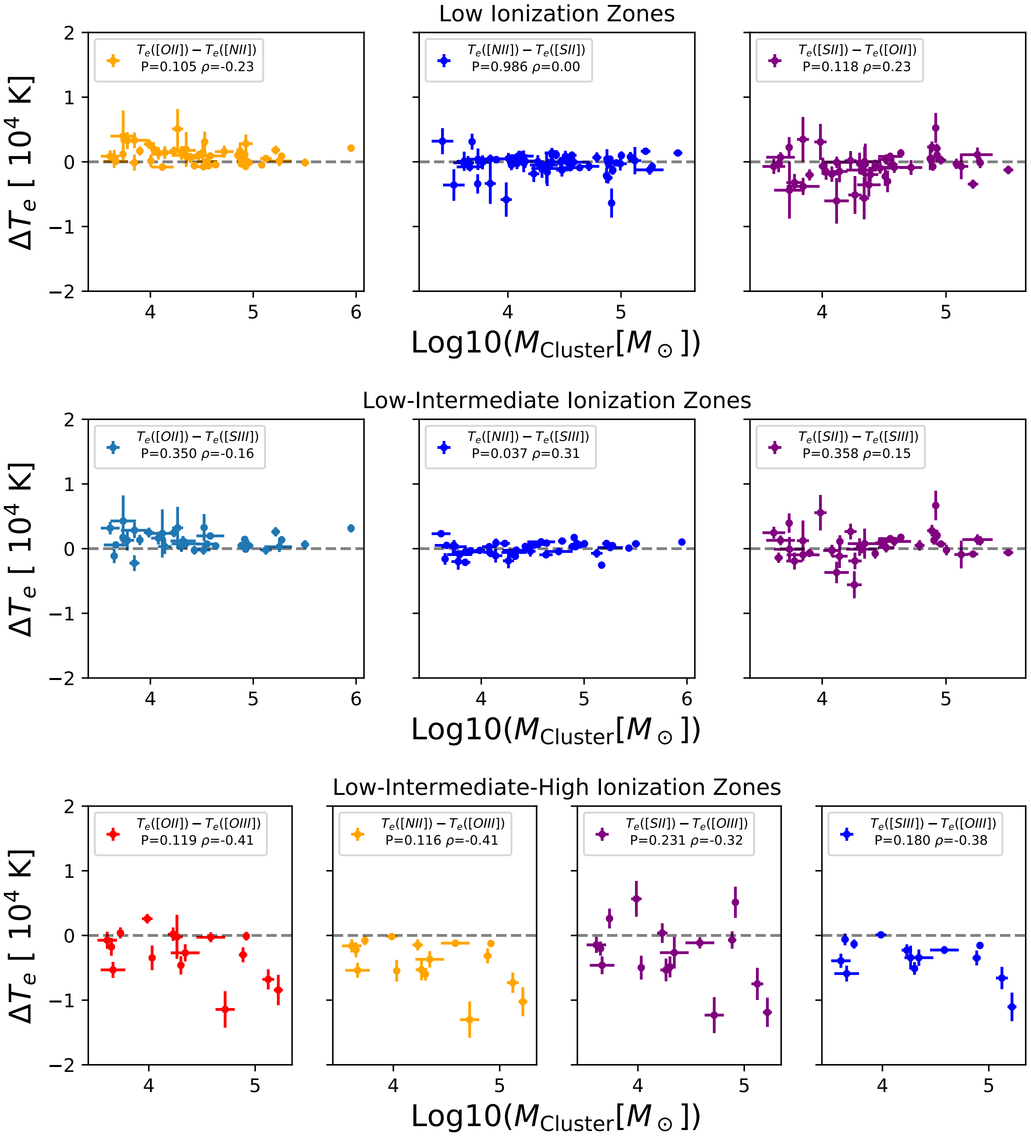

**Figure 2.33.** Electron temperature differences compared to the stellar cluster mass. The order of the panels follow those in Figure 2.30.

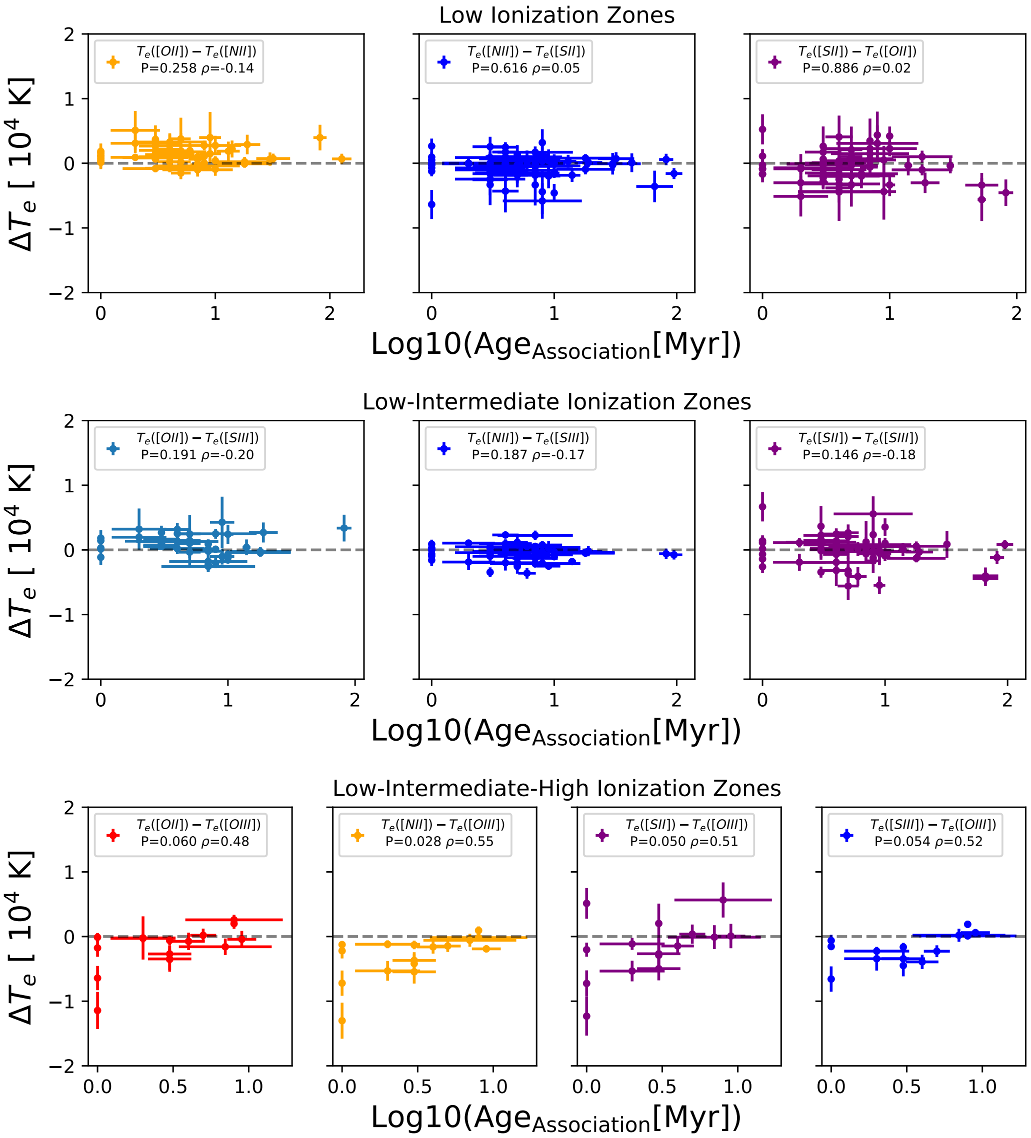

**Figure 2.34.** Electron temperature differences compared to the stellar association age. The order of the panels follow those in Figure 2.30.

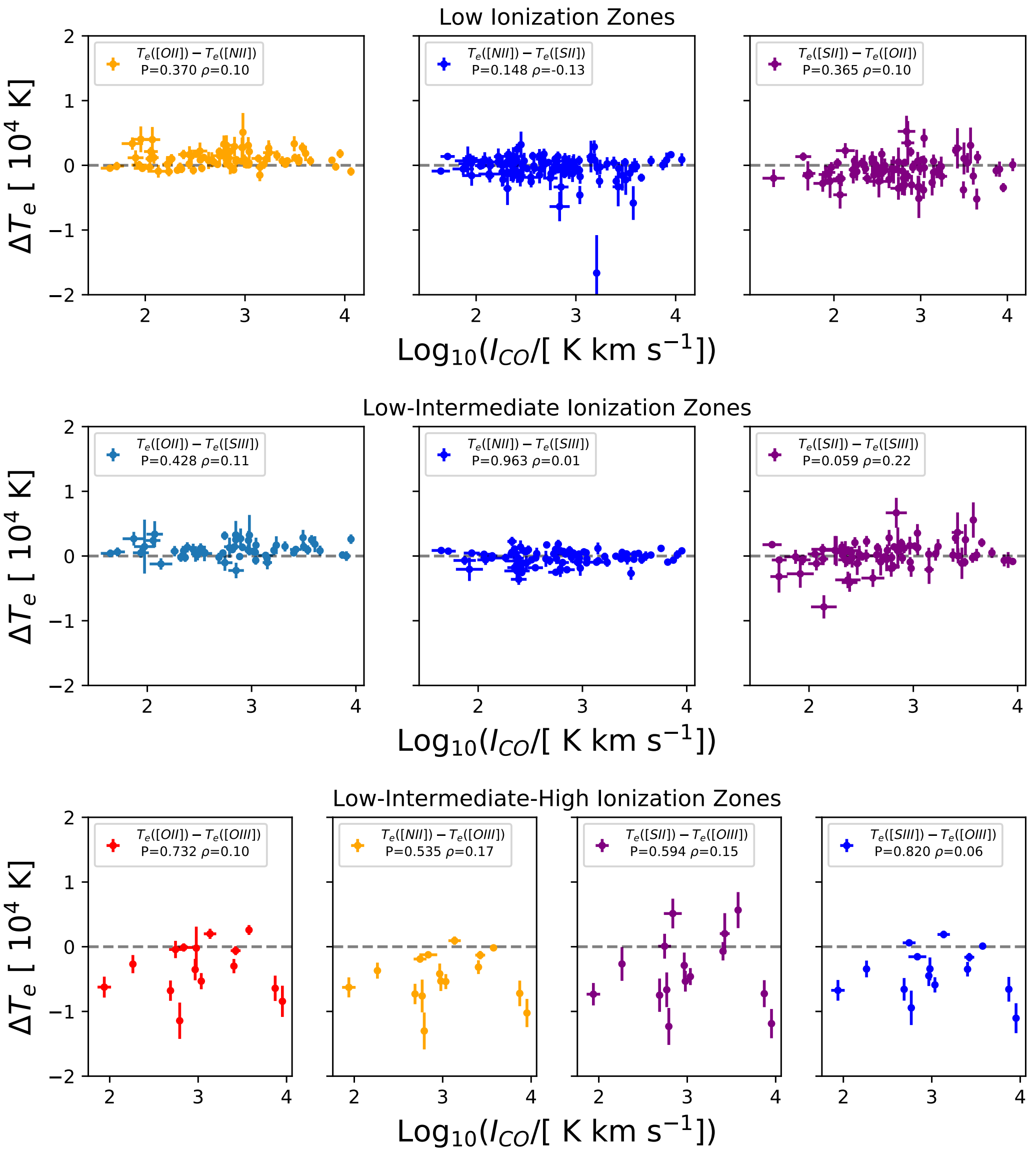

**Figure 2.35.** Electron temperature differences compared to the intensity of CO emission, $I_{\rm CO}$. The order of the panels follow those in Figure 2.30.

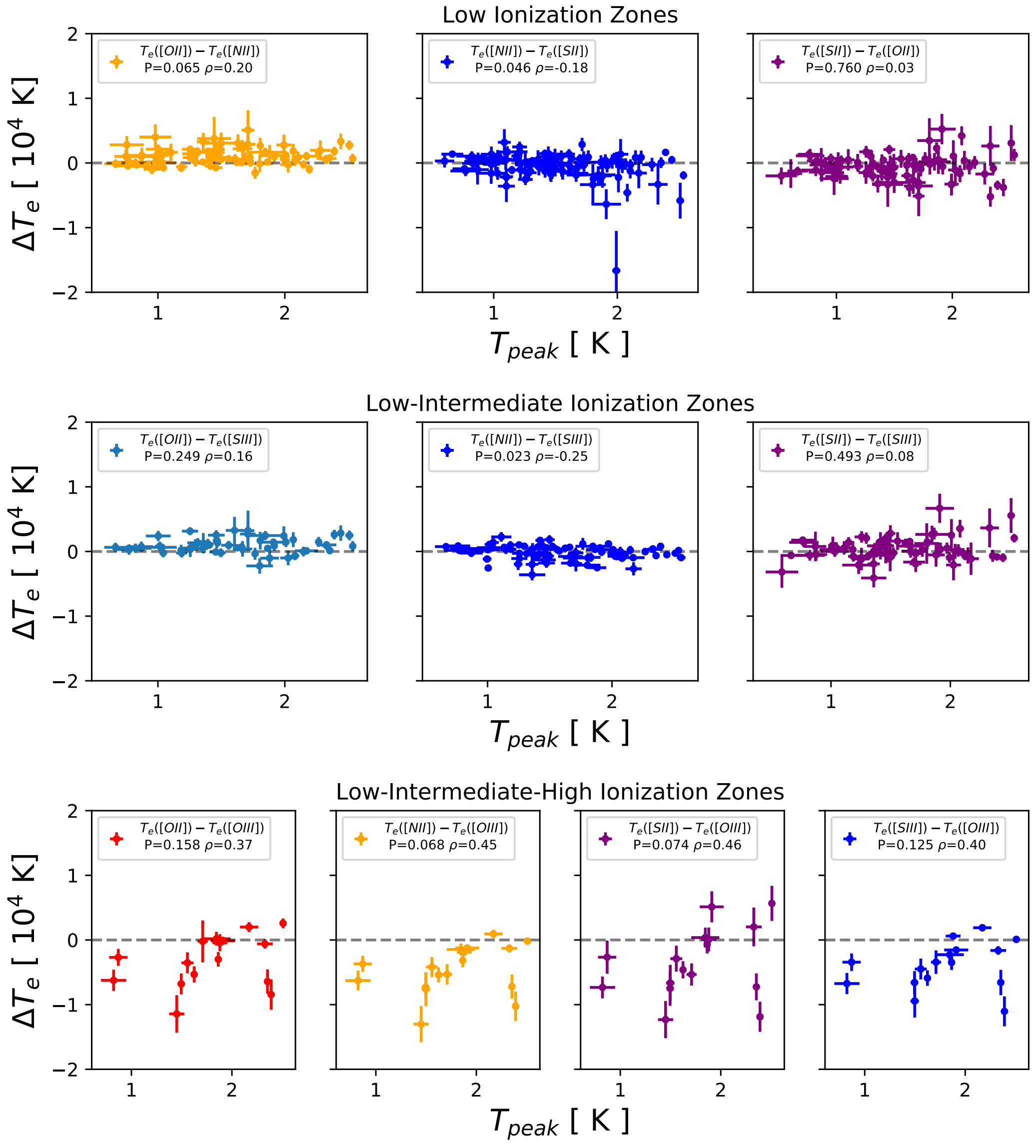

**Figure 2.36.** Electron temperature differences compared to the CO peak temperature, $T_{\rm peak}$. The order of the panels follow those in Figure 2.30.

**Table 2.9.** Measured and Derived Properties for H II Regions with two more auroral lines.

| ID | NGC5068_1 | NGC5068_2 | NGC5068_3 | NGC5068_4 | NGC5068_5 | NGC5068_6 |
|---|---|---|---|---|---|---|
| R.A.($^\circ$) | 199.714 | 199.719 | 199.702 | 199.7 | 199.696 | 199.714 |
| Dec.($^\circ$) | -21.027 | -21.016 | -21.012 | -21.013 | -21.014 | -21.015 |
| $E(B-V)$(Mag) | 0.24 | 0.19 | 0.25 | 0.19 | 0.41 | 0.34 |
| H$\beta^{(a)}$ | 54.2±0.1 | 70.7±0.4 | 140.3±0.6 | 1385.6±7.3 | 211.4±1.4 | 37.6±0.2 |
| [O III]$\lambda$4363 | - | - | - | 12.8±0.7 | - | - |
| [O III]$\lambda$5007 | 53.6±0.1 | 125.3±0.5 | 133.5±0.6 | 3239.9±15.0 | 415.7±1.8 | 35.6±0.1 |
| [O II]$\lambda$7320 | 0.8±0.1 | - | 2.4±0.8 | 35.7±2.2 | 3.9±0.8 | - |
| [O II]$\lambda$7331 | 0.8±0.1 | - | 2.6±0.8 | 31.1±2.2 | 3.9±0.8 | - |
| [O II]$\lambda$3727 | 79.0±0.5 | 128.0±1.4 | 515.4±2.6 | 3128.6±25.3 | 639.0±5.8 | 89.3±0.6 |
| [S II]$\lambda$4068 | 0.6±0.1 | 1.5±0.1 | 3.1±0.9 | 46.4±7.4 | 4.0±1.2 | 0.8±0.1 |
| [S II]$\lambda$4076 | 0.2±0.1 | 0.5±0.1 | 3.1±1.8 | 3.8±3.6 | 0.0±2.4 | 0.3±0.1 |
| [S III]$\lambda$6313 | 0.5±0.0 | 0.7±0.1 | 1.5±0.1 | 18.9±0.3 | 2.7±0.1 | 0.4±0.0 |
| [S II]$\lambda$6716 | 12.7±0.1 | 22.6±0.2 | 60.4±0.3 | 352.1±0.9 | 71.0±0.3 | 14.4±0.1 |
| [S II]$\lambda$6731 | 9.4±0.1 | 15.8±0.1 | 42.1±0.3 | 259.1±0.8 | 49.8±0.3 | 10.1±0.1 |
| [S III]$\lambda$9069 | 11.9±0.1 | 12.4±0.2 | 20.5±0.2 | 389.1±1.2 | 42.3±0.3 | 7.1±0.1 |
| [N II]$\lambda$5756 | 0.3±0.0 | 0.3±0.0 | 0.5±0.1 | 4.3±0.1 | 0.8±0.1 | 0.1±0.0 |

**Table 2.9.** Measured and Derived Properties for H II Regions with two more auroral lines.(Continued)

| | | | | | | |
|---|---|---|---|---|---|---|
| [N II]$\lambda$6548 | 10.2±0.0 | 9.1±0.1 | 20.3±0.1 | 152.5±0.3 | 25.2±0.1 | 6.2±0.0 |
| [N II]$\lambda$6584 | 30.1±0.1 | 26.9±0.2 | 59.7±0.3 | 449.8±1.0 | 74.1±0.3 | 18.3±0.1 |
| $n_{\mathrm{e}}(\mathrm{cm}^{-3})$ | 99 | 21 | 13 | 91 | 20 | 22 |
| [O III]/[O II] | 0.68±0.0 | 0.98±0.01 | 0.26±0.0 | 1.04±0.01 | 0.65±0.01 | 0.4±0.0 |
| [S III]/[S II] | 1.87±0.02 | 1.13±0.02 | 0.7±0.01 | 2.23±0.01 | 1.23±0.01 | 1.01±0.01 |
| $T_{\mathrm{e,[N\,II]}}$ (K) | 8179.0±291.0 | 8769.0±563.0 | 8122.0±489.0 | 8486.0±90.0 | 9056.0±458.0 | 7461.0±657.0 |
| $T_{\mathrm{e,[S\,II]}}$ (K) | 7580.0±768.0 | 10364.0±594.0 | 11467.0±3028.0 | 14318.0±2652.0 | 7704.0±2444.0 | 8661.0±1044.0 |
| $T_{\mathrm{e,[O\,II]}}$ (K) | 10941.0±1467.0 | - | 7999.0±1134.0 | 11243.0±700.0 | 8785.0±1009.0 | - |
| $T_{\mathrm{e,[S\,III]}}$ (K) | 8513.0±110.0 | 9528.0±421.0 | 10235.0±273.0 | 8755.0±52.0 | 9807.0±180.0 | 9249.0±365.0 |
| $T_{\mathrm{e,[O\,III]}}$ (K) | - | - | - | 8658.0±135.0 | - | - |

*Notes*: (a) Emission line strengths, and uncertainties, are reported in units of $10^{-16} \times$ ergs $\mathrm{s}^{-1}$ $\mathrm{cm}^{-2}$. Table 2.9 is published in its entirety in the machine-readable format. A portion is shown here for guidance regarding its form and content.

Chapter 2, in full, is a reformatted reprint of the material as it appears in Rickards Vaught, Ryan J.; Sandstrom, Karin M.; Belfiore, Francesco; Kreckel, Kathryn; Méndez-Delgado, José E.; Emsellem, Eric; Groves, Brent; Blanc Guillermo A.; Dale, Daniel A.; Egorov Oleg V; Glover, Simon C. O.; Grasha, Kathryn; Klessen, Ralf S.; Neumann, Justus; Williams Thomas G. "Investigating the Drivers of Electron Temperature Variations in H II Regions with Keck-KCWI and VLT-MUSE," The Astrophysical Journal, 966, 130, 2024. The dissertation author is the primary investigator and author of this material.

# Chapter 3

# Analysis of Oxygen, Sulfur, and Nitrogen Abundance Trends with Direct Abundances from H II Regions observed with Keck-KCWI and VLT-MUSE.

Abstract of Chapter 3.

The relative abundances of oxygen, sulfur, and nitrogen provide insight into the stellar and feedback processes that drive galaxy chemical evolution. Systematic variations in the electron temperature measured from different ions introduce uncertainty in their relative chemical abundances. Recent observations suggest that the auroral lines [N II]$\lambda$5756 and [S III]$\lambda$6312 are most accurate tracers of electron temperature in teh optical range. We present electron temperature measurements and direct abundances using new integral field spectroscopy measurements of [N II]$\lambda$5756 and [S III] $\lambda$6312 from H II regions observed with the Very Large Telescope Multi-Unit Spectroscopic Explorer and Keck Cosmic Web Imager alongside a compilation of literature H II regions. We observe that temperatures inferred from [S III]$\lambda$6312 are larger than the mean temperature, $T_0(\mathrm{O}^{2+})$, of the high-ionization zone calculated using $T_{\mathrm{e,[N\,II]}}$, which suggests [S III]$\lambda$6312 is affected by temperature fluctuations. Using sulfur and oxygen abundances derived using $T_0$, we observe strong correlations of S/O and N/O abundance ratios with metallicity traced by sulfur and nitrogen. We find that the N/O ratio increases with the

radiation field softness parameter and surrounding molecular gas velocity dispersion. This trend suggests that secondary nitrogen production and/or outflows are the source of the scatter in the N/O abundance. Finally, we show a disagreement between direct sulfur abundances and those from strong-line calibrations.

## 3.1 Introduction

Characterizing the 2D variation of a galaxy's metallicity is important to understanding the role of feedback, and other astrophysical processes, on the galaxy's chemical evolution. For example, negative radial metallicity gradients, as traced by the total gas-phase oxygen abundance (i.e. 12+log(O/H), Searle, 1971; Berg et al., 2015; Bresolin, 2019; Kreckel et al., 2019; Berg et al., 2020; Kreckel et al., 2020; Williams et al., 2022; Groves et al., 2023), are ubiquitous in nearby disk galaxies. Higher order variation around the gradient in disk galaxies are a measure of the recent injection and mixing of metals. Numerical studies have shown that the principal drivers of metal mixing are mechanisms connected to stellar feedback (Krumholz & Ting, 2018; Emerick et al., 2020; Spitoni et al., 2019; Mollá et al., 2019; Yates et al., 2021; Spitoni et al., 2023; Sharda et al., 2024).

A galaxy's gas-phase metallicity is traced by oxygen, nitrogen, and sulfur abundances, and can be inferred by observing their emission from the ionized gas located inside H II regions (e.g., Kennicutt & Garnett, 1996; Bresolin et al., 2012; Hernandez et al., 2013; Ho et al., 2017; Kreckel et al., 2019, 2020; van Loon et al., 2021; Grasha et al., 2022a). Although the magnitude of small-scale metallicity mixing (i.e. variations away from the gradient or with respect to a local median) are measurable in principle, the observational uncertainties associated with measurements of metallicities can interfere with characterizing the magnitude of metallicity variations (Kewley & Ellison, 2008). Moreover, these same uncertainties have led to conflicting results regarding the evolution of abundance ratios, N/O and S/O, with metallicity (e.g., Berg et al., 2020; Schaefer et al., 2020; Díaz & Zamora, 2022). A "direct" measurement of the metallicity requires a measurement of the observed gas volume's electron temperature, $T_\mathrm{e}$. One way to measure $T_\mathrm{e}$ is by using temperature sensitive auroral-to-nebular line ratios of collisionally excited lines (CEL; Peimbert, 1967; Osterbrock & Ferland, 2006; Peimbert et al., 2017).

Several physical processes compete in determining the ionization and temperature structure of H II regions. These include a radially decreasing intensity and hardening of the radiation field as well as a change in the ions which dominate gas cooling, and therefore the cooling efficiency (Stasińska, 1980; Garnett, 1992). Because of this, as shown in Figure 3.1, H II regions can be described using a low, intermediate and high-ionization zone (Garnett, 1992; Baldwin et al., 2000; Berg et al., 2015, 2021). The temperature of each ionisation zone are measured from auroral lines of their dominate ions, low$\rightarrow$ $\mathrm{S}^+$, $\mathrm{N}^+$ $\mathrm{O}^+$, intermediate$\rightarrow$ $\mathrm{S}^{2+}$, and high$\rightarrow$ $\mathrm{O}^{2+}$.

Because excitation to the auroral level require electrons of higher energy, auroral lines can be $>100$ times weaker than nebular lines (Kennicutt et al., 2003; Esteban et al., 2004; Berg et al., 2020; Rickards Vaught et al., 2024). In addition to being faint, auroral line based $T_\mathrm{e}$'s are subject to uncertainties arising from density inhmogeneities, shocks, and temperature fluctuations. Recent, deep, slit-spectroscopy and integral field spectrograph (IFU) observations of nearby H II regions have shown that temperatures obtained from the auroral lines [O II]$\lambda\lambda7320,7330$ and [S II]$\lambda\lambda4068,4076$ (i.e. $T_{\mathrm{e,[O\,II]}}$ and $T_{\mathrm{e,[S\,II]}}$) are biased high due to unresolved density inhomogeneities present within H II regions (Méndez-Delgado et al., 2023b; Rickards Vaught et al., 2024). Temperature fluctuations (due to presence of turbulence, density structure, and shocks associated with stellar winds), can cause auroral line temperatures to be biased higher than the average gas temperature (Peimbert, 1967; Peimbert & Costero, 1969). The average ion weighted temperature, $T_0(X^{i+})$ and the root-mean-square (RMS) of fluctuations $t^2(X^{i+})$ are used to characterize the degree of fluctuations, where $T_0(X^{i+})$, is given by,

$$T_0(X^{i+}) = \frac{\int T_\mathrm{e} n_\mathrm{e} n(X^{i+})\mathrm{dV}}{\int n_\mathrm{e} n(X^{i+})\mathrm{dV}}. \tag{3.1}$$

The RMS, $t^2(X^{i+})$, is related to the difference between $T_e$ and $T_0$ in the following way,

$$t^2(X^{i+}) = \frac{\int [T_{\rm e} - T_0(X^{i+})]^2 n_{\rm e} n(X^{i+}) {\rm dV}}{T_0(X^{i+})^2 \int n_{\rm e} n(X^{i+}) {\rm dV}}. \tag{3.2}$$

Méndez-Delgado et al. (2023a) suggested temperature fluctuations may only impact the high-ionization gas (i.e. $O^{2+}$) traced by [O III] and $T_{\rm e,[O\ III]}$. High values of temperature fluctuations can even be found low-metallicity regions (Esteban et al., 2002; Peimbert et al., 2012), even though one might expect the gas to have a larger fraction of the available gas at high enough temperature to excite the auroral lines (Yates et al., 2020; Rickards Vaught et al., 2024).

Another way to measure electron temperature is by using metal recombination lines (RL). RLs exhibit an almost linear sensitivity to temperature and will be less affected by temperature fluctuations (Peimbert, 1967; Osterbrock & Ferland, 2006; Peimbert et al., 2017). However, deriving $T_{\rm e}$ from RLs is difficult because they require deep, high signal-to-noise observations in order to be detected (Méndez-Delgado et al., 2023a). Since the work of Wyse (1942), Peimbert & Costero (1969), and Peimbert (1971), it commonly observed that the oxygen abundances derived using $T_{\rm e}$'s estimated from RLs are systematically more metal-rich than those using CELs. The ratio of the two abundances, $X^{i+}_{RL}/X^{i+}_{CEL}$ (or difference if using logarithmic units), is known as the abundance discrepancy factor (ADF). H II regions abundances typically exhibit ADFs between 1.5 and 3.0 (Esteban et al., 2014; Corradi et al., 2015; Peimbert et al., 2017; Méndez-Delgado et al., 2023a).

Unlike the direct method which is used to determine the abundance of a particular element, "strong line methods" are constructed assuming a proportionality between various strong CEL line ratios and metallicity. Strong-line calibrations are commonly calibrated to direct oxygen abundances from single/stacked galaxies, H II regions, or combination of (e.g. Bresolin, 2007; Pilyugin & Grebel, 2016; Curti et al., 2017; Nakajima et al., 2022). Other are constructed from photoionization models (e.g. Dopita et al., 2000; Kewley & Dopita, 2002). However, in addition to a large offsets ($\approx 0.7$ dex) between strong-line metallicities inferred by various calibrations (Kewley & Ellison, 2008), the same lines or set of lines can also exhibit sensitivity to other properties such as ionization parameter (see, Dopita et al., 2016), or can predict two different values of metallicity for a single value of a line ratio (see, Kobulnicky & Kewley, 2004; Pilyugin & Grebel, 2016). To bypass the uncertainties due to temperature fluctuations and CELs oxygen abundances, there are recent calibrations tied to sulfur direct abundances and oxygen recombination line abundances (Díaz & Zamora, 2022; Méndez-Delgado et al., 2023a). However, these calibrations have yet to be extensively compared to additional, independent, H II regions samples.

Due to the challenges in measuring RL temperatures and the inaccuracy of strong-line calibrations, it is important to determine reliable temperature prescriptions for direct abundances using CEL emission. Recent observations of auroral lines in nearby H II regions are finding that temperatures derived from the auroral lines [N II] and [S III] exhibit a robust relationship, but there is little understanding if these temperatures accurately reflect the gas temperature, or if they are impacted by fluctuations or other inhomogeneities (Berg et al., 2015, 2020; Zurita et al., 2021; Rogers et al., 2021; Méndez-Delgado et al., 2023a; Rickards Vaught et al., 2024).

Towards understanding how abundances derived using the auroral lines of [N II] and [S III] compare to abundances derived using $T_{\mathrm{e,[O\ II]}}$, $T_{\mathrm{e,[O\ III]}}$, and literature prescriptions from RLs, we derive oxygen abundances using $T_{\mathrm{e,[N\ II]}}$ and $T_{\mathrm{e,[S\ III]}}$ for a sample of new and literature H II regions. Using these temperatures, we also derive sulfur and nitrogen abundances and investigate their relative abundances with oxygen. Furthermore, we compare the abundances to strong-line calibrations determined from RLs of oxygen and sulfur nebular lines. We provide the details of the H II regions and sample constraints in Sections 3.2 and 3.2.1. We describe the calculation of direct abundances in Section 3.3. The results and discussion are presented in Sections 3.4 and 3.5.

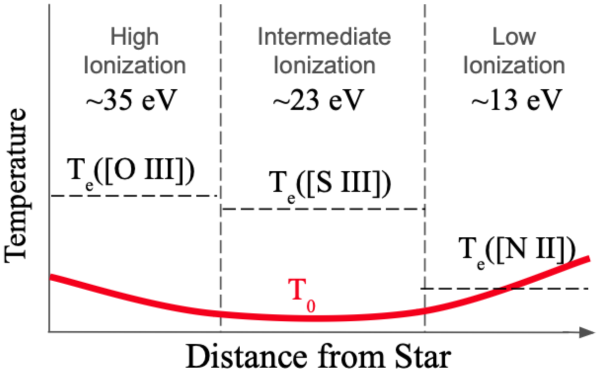

**Figure 3.1.** Diagram of the H II region three-ionization zone. For each zone, we show the typical ionization energy and electron temperatures that describe the zone. Furthermore, we show in red the temperature profile expected from photoionization models. The horizontal dashed black lines indicate the approximate temperature returned by aural-to-nebular lines relative to the "true" temperature profile. The x-axis is the distance from the ionizing star, and is not to scale.

## 3.2 Data

The sample of H II regions in this analysis are collected from Guseva et al. (2011), Zurita et al. (2021), and Rickards Vaught et al. (2024). These samples contain measurements of emission lines from auroral and nebular lines across the full optical wavelength range for H II regions across a wide range of metallicities.

The Guseva et al. (2011) is a sample includes 121 Very Large Telescope (VLT) FORS1 or UVES single-slit spectra of H II regions in 46 low-metallicity emission-line galaxies with auroral line detections. Of the spectra, 83 are archival. Guseva et al. (2011) present multiple observations of the same HII region in some cases. In those situations, we take the average of these measurements. In total, we obtain 85 H II regions from Guseva et al. (2011).

The sample from Zurita et al. (2021) is a compiled collection of emission-lines measured from single-slit observations for 2831 H II regions from the literature. The sample consists 51 nearby spiral galaxies, including the Milky Way. A subset totaling of 709 H II regions show significant auroral line emission. For the full list of references describing the original H II region measurements see Table A.1 in Zurita et al. (2021).

The Rickards Vaught et al. (2024) sample contains 421 H II regions from seven galaxies in the PHANGS-MUSE survey observed using both the VLT/Multi-Unit Spectroscopic Explorer (MUSE; Bacon et al., 2010; Emsellem et al., 2022) and the Keck Cosmic Web Imager (KCWI; Morrissey et al., 2018) integral field spectrographs (or IFU). These H II regions were were also observed as part of the PHANGS-ALMA and PHANGS-HST (Leroy et al., 2021a,b; Lee et al., 2022), and thus also have measurements of their molecular gas and their stellar populations. The spatial resolution of the optical observations is between $0.75''$ and $2.5''$. At the typical distances of PHANGS galaxies, $1''$ corresponds to approximately 100 pc spatial resolution.

We note that we are using observations from both IFUs and single-slit spectroscopy. Depending on the distance to the galaxy, IFUs can observe the full spatial extent of an H II regions, while single-slit spectroscopy will observe the central region of the H II region Kreckel et al. (2022). Because of this, the single-slit observations may have more contribution from high and intermediate-zone emission lines (e.g., [S III], [O III]) than low-ionization zone emission that originates from the outer edge of the H II region.

### 3.2.1 H II Region Constraints

In order to investigate abundances and temperatures derived from the auroral lines of [N II] and [S III], we select a sub-sample of high quality H II region measurements according to the following constraints.

First, based on our comparison between auroral lines S/N and the uncertainty on the final abundances, see Section 3.3.1, we exclude H II regions that lack significant, S/N $> 5$, detections of [N II]$\lambda$5756 and [S III]$\lambda$6312 emission. This constraint removes 56 of the 85 regions from the Guseva et al. (2011) sample, 2365 from the Zurita et al. (2021) sample, and 299 regions from the Rickards Vaught et al. (2024) sample.

Secondly, the H II regions identified in Rickards Vaught et al. (2024) are from nearby, 5 Mpc $<$ D $<$ 20 Mpc, IFU observations of galaxies, but the Guseva et al. (2011) and Zurita et al. (2021) contain regions from galaxies with distances between 1 Mpc $<$ D $<$ 100 Mpc, observed using slit spectroscopy. In order to mitigate any uncertainties arising from aperture effects and/or spatial resolution when comparing single-slit observations to IFU observations, we remove H II regions from both Guseva et al. (2011) and Zurita et al. (2021) with distances outside 5 Mpc $<$ D $<$ 20 Mpc. The removes 4 and 56 regions from Guseva et al. (2011) and Zurita et al. (2021).

Third, in order to compare the direct abundances to strong-line abundances, we require that all H II regions have significant, S/N $>$ 5, detections in H$\beta$, H$\alpha$, [O III]$\lambda\lambda$4959,5007, [O II]$\lambda$3727, [N II]$\lambda\lambda$6548,6584, [S III]$\lambda$9069, and [S II]$\lambda\lambda$6716,6731. This removes 10+1 regions from the Guseva et al. (2011) and Zurita et al. (2021) samples. The Rickards Vaught et al. (2024) sample, by design, is unaffected by this constraint. We note here that while the strong-line [S III]$\lambda$9532, has been measured for regions in the Zurita et al. (2021) sample, this line is not included in the Rickards Vaught et al. (2024) sample. This is due to the limited wavelength coverage of MUSE. For consistency we assume the fixed theoretical line ratio of [S III]$\lambda 9532/\lambda 9069 = 2.5$ (Froese Fischer et al., 2006) in calculations of all H II region properties. For 5 regions with both lines in the final Zurita et al. (2021) we find that their line ration exhibited deviations of $>$ 20% from theoretical. However, these regions do not appear as outliers in our analysis, so we choose to include them for completeness.

Next, using the emission from H$\beta$, H$\alpha$, [O III] and [N II] we construct Baldwin-Phillips-Terlevich (BPT, Baldwin et al., 1981) diagrams to determine which H II regions are consistent with photoionization by massive stars. We require the regions to fall below the empirical [O III]/H$\beta$ vs. [N II]/H$\alpha$ (Kauffmann et al., 2003) and the [O III]/H$\beta$ vs. [S II]/H$\alpha$ (Kewley et al., 2001) lines. The BPT diagram showing the location of each H II region is shown in Figure 3.2. Out of the sample, 3 (Guseva et al., 2011) and 1 (Zurita et al., 2021) H II regions are above the empirical and theoretical line cut-offs and are removed.

Finally, emission from low-ionization species [S II], [N II], and Balmer transitions originating from the diffuse ionized gas (DIG) surrounding H II regions can contaminate their emission (Belfiore et al., 2022). To minimize potential DIG contamination, we remove regions

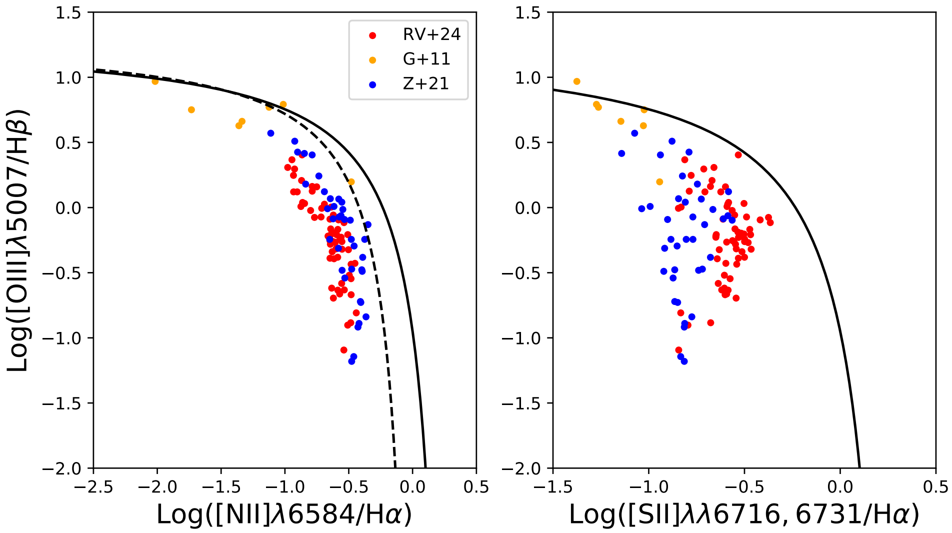

**Figure 3.2.** BPT diagrams showing [O III[/H$\beta$ vs. [N II[/H$\alpha$, in the left panel, and [O III[/H$\beta$ vs. [S II[/H$\alpha$ ratios, in the right panel, for the H II regions with significant auroral line detections and distances between 5 Mpc $<$ D $<$ 20 Mpc. Regions with emission line ratios consistent with photoionization by stars are expected to populate the parameter space below the theoretical (*solid-black,* Kewley et al., 2001) and empirical (*dashed-black*, Kauffmann et al., 2003) classification lines.

**Table 3.1.** Number of H II regions remaining after each applied constraint.

| Sample | $N_{\mathrm{Start}}$ | $N_{\mathrm{Auroral}}$ | $N_{\mathrm{D}}$ | $N_{\mathrm{Strong}}$ | $N_{\mathrm{BPT}}$ | $N_{\mathrm{Final}}$ |
|---|---|---|---|---|---|---|
| Guseva et al. (2011) | 85 | 21 | 17 | 7 | 4 | 4 |
| Zurita et al. (2021) | 2831 | 109 | 53 | 38 | 37 | 37 |
| Rickards Vaught et al. (2024) | 421 | 63 | 63 | 63 | 63 | 63 |

with [N II]/H$\alpha$ and [S II]/H$\alpha$ $< 0.5$. This constraint corresponds to model predictions of ratios for DIG ionized by escaped H II region photons (see, Belfiore et al., 2022). The full sample of H II regions pass this requirement.

The number of H II regions excluded by each step are summarized in Table 3.1. The final sample contains extinction corrected emission lines for 104 H II regions made up of 63 regions from Rickards Vaught et al. (2024), 4 regions from Guseva et al. (2011), and 37 regions from Zurita et al. (2021).

## 3.3 Direct and Calibrated Abundances

### 3.3.1 Direct Abundances using temperatures from [N II] and [S III] auroral lines

Abundances derived with direct knowledge of the electron temperature and density (i.e., direct abundances) represent a high confidence measure of the chemical abundance. The abundance of an ion relative to hydrogen is calculated using;

$$\frac{X^{i+}}{H^{+}} = \frac{I_{\lambda,i}}{I_{\mathrm{H}\beta}} \frac{j_{\mathrm{H}\beta}}{j_{\lambda,i}}, \tag{3.3}$$

where $j_{\lambda,i}$ and $I_{\lambda,i}$ are the emissivity and integrated intensity of the line. For the CELs, the emissivity, $j_{\lambda,i}$, exhibits exponential sensitivity to the adopted electron temperature, $T_{\mathrm{e}}$.

In the analysis presented in Rickards Vaught et al. (2024), the calculation of all physical values from emission lines were performed using PyNeb (Luridiana et al., 2015). For consistency, we re-derive the electron temperatures and densities for the Guseva et al. (2011) and Zurita et al. (2021) H II regions. Next, we derive direct oxygen, nitrogen and sulfur abundances for the full H II region sample using $T_{\mathrm{e,[N\ II]}}$ for $\mathrm{O^{+}/H^{+}}$, $\mathrm{N^{+}/H^{+}}$, $\mathrm{S^{+}/H^{+}}$, and $T_{\mathrm{e,[S\ III]}}$ for $\mathrm{O^{2+}/H^{+}}$, $\mathrm{S^{2+}/H^{+}}$.

In order to account for the unobserved ionization states of species $\mathrm{N^{2+}}$ or $\mathrm{S^{3+}}$, we correct the nitrogen and sulfur abundances using the ionization correction factors presented in Izotov et al. (2006). We note here that the results presented in this work are not sensitive to the choice of ICF. For sulfur there is likely very little $S^{3+}$ in the metal-rich H II regions (Berg et al., 2020; Díaz & Zamora, 2022). As a check on the assumed ICF for nitrogen, we calculated the nitrogen abundances using the assumption $\mathrm{N^{+}/O^{+}} \approx \mathrm{N/O}$ (Berg et al., 2020), and with $\mathrm{N^{+}/H^{+}} \times$ ICF, we find the choice between these two methods does not have any bearing on the results presented from this analysis.

To obtain uncertainties for each H II region abundance, we generate a large sample of abundance measurements by Monte Carlo (MC) sampling the uncertainty of the requisite emission lines. We use the $1\sigma$ width of the resulting abundance distribution as the error. In Figure 3.3 we show the S/N of the total oxygen abundances versus the S/N of both the [N II]$\lambda$5756 and [S III]$\lambda$6312 auroral lines and color coded by the logarithmic error of total gas-phase oxygen abundance. We observe that the S/N of the derived oxygen abundances is correlated with the S/N of the [N II]$\lambda$5756. Only for [N II]$\lambda$5756 with S/N $>$ 5 do the derived oxygen abundances exhibit S/N $>$ 3. For the comparison between oxygen abundances and [S III]$\lambda$6312, there is a much weaker correlation between the significance of the oxygen abundances and the S/N of the measured [S III]$\lambda$6312. As a result of these comparisons, we ensure high S/N abundances by constraining the sample of H II regions to those with S/N $>$ 5 in their auroral lines. The median uncertainty on the derived gas-phase oxygen, sulfur, and nitrogen abundances is on the order of and less than 0.1 dex.

One exception to the above threshold are for abundances shown in Figure 3.4. The temperatures returned from the auroral lines, [O II]$\lambda\lambda$7320, 7330 and [O III]$\lambda$4363, can be biased due to electron density inhomogeneities and shocks (Binette et al., 2012; Méndez-Delgado et al., 2023b; Rickards Vaught et al., 2024). To test how abundances derived using $T_{\mathrm{e,[N\,II]}}$ and $T_{\mathrm{e,[S\,III]}}$, differ from abundances derived using temperatures with known biases we also derive the "classical" direct oxygen abundances for the final sample if both the [O II]$\lambda\lambda$7320, 7330 and [O III]$\lambda$4363 auroral lines are measured with S/N $>$ 3. Using a higher threshold throws out most of the regions with measurements from [O III]$\lambda$4363. These abundances, while used to show difference between abundances derived using $T_{\mathrm{e,[N\,II]}}$, $T_{\mathrm{e,[O\,II]}}$, $T_{\mathrm{e,[O\,III]}}$, and $T_{\mathrm{e,[S\,III]}}$ are not used in the analysis of abundance trends.

### 3.3.2 Direct Abundances Using $T_e$-$T_e$ Relationships

Electron density inhomogeneities and other sources of temperature fluctuations are known to impact the auroral lines from [O II], [S II], and [O III]. To investigate the potential improvement of using the temperature prescription discussed in Section 3.3.1, we derive direct abundances using CEL and RL [O III] temperature estimated from $T_e$-$T_e$ relationships. The

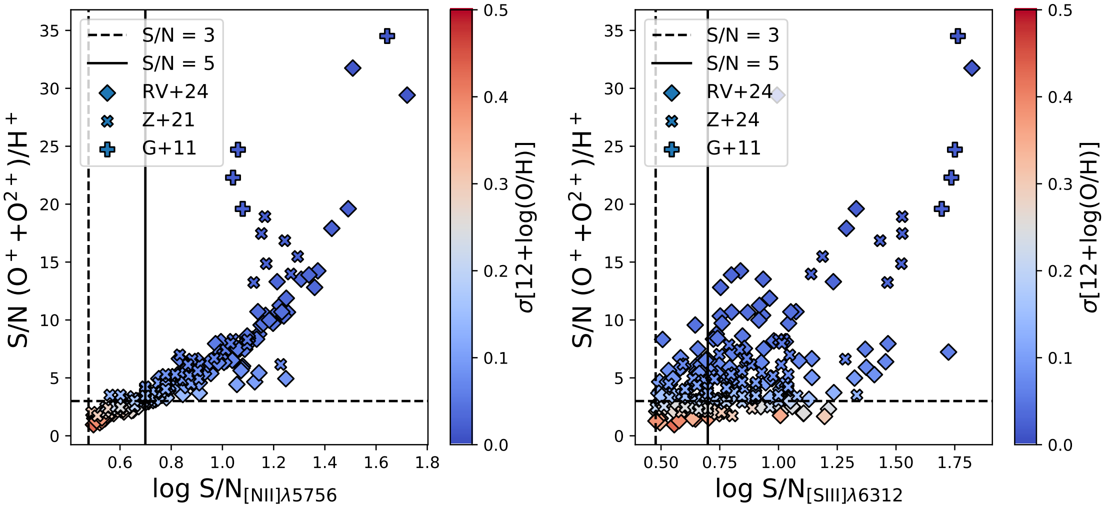

**Figure 3.3.** Comparisons of the S/N of the oxygen abundances to the S/N of the [N II]$\lambda$5756 and [S III]$\lambda$6312 auroral lines. We include vertical and horizontal lines indicating S/N of 5 in the auroral line (black-solid) and S/N of 3 in both the abundance and aural lines (black-dashed). The points are color coded by the total oxygen abundance logarithmic error in units of dex.

specific $T_e$-$T_e$ prescriptions we use are described below.

### CHAOS $T_{e,[N\,II]}$–$T_{e,[O\,III]}$ relationship

The auroral lines [N II] and [S III] are easier to detect than [S III] in high metallicity H II regions, as shown by the detection statistics presented in Rickards Vaught et al. (2024). To estimate the value of $T_{e,[O\,III]}$, we use the values of $T_{e,[N\,II]}$ combined with the Rogers et al. (2021), hereafter CHAOS, $T_e - T_e$ relations for $T_{e,[N\,II]}$–$T_{e,[O\,III]}$, Equation 3.4.

$$T_{e,[O\,III]} = 1.3 \times T_{e,[N\,II]} - 2000 \text{ [K]}. \tag{3.4}$$

The H II regions from Rickards Vaught et al. (2024) come with $T_{e,[O\,III]}$'s calculated using 3$\sigma$ [O III]$\lambda$4363 upper limits. We check that the $T_{e,[O\,III]}$'s calculated using Equation 3.4 are consistent with those calculated from the [O III]$\lambda$4363 upper limits. We find that Equation 3.4 temperatures are well below those determined from the upper limits. This indicates that we are not not artificially lowering the H II region abundances when calculating oxygen abundances using the calculated $T_{\mathrm{e,[O\,III]}}$. We label these $T_{\mathrm{e,[O\,III]}}$ and $T_{\mathrm{e,[N\,II]}}$ derived total gas-phase oxygen abundances, 12+log(O/H) [$T_{\mathrm{e,[N\,II]}}$, $T_{\mathrm{e,[O\,III],CHAOS}}$].

### MD23 $T_{\mathrm{e,[N\,II]}}$-$T_0(\mathrm{O}^{2+})$ relationship

In the presence of temperature fluctuations (i.e. $t^2 > 0$) the $T_{\mathrm{e}}$ measured from the CELs of an ion, $X^{i+}$, is expected to be hotter than the its average gas temperature (or ion-weighted temperature) $T_0(X^{i+})$. According to the argument that the auroral-to-nebular line ratio of [N II] is unaffected by temperature and density fluctuations (Méndez-Delgado et al., 2023a), the [N II] auroral-to-nebular line temperature assumed to be equal to $T_0(\mathrm{N}^+)$. By choosing to derive oxygen abundances using $T_{\mathrm{e,[N\,II]}}$ and $T_{\mathrm{e,[S\,III]}}$ we are assuming that $T_{\mathrm{e,[S\,III]}}$ traces $T_0(\mathrm{O}^{2+})$. To test this assumption, we calculate $T_0(\mathrm{O}^{2+})$ using the relationship between $T_{\mathrm{e,[N\,II]}}$ and $T_0(\mathrm{O}^{2+})$, see Equation 3.5, from Méndez-Delgado et al. (2023a),

$$T_0(\mathrm{O}^{2+}) = 1.17 \times T_{\mathrm{e,[N\,II]}} - 3340\ [\mathrm{K}], \tag{3.5}$$

We derive total gas-phase oxygen abundances, 12+log(O/H) [$T_{\mathrm{e,[N\,II]}}$, $T_0(\mathrm{O}^{2+})$], using the ion-weighted doubly-ionized oxygen temperature and the auroral-to-nebular line ratio of [N II] temperature for the derivation of $\mathrm{O}^{2+}/\mathrm{H}^+$ and $\mathrm{O}^+/\mathrm{H}^+$.

The uncertainties for 12+log(O/H) [$T_{\mathrm{e,[N\,II]}}$, $T_{\mathrm{e,[O\,III],CHAOS}}$] and 12+log(O/H) [$T_{\mathrm{e,[N\,II]}}$, $T_0(\mathrm{O}^{2+})$] are estimated using the same Monte Carlo procedure described in Section 3.3.1. We summarize in Table 3.2 the temperature priorities and set of emission lines used for the derived abundances.

**Table 3.2.** The set of temperature priorities, and emission lines, used in calculation of direct abundances.

| Label | $T_{\mathrm{e}}(X^{+})$ [K] | $T_{\mathrm{e}}(X^{2+})$ [K] | Emission Lines |
|---|---|---|---|
| 12+log(O/H) [$T_{\mathrm{e,[N\,II]}}$, $T_{\mathrm{e,[S\,III]}}$] | $T_{\mathrm{e,[N\,II]}}$ | $T_{\mathrm{e,[S\,III]}}$ | [O III]$\lambda\lambda$4959, 5007, [O II]$\lambda$3728 |
| 12+log(S/H) [$T_{\mathrm{e,[N\,II]}}$, $T_{\mathrm{e,[S\,III]}}$] | $T_{\mathrm{e,[N\,II]}}$ | $T_{\mathrm{e,[S\,III]}}$ | [S III]$\lambda$9069, [S II]$\lambda\lambda$6716,6731 |
| 12+log(N/H) | $T_{\mathrm{e,[N\,II]}}$ | - | [N II]$\lambda\lambda$6548,6584 |
| 12+log(O/H) [CHAOS] | $T_{\mathrm{e,[N\,II]}}$ | $T_{\mathrm{e,[O\,III]}}$=1.3$\times T_{\mathrm{e,[N\,II]}}$-2000 | [O III]$\lambda\lambda$4959, 5007, [O II]$\lambda$3728 |
| 12+log(O/H) [MD23] | $T_{\mathrm{e,[N\,II]}}$ | $T_0(\mathrm{O}^{2+})$=1.17$\times T_{\mathrm{e,[N\,II]}}$-3340 | [O III]$\lambda\lambda$4959, 5007, [O II]$\lambda$3728 |
| 12+log(S/H) [MD23] | $T_{\mathrm{e,[N\,II]}}$ | $T_0(\mathrm{O}^{2+})$ | [S III]$\lambda$9069, [S II]$\lambda\lambda$6716,6731 |

## 3.4 Results

### 3.4.1 Oxygen abundances: Assessing gas temperature with $T_{\mathrm{e,[S\ III]}}$ vs $T_{\mathrm{e,[O\ III]}}$

We derived direct oxygen abundances under the assumption that the temperatures $T_{\mathrm{e,[N\ II]}}$ and $T_{\mathrm{e,[S\ III]}}$ describe the ion weighted gas temperatures $T_0(\mathrm{N}^+)$ and $T_0(\mathrm{O}^{2+})$.

In Figure 3.4 we present a comparison of the oxygen abundances in the above manner to abundances derived using $T_{\mathrm{e,[O\ II]}}$ and $T_{\mathrm{e,[O\ III]}}$. We find that while a number of the H II regions exhibit similar total gas-phase oxygen abundances regardless of the temperature prescription used, a significant number of regions lie above the 1-1 line. Not including the region with a 0.8 dex difference, the average systematic offset between the abundances is 0.2 dex, with 12+log(O/H) [$T_{\mathrm{e,[N\ II]}}$, $T_{\mathrm{e,[S\ III]}}$] estimating higher metallicities.

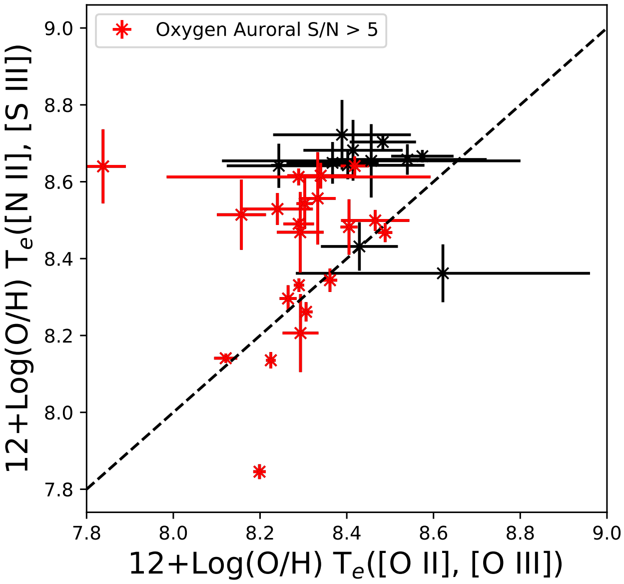

**Figure 3.4.** Comparison of oxygen abundances derived from $T_{\mathrm{e,[N\ II]}}$-$T_{\mathrm{e,[S\ III]}}$ and abundances derived from $T_{\mathrm{e,[O\ II]}}$-$T_{\mathrm{e,[O\ III]}}$. The dashed black line indicates a 1-1 relationship.

### 3.4.2 Comparing the different $T_\mathrm{e}$ prescriptions and their effect on abundances

We used $T_\mathrm{e}$–$T_\mathrm{e}$ relationships from Rogers et al. (2021) and Méndez-Delgado et al. (2023a) to derive oxygen abundances as Section 3.3 and 3.3.2.

In the left panel of Figure 3.5 we show comparisons of temperatures from the auroral-to-nebular lines of [S III], the calculated ion-weighted doubly-ionized oxygen gas temperature (MD23 Méndez-Delgado et al., 2023a), and the calculated [O III] auroral-to-nebular line temperature (CHAOS Rogers et al., 2021). It is clear that the average oxygen gas temperature is cooler than both of the auroral-to-nebular line temperatures of N II and S III. The average difference between MD23 temperatures is much larger, $0.20 \pm 0.1\ \times 10^4$ [K], than the average difference between CHAOS temperatures. This indicates that the auroral-to-nebular line temperature of [S III] is at most equal to, or marginally cooler than calculated [O III] auroral-to-nebular line temperature. These results suggest that in-spite of the tight $T_{\mathrm{e,[N\,II]}}$–$T_{\mathrm{e,[S\,III]}}$ relationship and agreement with photoionization models (Berg et al., 2015, 2020; Zurita et al., 2021; Rogers et al., 2021; Rickards Vaught et al., 2024), $T_{\mathrm{e,[S\,III]}}$ does not trace $T_0(\mathrm{O}^{2+})$.

In the middle panel of 3.5, we show the comparison between the derived $\mathrm{O}^{2+}/\mathrm{H}^{+}$ with choice of temperature. We find that the assumed temperature can have significant effect on the the resulting $\mathrm{O}^{2+}/\mathrm{H}^{+}$ abundances. The choice of the derived [S III] temperature over the CHAOS [O III] temperature will lead to $\sim 0.08$ dex higher $\mathrm{O}^{2+}/\mathrm{H}^{+}$ abundances. A significantly larger discrepancy arises when choosing oxygen ion-weighted temperature over the derived [S III] temperature. Here the abundances are $\sim 0.7$ dex more metal-rich than those using the [S III] temperature.

In the right panel of Figure 3.5, we show how these choices effect the total gas-phase oxygen abundances. We find that the difference between 12+log(O/H) [$T_{\mathrm{e,[N\,II]}}$, $T_{\mathrm{e,[S\,III]}}$] and 12+log(O/H) [$T_{\mathrm{e,[N\,II]}}$, $T_{\mathrm{e,[O\,III],CHAOS}}$] is almost negligible compared to the differences between abundances derived using the oxygen ion-weighted temperature and [S III] temperature. The

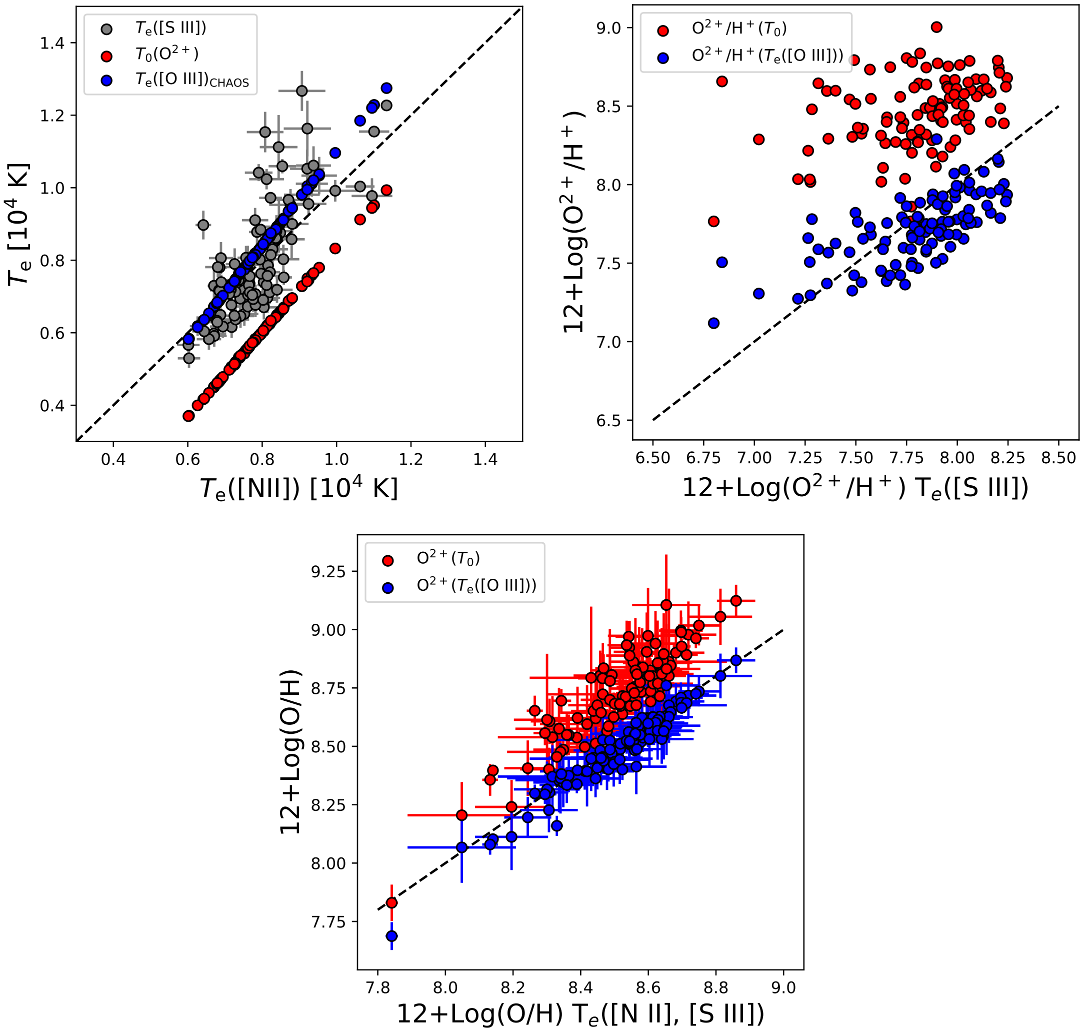

**Figure 3.5.** Comparison of $T_{e,[S\ III]}$, $T_0(O^{2+})$ and $T_{e,[O\ III],CHAOS}$ and abundances. In the top-left panel we show a comparison between the measured $T_{e,[S\ III]}$ and the calculated $T_0(O^{2+})$ and $T_{e,[O\ III],CHAOS}$. In the top-right panel, we show how the choice of temperature effects the $O^{2+}/H^+$ abundances. In the nottom panel, we the resulting total gas-phase oxygen abundances based on the choice of temperature. To aid the eye, we include the 1-1 line in each panel.

difference between 12+log(O/H) these two abundances is $0.24 \pm 0.7$ dex, which corresponds to a discrepancy factor of ADF$\sim$ 1.7.

The observation that 12+log(O/H)[$T_{e,[N\ II]}$, $T_{e,[S\ III]}$] $<$ 12+log(O/H) [$T_{e,[N\ II]}$, $T_{e,[S\ III]}$], or $T_{e,[S\ III]} > T_0(O^{2+})$, suggests that temperatures measured from the [S III]$\lambda$6312 auroral line may be biased due to the presence of temperature fluctuations. A product of many H II region photoionization models are predictions for their internal temperature profile (e.g., Jamet et al., 2005; Copetti, 2006a; Rodríguez & García-Rojas, 2010). Qualitatively, see Figure 3.1, these model profiles show that the initial or inner edge temperature, presumably traced by $T_0$($O^{2+}$), will decrease towards cooler values described by, $T_0$($S^{2+}$). Approaching the edge of the region, the temperature profile will increase to an a outer edge temperature, $T_0$($N^+$). This view of the temperature profile is supported by multiple studies of the Orion Nebula (see review O'Dell, 2001), and resolved LMC/SMC H II regions (Jin et al., 2023), which generally report increased temperature near the ionization front.

The above qualitative description of the temperature profile implies that $T_0$($O^{2+}$) is hotter than $T_0$($S^{2+}$). But, our temperature comparisons show that $T_{\mathrm{e,[S\,III]}}$ is hotter $T_0$($O^{2+}$). This suggests that $T_{\mathrm{e,[S\,III]}}$ is hotter than $T_0$($S^{2+}$) and therefore is affected by temperature fluctuations. We can calculate a lower limit on the magnitude of sulfur temperature fluctuations, $t^2$($S^{2+}$) by assuming that $T_0$($S^{2+}$)$\approx$$T_0$($O^{2+}$). Using Equation 3.2, we find that the temperature fluctuations for sulfur are on average, $t^2$($S^{2+}$)$= 0.11^{+0.19}_{-0.06}$ . However, without a direct measure of $T_0$($S^{2+}$), the degree which temperature fluctuations may effect sulfur is uncertain.

To further illuminate the degree the sulfur auroral-to-nebular line ratio may be affected by temperature fluctuations, we construct a field of temperatures with Gaussian injected temperature perturbations of magnitude 1000 K. We then calculated the auroral-to-nebular line rations for [O III] and [S III]. The [O III] auroral-line weighted average temperature return larger values of the temperature than the true average, $t^2 \sim 0.05$. The magnitude of these fluctuations are on order of what is observed (Méndez-Delgado et al., 2023b). Performing the same calculation and using the same temperature field, we find [S III] temperatures to have $t^2 \sim 0.03$. While this simple model ignores several complexities, it further shows that [S III] aural-to-nebular line temperatures can be impacted by temperature fluctuations.

Due to the potential bias in temperature determined from the auroral-to-nebular lines ratio of [S III], we continue our analysis of trends between oxygen, sulfur, and nitrogen abundances but only using abundances derived using $T_{\mathrm{e,[N\,II]}}$ and $T_0$($O^{2+}$). We show in Figure **??** the effect on sulfur abundances using this choice. The $T_0$($O^{2+}$)-based sulfur abundances are $\sim 0.3$ dex more metal-rich, and indicates that temperature fluctuations are introducing a large bias in sulfur abundance determinations.

### 3.4.3 Comparison of Oxygen, Sulfur, and Nitrogen Abundances

In Figure 3.6, we present comparisons between the total oxygen, sulfur, and nitrogen abundances. To gauge the significance and correlation for each comparison we calculate the Pearson correlation coefficient (i.e. p-value), as well as the Spearman Rank Correlation Coefficient, $\rho$, calculated via bootstrapping using `pymccorrelation` (Curran, 2014; Privon et al., 2020; Harris et al., 2020; Virtanen et al., 2020). A correlation is judged to be statistically significant if it exhibits p-value $< 10^{-3}$ or, as reported in the figures, a log(p-value) $< -3$.

We find that the nitrogen, sulfur, and oxygen abundances exhibit significant correlations between each other. Of the observed correlations, the nitrogen and sulfur abundances exhibit the strongest correlation, $\rho = 0.90$ and log(p-value)$<< -3$, the high slope suggests that the nitrogen yield increases faster than sulfur. The sulfur and oxygen abundances exhibit the second highest Spearman rank coefficient, $\rho = 0.77$, with accompanying log(p-value)$<< -3$. The average scatter around this trend line, $\Delta = -0.033 \pm 0.15$, is smaller than the nitrogen–sulfur scatter of $\Delta = -0.022 \pm 0.28$. The weakest correlation, and largest scatter, is between oxygen and nitrogen abundances. Discussed in further detail in Section 3.4.4, the scatter at high metallicities between oxygen and nitrogen is sensitive to time dependent secondary channel of nitrogen synthesis (Garnett, 1990; Henry et al., 2006; Nicholls et al., 2020; Berg et al., 2020) or outflows (Berg et al., 2019). Additionally, we find do scatter dependence with the ionization parameter traced by [O III]/[O II].

The correlations for each abundance comparison are described by the following best orthogonal distance regression (ODR, Virtanen et al., 2020) fit to the data, and where $z(\mathrm{O/H})$ = 12+log(O/H) and $z(\mathrm{S/H})$ = 12+log(S/H).

$$12 + \log(\mathrm{S/H}) = (1.16 \pm 0.07) \times \mathrm{z(O/H)} + (-2.95 \pm 0.6), \tag{3.6}$$

and

$$12+\log(\mathrm{N/H}) = (2.68\pm0.2)\times \mathrm{z(O/H)}+(-15.93\pm1.8), \tag{3.7}$$

$$12+\log(\mathrm{N/H}) = (2.28\pm0.1)\times \mathrm{z(S/H)}+(-8.83\pm0.9). \tag{3.8}$$

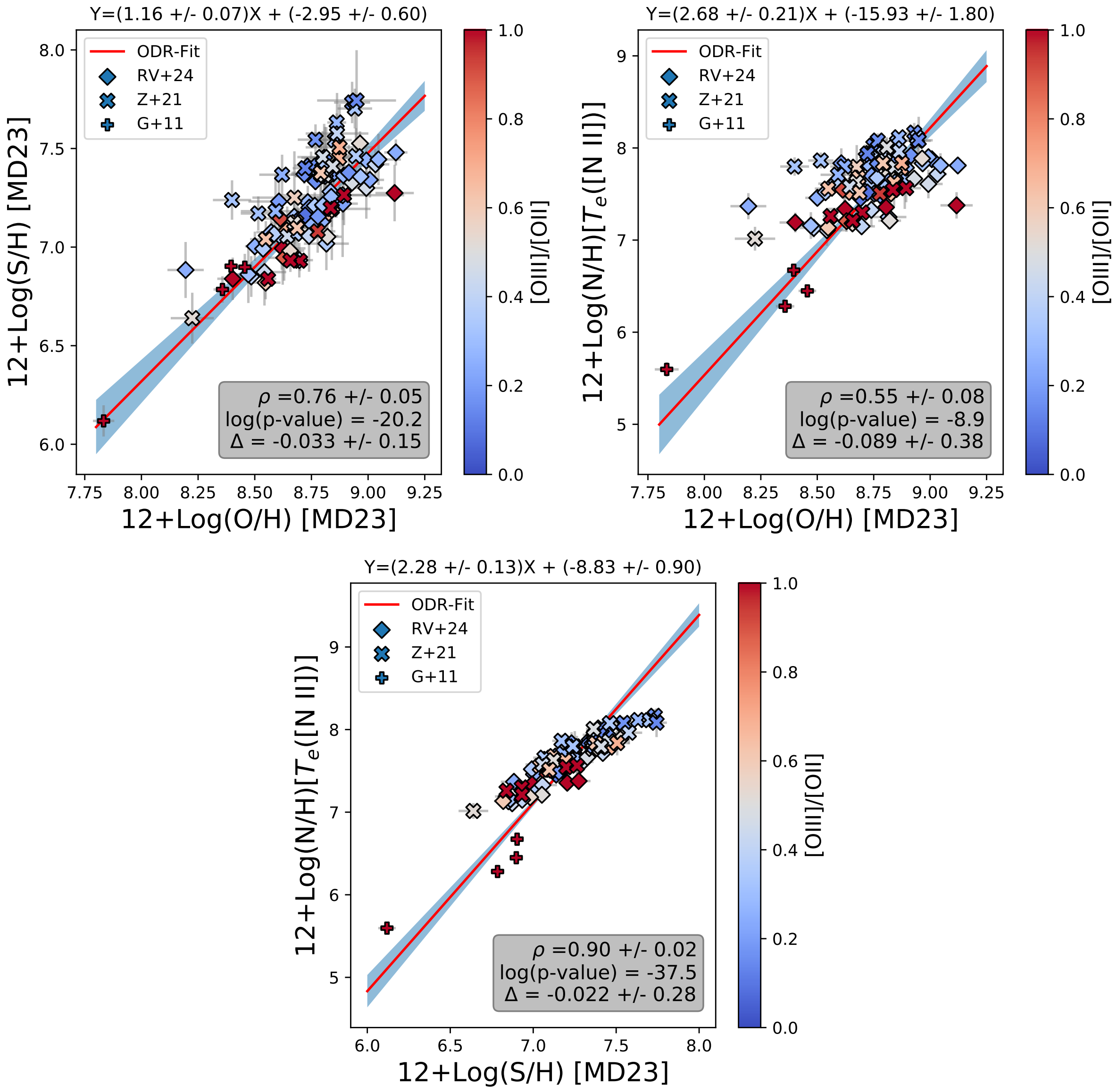

**Figure 3.6.** Top-Left panel: Direct total gas-phase sulfur abundances vs. the total gas-phase oxygen abundances. Top-Right panel: Direct total gas-phase nitrogen abundances vs. the total gas-phase oxygen abundances. Bottom panel: Direct total gas-phase nitrogen abundances vs. the total gas-phase sulfur abundances. Both sulfur and nitrogen abundances show a strong, positive, correlation with the oxygen abundance.

### 3.4.4 Abundance Ratios

We now discuss observed trends with metallicity between the abundance ratios of oxygen, nitrogen, and sulfur.

**Sulfur to Oxygen**

Oxygen and sulfur are $\alpha$ elements (Woosley & Weaver, 1995). If there are no other secondary channels, then the yields of the $\alpha$ elements are expected to be in a constant ratio. In Figure 3.7, we show the histogram the log sulfur-to-oxygen ratio, log(S/O). We find the 50th percentile and variance-weighted mean of the collected log(S/O) measurements to be $<$log(S/O)$>= -1.55^{+0.2}_{-0.1}$ and $<$log(S/O)$>_w= -1.50^{+0.16}_{-0.15}$ respectively. Within the uncertainty, both averages agree with the Solar log(S/O) value $= -1.57$ (Asplund et al., 2009). Within the literature, there is variation on reported log(S/O) values; $-1.56\pm0.10$ (Berg et al., 2013), $-1.34\pm0.15$ (Berg et al., 2020), $-1.42\pm0.17$ (Rogers et al., 2021) and even lower, log(S/O)$=$ $-1.89$, have been measured from infrared emission observed in star-forming galaxies and active galactic nuclei (Pérez-Díaz et al., 2024).

A possible reason for the variation in S/O may be due to different temperature assumptions. For example, if instead we continued the choice to use $T_{\mathrm{e,[S\ III]}}$ in our direct abundances, then the average log(S/O) we would measure is log(S/O)$= -1.60$. Another possible source of variation in the ported S/O may be to due aperture affects. Discussed earlier in Section 3.2, due to single-slit observations bias towards high ionization emission within the central portion of the H II regions. Observations of this type will observe less [S II] ([O II]) emission which will lead to an overestimate of the contribution of [S III]([O III]) to the total nebular emission. When we separate our sample into IFU versus single-slit observations, we measure log(S/O)$= -1.63 \pm 0.10$ using IFU observations and log(S/O)$= -1.53 \pm 0.13$ using single-slit spectrograph data.

In Berg et al. (2020), the authors suggest that the variation of log(S/O) is due to over/under estimations of the ratio that are introduced by a sensitivity to ionization that is not corrected by the sulfur ICF. However, this uncertainty is present only in high ionization H II regions with oxygen abundance ratios $O^+/O < 0.5$. According to oxygen abundances using temperatures from auroral-to-nebular line ratios of [N II] and [S III], only 6 of the 104 H II regions used in this analysis have ratios lower than this threshold. This number increase to 58 when using oxygen abundances derived from $T_0(O^{2+})$, though we expected the threshold to different for these abundances. Given the six regions that have the potential to be biased, relative to the total sample size, as well as the good agreement with the solar value, we do not suspect this effect to be significantly affecting the measured log(S/O) averages.

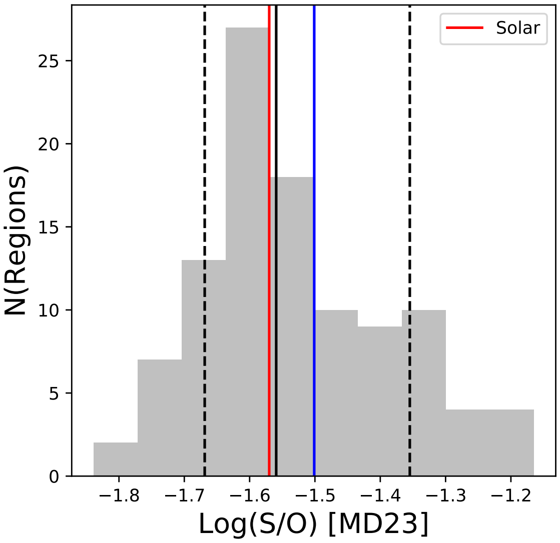

**Figure 3.7.** Histogram of the measured log(S/O). The black-solid and blue-solid indicate the average and variance weighted average log(S/O). The black-dashed show the 16th and 85th percentile of the distribution, centered around the mean. We also overlay a vertical red-solid line that indicates the solar value ($\log(S/O)_\odot$=-1.57, Asplund et al., 2009).

Next, shown in Figure 3.8, we compare log(S/O) to the total oxygen and nitrogen abundances. We find that log(S/O) is strongly correlated with the total gas-phase nitrogen abundance. We also observe that log(S/O) and oxygen abundances are not correlated. The nitrogen abundance exhibits a strong correlation with log(S/O) with Spearman rank coefficient, $\rho = 0.73$ and log(p-value)$<< -3$. The 4 outliers, particularly apparent in the log(S/O) vs. 12+log(N/H) panel, are high ionization H II regions that may possibly have sulfur abundances that are affected by uncertainties uncorrected by the ICF (Berg et al., 2020). Although the inclusion of these points does not significantly change the statistics of the correlation, we do not include them in the fit. If these outlier regions are real, they may hint at an overall non-linear behavior over the full N/H range and more regions would be needed to parameterize such behavior.

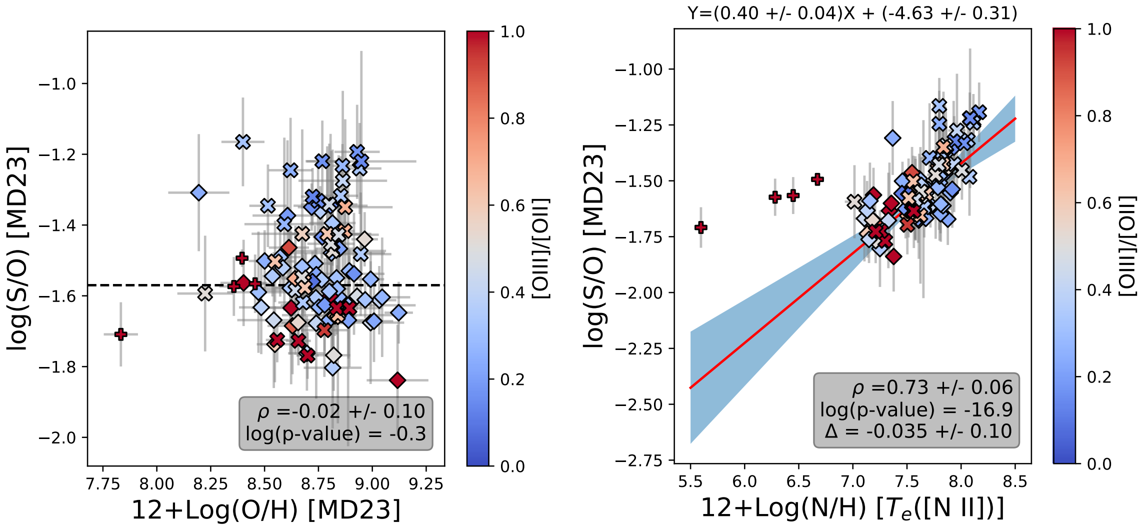

**Figure 3.8.** The log(S/O) abundance ratio compared to the total gas-phase abundances of oxygen and nitrogen. The color bar and marker symbols are the same as described in Figure 3.6.

To the best of our knowledge, this may be the first reported correlation between log(S/O) and 12+log(N/H). The correlation between log(S/O) and 12+log(N/H) is described by the following best-fit line,

$$\log(\mathrm{S/O}) = (0.40 \pm 0.04) \times \mathrm{z(N/H)} + (-4.63 \pm 0.3), \tag{3.9}$$

where $z(\mathrm{N/H})$ is equal to 12+log(N/H). We discuss in Section 3.5.2 possible mechanisms for the observed S/O variation and trend with metallicity traced by N/H.

### Nitrogen to Oxygen

Due to the metallicity dependence of secondary nitrogen synthesis, it has long been understood that abundance ratio of nitrogen and oxygen will vary with metallicity (Vila-Costas & Edmunds, 1993; van Zee & Haynes, 2006; Berg et al., 2012, 2020). We show in Figure 3.9 the comparison between log(N/O) to total gas-phase oxygen and sulfur abundances. As observed in previous studies (e.g Berg et al., 2020), we find large variations, $\sim 0.2$ dex, in the values of log(N/O) at high metallicity. A large number of the H II regions lie below the N/O-O/H trend line (Nicholls et al., 2017). However, this trend is sensitive to the assumption on the efficiencies between primary and secondary nitrogen production, and challenges in measuring nitrogen abundances for metal-poor stars (Nicholls et al., 2017).

A potential cause of the N/O scatter is due to effects from differential outflows (Vincenzo et al., 2016; Berg et al., 2019). Bursts of star-formation will cause periods of enhanced feedback. During these periods, nitrogen will still be locked inside older generations of stars, while oxygen is quickly produced and released. This oxygen is then preferentially lost to outflows well before the N enrichment occurs. After each successive burst of star-formation, N/O will decrease, followed later by an increase in N/O during periods of in-active star-formation. However, as pointed out by (Berg et al., 2020), the timescale of nitrogen release is on the order of 100's of Myr, while typical H II region lifetimes are on the order of 10's of Myr, thus nitrogen release may not have had enough time to occur. However, this may issue may be mitigated by nitrogen released from Wolf-Rayet (WR) stars. WR stars undergo a nitrogen rich phase in their evolution. WR also exhibit stellar winds that increases with increasing metallicity. If WR stars are polluting their surrounding ISM with nitrogen, then this may also explain the correlation between N/O and S/H that is shown in the right panel of Figure 3.9 and which was also observed in (Berg et al., 2020).

Another potential scenario was put forth by Berg et al. (2020), who noted that H II regions in their N/O-O/H diagram were grouped together by host galaxy. Berg et al. (2020) argue that the scatter is caused by the different time evolution of N/O for individual galaxy's based on their individual star-formation history. For example, a galaxy that has undergone an early burst of star-formation will quickly build up its metallicity while, due to the time-delay of nitrogen, keeping its N/O ratio low. For a galaxy which has undergone a late-burst of star-formation, it's metallicity and N/O will slowly increase during the quiescent time proceeding the late-burst of star-formation. If we color-code our sample regions by galaxy, we do see clustering of points according to galaxy, particularly NGC 5068 and NGC 1385, other galaxies have too few regions to make a proper assessment of clustering.

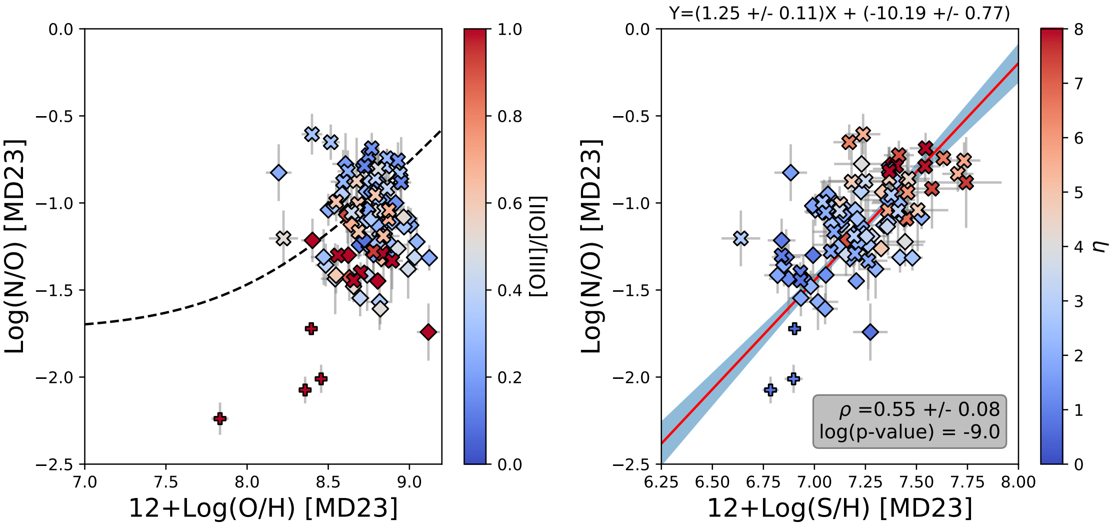

**Figure 3.9.** Comparisons between log(N/O) between total gas-phase oxygen and sulfur abundances. The color bar and marker symbols are the same as described in Figure 3.6. We overlay in the (left panel) the the empirical stellar N/O–O/H trend (Nicholls et al., 2017).

### Comparison of deviations in N/O with hardness of ionizing spectrum, and velocity dispersion of molecular gas

One measure of an aging stellar population is the hardness/softness of its ionizing spectrum (Chisholm et al., 2019; Berg et al., 2020). A harder spectrum will have characteristically steeper slopes in the ultraviolet. Older stellar populations will exhibit softer ionizing spectra compared to young or mixed-age populations, due to the heavily weighted presence of young stars. As a tracer of the age of the H II region's stellar populations we calculate the "softness" parameter ($\eta$ =([O II]/[O III])/([S II]/[S III]), Vilchez & Pagel, 1988). $\eta$ is a measure of the hardness of the stellar ionizing spectrum and is defined in such a way that lower values $\eta$ correspond to a harder ionizing spectrum (Pérez-Montero et al., 2023).

We show in left-panel Figure 3.10 the comparison between log(N/O) and radiation softness parameter. We find that the N/O ratios is strongly correlated with softness of the H II region ionizing spectrum. The statistics of the correlation is $\rho = 0.42$ and log(p-value)=-4.9. This results indicates that high N/O is associated with a softer UV spectra typically expected for an older stellar populations. This supports that that the N/O scatter is due to secondary nitrogen production.

A potential tracer of stellar feedback is the velocity dispersion of the molecular gas in the vicinity of an H II region (see, Watkins et al., 2023; Rickards Vaught et al., 2024). To investigate if feedback is introducing the scatter in N/O-O/H, we show in the right panel of Figure 3.10 the comparison between log(N/O) and the velocity dispersion of molecular gas as traced by CO. Because the Rickards Vaught et al. (2024) H II region sample is the only one that has contains measurements of log$\sigma_{\rm v,CO}$, this comparison is limited to 56 regions. Despite this, the bootstrapped statistics, $\rho = 0.50 \pm 0.08$, and log(p-value)$\ll -3$, indicate that log$\sigma(v,\mathrm{CO})$ is correlated with scatter of N/O. This indicates that outflows may also be preferentially removing oxygen and increasing N/O.

While we note that these correlations do not provide clear distinction on the dominant cause of N/O scatter at high metallicity, they do stress the importance of obtaining co-spatial observations of the different gas phases in the ISM.

### A trend between S/O-N/O

Motivated by the sulfur and nitrogen to oxygen ration trends with metallicity, we investigate whether the sufur-to-oxygen (S/O) and nitrogen-to-oxygen (N/O) ratios correlated with each other. Shown in Figure 3.11, we find a very strong positive correlation between S/O-N/O.

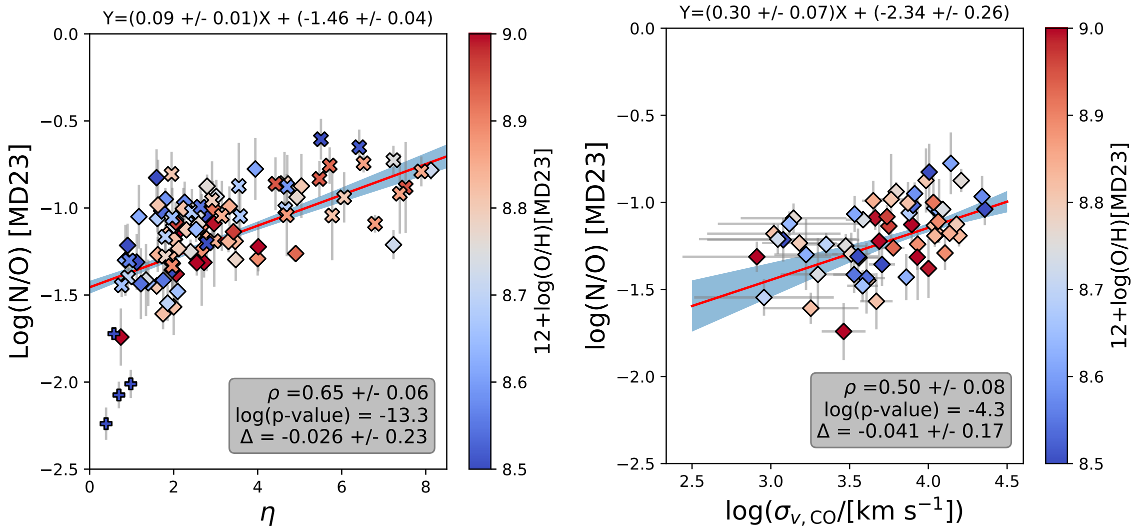

**Figure 3.10.** Log(N/O) comparisons between radiation softness and molecular gas velocity dispersion. The marker symbols are the same as those described in Figure 3.6. The markers are color coded by the softness parameter.

The best fit ODR line is described by the following expression;

$$\log(\mathrm{N/O}) = (1.79 \pm 0.1)\log(\mathrm{S/O}) + (1.65 \pm 0.2). \tag{3.10}$$

Figure 3.11 also makes clear that these two ratios exhibit a correlation with the radiation softness of the regions ionizing spectrum. We find that regions with soft ionizing spectra have higher values of both S/O and N/O. For lower values of S/O and N/O, the ionizing spectrum is harder. The four Guseva et al. (2011) regions are clear outliers, and it is unclear what may be driving their ratios away from the trend. Perhaps these regions, hosted with extreme emission line galaxies, have recently undergone a burst of star formation and have lost their oxygen to outflows. The effect of this would be a reduced N/O ratio. The trend in S/O and N/O is particularly surprising since S and N form through different synthesis channels. The increase of both ratios may be pointing towards a stellar nucleosyntheis or chemical evolution connection between S and N, and with an efficiency that may be tied to increasing metallicity.

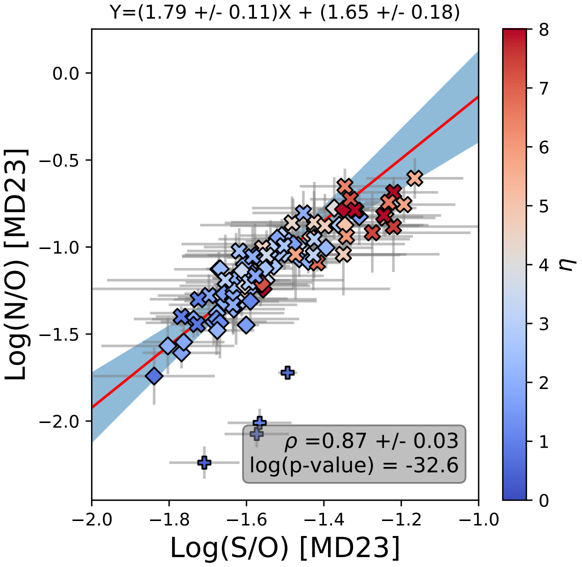

**Figure 3.11.** Trend between nitrogen and sulfur oxygen ratios. Each data point is color-coded by the value of its radiation softness parameter $\eta$. The red line is the best-fit linear regression line that is described by the expression on the top of the panel. The blue shaded region indicates the $\pm 3\sigma$ fit uncertainty.

### 3.4.5 Comparison of direct sulfur abundances to strong-line calibrations

Oxygen abundances have widely been considered the optimal tracer of ISM metallicity. However, the strong-lines of [S III] and [S II] have properties that make these nebular lines a suitable tracer of metallicity. The strong-line ratio $S_{23}$ =([S II]+[S III])/H$\beta$ (Vilchez & Esteban, 1996) is equivalent to the $R_{23}$ ratio of oxygen (Pagel et al., 1979), but with notable advantages. While the $R_{23}$ ratio is double valued, with a turnover at solar metallicities (Pagel et al., 1980), the $S_{23}$ remains single-valued beyond solar metallicities. The energies between the ionic transitions that make up $S_{23}$ also make this ratio observable in super solar metallicity gas, where near-infrared fine-structure emission lines become the dominant emission from oxygen. In Díaz & Zamora (2022), for a mixture of H II regions and compact galaxies, derived sulfur abundances using the temperature from [S III] auroral-to-nebular line ratio for both single and doubly-ionized sulfur abundances. From the abundances, the authors constructed a strong-line sulfur metallicity calibration that is dependent on the strong-line ratio $S_{23}$ (Vilchez & Esteban, 1996).

The calibration is described by the following equation,

$$12 + \log(\mathrm{S/H}) = 6.636 + 2.202 \times \mathrm{R} + 1.060 \times \mathrm{R}^2, \tag{3.11}$$

where $R$=log($S_{23}$). Although Equation 3.11 is valid over a large range of sulfur abundances, 5.0 $<$ 12+log(S/H) $<$ 8.0, The calibrating sample may introduce as of yet unknown uncertainties for lower sulfur abundances. This is because the calibrating sample for sulfur abundances, 12+log(S/H) $<$ 5.8, are from compact galaxies as opposed to H II regions which make up the high abundance calibrating sample.

In Figure 3.12, we show the comparison between sulfur abundances estimated using $S_{23}$ to our direct method sulfur abundances. We find these abundances are not correlated, with average offset equal to $0.3 \pm 0.3$ dex. The scatter around this trend is similar to the magnitude of scatter between direct and strong-line oxygen abundances that are shown in Appendix A Figures 3.13 3.14, and 3.15. This disagreement with our direct abundances suggests that the $S_{23}$ is not tracing the sulfur abundance under the presence temperature fluctuations.

# 3.5 Discussion

## 3.5.1 Is $T_{\mathrm{e,[S\ III]}}$ Affected by Temperature Fluctuations?

We found that oxygen abundances calculated using ion-weighted doubly ionized oxygen temperature (i.e. $T_0(\mathrm{O}^{2+})$; Méndez-Delgado et al., 2023a), do not agree with direct abundances that use the nitrogen and sulfur auroral-to-nebular line temperatures. As discussed in Section 3.4.2, we found that the [S III] electron temperature, $T_{\mathrm{e,[S\ III]}}$, is greater than ion-weighted doubly ionized oxygen temperature. Because photoionization models of H II region temperature profiles suggest that the ion weighted gas temperature of doubly ionized sulfur, $T_0(\mathrm{S}^{2+})$, is less than $T_0(\mathrm{O}^{2+})$, we determined that the temperature from inferred from [S III]$\lambda$6312 is subject to biases due to temperature fluctuations.

We calculated a lower limit on the magnitude of the temperature fluctuations by assuming

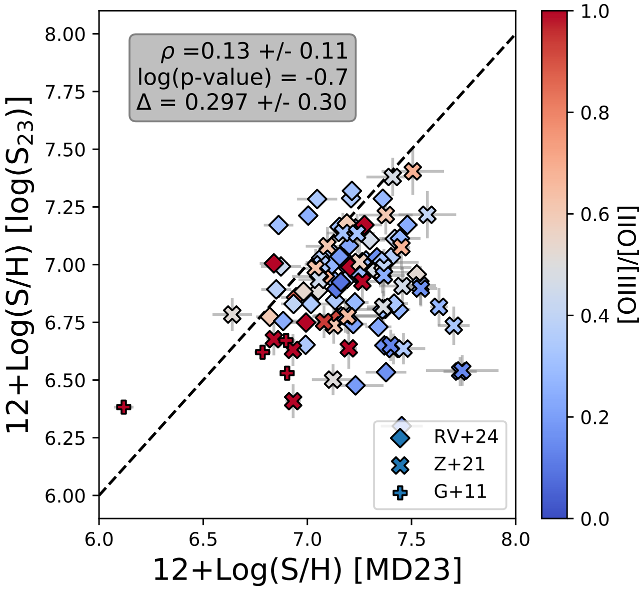

**Figure 3.12.** Total gas-phase sulfur abundances against 12+log(S/H) predicted from log($S_{23}$) (Díaz & Zamora, 2022). Each point is color-coded by the value of the ionization parameter as traced by the [O III]/[O II] ratio. We overlay the empirical relation between the parameters reported in Díaz & Zamora (2022). Additionally, in the upper-left corner, we include the p-value and the measured average percentage offset, Percent Δ.

the scenario that $T_0(\mathrm{S}^{2+})\approx T_0(\mathrm{O}^{2+})$. We found that the temperature fluctuations for $\mathrm{S}^{2+}$ are on average, $t^2(\mathrm{S}^{2+}) = 0.11^{+0.19}_{-0.06}$. This magnitude of fluctuations is on the high end for what has been observed between oxygen RL and CEL temperatures ($t^2(\mathrm{S}^{2+})\sim 0.05$ Binette et al., 2012; Peña-Guerrero et al., 2012; Méndez-Delgado et al., 2023a) and would likely require compounding effects from several mechanisms to produce such a degree of fluctuations (see Copetti, 2006b). If instead we assume that the magnitude of temperature fluctuations is similar for sulfur and oxygen (i.e. $t^2(\mathrm{S}^{2+}) \approx t^2(\mathrm{O}^{2+})$), than our measured $t^2(\mathrm{S}^{2+}) = 0.11$ would imply that $T_0(\mathrm{S}^{2+})$ would have to be greater than $T_0(\mathrm{O}^{2+})$. This comparison $T_0(\mathrm{S}^{2+})$ between and $T_0(\mathrm{O}^{2+})$ is qualitatively not supported by photoionization models(Jamet et al., 2005; Copetti, 2006a; Rodríguez & García-Rojas, 2010). A robust and quantitative determination of sulfur temperature fluctuations requires direct observations of $T_0(\mathrm{S}^{2+})$.

There exist extremely limited number of studies that provide a measure of $T_0(\mathrm{S}^{2+})$. One way to measure $T_0(\mathrm{S}^{2+})$ is using fine-structure CELs (e.g., [S III]$\lambda 18\ \mu$m). The temperature sensitivity of fine-structure line emissivities are comparable to the temperature dependence of RLs (Chen et al., 2023), making their derived temperatures insensitive to fluctuations. However, the critical densities of fine-structure lines are lower than optical CELs, making them strongly sensitive to density and density inhomogeneities. In Stasińska et al. (2013), the authors measure both [S III] fine-structure and optical auroral line emission for the giant H II region H1013. They found that the [S III]$\lambda$18 $\mu$m/[S III]$\lambda$9068 emission line ratio returned a temperature anywhere between 1000 K and 5000 K greater than the temperature implied by the [S III]$\lambda$6312/[S III]$\lambda$9068 ratio. This measurement suggests the potential for $T_0(S^{2+})$ to be quite high, and would favor $t^2(S^{2+}) \lesssim t^2(O^{2+})$.

Despite this, there is debate as to whether or not fine-structure temperatures are tracing the same low-density gas as those of optical auroral lines or RLs. In Zhang et al. (2004); Chen et al. (2023) these authors measured [O III] fine-structure and auroral line emission for planetary nebulae and the galaxy Markarian 71. Similar to the findings of Stasińska et al. (2013), Zhang et al. (2004) found that the fine-structure emission diagnostic returned a higher value of electron temperature than the auroral line diagnostic. Contrary to this observation, Chen et al. (2023) found in Markarian 71 that the fine-structure temperatures of [O III] agreed with the auroral-to-nebular line temperature but both were higher than the RL temperature. This varying hierarchy could be the result of diagnostics tracing different density gas within the H II regions (Zhang et al., 2007), further complicating our understanding of how different temperature diagnostics impact metallicities.

The above uncertainties on $T_0(S^{2+})$ and the expected level $t^2(S^{2+})$ stress the importance of alternative measurements of $T_{e,[S\ III]}$ via RL and fine-structure emission, as well as a better understanding of density inhomogeneities with the ISM.

### 3.5.2 Variation of S/O with Metallicity

Based on the results of Section 3.4.1, we investigated trends between sulfur and oxygen using abundances derived from [N II] temperatures and the ion-weighted doubly ionized oxygen gas temperature (MD23). With these abundances we found that the S/O ratio showed a variation that is correlated with metallicity traced by nitrogen.

There has been debate as to whether or not a relationship between sulfur-to-oxygen ratio and metallicity exists (Diaz et al., 1991; Vermeij & van der Hulst, 2002; Berg et al., 2020; Rogers et al., 2021; Díaz & Zamora, 2022). When significant trends are found, the sulfur-to-oxygen ratio has been observed to either decrease or increase with increasing metallicity (Díaz & Zamora, 2022).

One reason we may be seeing the sulfur-to-oxygen correlation with metallicity traced by nitrogen, and not oxygen, is that, as shown in Figure 3.6, nitrogen and sulfur abundances are themselves highly correlated with each other. Currently, there are several mechanisms that are have been considered as potential causes for variation of S/O including; variations in the initial mass function (Díaz & Zamora, 2022; Goswami et al., 2024), an overabundance of sulfur yields, relative to oxygen, produced in type Ia supernovae (Iwamoto et al., 1999), pair-instability supernovae (Goswami et al., 2024), sulfur depletion onto dust grains (Hily-Blant et al., 2022). However, the variation may very well be related to observational uncertainties in regards to constraining oxygen and sulfur abundances using CELs (Tan & Parker, 2024; Pérez-Díaz et al., 2024), particularly if [S III] temperatures are affected by temperature fluctuations. On this last point, we have shown that S/O variations are present even when using temperatures that are presumably not affected by temperature fluctuations.

### 3.5.3 Exploring Drivers of Scatter in N/O-O/H

As found in previous observations of the N/O-O/H trend (Nicholls et al., 2017; Berg et al., 2020; Skillman et al., 2020; Rogers et al., 2021), and shown in Figure 3.9, we observed increased scatter in the N/O ratio at high metallicity. The source of scatter in N/O, like sulfur-to-oxygen, is currently debated. A popular explanation for the source of scatter is the delayed release of secondary nitrogen (Garnett, 1990; Henry et al., 2006), and/or preferential loss of oxygen due to differential outflows from bursts of star-formation (Vincenzo et al., 2016; Berg et al., 2019).

Berg et al. (2020) suggest that the scatter is connected to the combined star-formation history of the observed galaxies. To investigate whether or not outflows or delayed-nitrogen are the source of scatter , we compared the N/O ratio to softness parameter $\eta$ (i.e. age) and velocity dispersion of molecular gas (feedback), as traced by ALMA observations of CO (Leroy et al., 2021b) and calculated in Rickards Vaught et al. (2024). We found that the N/O ratio strongly correlated with both of these parameters.

The correlation with $\eta$ suggests the N/O scatter is due to delayed nitrogen pollution by an ageing stellar population (Chisholm et al., 2019). With respect to the scatter in N/O for for high metallicities, a study by Skillman et al. (2020) observed that H II regions with carbon and oxygen ratios closest to solar values also lie on the lower bounds of their N/O-O/H trend. Though they acknowledge this may be an observational bias, they speculated that the stars in these regions are inefficient at releasing nitrogen into the ISM at the young ages (suggested by the high surface brightness of their H II regions that exhibit carbon emission). However, the long timescale of secondary nitrogen production, $\sim$ 100 Myrs, is longer than typical timescales of H II regions, $\sim$ 10 Myrs (Berg et al., 2020). While this concern may be abated by a succession of nitrogen production during multi-generational episodes star-formation (Coziol et al., 1999), another solution is nitrogen pollution due to the enhancement Wolf-Rayet winds at high-metallicity (Crowther & Hadfield, 2006; Berg et al., 2020). These winds, which are expected to increase with metallicity, can quickly inject metals, such as nitrogen, into their surrounding ISM. Alternatively, we may be under-estimating the oxygen abundance in high metallicity regions.

On the other hand, the scatter in the N/O ratio may be due to feedback processes preferentially blowing out oxygen relative to nitrogen. Our observations of enhanced molecular gas velocity dispersion may be tracing the effects of stellar feedback (Watkins et al., 2023; Rickards Vaught et al., 2024) in the process of reducing the H II regions of their oxygen yield. Similar to abundance gradients, Berg et al. (2020) and Rogers et al. (2021) have shown that galaxies exhibit radial gradients in N/O ratios. Given that radial abundance profiles are often attributed to a galaxy's history metal transport via outflows/inflows, the observation that the N/O ratio follows similar radially decreasing profiles suggests a similar connection to outflows/inflows.

Although we are unable to decisively provide the direct cause of N/O scatter, the results here are compelling and stress the need for multi-wavelength and multi-gas phase observations of H II regions.

## 3.6 Conclusions

We presented direct abundances of oxygen, sulfur, and nitrogen from new and literature observations of H II regions.

- We found that $T_{\mathrm{e,[S\ III]}}$ does not accurately trace the average gas temperature of the high-ionization zone, and we described evidence that the sulfur temperature derived from the [S III]$\lambda$6312 auroral line is affected by the presence of temperature fluctuations.
- We derived sulfur, oxygen, and nitrogen abundances using temperatures from the auroral-to-nebular ratio of [N II], and the ion-weighted doubly ionized oxygen gas temperature, derived from [N II] using the Méndez-Delgado et al. (2023b) relationship.
- From these abundances we found that the S/N and N/O ratios vary with metallicity. Motivated by these trends, we also found a strong, positive, correlation between the S/N and N/O ratios.
- We investigated potential drivers of the scatter in the N/O-O/H relationship. We found that the scatter is correlated with the radiation softness parameter, $\eta$, and velocity dispersion of surrounding molecular gas as traced by CO emission. These correlations provide evidence for both delayed nitrogen pollution by aging stellar populations or outflows as the sources of N/O scatter at high metallicity.
- We find that direct sulfur abundances, calculated using the ion-weighted doubly ionized

oxygen gas temperature, are not in agreement with the Díaz & Zamora (2022) strong-line sulfur calibration.

We investigated abundance trends using direct abundances of oxygen, sulfur and nitrogen for a sample of new and literature H II regions observed with IFU and single-slit spectroscopy. Our comparisons of temperatures measured directly from auroral-to-nebular line ratios, and inferred from temperature relationships, reveal a new complexity in our understanding of the temperature structure of H II regions. We demonstrated that abundance ratios vary with metallicity and are perturbed by feedback as well as by properties of the stellar population. From his study, we conclude that multi-ion abundances are needed to fully characterize the variation of galaxy metallicities. Future observations of spatially resolved H II regions and advanced modeling are needed to understand how different temperature diagnostics trace the different phases of ISM gas.

## 3.7 Comparison of Direct Abundances to Strong-Line Calibrations

### 3.7.1 Calibrated Abundances

When auroral lines are unobserved there exist an exhaustive number of calibrated or "strong-line" prescriptions that infer the abundance using strong nebular emission lines sensitive to the gas-phase metallicity. The common strong-line calibrations consist of the following emission line ratios:

$$R_2 = \text{[O II]}\lambda\lambda 3726, 3728/\text{H}\beta,$$

$$R_3 = \text{[O III]}\lambda 5007/\text{H}\beta,^{1}$$

$$N_2 = \text{[N II]}\lambda 6584/\text{H}\alpha,^{2}$$

---

[1] $R_3 = \text{[O III]}\lambda\lambda 4959, 5007/\text{H}\beta$ for S-calibration.

[2] $N_2 = \text{[N II]}\lambda\lambda 6548, 6584/\text{H}\beta$ for S-calibration.

$$S_2 = \text{[S II]}\lambda\lambda 6716,6731/\text{H}\alpha,^{3}$$

$$S_3 = \text{[S III]}\lambda 9069/\text{H}\alpha.$$

The source of metallicities used to calibrate strong-line metallicity relationships widely vary between different studies. For example, one can combine metallicities of metal-rich H II regions with metallicities from metal-poor single, or stacked, galaxies (e.g., Nakajima et al., 2022). Others studies may rely solely on metallicities derived from integrated single, or stacked, galaxies (e.g., Curti et al., 2017). A smaller number of calibrations exist which have been derived from photoionization models of H II regions (Dopita et al., 2000; Kewley & Dopita, 2002; Dopita et al., 2016). Finally, a rare class of strong-line relations exist that attempt to capture the effects of temperature fluctuations though the use of H II region RL abundances (see, Bresolin, 2007; Méndez-Delgado et al., 2023a). For a more thorough discussion of the many different types of calibrations see Kewley & Ellison (2008).

In this analysis, we choose to compare our direct abundances to calibrations that have been calibrated to photoioninzation models or H II RL abundances. This choice is motivated by two reasons. First, the inclusion of integrated, or stacked, galaxies in a calibration sample may not be ideal given uncertainties in the validity of comparing whole galaxies to H II regions. Secondly, by including calibrations from models and RL abundances, we can better investigate the impact of temperature fluctuations may have on our understanding of metallicities. We discuss in the following sub-sections the source and description of the calibrations used in the remainder of this analysis. The full list of calibrations are summarized in Table 3.3 and described in detail in the remaining sections of this Appendix.

In Figures 3.14, 3.13, and 3.15 we show comparisons between strong-line abundances and direct oxygen abundances derived using different pairs of temperatures. To gauge the significance and monotonicity for each comparison we calculate the Pearson correlation coefficient (i.e. p-value), as well as the Spearman Rank Correlation Coefficient, $\rho$, calculated via bootstrapping

---

[3] $S_2 = \text{[S II]}\lambda\lambda 6716,6731/\text{H}\beta$ for S-calibration.

using `pymccorrelation` (Curran, 2014; Privon et al., 2020; Harris et al., 2020; Virtanen et al., 2020). A correlation is judged to be statistically significant if it exhibits p-value $< 10^{-3}$ or, as reported in the figures, a log(p-value) $< -3$.

### 3.7.2 Dopita et al. (2016)

The calibration $N_2S_2$ reported by Dopita et al. (2016) are calibrated entirely to a grid of Mappings 5.0 (Sutherland et al., 2018) H II region photoionization models. The $N_2S_2$ was shown to be insensitive to the ionization parameter and dust extinction. However, due to the model assumptions, the calibration is critically sensitive to the assumed scaling scaling of N/O (Dopita et al., 2016). The calibrations are valid over the following range metallicities, 9.0 $>$ 12+Log(O/H) $>$ 7.5

### 3.7.3 Kewley & Dopita (2002)

The theoretical calibrations presented Kewley & Dopita (2002) were constructed using a combination of stellar population synthesis and the photoionization models generated in Dopita et al. (2000). The $N_2O_2$ calibration constructed here has been shown to be sensitive to high metallicity systems, above one half solar (i.e. 12+log(O/H) $>$ 8.6), due to the increase synthesis of nitrogen though its metal-sensitive secondary production channel (Kewley & Dopita, 2002).

**Table 3.3.** List of abundance calibrations and references.

| Calibration | Reference |
|---|---|
| S-Cal | Pilyugin & Grebel (2016) |
| $N_2S_2$ | Dopita et al. (2016) |
| $N_2O_2$ | Bresolin (2007) |
|  | Kewley & Dopita (2002) |
| 12+log(O/H)[$t^2 > 0$] | Méndez-Delgado et al. (2023a) |
| 12+log(S/H) – log($S_{23}$) | Díaz & Zamora (2022) |

### 3.7.4 Pilyugin & Grebel (2016)

Presented in (Pilyugin & Grebel, 2016), the S-calibration (or S-cal) is a calibration of the $R_3$, $N_2$, and $S_2$ emission lines ratios to a sample of 313 reliable direct H II region abundances. The use of several line ratios is beneficial for minimizing the calibrations sensitivity to ionization parameter. Unlike the calibrations discussed thus far, the S-cal is double-valued and best described by a lower and upper metallicity branch. The upper and lower 12+log(O/H) branches, where the upper branch threshold is set by $\log N_2 > -0.6$, for the S-cal are:

$$\begin{aligned} 12+\log(\mathrm{O/H}) &= 8.424+0.030\,\log(R_3/S_2) \\ &\quad +0.751\,\log N_2+(-0.349+0.182\,\log(R_3/S_2)+0.508\,\log N_2)\times\log S_2, \end{aligned} \tag{3.12}$$

and

$$\begin{aligned} 12+\log(\mathrm{O/H}) &= 8.072+0.789\,\log(R_3/S_2) \\ &\quad +0.726\,\log N_2+(1.069-0.170\,\log(R_3/S_2)+0.022\,\log N_2)\times\log S_2. \end{aligned} \tag{3.13}$$

The S-calibration is valid over the following range metallicities, $9.0 > 12+\mathrm{Log(O/H)} > 7.0$.

### 3.7.5 Bresolin (2007)

Using a sample of H II regions with both CEL and RL abundances, Bresolin (2007) constructed a $N_2O_2$ calibration. The combined use of CEL and RL abundances is an attempt to include the effects of temperature fluctuations on the calibrated abundances. The $N_2O_2$ calibration here is valid over the following range metallicities, $9.5 > 12+\mathrm{Log(O/H)} > 7.6$.

### 3.7.6 $N_2S_2$ - Dopita et al. (2016)

We show in Figure 3.13 the $N_2S_2$ (Dopita et al., 2016) compared to each of the 12 + log(O/H) prescriptions. We find that this calibration shows significant correlations between all three oxygen abundance temperature prescriptions, in fact, the Spearman rank coefficients, $\rho = 0.4 \pm 0.09$ and p-value, log(p-value)$\approx -4.5$, are stable across all the comparisons.

Chapter 3, in part is currently being prepared for submission in The Astrophysical Journal. Rickards Vaught, Ryan J.; Sandstrom, Karin. M. The dissertation author is the primary investigator and author of this material.

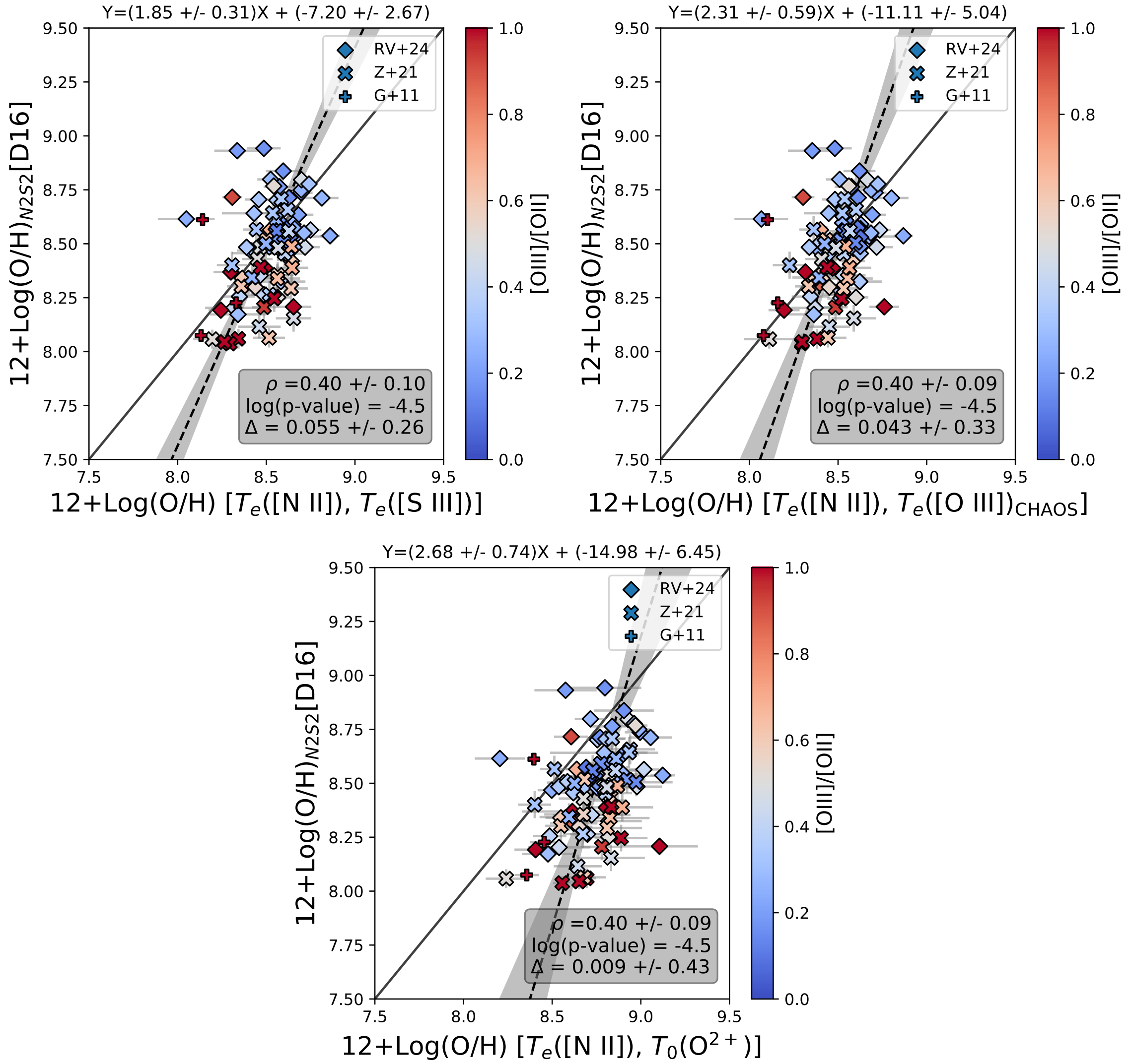

**Figure 3.13.** Comparison between the $N_2S_2$ strong-line calibration (Dopita et al., 2016) and direct abundances: 12+log(O/H) [$T_{\rm e,[N\,II]}$, $T_{\rm e,[S\,III]}$], [$T_{\rm e,[N\,II]}$, $T_{\rm e,[O\,III],CHAOS}$], and 12+log(O/H) [$T_{\rm e,[N\,II]}$, $T_0(\rm O^{2+})$]. The data points are color coded according by its ionization parameter as traced by the oxygen line ratio [OIII]/[OII]. Moreover, the marker symbol is determined by it's source catalog. We include the Spearman rank correlation coefficient, and log(p-value), in the lower right corner of each panel. Moreover, we also show in (red-solid) the best-fit linear regression line and it's corresponding $\pm 3\sigma$ uncertainty (grey). The Y and X parameters of the best fit line, printed above the figure, are the abundance of the calibration and the abundance of the direct abundance respectively.

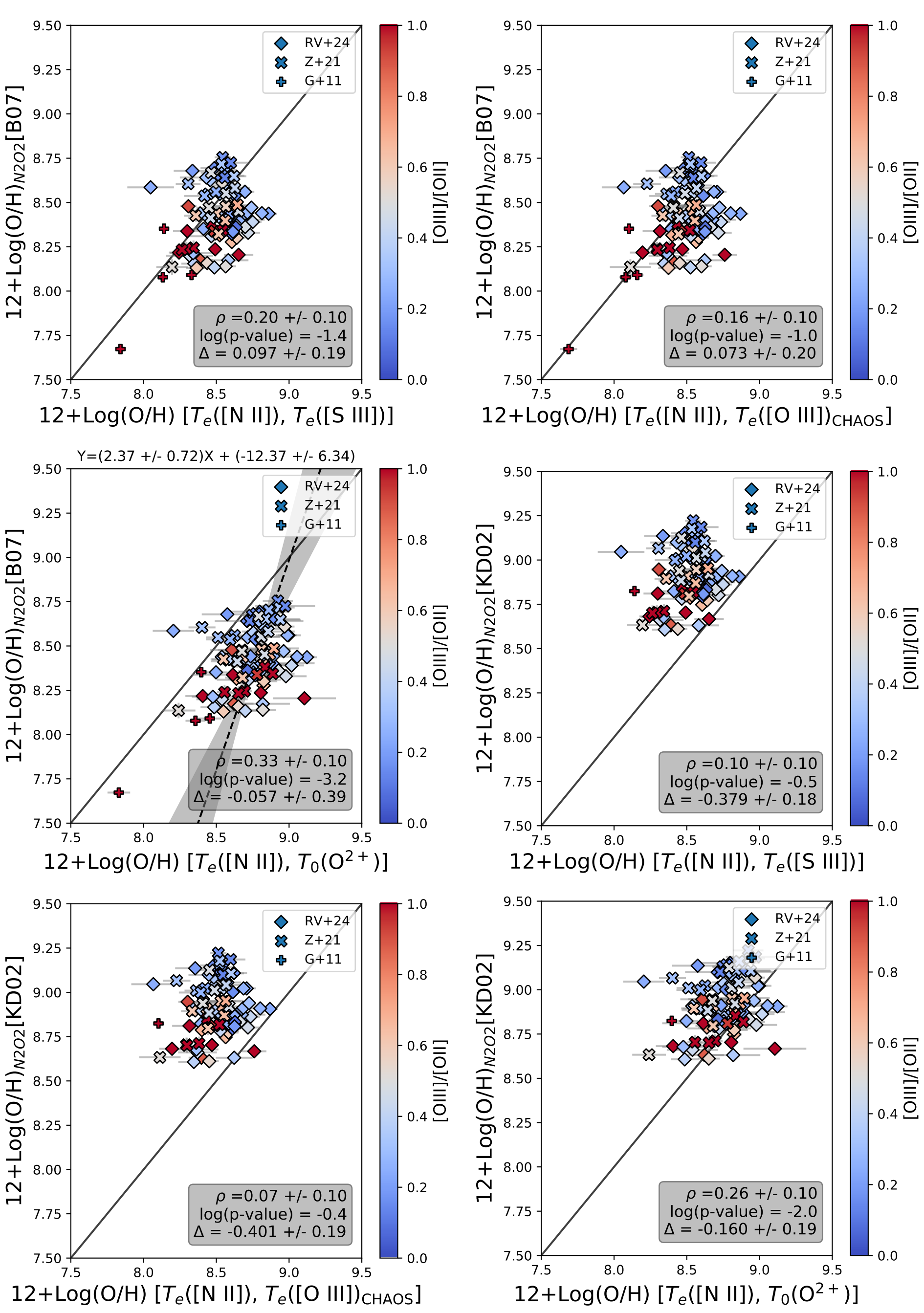

**Figure 3.14.** Comparison of $N_2O_2$ calibration. Description of panel is the same as Figure 3.13.

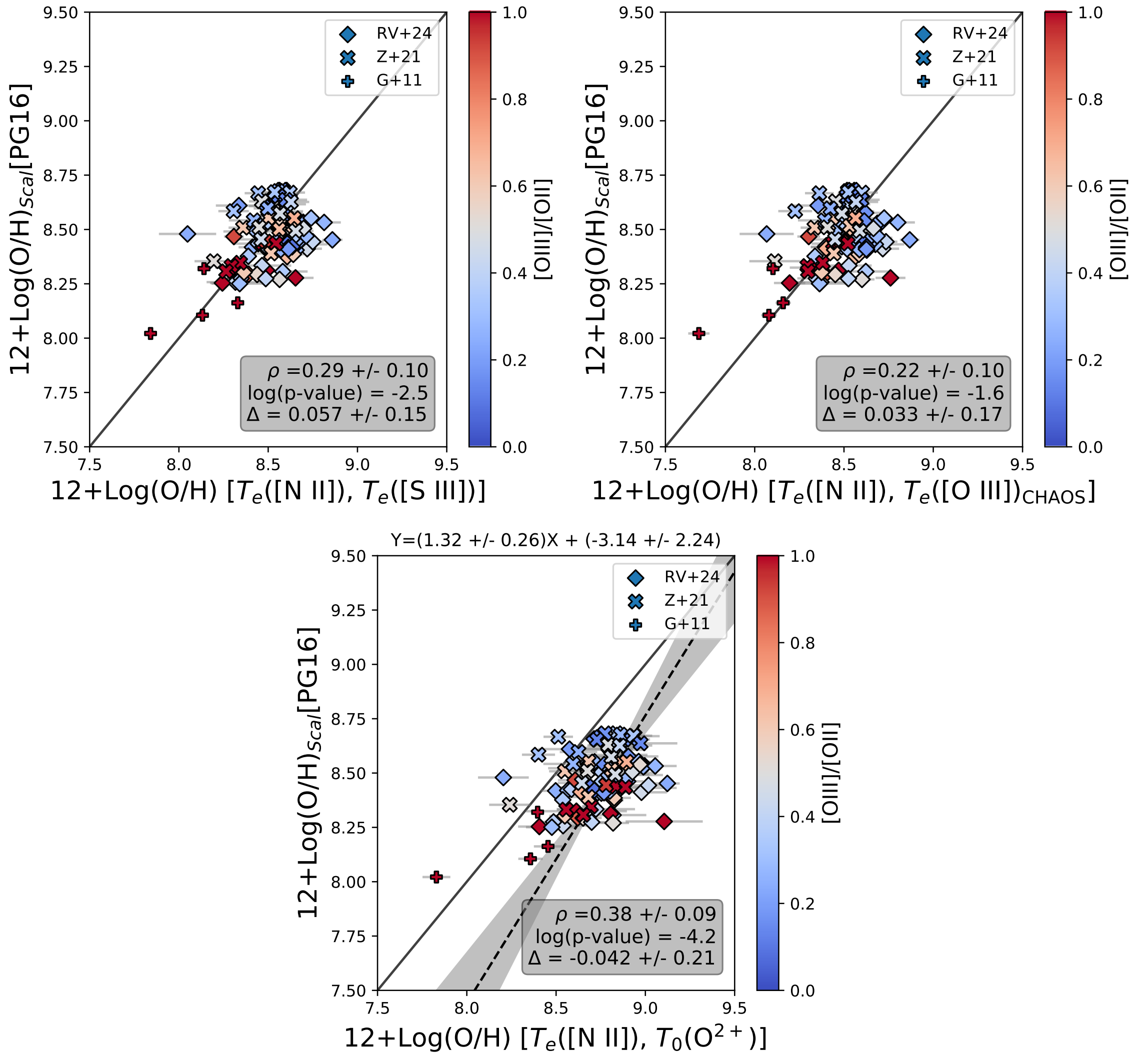

**Figure 3.15.** Comparison of The S-cal calibrations. Description of panels is the same as Figure 3.13.

# Chapter 4

# Keck Cosmic Web Imager Observations of He II Emission in I Zw 18

Abstract of Chapter 4.

With a metallicity of 12+Log(O/H) $\approx 7.1 - 7.2$, I Zw 18 is a canonical low metallicity blue compact dwarf (BCD) galaxy. A growing number of BCDs, including I Zw 18, have been found to host strong, narrow-lined, nebular He II ($\lambda$4686) emission with enhanced intensities compared to H$\beta$ (e.g. He II($\lambda$4686)/H$\beta$ $> 1\%$). We present new observations of I Zw 18 using the Keck Cosmic Web Imager. These observations reveal two nebular He II emission regions (or He III regions) northwest and southeast of the He III region in the galaxy's main body investigated in previous studies. All regions exhibit He II($\lambda$4686)/H$\beta$ greater than 2%. The two newly resolved He III regions lie along an axis which intercepts the position of I Zw 18's Ultra-luminous X-ray (ULX) source. We explore whether the ULX could power the two He III regions via shock activity and/or beamed X-ray emission. We find no evidence of shocks from the gas kinematics. If the ULX powers the two regions, the X-ray emission would need to be beamed. Another potential explanation is that a class of early-type nitrogen-rich Wolf-Rayet stars with low winds could power the two He III regions, in which case the alignment with the ULX would be coincidental.

## 4.1 Introduction

Narrow-lined, nebular He II($\lambda$4686) emission (He II emission) is observed in an increasing number of Blue Compact Dwarf (BCD) galaxies. Emission from He II arises from the recombination of doubly-ionized Helium, which requires energetic photons $> 54$ eV. Although there have been several studies into the origin of He II emission (Garnett et al., 1991; Izotov & Thuan, 1998; Cerviño et al., 2002; Thuan & Izotov, 2005; Kehrig et al., 2011; Shirazi & Brinchmann, 2012; Kehrig et al., 2015, 2018; Schaerer et al., 2019; Senchyna et al., 2020) the source(s) of the required ionizing flux remains uncertain.

Of the BCDs that exhibit He II emission, I Zw 18 is of unique interest as it is relatively nearby ($18.2 \pm 1.5$ Mpc; Aloisi et al., 2007), corresponding to a distance modulus of 31.3 Mag, and has one of the lowest metallicities, 12+Log(O/H) $\approx 7.1 - 7.2$ (Rickards Vaught et al. in prep, Searle & Sargent, 1972; Izotov & Thuan, 1999; Kehrig et al., 2016, and references therein). He II emission in I Zw 18 has a history of being observed via single-slit spectroscopy (Bergeron, 1977; Garnett et al., 1991; Izotov et al., 1997; Izotov & Thuan, 1998; Vílchez & Iglesias-Páramo, 1998) which has the disadvantage of sparse spatial sampling. Recently, integral field spectroscopy (IFS) of I Zw 18 has spatially resolved the extent of He II emission near the NW stellar cluster (Kehrig et al., 2015).

I Zw 18 also hosts an X-ray Binary (XRB), near this He III region. The first reported X-ray luminosity, $L_X$, of this XRB, via *Chandra* imaging (Bomans & Weis, 2002), was $\sim 10^{39}$ erg s$^{-1}$ in the $0.5 - 10$ keV band (Thuan & Izotov, 2005). Kehrig et al. (2015) modeled the XRB contribution to the He II luminosity, $L_{\lambda 4686}$, and found that the predicted $L_{\lambda 4686}$ is $\sim 100\times$ weaker then their observed value. However, deeper *XMM-Newton* imaging and analysis of the XRB by Kaaret & Feng (2013) report a $0.3 - 10$ keV band luminosity, $L_X = 1.4\times 10^{40}$ ergs s$^{-1}$, with a harder spectrum than observed with *Chandra*. With $L_X > 10^{39}$ ergs s$^{-1}$ this XRB is considered an Ultra-luminous X-ray (ULX) source (Pakull et al., 2006; Kaaret & Feng, 2013). Although the best fit to the *XMM-Newton* spectrum, assuming sub-Eddington accretion, suggests a black hole with mass $> 154\mathrm{M}_{\odot}$ (Kaaret & Feng, 2013), recent work suggests that a significant fraction of ULXs are instead stellar-mass binary systems undergoing super-Eddington accretion (King & Lasota, 2020, and references therein). Recently, infrared observations and photoionization modeling by Lebouteiller et al. (2017) suggest that I Zw 18's neutral gas heating can be explained by this single XRB, if the $10^4$ yr time averaged $L_X$ is $4 \times 10^{40}$ ergs s$^{-1}$.

In our deeper, higher angular and velocity resolution Keck Cosmic Web Imager (KCWI) observations, we detect two additional He III regions in I Zw 18. These regions are NW and SE of the emission reported by Kehrig et al. (2015), and lie along an axis that intercepts the position of I Zw 18's ULX. The alignment may be coincidental or may suggest that the ULX powers these two regions. We describe our observations and data reduction in Section 4.2. Our emission line fitting is detailed in Section 4.2.3. Section 4.3 outlines how we determine the position of the ULX source. We present our results in Section 4.4. We discuss possible ionizing sources of the two newly resolved He III regions in Section 4.5. We conclude this letter in Section 4.6.

## 4.2 Observations and Data Analysis

### 4.2.1 Archival Data

Several archival datasets are used in the course of analyzing our KCWI observations. We downloaded archival Hubble Space Telescope[1] (*HST*) images in the F439W and F814W filters (Program ID: 5434, 10586) as well as *r*-band Sloan Digital Sky Survey (SDSS, Abazajian et al., 2003) images of I Zw 18 (Fields: 157, 158, 238, and 239). To compare with the ULX in I Zw 18, we also downloaded *Chandra* X-ray imaging of the galaxy (Bomans & Weis, 2002).

---

[1] Based on observations made with the NASA/ESA Hubble Space Telescope, and obtained from the Hubble Legacy Archive, which is a collaboration between the Space Telescope Science Institute (STScI/NASA), the Space Telescope European Coordinating Facility (ST-ECF/ESA) and the Canadian Astronomy Data Centre (CADC/NRC/CSA).

### 4.2.2 KCWI Observations and Data Reduction

The IFS data were taken in clear conditions on December 25th, 2017 using KCWI installed on the 10-meter Keck II Telescope. We used the small slicer and BL grating centered at 4550 Å with a usable spectral range of 3700-5500 Å. The spectral resolution, R$\sim$3600 corresponds to a full-width-half-max (FWHM) $\sim$ 1.26 Å at 4550Å. The slice width is $0.35''$. Each pointing covers a field of view (FoV) $8.5''$ perpendicular and $20.4''$ parallel to the slicer. Using images of the standard star Feige 34, taken in the same conditions, we measured the FWHM of the point spread function to be $\sim 0.7''$.

The main body of I Zw 18 comprises two stellar clusters (IZW18-NW and IZW18-SE, Skillman & Kennicutt, 1993), shown in Figure 4.1, and is not covered by a single instrumental FoV. To cover the galaxy, we observed I Zw 18 with 4 pointings. The exposure per image was 1200s. To remove the background sky spectrum in each pointing, we integrated for 600s on an "off" galaxy position between science exposures. We chose the nearest in time sky spectrum to scale and subtract from each science frame. The data were reduced and flux calibrated with the standard star Feige 34 using Version 1.2.1 of the KCWI Data Extraction Reduction Pipeline[2] (Morrissey et al., 2018). The reduced cubes are astrometrically aligned to the *HST* F814W image, and then placed on a common grid, with pixel size $0.15''\times 0.15''$, using the astronomical mosaic image engine `Montage`[3] in combination with custom `Python` scripts. A description of these steps was presented in Chapter 2.

### 4.2.3 Emission Line Fitting

Two-dimensional emission line maps were created using `LZIFU` (Ho et al., 2016). `LZIFU` simultaneously fits a single (or multi) component Gaussian model to multiple emission lines in a spectrum. The stellar contribution is fit using an implementation of the penalized pixel fitting routine (`pPFX`, Cappellari & Emsellem, 2004). To determine if the observed He II emission

---

[2] https://github.com/Keck-DataReductionPipelines/KcwiDRP

[3] http://montage.ipac.caltech.edu

line has distinct kinematics, we perform separate `LZIFU` fits specifically for He II and H$\beta$ alone. These resulting maps are shown in Figures 4.1 and 4.2.

## 4.3 Astrometry of the ULX Source

To establish how the ULX in I Zw 18 impacts the strength of He II emission it is necessary to determine the location of the ULX. To achieve this, we follow the X-ray source detection procedure in Thuan et al. (2004)[4]. Next, we overlay the *Chandra* source region file on top of *r*-band SDSS images. We chose to match to SDSS imaging rather than *HST* images because the SDSS imaging covers a larger portion of the *Chandra* FoV. We are to able determine the positional offsets between the optical/X-ray positions using 5 X-Ray sources matched to SDSS optical counterparts with RMS scatter of $\sim 0.5''$. Because the astrometry of our KCWI data is anchored to the F814W *HST* image, we then compute off-sets using a multitude of bright sources in both our SDSS and F814W image. The resulting RMS scatter of the offsets is $\sim 0.2''$. The position of the ULX in the KCWI image is found after applying the above offsets directly to the *Chandra* position of the ULX. The final co-ordinates, (9h34m1.97s, +55d34m28.33s), place the ULX near IZW18-NW, consistent with the position reported in Thuan et al. (2004), with RMS scatter $0.55''$. The position of the ULX source as it compares to H$\beta$ and He II emission[5] is shown in Figure 4.1.

## 4.4 Results

### 4.4.1 3 He III Regions

Our KCWI observations detect three He III regions. First, northwest of IZW18-NW, and coincident with the H II region HT15 (Hunter & Thronson, 1995) is the He III region which we designate as HT15. Next, coincident with IZW18-SE is a second He III region. This region,

---

[4] We run the CIAO, v4.12, wavelet algorithm WAVDETECT on a 0.5-10 keV image, with a probability threshold set to $10^{-7}$.

[5] The position of the ULX shown in Kehrig et al. (2021) agree, within the positional uncertainties, with this work.

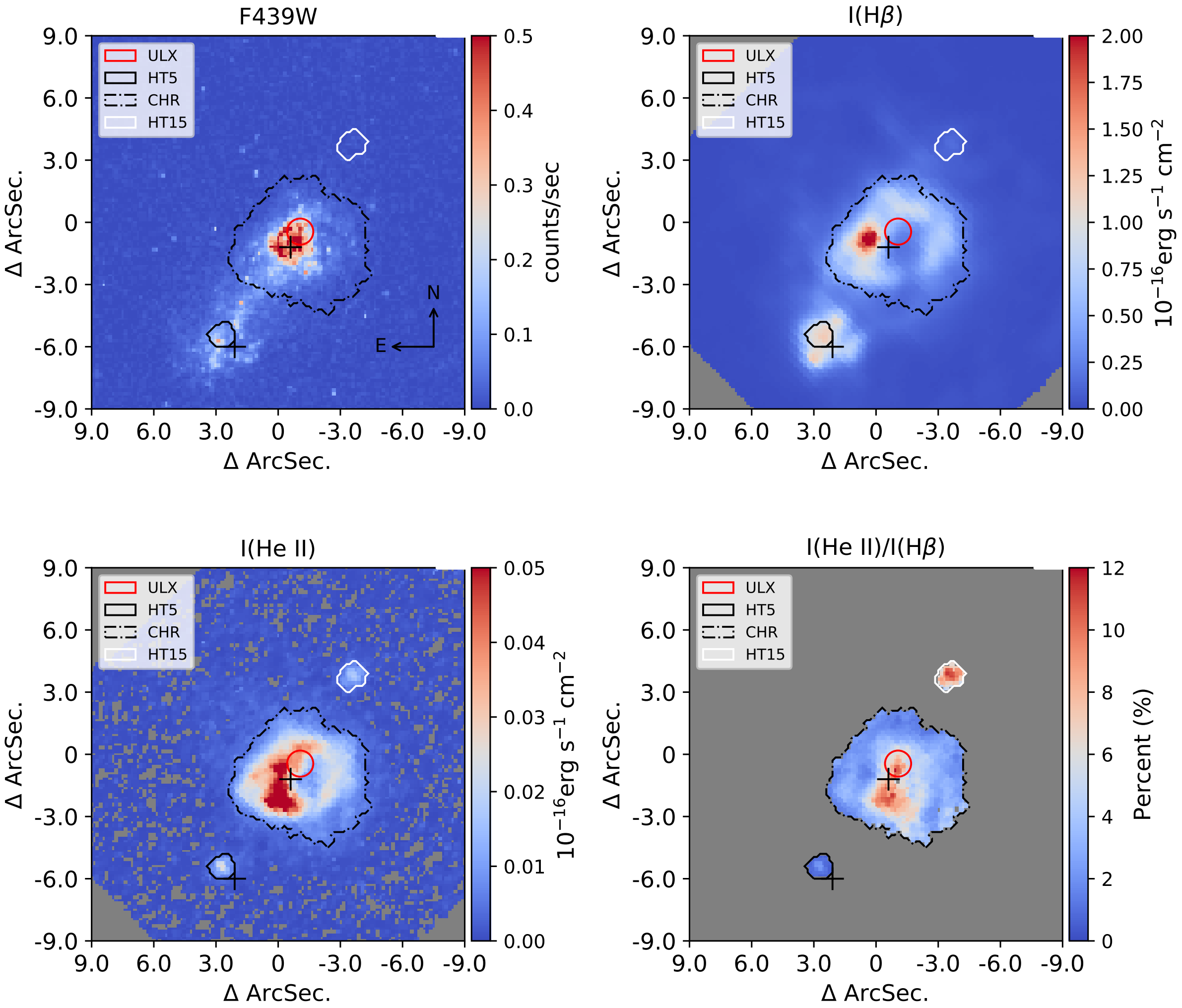

**Figure 4.1.** 2D imaging of I Zw 18. *Top Left:* The *HST* F439W image of I Zw 18 shows the approximate locations of the IZW18-SE/NW (cross-hairs) in comparison to the He III regions. The borders of the three He II emitting regions, HT5 (black-dashed), CHR (black-Solid) and the HT15 (white-solid) are defined to contain pixels with He II emission S/N $> 3$. Also shown is the position and astrometric uncertainty of the ULX (red-solid). *Top right and bottom left:* The integrated H$\beta$ and He II emission line maps. *Bottom right:* He II($\lambda$4686)/H$\beta$ for the three He II emitting regions.

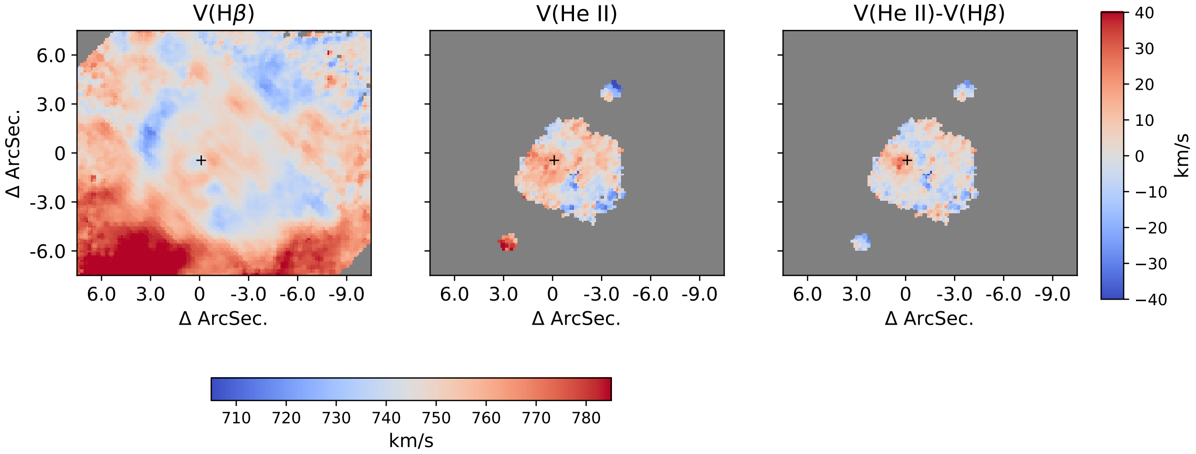

**Figure 4.2.** Two-dimensional `LZIFU` velocity maps. The panels show the velocity maps measured from (left) H$\beta$, (middle) He II and (right) the difference between the two velocities. The He II velocities of the HT5 and HT15 region are very close to the H$\beta$ velocity, traced by H$\beta$, providing no clear evidence for distinct kinematics in the He II emitting gas. A velocity difference of $\sim 30$ km s$^{-1}$ can be seen near the the pixel of peak H$\beta$ emission (+), which has been attributed to a possible Supernovae Remnant (Östlin & Mouhcine, 2005).

whose He II emission has been reported in Skillman & Kennicutt (1993) and Izotov et al. (1997), appears to sit close to (or on) the identified H II region HT5 (Hunter & Thronson, 1995); as such we designate this He III region as HT5. The last of the three we define as the Central He III Region (CHR) as it is coincident with the ionized gas around IZW18-NW and in-between HT5 and HT15. CHR corresponds to the region previously mapped in Kehrig et al. (2015). Our observed He II emission map is shown in Figure 4.1 with the He III regions highlighted.

At a distance of 18.2 Mpc and assuming negligible reddening by dust (for more details on the very low dust attenuation in I Zw 18, see Rickards Vaught et al. in prep; Cannon et al. 2002; Fisher et al. 2014) the total $L_{\lambda 4686}$ measured within the contours, shown in Figure 4.1, in the CHR is $(102 \pm 15.0) \times 10^{36}$ ergs s$^{-1}$. $L_{\lambda 4686}$ for the regions HT5 and HT15 are $(1.96 \pm 0.29) \times 10^{36}$ and $(2.05 \pm 0.31) \times 10^{36}$ ergs s$^{-1}$. We also report here the luminosity in H$\beta$, $L_{\mathrm{H}\beta}$. For CHR $L_{\mathrm{H}\beta}$ is $(208 \pm 43) \times 10^{37}$ ergs s$^{-1}$. $L_{\mathrm{H}\beta}$ for HT5 and HT15 are $(17.7 \pm 2.6) \times 10^{37}$ and $(2.47 \pm 0.37) \times 10^{37}$ ergs s$^{-1}$ respectively. The uncertainties in the reported luminosities are dominated by an estimated calibration error of 15%. HT5 and HT15 are separated by a distance of $\sim$ 900 pc and are co-linear with an axis that runs through the position of the ULX. Because of our high resolution, $0.7''$ or $\sim$ 60 pc at 18.2 Mpc, we are able to resolve the morphology of the He II emitting gas in the CHR of I Zw 18. The He II and H$\beta$ emission trace a horseshoe-like shell with major/minor diameters of $\sim$ 550 and 450 pc, respectively. Nearly coincident with the ULX is an apparent cavity, likely created by stellar feedback (Stasińska & Schaerer, 1999; Péquignot, 2008), with projected radius, $R_C \sim 80$ pc. The He II emission is preferentially extended $\sim$ 250 pc away from the ULX towards the SE.

To date, there has only been one published IFS analysis of the He II emission in I Zw 18. Kehrig et al. (2015) spatially resolved the He II emission of the CHR and measured a total He II luminosity of $(112 \pm 7) \times 10^{36}$ erg s$^{-1}$; a value that is within the uncertainty reported in this work. Kehrig et al. (2015) do not report any He II emission near the location of HT5 and HT15. The absence of these regions in their data is expected given their sensitivity.

### 4.4.2 The He II($\lambda$4686)/H$\beta$ Ratio

The He II($\lambda$4686)/H$\beta$ intensity ratio is sensitive to shape of the Lyman continuum spectrum shortwards of 228 Å, ionization parameter (Garnett et al., 1991; Guseva et al., 2000; Schaerer et al., 2019; Barrow, 2020; Stasińska & Schaerer, 1999) and/or the shock velocity (Allen et al., 2008). We create a He II($\lambda$4686)/H$\beta$ map by dividing maps of He II and H$\beta$ in regions where S/N $> 3$ in both lines. This map, shown in Figure 4.1, reveals He II($\lambda$4686)/H$\beta$ as high as 12% in the CHR and HT15, indicative of a high ionization parameter/harder ionizing spectrum object and/or shocks near the ULX and in HT15. The He II emission along the eastern edge of the shell, and the emission co-spatial with the ULX, exhibits the largest He II($\lambda$4686)/H$\beta$ enhancement. Compared to HT15 and the CHR, HT5 exhibits a low peak He II($\lambda$4686)/H$\beta$ value of $\sim$ 2%. Because HT5 is located within IZW18-SE, there may be excess H$\beta$ emission from gas ionized by stellar sources contributing to the spectrum of HT5. To remove the effects of such an ionized gas component we subtract the median local spectrum in an annulus between 0.5-$1''$ surrounding HT5. The results of this subtraction are shown in Figure 4.3; the spectrum of

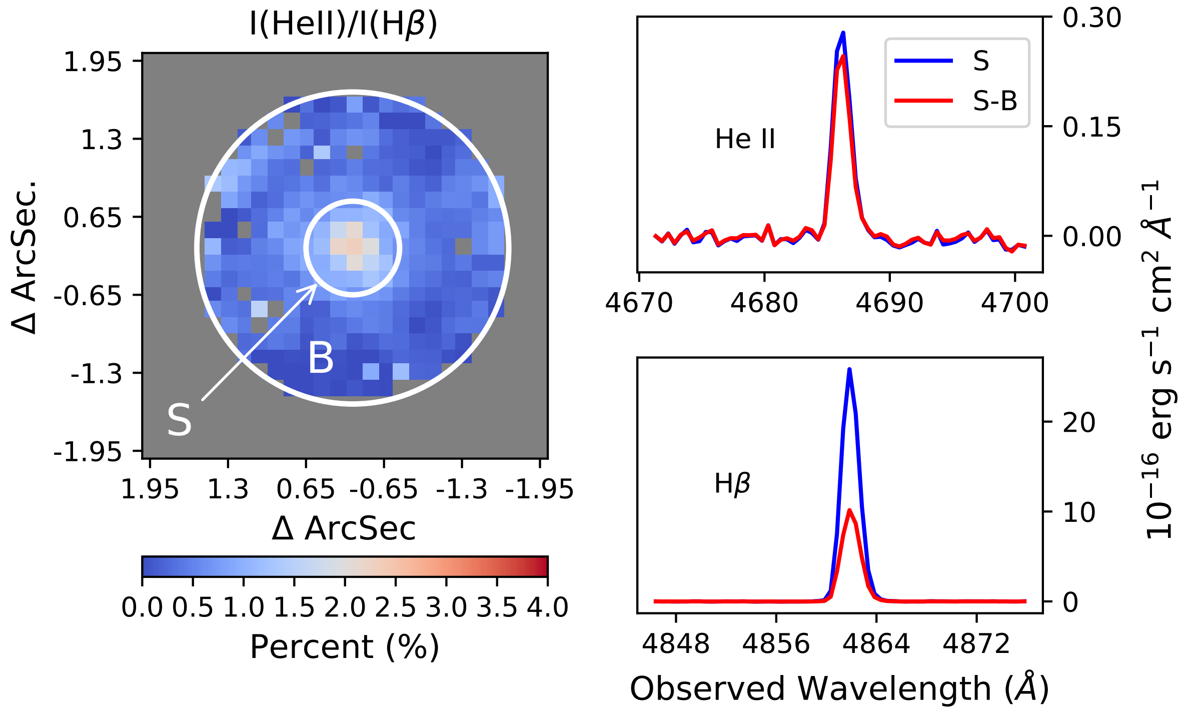

**Figure 4.3.** He II($\lambda$4686)/H$\beta$ in HT5. *Left:* A $4'' \times 4''$ stamp of the 2D map of He II($\lambda$4686)/H$\beta$ in HT5. Contained in the inner annulus is the "source" S and contained in by the outer annulus but outside the inner annulus is the "background" B. *Right:* The two panels show the continuum subtracted integrated line profile of He II and H$\beta$ of the source before (blue) and after (red) background subtraction. The "background" contributes a larger fraction to the integrated line intensity of H$\beta$ than to the He II profile.

HT5 with the local spectrum removed is revealed to have He II($\lambda$4686)/H$\beta$ closer to $\sim 4.5\%$.

### 4.4.3 Undetected Stellar Continuum in HT15

Of the three regions, HT15 has a non-detected stellar continuum in our observations. This can be seen in Figure 4.4, where we plot the integrated spectrum of HT15 measured using a $\sim 1$ arcsec$^2$ aperture covering HT15. After adding in quadrature the $\pm 1$-$\sigma$ error spectrum for each pixel, we find that the continuum flux across all wavelengths is within the integrated 1-$\sigma$ errors. If a stellar contribution to the continuum were present, it is undetected below a representative $\bar{\sigma} \approx 1.3 \times 10^{-18}$ erg s$^{-1}$ cm$^{-2}$ Å$^{-1}$, where $\bar{\sigma}$ is the median 1-$\sigma$ error across all wavelengths. This flux corresponds to a limiting apparent magnitude of $m_V > 24$. This result is similar to those of Hunter & Thronson (1995) and Hunt et al. (2003), whose H$\alpha$ and NIR observations of HT15 also lack a measurable stellar component, but instead, only show emission lines from ionized gas. Furthermore, the Hubble Source Catalog (Whitmore et al., 2016) classification of object, 766559, at the position of HT15 suggests an extended object, rather than a point source according to photometry in the filters: F450W, F555W, F702W, F814W.

### 4.4.4 Kinematics of the He II gas

To test whether or not the kinematics of He II gas are distinct from that of H$\beta$, as might be expected if He II emission is the result of shocks while H$\beta$ is largely from photoionization, we perform single line `LZIFU` fits. The results/comparisons of the velocity fits are shown in Figure 4.2. We find that the difference between the He II and H$\beta$ velocities in the HT15/ HT5 regions is negligible, signifying that dynamics of the He II-emitting gas around HT15 and HT5 have velocities similar to those traced by H$\beta$. We measure a velocity difference of $\sim$ 30 km s$^{-1}$ near the position of peak H$\beta$ emission, however this may be associated with a supernova remnant or young stellar cluster (Östlin & Mouhcine, 2005).

## 4.5 Discussion

We use our measurements of the spatial distribution of He II emission in I Zw 18 to discuss possible origins of the high ionization state gas in the two newly resolved He III regions. This includes Wolf-Rayet stars and ULX generated phenomena. In the ULX case, the alignment of the two He III regions with the ULX source leads us to explore the possibility that HT15 and HT5 are observable effects from jet/outflow generated shocks or beamed X-ray emission originating from the ULX. But first, we discuss if Wolf-Rayet stars are consistent with the properties of the He II emission in HT15 and HT5.

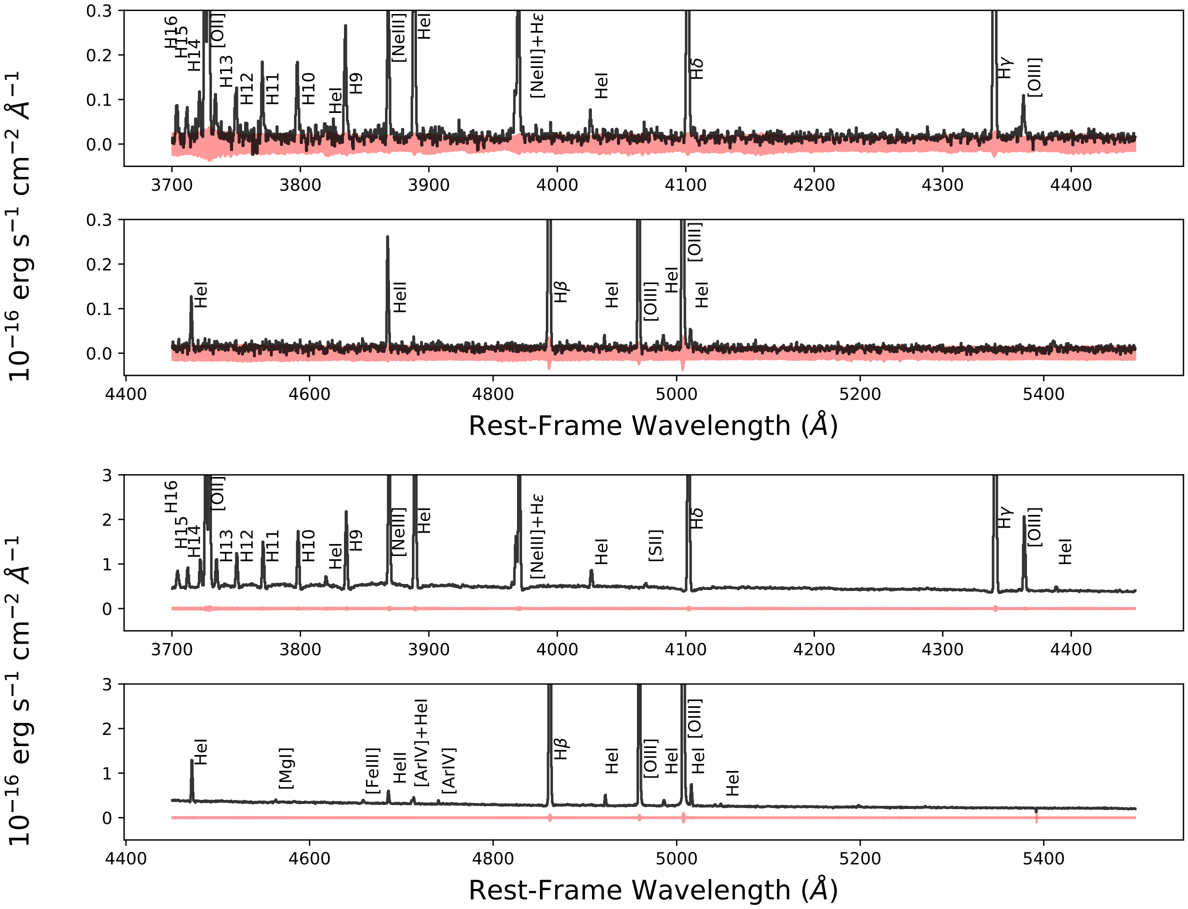

**Figure 4.4.** The integrated spectrum of HT15 and HT5 (labels of lines shortward/longward of [O II] are shifted 3 Å to the left/right for clarity). *Top:* The integrated spectrum of HT15 (black) is shown with the error (red). The continuum flux density of HT15 region is observed to be within the instrumental noise along the full wavelength range. We infer from this that the HT15 region stellar population is not detected in these data. *Bottom:* Integrated spectrum of HT5. The highest ionization line in either of these spectra is He II($\lambda$4686).

### 4.5.1 Wolf-Rayet Stars

Although the spectra of HT5 and HT15 lack broad-lined, stellar He II emission, a signature of WR stars (Crowther & Hadfield, 2006), we are unable to eliminate these objects as the source of He II emission. The absence of broad-lined, stellar He II emission in our data would be consistent with a population of nitrogen rich WR (WN) stars, as modeling of WN atmospheres in Crowther & Hadfield (2006) has demonstrated that WN winds are reduced at sub Large and Small Magellanic Clouds (LMC/SMC) metallicities. Reduced winds diminish the production of broad-lined He II emission, and could explain the absence of this feature in these regions while still potentially powering nebular He II emission.

He III regions have been observed around WN stars Brey2 and AB7 in the LMC and SMC respectively (Nazé et al., 2003a,b). In Nazé et al. (2003a) the He III region around Brey2 has a He II luminosity, $L_{\lambda 4686} = 3.5 \times 10^{35}$ erg s$^{-1}$. For the AB7 He III region, $L_{\lambda 4686}$ is 10× greater than Brey2 (Nazé et al., 2003b). Both objects exhibit regions with He II($\lambda$4686)/H$\beta$ greater than 10%. Compared to our HT15 and HT5 $L_{\lambda 4686}$ budget, 6 Brey2-like stars could account for the He II luminosities in HT15 and HT5 while, to order of magnitude, a single AB7-like star could solely power He II emission in both HT15 and HT5. Applying the distance modulus to the absolute magnitude, $M_V \sim -3$, for WN stars (Crowther & Hadfield, 2006) these populations wouldn't appear brighter than $m_V \sim 24$. Compared to these He$^+$ ionizing WN2-4 sub-types, brighter WN5-10 stars are too cool and are unable to doubly ionize He. WN stars are viable candidates for the production of He II emission in HT15 and HT5.

### 4.5.2 Jet or Beamed X-ray powered He II emission in I Zw 18

Supposing that the alignment of HT15 and HT5 with the ULX arises from a physical link, then jet/outflow generated shocks or beamed X-rays originating from the ULX would be needed to explain the alignment and emission.

Various collisional and radiative processes generated behind shock fronts have been modeled by Allen et al. (2008). This modeling shows that shock speeds between $100-150$ km s$^{-1}$ can produce He II($\lambda$4686)/H$\beta$ ratios consistent with those observed for HT15 and HT5. Because shock-sensitive lines such as [O I]($\lambda$6300), [N II]($\lambda$6584), [S II]($\lambda$6717, 6731) and [Ne V]($\lambda$3346, 3426) lie outside our spectral range, we are unable to compare to those with shock velocity estimates inferred from He II($\lambda$4686)/H$\beta$. Kehrig et al. (2016) report measurements of these lines, excluding [Ne V], for the CHR. The observed line ratios are found to be inconsistent with shock ionization. We note that shock templates at I Zw 18-like metallicities are uncertain as shock models only exist for metallicities $\geq$ SMC. Moreover, the difference between the He II and H$\beta$ derived velocities, as shown in Figure 4.2, does not show evidence of $\sim 100$ km s$^{-1}$ jet/outflow generated shocks at the locations of HT15 and HT5. The absence of such velocities does not necessarily discount the possibility of jet/outflow activity if the motion were primarily in the plane of the sky. Low spatial resolution radio observations of I Zw 18 by Hunt et al. (2005) show an extended synchotron halo + lobe structure in the radio continuum which they take as evidence of a wind-blown super-bubble accompanied by bi-polar outflows. However, the direction of these outflows is perpendicular to the axis connecting HT15 and HT5.

Next, we test whether isotropic X-ray emission from the ULX could be sufficient to power the He II emission, or if beaming would be needed. The X-ray flux, using $L_X = 1 \times 10^{40}$ erg s$^{-1}$, at a distance of, $R \sim 450$ pc, is $F_X \sim 4 \times 10^{33}$ erg s$^{-1}$ pc$^2$. The power passing through a surface area of $\pi r^2$, where $r$ is the radial size of HT15/HT5 with the value $r = 0.3''$ or 30 pc, is $P_X = F_X \times \pi r^2 \sim 1 \times 10^{37}$ erg s$^{-1}$.

As observed in a number of cases and reproduced by photoionization modeling calculations, X-ray ionized nebulae around ULXs appear to exhibit He II emission to total X-ray luminosity ratios of $L_{\lambda 4686}/L_X \sim 10^{-4}$ (Pakull & Angebault, 1986; Pakull & Mirioni, 2002; Kaaret et al., 2004; Kaaret & Corbel, 2009; Moon et al., 2011). Assuming this same fraction of power goes into producing He II emission in HT5 and HT15, the power for He II emission is $P_{\lambda 4686} = P_X \times 10^{-4} \sim 10^{33}$ ergs s$^{-1}$. When compared to the observed $L_{\lambda 4686}$ for HT15/HT5 the

He II production budget is short by orders of magnitude. Even using $L_{\lambda4686}/L_X \sim 10^{-2}$, which one gets assuming the ULX is responsible for all of the He II emission in the CHR, the power available to produce He II emission is short by two orders of magnitude. This shows that if the X-ray emission from the ULX powers these two He III regions, the emission needs to be beamed rather than isotropic.

## 4.6 Conclusion

We presented KCWI observations of I Zw 18. Our observations revealed the presence of two He III regions, HT15 and HT5, in addition to the He III region mapped by Kehrig et al. (2015). Enhanced He II($\lambda$4686)/H$\beta$ ratios between 4% and up to 12% are measured in HT5 and HT15. Region HT15, which shows some of highest He II($\lambda$4686)/H$\beta$ values, has an undetected stellar population ($m_V > 24$). We compared the observed He II luminosity in HT15 and HT5 to He III regions surrounding LMC/SMC WN stars and find that similar objects are sufficient to produce the He II luminosity and He II($\lambda$4686)/H$\beta$ enhancement of HT15 and HT5 as well as the absence of broad-lined, spectral He II features, whilst remaining below our detection limit.

Based on the alignment of the two He III regions and the ULX, we explored a scenario in which jet/outflow activity or beamed X-ray emission originating from the ULX powers the observed He II emission in HT15 and HT5. Due to our spectral coverage and the lack of shock models appropriate for the galaxy's metallicity, we cannot put a strong constraint on whether shocks could be powering He II emission. We assessed the velocity structure of the ionized gas and found no kinematic anomalies driven by jet/outflow activity. Assuming that HT15 and HT5 are illuminated by isotropic X-ray emission, we found that the ULX would not produce sufficient X-ray flux to generate the observed He II emission. If the X-ray emission from the ULX powers these sources, it would require beaming. We will present further analysis of the metallicity and temperature structure of I Zw 18 in an upcoming publication.

## 4.7 Acknowledgments

The authors thank the referee for very thorough and enlightening reports which significantly improved the analysis presented in this letter. The authors also thank Brent Groves for useful conversations. The data presented herein were obtained at the W. M. Keck Observatory, which is operated as a scientific partnership among the California Institute of Technology, the University of California and the National Aeronautics and Space Administration. The Observatory was made possible by the generous financial support of the W. M. Keck Foundation. The authors wish to recognize and acknowledge the very significant cultural role and reverence that the summit of Maunakea has always had within the indigenous Hawaiian community. We are most fortunate to have the opportunity to conduct observations from this mountain. We also wish to thank Luca Rizzi and all the Keck Observatory staff for observational support. RRV and KS acknowledge funding support from National Science Foundation Award No. 1816462. This research made use of Montage. It is funded by the National Science Foundation under Grant Number ACI-1440620, and was previously funded by the National Aeronautics and Space Administration's Earth Science Technology Office, Computation Technologies Project, under Cooperative Agreement Number NCC5-626 between NASA and the California Institute of Technology. Funding for the Sloan Digital Sky Survey IV has been provided by the Alfred P. Sloan Foundation, the U.S. Department of Energy Office of Science, and the Participating Institutions.

Chapter 4, in full, is a reformatted reprint of the material as it appears in Rickards Vaught, Ryan J.; Sandstrom, Karin. M.; Hunt, Leslie. K.;"Keck Cosmic Web Imager Observations of He II Emission in I Zw 18," The Astrophysical Journal Letters, 911, L17, 2021. The dissertation author was the primary investigator and author of this paper.

# Chapter 5

# Conclusions and Future Work

In my dissertation, I have presented integral field observations of H II and He III regions in nearby galaxies. I summarize the results and their implications here:

1. In Chapter 2, we confirmed a previous finding that temperatures obtained from the auroral-to-nebular line ratios of [S II] or [O II] can be overestimated due to the presence of unresolved density inhomogeneities inside H II regions. Because of these potential biases, we argued that the [N II] temperatures should be prioritized for direct abundances.
2. We found that the [N II] and [S III] auroral-to-nebular line temperatures exhibited the lowest scatter of the $T_{\rm e}$– $T_{\rm e}$ relations and closely follows trends predicted from theoretical models and observations. The well-behaved relationship between [N II] and [S III] temperatures, even in potentially inhomogeneous conditions, suggests that these temperatures may be potentially better at tracing the underlying H II region low/intermediate zone temperature. These observations further stress the prioritization of [N II] and [S III] temperatures for metallicity determinations.
3. We observed a subset of H II regions with very high [O III] auroral-to-nebular line temperatures that do not agree with the cooler temperatures measured in the low and intermediate ionization zones. We found that the regions with high [O III] temperature tended to exhibit both enhanced molecular gas velocity dispersion and lower ionization parameter than the regions with [O III] temperatures that are in better agreement with other

ionization zones. These regions also showed enhanced [S II]/H$\alpha$, [O I]/H$\alpha$, and He II/H$\beta$ ratios suggesting the presence of secondary ionization sources (e.g. shocks, Wolf-Rayet stars). Absent detections of Wolf-Rayet features in the H II region spectra, we argued that low-velocity shocks are enhancing the [O III] temperature.

4. In Chapter 3, we determined that the auroral-to-nebular line temperature of [S III] does not accurately trace the average gas temperature of the high-ionization zone. We presented evidence that the temperature derived from the [S III]$\lambda$6312 auroral line is affected by the presence of temperature fluctuations.

5. We derived sulfur, oxygen, and nitrogen abundances using temperatures from the auroral-to-nebular ratio of [N II], and the ion-weighted doubly ionized oxygen gas temperature, derived from [N II] using the Méndez-Delgado et al. (2023b) relationship. From these abundances we found that the sulfur-to-nitrogen and nitrogen-to-oxygen ratios vary with metallicity.

6. We investigated potential drivers of the scatter in the N/O-O/H relationship. We found that the scatter is correlated with the radiation softness parameter, $\eta$, and velocity dispersion of surrounding molecular gas as traced by CO emission. These correlations provide evidence for both delayed nitrogen pollution by aging stellar populations or outflows as the sources of N/O scatter at high metallicity.

7. We observed a strong correlation between the S/N and N/O ratios. Regions with high ratios in both sulfur and nitrogen also have softer ionizing spectra according to the radiation softness parameter.

8. We find that direct sulfur abundances, calculated using the ion-weighted doubly ionized oxygen gas temperature, are not in agreement with the Díaz & Zamora (2022) strong-line sulfur calibration.

9. In Chapter 4, we presented observations of two He III regions in the metal-poor galaxy I Zw 18. Motivated by the alignment of these regions with I Zw 18's ultra-luminous X-ray source, we explored if there was a physical connection. Under the assumption that the X-ray emission is isotropic, we found that the ultra-luminous X-ray source could not produce the requisite flux to generate the observed He II emission; indicative that the X-ray emission would have to be beamed.

These results stress the importance of high spatial resolution observations of H II regions to better understand the effects of inhomogeneous physical conditions on the different $T_e$ tracers and abundances. Observations that meet this need are now possible with the recently commissioned Local Volume Mapper (LVM) and the recently expanded wavelength coverage, $3700$ Å $< \lambda <$ $10,000$ Å, of KCWI (i.e. Keck Cosmic Re-ionization Mapper). The LVM is observing the full optical spectrum for Milky Way plane H II regions, the Orion Nebula, as well as the Small and Large Magellanic Clouds. In addition, the LVM will be observing all of these targets at sub-pc scales, which will unlock a high spatial resolution view of the temperature and ionization structure of H II regions.

This new view of Milky Way H II regions can be extended to extra-galactic H II regions using KCWI. In the near future, I will use in-hand observations of H II regions in the galaxy M33 to map their temperature and density inhomogeneities. Furthermore, I will use in-hand KCWI observations of I Zw 18, with the high velocity resolution configuration, to investigate the presence of high velocity gas in the direction of the two high-ionization regions observed in Rickards Vaught et al. (2021).

In my post-doctoral work, to be performed at the Space Telescope Science Institute, I will use mid-IR observations obtained with the James Webb Space Telescope to measure the ISM properties of metal-poor galaxies. I will compare the physical gas properties determined from the near-infrared to those from the optical to expand our understanding of the multi-phase structure of the ISM and its gas physics. Extending beyond the local Universe, future James

Webb Space Telescope observations allow for multi-element direct abundance measurements in galaxies up to epoch of cosmic reionization. Using direct abundances measured for galaxies at several redshifts, we can better trace the chemical evolution of galaxies.

# Bibliography

Abazajian, K., Adelman-McCarthy, J. K., Agüeros, M. A., Allam, S. S., Anderson, S. F., Annis, J., Bahcall, N. A., Baldry, I. K., Bastian, S., Berlind, A., Bernardi, M., Blanton, M. R., Blythe, N., Bochanski, John J., J., Boroski, W. N., Brewington, H., Briggs, J. W., Brinkmann, J., Brunner, R. J., Budavári, T., Carey, L. N., Carr, M. A., Castander, F. J., Chiu, K., Collinge, M. J., Connolly, A. J., Covey, K. R., Csabai, I., Dalcanton, J. J., Dodelson, S., Doi, M., Dong, F., Eisenstein, D. J., Evans, M. L., Fan, X., Feldman, P. D., Finkbeiner, D. P., Friedman, S. D., Frieman, J. A., Fukugita, M., Gal, R. R., Gillespie, B., Glazebrook, K., Gonzalez, C. F., Gray, J., Grebel, E. K., Grodnicki, L., Gunn, J. E., Gurbani, V. K., Hall, P. B., Hao, L., Harbeck, D., Harris, F. H., Harris, H. C., Harvanek, M., Hawley, S. L., Heckman, T. M., Helmboldt, J. F., Hendry, J. S., Hennessy, G. S., Hindsley, R. B., Hogg, D. W., Holmgren, D. J., Holtzman, J. A., Homer, L., Hui, L., Ichikawa, S.-i., Ichikawa, T., Inkmann, J. P., Ivezić, Ž., Jester, S., Johnston, D. E., Jordan, B., Jordan, W. P., Jorgensen, A. M., Jurić, M., Kauffmann, G., Kent, S. M., Kleinman, S. J., Knapp, G. R., Kniazev, A. Y., Kron, R. G., Krzesiński, J., Kunszt, P. Z., Kuropatkin, N., Lamb, D. Q., Lampeitl, H., Laubscher, B. E., Lee, B. C., Leger, R. F., Li, N., Lidz, A., Lin, H., Loh, Y.-S., Long, D. C., Loveday, J., Lupton, R. H., Malik, T., Margon, B., McGehee, P. M., McKay, T. A., Meiksin, A., Miknaitis, G. A., Moorthy, B. K., Munn, J. A., Murphy, T., Nakajima, R., Narayanan, V. K., Nash, T., Neilsen, Eric H., J., Newberg, H. J., Newman, P. R., Nichol, R. C., Nicinski, T., Nieto-Santisteban, M., Nitta, A., Odenkirchen, M., Okamura, S., Ostriker, J. P., Owen, R., Padmanabhan, N., Peoples, J., Pier, J. R., Pindor, B., Pope, A. C., Quinn, T. R., Rafikov, R. R., Raymond, S. N., Richards, G. T., Richmond, M. W., Rix, H.-W., Rockosi, C. M., Schaye, J., Schlegel, D. J., Schneider, D. P., Schroeder, J., Scranton, R., Sekiguchi, M., Seljak, U., Sergey, G., Sesar, B., Sheldon, E., Shimasaku, K., Siegmund, W. A., Silvestri, N. M., Sinisgalli, A. J., Sirko, E., Smith, J. A., Smolčić, V., Snedden, S. A., Stebbins, A., Steinhardt, C., Stinson, G., Stoughton, C., Strateva, I. V., Strauss, M. A., SubbaRao, M., Szalay, A. S., Szapudi, I., Szkody, P., Tasca, L., Tegmark, M., Thakar, A. R., Tremonti, C., Tucker, D. L., Uomoto, A., Vanden Berk, D. E., Vandenberg, J., Vogeley, M. S., Voges, W., Vogt, N. P., Walkowicz, L. M., Weinberg, D. H., West, A. A., White, S. D. M., Wilhite, B. C., Willman, B., Xu, Y., Yanny, B., Yarger, J., Yasuda, N., Yip, C.-W., Yocum, D. R., York, D. G., Zakamska, N. L., Zehavi, I., Zheng, W., Zibetti, S., & Zucker, D. B. 2003, AJ, 126, 2081

Abolmasov, P., Fabrika, S., Sholukhova, O., & Afanasiev, V. 2007, Astrophysical Bulletin, 62, 36

Allen, M. G., Groves, B. A., Dopita, M. A., Sutherland, R. S., & Kewley, L. J. 2008, ApJS, 178, 20

Aloisi, A., Clementini, G., Tosi, M., Annibali, F., Contreras, R., Fiorentino, G., Mack, J., Marconi, M., Musella, I., Saha, A., Sirianni, M., & van der Marel, R. P. 2007, ApJL, 667, L151

Anand, G. S., Lee, J. C., Van Dyk, S. D., Leroy, A. K., Rosolowsky, E., Schinnerer, E., Larson, K., Kourkchi, E., Kreckel, K., Scheuermann, F., Rizzi, L., Thilker, D., Tully, R. B., Bigiel, F., Blanc, G. A., Boquien, M., Chandar, R., Dale, D., Emsellem, E., Deger, S., Glover, S. C. O., Grasha, K., Groves, B., S. Klessen, R., Kruijssen, J. M. D., Querejeta, M., Sánchez-Blázquez, P., Schruba, A., Turner, J., Ubeda, L., Williams, T. G., & Whitmore, B. 2021, MNRAS, 501, 3621

Arellano-Córdova, K. Z., & Rodríguez, M. 2020, MNRAS, 497, 672

Asano, R. S., Takeuchi, T. T., Hirashita, H., & Inoue, A. K. 2013, Earth, Planets and Space, 65, 213

Asplund, M., Grevesse, N., Sauval, A. J., & Scott, P. 2009, ARA&A, 47, 481

Astropy Collaboration, Robitaille, T. P., Tollerud, E. J., Greenfield, P., Droettboom, M., Bray, E., Aldcroft, T., Davis, M., Ginsburg, A., Price-Whelan, A. M., Kerzendorf, W. E., Conley, A., Crighton, N., Barbary, K., Muna, D., Ferguson, H., Grollier, F., Parikh, M. M., Nair, P. H., Unther, H. M., Deil, C., Woillez, J., Conseil, S., Kramer, R., Turner, J. E. H., Singer, L., Fox, R., Weaver, B. A., Zabalza, V., Edwards, Z. I., Azalee Bostroem, K., Burke, D. J., Casey, A. R., Crawford, S. M., Dencheva, N., Ely, J., Jenness, T., Labrie, K., Lim, P. L., Pierfederici, F., Pontzen, A., Ptak, A., Refsdal, B., Servillat, M., & Streicher, O. 2013, A&A, 558, A33

Bacon, R., Accardo, M., Adjali, L., Anwand, H., Bauer, S., Biswas, I., Blaizot, J., Boudon, D., Brau-Nogue, S., Brinchmann, J., Caillier, P., Capoani, L., Carollo, C. M., Contini, T., Couderc, P., Daguisé, E., Deiries, S., Delabre, B., Dreizler, S., Dubois, J., Dupieux, M., Dupuy, C., Emsellem, E., Fechner, T., Fleischmann, A., François, M., Gallou, G., Gharsa, T., Glindemann, A., Gojak, D., Guiderdoni, B., Hansali, G., Hahn, T., Jarno, A., Kelz, A., Koehler, C., Kosmalski, J., Laurent, F., Le Floch, M., Lilly, S. J., Lizon, J. L., Loupias, M., Manescau, A., Monstein, C., Nicklas, H., Olaya, J. C., Pares, L., Pasquini, L., Pécontal-Rousset, A., Pelló, R., Petit, C., Popow, E., Reiss, R., Remillieux, A., Renault, E., Roth, M., Rupprecht, G., Serre, D., Schaye, J., Soucail, G., Steinmetz, M., Streicher, O., Stuik, R., Valentin, H., Vernet, J., Weilbacher, P., Wisotzki, L., & Yerle, N. 2010, in Society of Photo-Optical Instrumentation Engineers (SPIE) Conference Series, Vol. 7735, Ground-based and Airborne Instrumentation for Astronomy III, ed. I. S. McLean, S. K. Ramsay, & H. Takami, 773508

Baldwin, J. A., Ferland, G. J., Martin, P. G., Corbin, M. R., Cota, S. A., Peterson, B. M., & Slettebak, A. 1991, ApJ, 374, 580

Baldwin, J. A., Phillips, M. M., & Terlevich, R. 1981, PASP, 93, 5

Baldwin, J. A., Verner, E. M., Verner, D. A., Ferland, G. J., Martin, P. G., Korista, K. T., & Rubin, R. H. 2000, ApJS, 129, 229

Barman, S., Neelamkodan, N., Madden, S. C., Sewilo, M., Kemper, F., Tokuda, K., Sanyal, S., & Onishi, T. 2022, ApJ, 930, 100

Barrow, K. S. S. 2020, MNRAS, 491, 4509

Belfiore, F., Westfall, K. B., Schaefer, A., Cappellari, M., Ji, X., Bershady, M. A., Tremonti, C., Law, D. R., Yan, R., Bundy, K., Shetty, S., Drory, N., Thomas, D., Emsellem, E., & Sánchez, S. F. 2019, AJ, 158, 160

Belfiore, F., Santoro, F., Groves, B., Schinnerer, E., Kreckel, K., Glover, S. C. O., Klessen, R. S., Emsellem, E., Blanc, G. A., Congiu, E., Barnes, A. T., Boquien, M., Chevance, M., Dale, D. A., Kruijssen, J. M. D., Leroy, A. K., Pan, H. A., Pessa, I., Schruba, A., & Williams, T. G. 2022, A&A, 659, A26

Berg, D. A., Chisholm, J., Erb, D. K., Skillman, E. D., Pogge, R. W., & Olivier, G. M. 2021, ApJ, 922, 170

Berg, D. A., Erb, D. K., Henry, R. B. C., Skillman, E. D., & McQuinn, K. B. W. 2019, ApJ, 874, 93

Berg, D. A., Pogge, R. W., Skillman, E. D., Croxall, K. V., Moustakas, J., Rogers, N. S. J., & Sun, J. 2020, ApJ, 893, 96

Berg, D. A., Skillman, E. D., Croxall, K. V., Pogge, R. W., Moustakas, J., & Johnson-Groh, M. 2015, ApJ, 806, 16

Berg, D. A., Skillman, E. D., Garnett, D. R., Croxall, K. V., Marble, A. R., Smith, J. D., Gordon, K., & Kennicutt, Robert C., J. 2013, ApJ, 775, 128

Berg, D. A., Skillman, E. D., Marble, A. R., van Zee, L., Engelbracht, C. W., Lee, J. C., Kennicutt, Robert C., J., Calzetti, D., Dale, D. A., & Johnson, B. D. 2012, ApJ, 754, 98

Bergeron, J. 1977, ApJ, 211, 62

Binette, L., Matadamas, R., Hägele, G. F., Nicholls, D. C., Magris C., G., Peña-Guerrero, M. Á., Morisset, C., & Rodríguez-González, A. 2012, A&A, 547, A29

Blanc, G. A., Kewley, L., Vogt, F. P. A., & Dopita, M. A. 2015, ApJ, 798, 99

Bomans, D. J., & Weis, K. 2002, in Astronomical Society of the Pacific Conference Series, Vol. 262, The High Energy Universe at Sharp Focus: Chandra Science, ed. E. M. Schlegel & S. D. Vrtilek, 141

Bresolin, F. 2007, ApJ, 656, 186

—. 2019, MNRAS, 488, 3826

Bresolin, F., Gieren, W., Kudritzki, R.-P., Pietrzyński, G., Urbaneja, M. A., & Carraro, G. 2009, ApJ, 700, 309

Bresolin, F., Kennicutt, R. C., & Ryan-Weber, E. 2012, ApJ, 750, 122

Calzetti, D., Lee, J. C., Sabbi, E., Adamo, A., Smith, L. J., Andrews, J. E., Ubeda, L., Bright, S. N., Thilker, D., Aloisi, A., Brown, T. M., Chandar, R., Christian, C., Cignoni, M., Clayton, G. C., da Silva, R., de Mink, S. E., Dobbs, C., Elmegreen, B. G., Elmegreen, D. M., Evans, A. S., Fumagalli, M., Gallagher, J. S., I., Gouliermis, D. A., Grebel, E. K., Herrero, A., Hunter, D. A., Johnson, K. E., Kennicutt, R. C., Kim, H., Krumholz, M. R., Lennon, D., Levay, K., Martin, C., Nair, P., Nota, A., Östlin, G., Pellerin, A., Prieto, J., Regan, M. W., Ryon, J. E., Schaerer, D., Schiminovich, D., Tosi, M., Van Dyk, S. D., Walterbos, R., Whitmore, B. C., & Wofford, A. 2015, AJ, 149, 51

Cameron, A. J., Katz, H., Rey, M. P., & Saxena, A. 2023, MNRAS, 523, 3516

Campbell, A., Terlevich, R., & Melnick, J. 1986, MNRAS, 223, 811

Cannon, J. M., Skillman, E. D., Garnett, D. R., & Dufour, R. J. 2002, ApJ, 565, 931

Cappellari, M. 2017, MNRAS, 466, 798

Cappellari, M., & Emsellem, E. 2004, PASP, 116, 138

Casini, R., & de Wijn, A. G. 2014, Journal of the Optical Society of America A, 31, 2002

Cerviño, M., Mas-Hesse, J. M., & Kunth, D. 2002, A&A, 392, 19

Chen, Y., Jones, T., Sanders, R., Fadda, D., Sutter, J., Minchin, R., Huntzinger, E., Senchyna, P., Stark, D., Spilker, J., Weiner, B., & Roberts-Borsani, G. 2023, Nature Astronomy, arXiv:2304.09898 [astro-ph.GA]

Chisholm, J., Rigby, J. R., Bayliss, M., Berg, D. A., Dahle, H., Gladders, M., & Sharon, K. 2019, ApJ, 882, 182

Congiu, E., Blanc, G. A., Belfiore, F., Santoro, F., Scheuermann, F., Kreckel, K., Emsellem, E., Groves, B., Pan, H.-A., Bigiel, F., Dale, D. A., Glover, S. C. O., Grasha, K., Egorov, O. V., Leroy, A., Schinnerer, E., Watkins, E. J., & Williams, T. G. 2023, A&A, 672, A148

Copetti, M. V. F. 2006a, A&A, 453, 943

—. 2006b, A&A, 453, 943

Corradi, R. L. M., García-Rojas, J., Jones, D., & Rodríguez-Gil, P. 2015, ApJ, 803, 99

Corradi, R. L. M., Grosso, N., Acker, A., Greimel, R., & Guillout, P. 2014, A&A, 570, A105

Cosens, M., Wright, S. A., Murray, N., Armus, L., Sandstrom, K., Do, T., Larson, K., Martinez, G., Sabhlok, S., Vayner, A., & Wiley, J. 2022, ApJ, 929, 74

Coziol, R., Reyes, R. E. C., Considère, S., Davoust, E., & Contini, T. 1999, A&A, 345, 733

Crowther, P. A., & Hadfield, L. J. 2006, A&A, 449, 711

Curran, P. A. 2014, arXiv e-prints, arXiv:1411.3816

Curti, M., Cresci, G., Mannucci, F., Marconi, A., Maiolino, R., & Esposito, S. 2017, MNRAS, 465, 1384

Curti, M., D'Eugenio, F., Carniani, S., Maiolino, R., Sandles, L., Witstok, J., Baker, W. M., Bennett, J. S., Piotrowska, J. M., Tacchella, S., Charlot, S., Nakajima, K., Maheson, G., Mannucci, F., Amiri, A., Arribas, S., Belfiore, F., Bonaventura, N. R., Bunker, A. J., Chevallard, J., Cresci, G., Curtis-Lake, E., Hayden-Pawson, C., Jones, G. C., Kumari, N., Laseter, I., Looser, T. J., Marconi, A., Maseda, M. V., Scholtz, J., Smit, R., Übler, H., & Wallace, I. E. B. 2023, MNRAS, 518, 425

da Silva, R. L., Fumagalli, M., & Krumholz, M. 2012, ApJ, 745, 145

Diaz, A. I., Terlevich, E., Vilchez, J. M., Pagel, B. E. J., & Edmunds, M. G. 1991, MNRAS, 253, 245

Díaz, Á. I., & Zamora, S. 2022, MNRAS, 511, 4377

Dopita, M. A., Kewley, L. J., Heisler, C. A., & Sutherland, R. S. 2000, ApJ, 542, 224

Dopita, M. A., Kewley, L. J., Sutherland, R. S., & Nicholls, D. C. 2016, Ap&SS, 361, 61

Dopita, M. A., & Sutherland, R. S. 1996, ApJS, 102, 161

Dors, O. L., J., Krabbe, A., Hägele, G. F., & Pérez-Montero, E. 2011, MNRAS, 415, 3616

Draine, B. T. 2011, Physics of the Interstellar and Intergalactic Medium (Princton University Press)

Egorov, O. V., Lozinskaya, T. A., Moiseev, A. V., & Shchekinov, Y. A. 2017, MNRAS, 464, 1833

Egorov, O. V., Lozinskaya, T. A., Moiseev, A. V., & Smirnov-Pinchukov, G. V. 2014, MNRAS, 444, 376

Egorov, O. V., Kreckel, K., Glover, S. C. O., Groves, B., Belfiore, F., Emsellem, E., Klessen, R. S., Leroy, A. K., Meidt, S. E., Sarbadhicary, S. K., Schinnerer, E., Watkins, E. J., Whitmore, B. C., Barnes, A. T., Congiu, E., Dale, D. A., Grasha, K., Larson, K. L., Lee, J. C., Méndez-Delgado, J. E., Thilker, D. A., & Williams, T. G. 2023, arXiv e-prints, arXiv:2307.10277

Emerick, A., Bryan, G. L., & Mac Low, M.-M. 2020, ApJ, 890, 155

Emsellem, E., Schinnerer, E., Santoro, F., Belfiore, F., Pessa, I., McElroy, R., Blanc, G. A., Congiu, E., Groves, B., Ho, I. T., Kreckel, K., Razza, A., Sanchez-Blazquez, P., Egorov, O., Faesi, C., Klessen, R. S., Leroy, A. K., Meidt, S., Querejeta, M., Rosolowsky, E., Scheuermann, F., Anand, G. S., Barnes, A. T., Bešlić, I., Bigiel, F., Boquien, M., Cao, Y., Chevance, M., Dale, D. A., Eibensteiner, C., Glover, S. C. O., Grasha, K., Henshaw, J. D., Hughes, A., Koch, E. W., Kruijssen, J. M. D., Lee, J., Liu, D., Pan, H.-A., Pety, J., Saito, T., Sandstrom, K. M., Schruba, A., Sun, J., Thilker, D. A., Usero, A., Watkins, E. J., & Williams, T. G. 2022, A&A, 659, A191

Esteban, C., García-Rojas, J., Carigi, L., Peimbert, M., Bresolin, F., López-Sánchez, A. R., & Mesa-Delgado, A. 2014, MNRAS, 443, 624

Esteban, C., Peimbert, M., García-Rojas, J., Ruiz, M. T., Peimbert, A., & Rodríguez, M. 2004, MNRAS, 355, 229

Esteban, C., Peimbert, M., Torres-Peimbert, S., & Rodríguez, M. 2002, ApJ, 581, 241

Ferland, G. J., Porter, R. L., van Hoof, P. A. M., Williams, R. J. R., Abel, N. P., Lykins, M. L., Shaw, G., Henney, W. J., & Stancil, P. C. 2013, RMxAA, 49, 137

Ferland, G. J., Chatzikos, M., Guzmán, F., Lykins, M. L., van Hoof, P. A. M., Williams, R. J. R., Abel, N. P., Badnell, N. R., Keenan, F. P., Porter, R. L., & Stancil, P. C. 2017, RMxAA, 53, 385

Field, G. B., Goldsmith, D. W., & Habing, H. J. 1969, ApJL, 155, L149

Fisher, D. B., Bolatto, A. D., Herrera-Camus, R., Draine, B. T., Donaldson, J., Walter, F., Sandstrom, K. M., Leroy, A. K., Cannon, J., & Gordon, K. 2014, Nature, 505, 186

Fitzpatrick, E. L. 1999, PASP, 111, 63

Freedman, W. L., Madore, B. F., Gibson, B. K., Ferrarese, L., Kelson, D. D., Sakai, S., Mould, J. R., Kennicutt, Robert C., J., Ford, H. C., Graham, J. A., Huchra, J. P., Hughes, S. M. G., Illingworth, G. D., Macri, L. M., & Stetson, P. B. 2001, ApJ, 553, 47

Froese Fischer, C., & Tachiev, G. 2004, Atomic Data and Nuclear Data Tables, 87, 1

Froese Fischer, C., Tachiev, G., & Irimia, A. 2006, Atomic Data and Nuclear Data Tables, 92, 607

García-Rojas, J., & Esteban, C. 2007, ApJ, 670, 457

Garnett, D. R. 1990, ApJ, 363, 142

—. 1992, AJ, 103, 1330

Garnett, D. R., Kennicutt, Robert C., J., Chu, Y.-H., & Skillman, E. D. 1991, ApJ, 373, 458

Goswami, S., Vilchez, J. M., Perez-Diaz, B., Silva, L., Bressan, A., & Perez-Montero, E. 2024, arXiv e-prints, arXiv:2402.13240

Grasha, K., Calzetti, D., Adamo, A., Kennicutt, R. C., Elmegreen, B. G., Messa, M., Dale, D. A., Fedorenko, K., Mahadevan, S., Grebel, E. K., Fumagalli, M., Kim, H., Dobbs, C. L., Gouliermis, D. A., Ashworth, G., Gallagher, J. S., Smith, L. J., Tosi, M., Whitmore, B. C., Schinnerer, E., Colombo, D., Hughes, A., Leroy, A. K., & Meidt, S. E. 2019, MNRAS, 483, 4707

Grasha, K., Chen, Q. H., Battisti, A. J., Acharyya, A., Ridolfo, S., Poehler, E., Mably, S., Verma, A. A., Hayward, K. L., Kharbanda, A., Poetrodjojo, H., Seibert, M., Rich, J. A., Madore, B. F., & Kewley, L. J. 2022a, ApJ, 929, 118

—. 2022b, ApJ, 929, 118

Grisé, F., Pakull, M. W., Soria, R., Motch, C., Smith, I. A., Ryder, S. D., & Böttcher, M. 2008, A&A, 486, 151

Groves, B., Kreckel, K., Santoro, F., Belfiore, F., Zavodnik, E., Congiu, E., Egorov, O. V., Emsellem, E., Grasha, K., Leroy, A., Scheuermann, F., Schinnerer, E., Watkins, E. J., Barnes, A. T., Bigiel, F., Dale, D. A., Glover, S. C. O., Pessa, I., Sanchez-Blazquez, P., & Williams, T. G. 2023, MNRAS, 520, 4902

Guseva, N. G., Izotov, Y. I., Stasińska, G., Fricke, K. J., Henkel, C., & Papaderos, P. 2011, A&A, 529, A149

Guseva, N. G., Izotov, Y. I., & Thuan, T. X. 2000, ApJ, 531, 776

Harris, C. R., Millman, K. J., van der Walt, S. J., Gommers, R., Virtanen, P., Cournapeau, D., Wieser, E., Taylor, J., Berg, S., Smith, N. J., Kern, R., Picus, M., Hoyer, S., van Kerkwijk, M. H., Brett, M., Haldane, A., del Río, J. F., Wiebe, M., Peterson, P., Gérard-Marchant, P., Sheppard, K., Reddy, T., Weckesser, W., Abbasi, H., Gohlke, C., & Oliphant, T. E. 2020, Nature, 585, 357

Henry, R. B. C., Nava, A., & Prochaska, J. X. 2006, ApJ, 647, 984

Hernandez, A. K., Wakker, B. P., Benjamin, R. A., French, D., Kerp, J., Lockman, F. J., O'Toole, S., & Winkel, B. 2013, ApJ, 777, 19

Hill, J. K., & Hollenbach, D. J. 1978, ApJ, 225, 390

Hily-Blant, P., Pineau des Forêts, G., Faure, A., & Lique, F. 2022, A&A, 658, A168

Ho, I. T., Medling, A. M., Groves, B., Rich, J. A., Rupke, D. S. N., Hampton, E., Kewley, L. J., Bland-Hawthorn, J., Croom, S. M., Richards, S., Schaefer, A. L., Sharp, R., & Sweet, S. M. 2016, Ap&SS, 361, 280

Ho, I. T., Seibert, M., Meidt, S. E., Kudritzki, R.-P., Kobayashi, C., Groves, B. A., Kewley, L. J., Madore, B. F., Rich, J. A., Schinnerer, E., D'Agostino, J., & Poetrodjojo, H. 2017, ApJ, 846, 39

Hunt, L. K., Dyer, K. K., & Thuan, T. X. 2005, A&A, 436, 837

Hunt, L. K., Thuan, T. X., & Izotov, Y. I. 2003, ApJ, 588, 281

Hunter, D. A., & Thronson, Harley A., J. 1995, ApJ, 452, 238

Iwamoto, K., Brachwitz, F., Nomoto, K., Kishimoto, N., Umeda, H., Hix, W. R., & Thielemann, F.-K. 1999, ApJS, 125, 439

Izotov, Y. I., Foltz, C. B., Green, R. F., Guseva, N. G., & Thuan, T. X. 1997, ApJL, 487, L37

Izotov, Y. I., Stasińska, G., Meynet, G., Guseva, N. G., & Thuan, T. X. 2006, A&A, 448, 955

Izotov, Y. I., & Thuan, T. X. 1998, ApJ, 497, 227

—. 1999, ApJ, 511, 639

Jacobs, B. A., Rizzi, L., Tully, R. B., Shaya, E. J., Makarov, D. I., & Makarova, L. 2009, AJ, 138, 332

Jamet, L., Stasińska, G., Pérez, E., González Delgado, R. M., & Vílchez, J. M. 2005, A&A, 444, 723

Jin, Y., Kewley, L. J., & Sutherland, R. S. 2022, ApJL, 934, L8

Jin, Y., Sutherland, R., Kewley, L. J., & Nicholls, D. C. 2023, ApJ, 958, 179

Kaaret, P., & Corbel, S. 2009, ApJ, 697, 950

Kaaret, P., & Feng, H. 2013, ApJ, 770, 20

Kaaret, P., Ward, M. J., & Zezas, A. 2004, MNRAS, 351, L83

Kainulainen, J., Stutz, A. M., Stanke, T., Abreu-Vicente, J., Beuther, H., Henning, T., Johnston, K. G., & Megeath, S. T. 2017, A&A, 600, A141

Kaler, J. B., Aller, L. H., Czyzak, S. J., & Epps, H. W. 1976, ApJS, 31, 163

Kauffmann, G., Heckman, T. M., Tremonti, C., Brinchmann, J., Charlot, S., White, S. D. M., Ridgway, S. E., Brinkmann, J., Fukugita, M., Hall, P. B., Ivezić, Ž., Richards, G. T., & Schneider, D. P. 2003, MNRAS, 346, 1055

Kehrig, C., Guerrero, M. A., Vílchez, J. M., & Ramos-Larios, G. 2021, The Astrophysical Journal, 908, L54

Kehrig, C., Vílchez, J. M., Guerrero, M. A., Iglesias-Páramo, J., Hunt, L. K., Duarte-Puertas, S., & Ramos-Larios, G. 2018, MNRAS, 480, 1081

Kehrig, C., Vílchez, J. M., Pérez-Montero, E., Iglesias-Páramo, J., Brinchmann, J., Kunth, D., Durret, F., & Bayo, F. M. 2015, ApJL, 801, L28

Kehrig, C., Oey, M. S., Crowther, P. A., Fogel, J., Pellegrini, E., Schnurr, O., Schaerer, D., Massey, P., & Roth, K. 2011, A&A, 526, A128

Kehrig, C., Vílchez, J. M., Pérez-Montero, E., Iglesias-Páramo, J., Hernández-Fernández, J. D., Duarte Puertas, S., Brinchmann, J., Durret, F., & Kunth, D. 2016, MNRAS, 459, 2992

Kelly, B. C. 2007, ApJ, 665, 1489

Kennicutt, R. C., J. 1984, ApJ, 287, 116

Kennicutt, Robert C., J., Bresolin, F., & Garnett, D. R. 2003, ApJ, 591, 801

Kennicutt, Robert C., J., & Garnett, D. R. 1996, ApJ, 456, 504

Kewley, L. J., & Dopita, M. A. 2002, ApJS, 142, 35

Kewley, L. J., & Ellison, S. L. 2008, ApJ, 681, 1183

Kewley, L. J., Heisler, C. A., Dopita, M. A., & Lumsden, S. 2001, ApJS, 132, 37

King, A., & Lasota, J.-P. 2020, MNRAS, 494, 3611

Kisielius, R., Storey, P. J., Ferland, G. J., & Keenan, F. P. 2009, MNRAS, 397, 903

Kobulnicky, H. A., & Kewley, L. J. 2004, ApJ, 617, 240

Konidaris, N. P., Drory, N., Froning, C. S., Hebert, A., Bilgi, P., Blanc, G. A., Lanz, A. E., Hull, C. L., Kollmeier, J. A., Ramirez, S., Wachter, S., Kreckel, K., Pak, S., Pellegrini, E., Almeida, A., Case, S., Zhelem, R., Feger, T., Lawrence, J., Lesser, M., Herbst, T., Sanchez-Gallego, J., Bershady, M. A., Chattopadhyay, S., Hauser, A., Smith, M., Wolf, M. J., & Yan, R. 2020, in Society of Photo-Optical Instrumentation Engineers (SPIE) Conference Series, Vol. 11447, Ground-based and Airborne Instrumentation for Astronomy VIII, ed. C. J. Evans, J. J. Bryant, & K. Motohara, 1144718

Koo, B.-C., Rho, J., Reach, W. T., Jung, J., & Mangum, J. G. 2001, ApJ, 552, 175

Kothes, R., & Kerton, C. R. 2002, A&A, 390, 337

Kourkchi, E., Courtois, H. M., Graziani, R., Hoffman, Y., Pomarède, D., Shaya, E. J., & Tully, R. B. 2020, AJ, 159, 67

Kourkchi, E., & Tully, R. B. 2017, ApJ, 843, 16

Kreckel, K., Ho, I. T., Blanc, G. A., Groves, B., Santoro, F., Schinnerer, E., Bigiel, F., Chevance, M., Congiu, E., Emsellem, E., Faesi, C., Glover, S. C. O., Grasha, K., Kruijssen, J. M. D., Lang, P., Leroy, A. K., Meidt, S. E., McElroy, R., Pety, J., Rosolowsky, E., Saito, T., Sandstrom, K., Sanchez-Blazquez, P., & Schruba, A. 2019, ApJ, 887, 80

Kreckel, K., Ho, I. T., Blanc, G. A., Glover, S. C. O., Groves, B., Rosolowsky, E., Bigiel, F., Boquíen, M., Chevance, M., Dale, D. A., Deger, S., Emsellem, E., Grasha, K., Kim, J. J., Klessen, R. S., Kruijssen, J. M. D., Lee, J. C., Leroy, A. K., Liu, D., McElroy, R., Meidt, S. E., Pessa, I., Sanchez-Blazquez, P., Sandstrom, K., Santoro, F., Scheuermann, F., Schinnerer, E., Schruba, A., Utomo, D., Watkins, E. J., & Williams, T. G. 2020, MNRAS, 499, 193

Kreckel, K., Egorov, O. V., Belfiore, F., Groves, B., Glover, S. C. O., Klessen, R. S., Sandstrom, K., Bigiel, F., Dale, D. A., Grasha, K., Scheuermann, F., Schinnerer, E., & Williams, T. G. 2022, A&A, 667, A16

Krumholz, M. R., & Ting, Y.-S. 2018, MNRAS, 475, 2236

Larson, K. L., Lee, J. C., Thilker, D. A., Whitmore, B. C., Deger, S., Lilly, J., Chandar, R., Dale, D. A., Bigiel, F., Grasha, K., Groves, B., Hannon, S., Klessen, R. S., Kreckel, K., Kruijssen, J. M. D., Leroy, A. K., Pan, H.-A., Rosolowsky, E., Schinnerer, E., Schruba, A., Watkins, E. J., & Williams, T. G. 2023, MNRAS, 523, 6061

Laseter, I. H., Maseda, M. V., Curti, M., Maiolino, R., D'Eugenio, F., Cameron, A. J., Looser, T. J., Arribas, S., Baker, W. M., Bhatawdekar, R., Boyett, K., Bunker, A. J., Carniani, S., Charlot, S., Chevallard, J., Curtis-lake, E., Egami, E., Eisenstein, D. J., Hainline, K., Hausen, R., Ji, Z., Kumari, N., Perna, M., Rawle, T., Rix, H.-W., Robertson, B., Rodríguez Del Pino, B., Sandles, L., Scholtz, J., Smit, R., Tacchella, S., Übler, H., Williams, C. C., Willott, C., & Witstok, J. 2024, A&A, 681, A70

Law, D. R., Cherinka, B., Yan, R., Andrews, B. H., Bershady, M. A., Bizyaev, D., Blanc, G. A., Blanton, M. R., Bolton, A. S., Brownstein, J. R., Bundy, K., Chen, Y., Drory, N., D'Souza, R., Fu, H., Jones, A., Kauffmann, G., MacDonald, N., Masters, K. L., Newman, J. A., Parejko, J. K., Sánchez-Gallego, J. R., Sánchez, S. F., Schlegel, D. J., Thomas, D., Wake, D. A., Weijmans, A.-M., Westfall, K. B., & Zhang, K. 2016, AJ, 152, 83

Lebouteiller, V., Péquignot, D., Cormier, D., Madden, S., Pakull, M. W., Kunth, D., Galliano, F., Chevance, M., Heap, S. R., Lee, M. Y., & Polles, F. L. 2017, A&A, 602, A45

Lee, J. C., Whitmore, B. C., Thilker, D. A., Deger, S., Larson, K. L., Ubeda, L., Anand, G. S., Boquien, M., Chandar, R., Dale, D. A., Emsellem, E., Leroy, A. K., Rosolowsky, E., Schinnerer, E., Schmidt, J., Lilly, J., Turner, J., Van Dyk, S., White, R. L., Barnes, A. T., Belfiore, F., Bigiel, F., Blanc, G. A., Cao, Y., Chevance, M., Congiu, E., Egorov, O. V., Glover, S. C. O., Grasha, K., Groves, B., Henshaw, J. D., Hughes, A., Klessen, R. S., Koch, E., Kreckel, K., Kruijssen, J. M. D., Liu, D., Lopez, L. A., Mayker, N., Meidt, S. E., Murphy, E. J., Pan, H.-A., Pety, J., Querejeta, M., Razza, A., Saito, T., Sánchez-Blázquez, P., Santoro, F., Sardone, A., Scheuermann, F., Schruba, A., Sun, J., Usero, A., Watkins, E., & Williams, T. G. 2022, ApJS, 258, 10

Lequeux, J., Peimbert, M., Rayo, J. F., Serrano, A., & Torres-Peimbert, S. 1979, A&A, 80, 155

Leroy, A. K., Schinnerer, E., Hughes, A., Rosolowsky, E., Pety, J., Schruba, A., Usero, A., Blanc, G. A., Chevance, M., Emsellem, E., Faesi, C. M., Herrera, C. N., Liu, D., Meidt, S. E., Querejeta, M., Saito, T., Sandstrom, K. M., Sun, J., Williams, T. G., Anand, G. S., Barnes, A. T., Behrens, E. A., Belfiore, F., Benincasa, S. M., Bešlić, I., Bigiel, F., Bolatto, A. D., den Brok, J. S., Cao, Y., Chandar, R., Chastenet, J., Chiang, I. D., Congiu, E., Dale, D. A., Deger, S., Eibensteiner, C., Egorov, O. V., García-Rodríguez, A., Glover, S. C. O., Grasha, K., Henshaw, J. D., Ho, I. T., Kepley, A. A., Kim, J., Klessen, R. S., Kreckel, K., Koch, E. W., Kruijssen, J. M. D., Larson, K. L., Lee, J. C., Lopez, L. A., Machado, J., Mayker, N., McElroy, R., Murphy, E. J., Ostriker, E. C., Pan, H.-A., Pessa, I., Puschnig, J., Razza, A., Sánchez-Blázquez, P., Santoro, F., Sardone, A., Scheuermann, F., Sliwa, K., Sormani, M. C., Stuber, S. K., Thilker, D. A., Turner, J. A., Utomo, D., Watkins, E. J., & Whitmore, B. 2021a, ApJS, 257, 43

Leroy, A. K., Hughes, A., Liu, D., Pety, J., Rosolowsky, E., Saito, T., Schinnerer, E., Schruba, A., Usero, A., Faesi, C. M., Herrera, C. N., Chevance, M., Hygate, A. P. S., Kepley, A. A., Koch, E. W., Querejeta, M., Sliwa, K., Will, D., Wilson, C. D., Anand, G. S., Barnes, A., Belfiore, F., Bešlić, I., Bigiel, F., Blanc, G. A., Bolatto, A. D., Boquien, M., Cao, Y., Chandar, R., Chastenet, J., Chiang, I.-D., Congiu, E., Dale, D. A., Deger, S., den Brok, J. S., Eibensteiner, C., Emsellem, E., García-Rodríguez, A., Glover, S. C. O., Grasha, K., Groves, B., Henshaw, J. D., Jiménez Donaire, M. J., Kim, J., Klessen, R. S., Kreckel, K., Kruijssen, J. M. D., Larson, K. L., Lee, J. C., Mayker, N., McElroy, R., Meidt, S. E., Mok, A., Pan, H.-A., Puschnig, J., Razza, A., Sánchez-Bl'azquez, P., Sandstrom, K. M., Santoro, F., Sardone, A., Scheuermann, F., Sun, J., Thilker, D. A., Turner, J. A., Ubeda, L., Utomo, D., Watkins, E. J., & Williams, T. G. 2021b, ApJS, 255, 19

Luridiana, V., Morisset, C., & Shaw, R. A. 2015, A&A, 573, A42

Makarov, D., Prugniel, P., Terekhova, N., Courtois, H., & Vauglin, I. 2014, A&A, 570, A13

Mayya, Y. D., Plat, A., Gómez-González, V. M. A., Zaragoza-Cardiel, J., Charlot, S., & Bruzual, G. 2023, MNRAS, 519, 5492

McLeod, A. F., Weilbacher, P. M., Ginsburg, A., Dale, J. E., Ramsay, S., & Testi, L. 2016, MNRAS, 455, 4057

Méndez-Delgado, J. E., Esteban, C., García-Rojas, J., & Henney, W. J. 2022, MNRAS, 514, 744

Méndez-Delgado, J. E., Esteban, C., García-Rojas, J., Henney, W. J., Mesa-Delgado, A., & Arellano-Córdova, K. Z. 2021, MNRAS, 502, 1703

Méndez-Delgado, J. E., Esteban, C., García-Rojas, J., Kreckel, K., & Peimbert, M. 2023a, Nature, 618, 249

Méndez-Delgado, J. E., Esteban, C., García-Rojas, J., Arellano-Córdova, K. Z., Kreckel, K., Gómez-Llanos, V., Egorov, O. V., Peimbert, M., & Orte-García, M. 2023b, MNRAS, 523, 2952

Mendoza, C., & Bautista, M. A. 2014, ApJ, 785, 91

Mendoza, C., Méndez-Delgado, J. E., Bautista, M., García-Rojas, J., & Morisset, C. 2023, Atoms, 11, 63

Mollá, M., Wekesa, S., Cavichia, O., Díaz, Á. I., Gibson, B. K., Rosales-Ortega, F. F., Ascasibar, Y., Wamalwa, D. S., & Sánchez, S. F. 2019, MNRAS, 490, 665

Moon, D.-S., Harrison, F. A., Cenko, S. B., & Shariff, J. A. 2011, ApJL, 731, L32

Morisset, C. 2009, MmSAI, 80, 397

Morrissey, P., Matuszewski, M., Martin, D. C., Neill, J. D., Epps, H., Fucik, J., Weber, B., Darvish, B., Adkins, S., Allen, S., Bartos, R., Belicki, J., Cabak, J., Callahan, S., Cowley, D., Crabill, M., Deich, W., Delecroix, A., Doppman, G., Hilyard, D., James, E., Kaye, S., Kokorowski, M., Kwok, S., Lanclos, K., Milner, S., Moore, A., O'Sullivan, D., Parihar, P., Park, S., Phillips, A., Rizzi, L., Rockosi, C., Rodriguez, H., Salaun, Y., Seaman, K., Sheikh, D., Weiss, J., & Zarzaca, R. 2018, ApJ, 864, 93

Nakajima, K., Ouchi, M., Xu, Y., Rauch, M., Harikane, Y., Nishigaki, M., Isobe, Y., Kusakabe, H., Nagao, T., Ono, Y., Onodera, M., Sugahara, Y., Kim, J. H., Komiyama, Y., Lee, C.-H., & Zahedy, F. S. 2022, ApJS, 262, 3

Nazé, Y., Rauw, G., Manfroid, J., Chu, Y. H., & Vreux, J. M. 2003a, A&A, 401, L13

—. 2003b, A&A, 408, 171

Nicholls, D. C., Kewley, L. J., & Sutherland, R. S. 2020, PASP, 132, 033001

Nicholls, D. C., Sutherland, R. S., Dopita, M. A., Kewley, L. J., & Groves, B. A. 2017, MNRAS, 466, 4403

Núñez-Díaz, M., Esteban, C., & Mesa-Delgado, A. 2013, in Highlights of Spanish Astrophysics VII, ed. J. C. Guirado, L. M. Lara, V. Quilis, & J. Gorgas, 594

Nugent, P., Sullivan, M., Ellis, R., Gal-Yam, A., Leonard, D. C., Howell, D. A., Astier, P., Carlberg, R. G., Conley, A., Fabbro, S., Fouchez, D., Neill, J. D., Pain, R., Perrett, K., Pritchet, C. J., & Regnault, N. 2006, ApJ, 645, 841

O'Dell, C. R. 2001, ARA&A, 39, 99

O'Dell, C. R., Ferland, G. J., & Peimbert, M. 2017, MNRAS, 464, 4835

O'Donnell, J. E. 1994, ApJ, 422, 158

Oh, K., Sarzi, M., Schawinski, K., & Yi, S. K. 2011, ApJS, 195, 13

Osterbrock, D. E., & Ferland, G. J. 2006, Astrophysics of gaseous nebulae and active galactic nuclei (University Science Books)

Östlin, G., & Mouhcine, M. 2005, A&A, 433, 797

Ostriker, E. C., McKee, C. F., & Leroy, A. K. 2010, ApJ, 721, 975

Padmanabhan, N., Schlegel, D. J., Finkbeiner, D. P., Barentine, J. C., Blanton, M. R., Brewington, H. J., Gunn, J. E., Harvanek, M., Hogg, D. W., Ivezić, Ž., Johnston, D., Kent, S. M., Kleinman, S. J., Knapp, G. R., Krzesinski, J., Long, D., Neilsen, Eric H., J., Nitta, A., Loomis, C., Lupton, R. H., Roweis, S., Snedden, S. A., Strauss, M. A., & Tucker, D. L. 2008, ApJ, 674, 1217

Pagel, B. E. J., Edmunds, M. G., Blackwell, D. E., Chun, M. S., & Smith, G. 1979, MNRAS, 189, 95

Pagel, B. E. J., Edmunds, M. G., & Smith, G. 1980, MNRAS, 193, 219

Pakull, M. W., & Angebault, L. P. 1986, Nature, 322, 511

Pakull, M. W., Grisé, F., & Motch, C. 2006, in IAU Symposium, Vol. 230, Populations of High Energy Sources in Galaxies, ed. E. J. A. Meurs & G. Fabbiano, 293

Pakull, M. W., & Mirioni, L. 2002, arXiv e-prints, astro

Peña-Guerrero, M. A., Peimbert, A., & Peimbert, M. 2012, ApJL, 756, L14

Peimbert, A., Peña-Guerrero, M. A., & Peimbert, M. 2012, ApJ, 753, 39

Peimbert, M. 1967, ApJ, 150, 825

—. 1971, Boletin de los Observatorios Tonantzintla y Tacubaya, 6, 29

Peimbert, M., & Costero, R. 1969, Boletin de los Observatorios Tonantzintla y Tacubaya, 5, 3

Peimbert, M., Peimbert, A., & Delgado-Inglada, G. 2017, PASP, 129, 082001

Peimbert, M., Sarmiento, A., & Fierro, J. 1991, PASP, 103, 815

Péquignot, D. 2008, A&A, 478, 371

Pérez-Díaz, B., Pérez-Montero, E., Fernández-Ontiveros, J. A., Vílchez, J. M., Hernán-Caballero, A., & Amorín, R. 2024, arXiv e-prints, arXiv:2403.02903

Pérez-Montero, E., Zinchenko, I. A., Vílchez, J. M., Zurita, A., Florido, E., & Pérez-Díaz, B. 2023, A&A, 669, A88

Pilyugin, L. S., & Grebel, E. K. 2016, MNRAS, 457, 3678

Pogge, R. W., Owen, J. M., & Atwood, B. 1992, ApJ, 399, 147

Privon, G. C., Ricci, C., Aalto, S., Viti, S., Armus, L., Díaz-Santos, T., González-Alfonso, E., Iwasawa, K., Jeff, D. L., Treister, E., Bauer, F., Evans, A. S., Garg, P., Herrero-Illana, R., Mazzarella, J. M., Larson, K., Blecha, L., Barcos-Muñoz, L., Charmandaris, V., Stierwalt, S., & Pérez-Torres, M. A. 2020, ApJ, 893, 149

Rickards Vaught, R. J., Sandstrom, K. M., & Hunt, L. K. 2021, ApJL, 911, L17

Rickards Vaught, R. J., Sandstrom, K. M., Belfiore, F., Kreckel, K., Méndez-Delgado, J. E., Emsellem, E., Groves, B., Blanc, G. A., Dale, D. A., Egorov, O. V., Glover, S. C. O., Grasha, K., Klessen, R. S., Neumann, J., & Williams, T. G. 2024, ApJ, 966, 130

Rodríguez, M. 1999, A&A, 348, 222

Rodríguez, M., & García-Rojas, J. 2010, ApJ, 708, 1551

Rogers, N. S. J., Skillman, E. D., Pogge, R. W., Berg, D. A., Croxall, K. V., Bartlett, J., Arellano-Córdova, K. Z., & Moustakas, J. 2022, ApJ, 939, 44

Rogers, N. S. J., Skillman, E. D., Pogge, R. W., Berg, D. A., Moustakas, J., Croxall, K. V., & Sun, J. 2021, ApJ, 915, 21

Rola, C., & Pelat, D. 1994, A&A, 287, 676

Rubin, R. H. 1989, ApJS, 69, 897

Rubin, R. H., Simpson, J. P., Colgan, S. W. J., Dufour, R. J., Kader, J., McNabb, I. A., Pauldrach, A. W. A., & Weber, J. A. 2016, MNRAS, 459, 1875

Rynkun, P., Gaigalas, G., & Jönsson, P. 2019, A&A, 623, A155

Sanders, R. L., Shapley, A. E., Topping, M. W., Reddy, N. A., & Brammer, G. B. 2024, ApJ, 962, 24

Santoro, F., Kreckel, K., Belfiore, F., Groves, B., Congiu, E., Thilker, D. A., Blanc, G. A., Schinnerer, E., Ho, I. T., Diederik Kruijssen, J. M., Meidt, S., Klessen, R. S., Schruba, A., Querejeta, M., Pessa, I., Chevance, M., Kim, J., Emsellem, E., McElroy, R., Barnes, A. T., Bigiel, F., Boquien, M., Dale, D. A., Glover, S. C. O., Grasha, K., Lee, J., Leroy, A. K., Pan, H.-A., Rosolowsky, E., Saito, T., Sanchez-Blazquez, P., Watkins, E. J., & Williams, T. G. 2022, A&A, 658, A188

Sarzi, M., Falcón-Barroso, J., Davies, R. L., Bacon, R., Bureau, M., Cappellari, M., de Zeeuw, P. T., Emsellem, E., Fathi, K., Krajnović, D., Kuntschner, H., McDermid, R. M., & Peletier,

R. F. 2006, MNRAS, 366, 1151

Schaefer, A. L., Tremonti, C., Belfiore, F., Pace, Z., Bershady, M. A., Andrews, B. H., & Drory, N. 2020, ApJL, 890, L3

Schaerer, D., Fragos, T., & Izotov, Y. I. 2019, A&A, 622, L10

Scheuermann, F., Kreckel, K., Anand, G. S., Blanc, G. A., Congiu, E., Santoro, F., Van Dyk, S. D., Barnes, A. T., Bigiel, F., Glover, S. C. O., Groves, B., Klessen, R. S., Kruijssen, J. M. D., Rosolowsky, E., Schinnerer, E., Schruba, A., Watkins, E. J., & Williams, T. G. 2022, MNRAS, 511, 6087

Scheuermann, F., Kreckel, K., Barnes, A. T., Belfiore, F., Groves, B., Hannon, S., Lee, J. C., Minsley, R., Rosolowsky, E., Bigiel, F., Blanc, G. A., Boquien, M., Dale, D. A., Deger, S., Egorov, O. V., Emsellem, E., Glover, S. C. O., Grasha, K., Hassani, H., Jeffreson, S. M. R., Klessen, R. S., Kruijssen, J. M. D., Larson, K. L., Leroy, A. K., Lopez, L. A., Pan, H.-A., Sánchez-Blázquez, P., Santoro, F., Schinnerer, E., Thilker, D. A., Whitmore, B. C., Watkins, E. J., & Williams, T. G. 2023, MNRAS, 522, 2369

Searle, L. 1971, ApJ, 168, 327

Searle, L., & Sargent, W. L. W. 1972, ApJ, 173, 25

Seaton, M. J., & Osterbrock, D. E. 1957, ApJ, 125, 66

Senchyna, P., Stark, D. P., Mirocha, J., Reines, A. E., Charlot, S., Jones, T., & Mulchaey, J. S. 2020, MNRAS, 494, 941

Sharda, P., Ginzburg, O., Krumholz, M. R., Forbes, J. C., Wisnioski, E., Mingozzi, M., Zovaro, H. R. M., & Dekel, A. 2024, MNRAS, 528, 2232

Shaya, E. J., Tully, R. B., Hoffman, Y., & Pomarède, D. 2017, ApJ, 850, 207

Shirazi, M., & Brinchmann, J. 2012, MNRAS, 421, 1043

Skillman, E. D., Berg, D. A., Pogge, R. W., Moustakas, J., Rogers, N. S. J., & Croxall, K. V. 2020, ApJ, 894, 138

Skillman, E. D., & Kennicutt, Robert C., J. 1993, ApJ, 411, 655

Spitoni, E., Cescutti, G., Minchev, I., Matteucci, F., Silva Aguirre, V., Martig, M., Bono, G., & Chiappini, C. 2019, A&A, 628, A38

Spitoni, E., Cescutti, G., Recio-Blanco, A., Minchev, I., Poggio, E., Palicio, P. A., Matteucci, F., Peirani, S., Barbillon, M., & Vasini, A. 2023, A&A, 680, A85

Stasińska, G. 1980, A&A, 84, 320

Stasińska, G., Morisset, C., Simón-Díaz, S., Bresolin, F., Schaerer, D., & Brandl, B. 2013, A&A, 551, A82

Stasińska, G., & Schaerer, D. 1999, A&A, 351, 72

Storey, P. J., & Hummer, D. G. 1995, MNRAS, 272, 41

Storey, P. J., Sochi, T., & Badnell, N. R. 2014, MNRAS, 441, 3028

Sutherland, R., Dopita, M., Binette, L., & Groves, B. 2018, MAPPINGS V: Astrophysical plasma modeling code, Astrophysics Source Code Library, record ascl:1807.005

Tan, S., & Parker, Q. A. 2024, ApJL, 961, L47

Tayal, S. S. 2011, ApJS, 195, 12

Tayal, S. S., & Gupta, G. P. 1999, ApJ, 526, 544

Tayal, S. S., & Zatsarinny, O. 2010, ApJS, 188, 32

Taylor, J. 1997, Introduction to Error Analysis, the Study of Uncertainties in Physical Measurements, 2nd Edition (Princton University Press)

Thilker, D. A., Braun, R., & Walterbos, R. A. M. 2000, AJ, 120, 3070

Thilker, D. A., Whitmore, B. C., Lee, J. C., Deger, S., Chandar, R., Larson, K. L., Hannon, S., Ubeda, L., Dale, D. A., Glover, S. C. O., Grasha, K., Klessen, R. S., Kruijssen, J. M. D., Rosolowsky, E., Schruba, A., White, R. L., & Williams, T. G. 2022, MNRAS, 509, 4094

Thuan, T. X., Bauer, F. E., Papaderos, P., & Izotov, Y. I. 2004, ApJ, 606, 213

Thuan, T. X., & Izotov, Y. I. 2005, ApJS, 161, 240

Tokunaga, A. T., & Vacca, W. D. 2005, PASP, 117, 421

Topping, M. W., Stark, D. P., Senchyna, P., Plat, A., Zitrin, A., Endsley, R., Charlot, S., Furtak, L. J., Maseda, M. V., Smit, R., Mainali, R., Chevallard, J., Molyneux, S., & Rigby, J. R. 2024, MNRAS, 529, 3301

Tremblin, P., Anderson, L. D., Didelon, P., Raga, A. C., Minier, V., Ntormousi, E., Pettitt, A., Pinto, C., Samal, M. R., Schneider, N., & Zavagno, A. 2014, A&A, 568, A4

Vale Asari, N., Stasińska, G., Morisset, C., & Cid Fernandes, R. 2016, MNRAS, 460, 1739

van der Marel, R. P., & Franx, M. 1993, ApJ, 407, 525

van Dokkum, P., Wasserman, A., Danieli, S., Abraham, R., Brodie, J., Conroy, C., Forbes, D. A., Martin, C., Matuszewski, M., Romanowsky, A. J., & Villaume, A. 2019, ApJ, 880, 91

van Loon, M. L., Mitchell, P. D., & Schaye, J. 2021, MNRAS, arXiv:2101.11021 [astro-ph.GA]

van Zee, L., & Haynes, M. P. 2006, ApJ, 636, 214

Vazdekis, A., Koleva, M., Ricciardelli, E., Röck, B., & Falcón-Barroso, J. 2016, MNRAS, 463, 3409

Vazdekis, A., Sánchez-Blázquez, P., Falcón-Barroso, J., Cenarro, A. J., Beasley, M. A., Cardiel, N., Gorgas, J., & Peletier, R. F. 2010, MNRAS, 404, 1639

Vermeij, R., & van der Hulst, J. M. 2002, A&A, 391, 1081

Vila-Costas, M. B., & Edmunds, M. G. 1993, MNRAS, 265, 199

Vilchez, J. M., & Esteban, C. 1996, MNRAS, 280, 720

Vílchez, J. M., & Iglesias-Páramo, J. 1998, ApJ, 508, 248

Vilchez, J. M., & Pagel, B. E. J. 1988, MNRAS, 231, 257

Vincenzo, F., Belfiore, F., Maiolino, R., Matteucci, F., & Ventura, P. 2016, MNRAS, 458, 3466

Virtanen, P., Gommers, R., Oliphant, T. E., Haberland, M., Reddy, T., Cournapeau, D., Burovski, E., Peterson, P., Weckesser, W., Bright, J., van der Walt, S. J., Brett, M., Wilson, J., Millman, K. J., Mayorov, N., Nelson, A. R. J., Jones, E., Kern, R., Larson, E., Carey, C. J., Polat, İ., Feng, Y., Moore, E. W., VanderPlas, J., Laxalde, D., Perktold, J., Cimrman, R., Henriksen, I., Quintero, E. A., Harris, C. R., Archibald, A. M., Ribeiro, A. H., Pedregosa, F., van Mulbregt, P., & SciPy 1.0 Contributors. 2020, Nature Methods, 17, 261

Watkins, E. J., Kreckel, K., Groves, B., Glover, S. C. O., Whitmore, B. C., Leroy, A. K., Schinnerer, E., Meidt, S. E., Egorov, O. V., Barnes, A. T., Lee, J. C., Bigiel, F., Boquien, M., Chandar, R., Chevance, M., Dale, D. A., Grasha, K., Klessen, R. S., Kruijssen, J. M. D., Larson, K. L., Li, J., Méndez-Delgado, J. E., Pessa, I., Saito, T., Sanchez-Blazquez, P., Sarbadhicary, S. K., Scheuermann, F., Thilker, D. A., & Williams, T. G. 2023, A&A, 676, A67

Weilbacher, P. M., Monreal-Ibero, A., Kollatschny, W., Ginsburg, A., McLeod, A. F., Kamann, S., Sandin, C., Palsa, R., Wisotzki, L., Bacon, R., Selman, F., Brinchmann, J., Caruana, J., Kelz, A., Martinsson, T., Pécontal-Rousset, A., Richard, J., & Wendt, M. 2015, A&A, 582, A114

Whitmore, B. C., Allam, S. S., Budavári, T., Casertano, S., Downes, R. A., Donaldson, T., Fall, S. M., Lubow, S. H., Quick, L., Strolger, L.-G., Wallace, G., & White, R. L. 2016, AJ, 151, 134

Williams, T. G., Kreckel, K., Belfiore, F., Groves, B., Sandstrom, K., Santoro, F., Blanc, G. A., Bigiel, F., Boquien, M., Chevance, M., Congiu, E., Emsellem, E., Glover, S. C. O., Grasha, K., Klessen, R. S., Koch, E., Kruijssen, J. M. D., Leroy, A. K., Liu, D., Meidt, S., Pan, H.-A., Querejeta, M., Rosolowsky, E., Saito, T., Sánchez-Blázquez, P., Schinnerer, E., Schruba, A., & Watkins, E. J. 2022, MNRAS, 509, 1303

Wolfire, M. G., Hollenbach, D., McKee, C. F., Tielens, A. G. G. M., & Bakes, E. L. O. 1995, ApJ, 443, 152

Wood, D. O. S., & Churchwell, E. 1989, ApJS, 69, 831

Woosley, S. E., & Weaver, T. A. 1995, ApJS, 101, 181

Wyse, A. B. 1942, ApJ, 95, 356

Yates, R. M., Henriques, B. M. B., Fu, J., Kauffmann, G., Thomas, P. A., Guo, Q., White, S. D. M., & Schady, P. 2021, MNRAS, 503, 4474

Yates, R. M., Schady, P., Chen, T. W., Schweyer, T., & Wiseman, P. 2020, A&A, 634, A107

Zakardjian, A., Pety, J., Herrera, C. N., Hughes, A., Oakes, E., Kreckel, K., Faesi, C., Glover, S. C. O., Groves, B., Klessen, R. S., Meidt, S., Barnes, A., Belfiore, F., Bešlić, I., Bigiel, F., Blanc, G. A., Chevance, M., Dale, D. A., den Brok, J., Eibensteiner, C., Emsellem, E., García-Rodríguez, A., Grasha, K., Koch, E. W., Leroy, A. K., Liu, D., Mc Elroy, R., Neumann, L., Pan, H.-A., Querejeta, M., Razza, A., Rosolowsky, E., Saito, T., Santoro, F., Schinnerer, E., Sun, J., Usero, A., Watkins, E. J., & Williams, T. 2023, A&A, 678, A171

Zaritsky, D., Kennicutt, Robert C., J., & Huchra, J. P. 1994, ApJ, 420, 87

Zeippen, C. J. 1982, MNRAS, 198, 111

Zhang, S., Zavagno, A., López-Sepulcre, A., Liu, H., Louvet, F., Figueira, M., Russeil, D., Wu, Y., Yuan, J., & Pillai, T. G. S. 2021, A&A, 646, A25

Zhang, Y., Ercolano, B., & Liu, X. W. 2007, A&A, 464, 631

Zhang, Y., Liu, X. W., Wesson, R., Storey, P. J., Liu, Y., & Danziger, I. J. 2004, MNRAS, 351, 935

Zhou, X., Su, Y., Yang, J., Chen, X., Sun, Y., Jiang, Z., Wang, M., Wang, H., Zhang, S., Xu, Y., Yan, Q., Yuan, L., Chen, Z., Ao, Y., & Ma, Y. 2023, arXiv e-prints, arXiv:2308.03484

Zurita, A., Florido, E., Bresolin, F., Pérez-Montero, E., & Pérez, I. 2021, MNRAS, 500, 2359